PEOPLE'S DEMOCRATIC REPUBLIC OF ALGERIA
MINISTRY OF HIGHER EDUCATION AND SCIENTIFIC RESEARCH
UNIVERSITY OF YAHIA FARES, MEDEA
FACULTY OF TECHNOLOGY
DEPARTMENT OF MECHANICAL ENGINEERING



THESIS Entitled:

Study of the Linear and non-Linear Stability of Thermosolutal Convection Within a Porous Medium Saturated by a non-Newtonian Binary Fluid

IS SUBMITTED FOR THE PURPOSE OF OBTAINING

PH.D. DEGREE IN MECHANICAL ENGINEERING

Option: Energy

By

KHIR Saleh

Presented on: 06/29/2024

IN FRONT OF THE JURY COMPOSED OF:

ZIRARI Mounir	Professor	Medea University	President
HENNICHE Rabah	MCA	Medea University	Examiner
BENSEDIRA Sidali	MCA	Blida 1 University	Examiner
REBHI Redha	MCA	Medea University	Research Supervisor
KEZRANE Mohamed	Professor	Medea University	Research Co-supervisor

RÉPUBLIQUE ALGÉRIENNE DÉMOCRATIQUE ET POPULAIRE

MINISTÈRE DE L'ENSEIGNEMENT SUPÉRIEUR ET DE LA RECHERCHE SCIENTIFIQUE

UNIVERSITÉ YAHIA FARES DU MÉDÉE

FACULTÉ DE TECHNOLOGIE

DÉPARTEMENT DE GÉNIE MÉCANIQUE



Cette thèse intitulée :

Etude de La Stabilité Linéaire et Non-Linéaire de La Convection Thermosolutale au Sein d'un Milieu Poreux Saturé Par un Fluide Binaire Non-Newtonien

EST PRÉSENTÉE EN VUE DE L'OBTENTION

DU DIPLÔME DE DOCTORAT EN GÉNIE MÉCANIQUE

Option : Énergétique

Par

KHIR Saleh

Soutenue le : 29/06/2024

DEVANT LE JURY COMPOSÉ DE :

ZIRARI Mounir	Professeur	Université de Médéa	Président
HENNICHE Rabah	MCA	Université de Médéa	Examinateur
BENSEDIRA Sidali	MCA	Université de Blida 1	Examinateur
REBHI Redha	MCA	Université de Médéa	Directeur de recherche
KEZRANE Mohamed	Professeur	Université de Médéa	Co-directeur de recherche

DEDICATIONS

This work is dedicated to my dear parents, my brothers, and my sisters.

ACKNOWLEDGMENT

I must first thank Allah, my creator, for giving me the strength to accomplish this work and for guiding me towards the right path of light and knowledge.

I extend my heartfelt gratitude to all those who have contributed to the completion of this endeavor. Their support, encouragement, and guidance have been invaluable throughout this journey.

First and foremost, I would like to express my deepest appreciation to my supervisor, **REBHI Redha**, whose expertise, insight, and unwavering support have been instrumental in shaping this project. Your guidance has challenged me to reach new heights and has profoundly enriched my understanding of the subject matter, and I am truly fortunate to have had the opportunity to work alongside such supervisor.

Furthermore, I extend my thanks to my Co-supervisor Professor **KEZRAN Mohamed** for his support, which enabled me to pursue this research with dedication and focus.

I would also like to address my thanks to Pr. **ZIRARI Mounir** for agreeing to chair the examination jury for this thesis. I also thank the Dr. **HENNICHE Rabah**, and the Dr **BENSEDIRA Sidali** for having accepted to examine this thesis and to participate in my jury and for the interest they have shown in our research work, despite their multiple occupations.

Last but not least, I wish to thank my family and friends for their unwavering love, encouragement, and understanding throughout this journey. Your belief in me has been a source of strength, and I am profoundly grateful for your unwavering support.

To all those who have contributed in any way, large or small, to the completion of this project, please accept my sincerest thanks. Your support has been truly invaluable, and I am deeply appreciative of the role you have played in bringing this endeavor to fruition.

With heartfelt gratitude,

KHIR Saleh

ABSTRACT

This study, presents a numerical study of the linear and non-linear stability of thermosolutary convection within a porous medium saturated by a non-Newtonian binary fluid. The power-law model is utilized for modeling the behavior of the working medium. The given statement implies that the long side of the cavity experience thermal and solutal flow rates, whereas the others walls are impermeable and thermally isolated. The problem is characterized by a set of tightly linked non-linear differential equations, named governing equations, that include the mass conservation equation (known as the continuity equation), the momentum equation, the energy equation, and the species equation. The relevant factors that govern the problem being investigated are the Rayleigh number, R_T, the power-law index, n, the angle of inclination, Φ, the cavity aspect ratio, A, the Lewis number, Le, the normalized porosity, ξ, and the buoyancy ratio, N, three types of cavity configuration have been studied: horizontal cavity (i.e. $\Phi = 0°$), inclined cavity (i.e. $\Phi \neq 0°$), then we have studied the case of a vertical cavity (i.e. $\Phi = 90°$) where the buoyancy forces induced by the thermal and solutal effects are opposing each other and of equal intensity ($N = -1$). An analytical solution is obtained for shallow enclosures ($A >> 1$) using the parallel flow approximation, and a modified form of the Darcy equation. By solving the entire set of governing equations, a numerical investigation of the same phenomenon was conducted. One of the most intriguing discoveries from this research is that it identifies a bi-stability phenomenon, this particular phenomenon signifies the existence of two stable solutions. Plus, it is demonstrated that both the inclination of the layer, Φ, and the power-law index, n, have a strong influence on the strength of the intensity of flow, Ψ_0, the heat transfer rate, Nu, and the mass transfer rate, Sh, within the enclosure. The results obtained from both methods demonstrate a good level of agreement across a diverse range of these governing parameters.

Keywords: Bi-stability, Thermosolutal convection, power-law fluid, porous layer, non-Newtonian binary fluid.

RÉSUMÉ

Cette étude, présente une étude numérique de la stabilité linéaire et non linéaire de la convection Thermosolutal dans un milieu poreux saturé par un fluide binaire non-Newtonien. Le modèle de loi de puissance est utilisé pour modéliser le comportement du milieu de travail. L'énoncé donné implique que le côté long de la cavité subit des débits de flux thermique et solutal, tandis que les autres parois sont imperméables et thermiquement isolées. Le problème est caractérisé par un ensemble d'équations différentielles non linéaires étroitement liées, appelées équations gouvernantes, comprenant l'équation de conservation de la masse (connue sous le nom d'équation de continuité), l'équation de la quantité de mouvement, l'équation de l'énergie et l'équation des espèces. Les facteurs pertinents qui régissent le problème étudié sont le nombre de Rayleigh, R_T, l'indice de la loi de puissance, n, l'angle d'inclinaison, Φ, le rapport d'aspect de la cavité, A, le nombre de Lewis, Le, la porosité normalisée, ξ, et le rapport de flottabilité, N. Trois types de configuration de cavité ont été étudiés : cavité horizontale (c'est-à-dire $\Phi = 0°$), cavité inclinée (c'est-à-dire $\Phi \neq 0°$), puis nous avons étudié le cas d'une cavité verticale (c'est-à-dire $\Phi = 90°$) où les forces de flottabilité induites par les effets thermiques et solutaux s'opposent et sont d'intensité égale ($N = -1$). Une solution analytique est obtenue pour les enceintes peu profondes ($A >> 1$) en utilisant l'approximation du flux parallèle et une forme modifiée de l'équation de Darcy. En résolvant l'ensemble des équations gouvernantes, une investigation numérique du même phénomène a été menée. Une des découvertes les plus intrigantes de cette recherche est qu'elle identifie un phénomène de bistabilité, ce phénomène particulier signifie l'existence de deux solutions stables. De plus, il est démontré que tant l'inclinaison de la couche, Φ, que l'indice de la loi de puissance, n, ont une forte influence sur la force de l'intensité du flux, Ψ_0, le taux de transfert de chaleur, Nu, et le taux de transfert de masse, Sh, à l'intérieur de l'enceinte. Les résultats obtenus à partir des deux méthodes démontrent un bon niveau d'accord sur une gamme diversifiée de ces paramètres gouvernants.

Mots-clés : Bi-stabilité, convection Thermosolutale, fluide de loi de puissance, couche poreuse, fluide binaire non-Newtonien.

ملخص

تقدم هذه الورقة دراسة عددية لاستقرار الحركة المؤثرة بالحرارة والمحاليل الذائبة بشكل خطي وغير خطي داخل وسط مسامي مشبع بسائل ثنائي غير نيوتوني. يتم استخدام نموذج القوة القانونية لتصميم سلوك الوسط العامل. البيان المعطى يعني أن الجانب الطويل للتجويف يتعرض لمعدلات تدفق حرارية وكيميائية، بينما تكون الجدران الأخرى غير مسامية ومعزولة حراريا. يتميز الموضوع بمجموعة من المعادلات التفاضلية غير الخطية المترابطة بإحكام، تُعرف بمعادلات الحكم، تشمل معادلة حفظ الكتلة (المعروفة بمعادلة الاستمرارية)، ومعادلة الحركة، ومعادلة الطاقة، ومعادلة النوع. العوامل ذات الصلة التي تحكم المشكلة المدروسة هي عدد رايلي، R_T، ومؤشر القانون القوي، n، وزاوية الانحدار، Φ، ونسبة جانب التجويف، A، وعدد لويس، Le، والمسامية الموحدة، ξ، ونسبة الطفو، N تمت دراسة ثلاثة أنواع من تكوينات التجويف: تجويف أفقي أي($\Phi = 0°$)، وتجويف مائل أي($\Phi \neq 0°$)، ثم تمت دراسة حالة تجويف رأسي أي ($\Phi = 90°$) حيث تكون القوى الطافية الناتجة عن التأثيرات الحرارية والكيميائية معارضة لبعضها البعض ومتساوية الشدة ($N = -1$). يتم الحصول على حلاً تحليلياً للتجاويف الضحلة ($A >> 1$) باستخدام تقريب التدفق الموازي ونموذج معدل لمعادلة دارسي. من خلال حل مجموعة كاملة من معادلات الحاكمة، تم إجراء تحقيق عددي لنفس الظاهرة. واحدة من أكثر الاكتشافات الشيقة من هذا البحث هو أنه يحدد ظاهرة الاستقرار المزدوج، هذه الظاهرة الخاصة تعني وجود حلين مستقرين. بالإضافة إلى ذلك، يُظهر أن كل من انحدار الطبقة، Φ، ومؤشر القانون القوي، n، لهما تأثير قوي على قوة شدة التدفق، Ψ_0، ومعدل نقل الحرارة، Nu، ومعدل نقل الكتلة، Sh، داخل التجويف. تُظهر النتائج المتحصلة من كلتا الطريقتين مستوى جيدًا من التوافق عبر مجموعة متنوعة من هذه المعلمات الحاكمة.

الكلمات المفتاحية: استقرار مزدوج، حركة مؤثرة بالحرارة والمحاليل الذائبة، سائل قانوني السلوك، طبقة مسامية، سائل ثنائي غير نيوتوني.

TABLE OF CONTENTS

DEDICATIONS ..... **i**

ACKNOWLEDGMENT ..... **ii**

ABSTRACT ..... **iii**

RÉSUMÉ ..... **iv**

ملخص ..... **v**

TABLE OF CONTENTS ..... **vi**

LIST OF FIGURES ..... **x**

LIST OF TABLES ..... **xiv**

NOMENCLATURE ..... **xv**

GENERAL INTRODUCTION **1**

CHAPTER I : GENERALITIES **4**

1.1. HEAT TRANSFER **4**

1.1.1 HEAT CONVECTION 4

1.2 MASSE TRENSFER **6**

1.2.1 MASSE DIFFUSION 6

1.2.2 MASSE CONVECTION 6

1.3 THERMO-SOLUTALE CONVECTION **7**

1.4 DIMENSIONLESS NUMBERS **7**

1.4.1 THE RAYLEIGH NUMBER 8

1.4.2 THE NUSSELT NUMBER 8

1.4.3 SHERWOOD NUMBER 8

1.4.4 LEWIS NUMBER 9

1.5 BOUSSINESQ APPROXIMATION **9**

1.6 NON-NEWTONIAN FLUIDS **11**

1.6.1 TIME-INDEPENDENT FLUIDS 12

1.6.2 TIME-DEPENDENT FLUIDS 13

1.6.3 VISCOELASTIC MATERIAL 14

1.7 NON-NEWTONIAN RHEOLOGICAL MODELS **14**

1.7.1 POWER-LAW MODEL 14

1.7.2 CROSS MODEL 16

1.7.3 ELLIS MODEL 17

1.7.4 BINGHAM MODEL 17

1.7.5 HERSCHEL-BULKLEY MODEL 18

1.7.6 SISKO MODEL 19

1.7.7 CARREAU-YASUDA MODEL 19

1.8 POROUS MEDIA **20**

1.8.1 CONCEPT OF REPRESENTATIVE ELEMENTARY VOLUME (R.E.V) 21

1.8.2 CLASSIFICATION AND CHARACTERIZATION OF POROUS MEDIA 22

1.8.2.1 CLASSIFICATION 22

1.8.2.2 CHARACTERIZATION 23

1.8.3 FLOW MODELS IN POROUS MEDIA 26

1.8.3.1 DARCY'S LAW 1875 26

1.8.3.2 DUPUIT-DARCY'S LAW 29

1.8.3.3 DARCY-BRINKAMAN'S LAW 30

1.8.3.4 GENERAL MODEL 30

1.9 LITERATURE REVIEW **31**

CHAPTER II : PHYSICAL MODEL AND MATHEMATICAL FORMULATION **37**

2.1 PROBLEM DESCRIPTION **37**

2.2 SIMPLIFYING ASSUMPTIONS **38**

2.3 MATHEMATICAL FORMULATION **39**

2.3.1 CONTINUITY EQUATION 39

2.3.2 EQUATION OF MOTION: Darcy's Law 39

2.3.3 EQUATION OF VISCOSITY 40

2.3.3 ENERGY CONSERVATION EQUATION 40

2.3.4 MASS CONSERVATION EQUATION 40

2.4 STREAM FUNCTION EQUATION **42**

2.5 BOUNDARY CONDITIONS **42**

2.5.1 HYDRODYNAMIC BOUNDARY CONDITIONS 42

2.5.3 DIMENSIONLESS BOUNDARY CONDITIONS 42

2.6 THERMAL AND MASS TRANSFER RATE **43**

CHAPTER III : ANALYTICAL SOLUTION **44**

3.1 HORIZONTAL LAYER: $\Phi = 0°$ AND $\Phi = 180°$ **45**

3.1.1 NON-NEWTONIAN FLUID $n \neq 1$ 46

3.1.2 NEWTONIAN FLUID $n = 1$ 48

3.2 INCLINED LAYER: $0° \leq \Phi \leq 180°$ **49**

CHAPTER IV : NUMERICAL SOLUTION **51**

4.1 DISCRETIZATION OF THERMAL BOUNDARY CONDITIONS **52**

4.2 DISCRETIZATION OF THE ENERGY EQUATION **52**

4.3 DISCRETIZATION OF THE CONCENTRATION EQUATION **54**

4.4 DISCRETIZATION OF THE VELOCITY **56**

4.5 DISCRETIZATION OF VELOCITY BOUNDARY CONDITIONS **56**

4.6 DISCRETIZATION OF THE VISCOSITY **56**

4.7 DISCRETIZATION OF THE MOTION EQUATION **57**

4.8 CALCULATION ALGORITHM **58**

4.9 CALCULATION ORGANIGRAM **59**

4.10 MESH CHOICE **60**

4.11 VALIDATION OF NUMERICAL CODE **61**

CHAPTER V: LINEAR STABILITY ANALYSIS IN A POROUS LAYER **64**

5.1 THEORY OF LINEAR STABILITY FOR CONVECTIVE FLOW **65**

5.2 NUMERICAL SOLUTION **66**

5.3 STABILITY OF THE REST STATE **70**

5.3.1 LINEAR STABILITY THEORY 70

5.3.2 MARGINAL STABILITY: P=0 70

5.3.3 TRANSIENT STABILITY: $p \neq 0$ 72

CHAPTER VI : RESULTS AND DISCUSSION **74**

6.1 HORIZONTAL LAYER: $\Phi = 0°$ **74**

6.1.1 CASE OF SHALLOW LAYER: $A \gg 1$ 75

4.1.2 CASE OF SQUARE CAVITY: $A = 1$ 95

6.2 INCLINED LAYER: $-180° \leq \Phi \leq +180°$ **111**

6.3 VERTICAL LAYER: $\Phi = 90°$ **119**

CHAPTER VII: GENERAL CONCLUSIONS **125**

7.1 HORIZONTAL LAYER ($A \gg 1$) **125**

7.2 SQUARE LAYER ($A = 1$) **127**

7.3 INCLINED LAYER ($A \gg 1$) **127**

7.4 VERTICAL LAYER ($A \gg 1$) **128**

7.5 RECOMMENDATIONS AND PERSPECTIVES **129**

REFERENCES **130**

LIST OF FIGURES

Figure 1.1	heat transfer by convection.	4
Figure 1.2	The three differents modes of convection.	4
Figure 1.3	mass Transfer.	5
Figure 1.4	Typical shear stress and shear rate relationships for non-Newtonian fluids.	12
Figure 1.5	Typical Time-independent fluids.	13
Figure 1.6	Flow curves for time-dependent thixotropic and rheopectic non-Newtonian fluids.	13
Figure 1.7	Evolution of the strain rate within a viscoelastic fluid during a creep test.	14
Figure 1.8	Viscosity behavior of pseudoplastic shear-thinning fluids, with maximum and minimum limiting viscosities.	15
Figure 1.9	Rheogram of an ideal plastic fluid (Bingham fluid).	18
Figure 1.10	Rheogram of a shear-thinning plastic fluid.	18
Figure 1.11	Carreau-Yasuda model for three polymer solutions expressing apparent viscosity (vertical axis) as a function of shear rate (horizontal axis).	20
Figure 1.12	Some examples of porous media	21
Figure 1.13	The representative elementary volume (r.e.v.): the figure illustrates the intermediate size relative to the sizes of the flow domain and the pores.	22
Figure 1.14	Schematic Definition of Tortuosity	25
Figure 1.15	Permeability Measuring Device on Consolidated Material.	27
Figure 2.1	Schematic representation of the physical model and the coordinate system.	37
Figure 4.1	Mesh of the calculation domain in (i, j).	51
Figure 4.2	Influence of the cavity aspect ratio, A, on (a) the flow intensity at the cavity center, Ψ_0, (b) the heat transfers, (Nu_c and Nu_m), (c) the mass transfers, (Sh_c and Sh_m), for $n = 1.1$, $R_T = 100$, $Le = 5$, and $N = -0.1$.	63
Figure 5.1	Schematic representation of the cubic Hermite element.	68
Figure 6.1	Contours of streamlines, Ψ, Temperature, T, Concentration, S, horizontal velocity, U, and apparent viscosity, μ_a, for $R_T = 100$, $Le = 5$, $N = -0.1$ and various values of n.	76
Figure 6.2	Effect of the power-law index, n, on (a) the horizontal velocity, U, (b) apparent viscosity, μ_a, (c) temperature, T, and (d) concentration, S	77
Figure 6.3	Bifurcation diagram in terms of Ψ_0 as the function of R_T and n	78
Figure 6.4	Bifurcation diagram as a function of R_T and n: (a) flow intensity Ψ_0, (b) Nusselt number Nu, and (c) Sherwood number, Sh.	80
Figure 6.5	Contours of streamlines, Ψ_0, temperature, T, concentration, S, and apparent viscosity μ_a.	81

Figure 6.6	Buoyancy ratio, N, and power-law index, n, effects on the critical Rayleigh numbers (R_{TC}^{sub}, R_{TC}^{tur}, and R_{TC}^{sup})	83
Figure 6.7	Bifurcation diagram as a function of R_T and N: (a) flow intensity Ψ_0, (b) Nusselt number Nu, and (c) Sherwood number Sh	84
Figure 6.8	Contours of streamlines, Ψ_0, temperature, T, concentration, S, and apparent viscosity μ_a	85
Figure 6.9	Effect of Lewis number, Le, and Power-law index, n, on the critical Rayleigh numbers (R_{TC}^{sub}, R_{TC}^{tur}, and R_{TC}^{sup}).	86
Figure 6.10	Bifurcation diagram as a function of R_T and Le: (a) flow intensity Ψ_0, (b) Nusselt number Nu, and (c) Sherwood number Sh	88
Figure 6.11	Effect of the buoyancy ratio, N, and Power-law index, n, on (a) flow intensity Ψ_0, (b) Nusselt number Nu, and (c) Sherwood number Sh	89
Figure 6.12	Effect of the Lewis number, Le, and Power-law index, n, on (a) flow intensity Ψ_0, (b) Nusselt number Nu, and (c) Sherwood number Sh For $N = 0.0, -0.1, and\ -0.8$	91
Figure 6.13	Large Rayleigh number R_T and power-law index n effects on (a) the flow intensity Ψ_0 and (b) the Nusselt Nu and Sherwood Sh number	92
Figure 6.14	Effect of the power-law index, n, and the buoyancy ratio, N, on: (a) the flow intensity at the center of the cavity Ψ_0, (b) the Nusselt number, Nu, and (c) the Sherwood number, Sh, for $R_T = 100$, $Le = 5$.	94
Figure 6.15	Contours of streamlines, Ψ, Temperature, T, Concentration, S, horizontal velocity, U, and apparent viscosity, μ_a, for $R_T = 100$, $Le = 5$, $N = -0.1$ and various values of n, with Neumann-type boundary conditions	96
Figure 6.16	Contours of streamlines, Ψ, Temperature, T, Concentration, S, horizontal velocity, U, and apparent viscosity, μ_a, for $R_T = 100$, $Le = 5$, $N = -0.1$ and various values of n, with Dirichlet-type boundary conditions	97
Figure 6.17	Contours of streamlines, Ψ, Temperature, T, Concentration, S, horizontal velocity, U, and apparent viscosity, μ_a, for $R_T = 100$, $Le = 5$, $N = -0.1$, $n = 1.2$ and various values of Φ, with Neumann-type boundary conditions	99
Figure 6.18	Contours of streamlines, Ψ, Temperature, T, Concentration, S, and apparent viscosity, μ_a, for $R_T = 100$, $Le = 5$, $N = -0.1$, $n = 1.2$ and various values of Φ, with Dirichlet-type boundary conditions	99
Figure 6.19	Effect of the power-law index, n, on the profiles of (a) the horizontal velocity, U, (b) apparent viscosity, μ_a, (c) temperature, T, and (d) concentration, S, under Neumann-type boundary conditions	101
Figure 6.20	Effect of the power-law index, n, on the profiles of (a) the horizontal velocity, U, (b) apparent viscosity, μ_a, (c) temperature, T, and (d) concentration, S, under Dirichlet-type boundary conditions	102
Figure 6.21	Effects of the inclination angle, Φ, and the power-law index, n, for $R_T = 100$, on: (a) stream function at the center of the cavity Ψ_0, (b) Nusselt number Nu, and (c) Sherwood number Sh. exposed to Neumann-type boundary conditions	104

Figure 6.22	Effects of the inclination angle, Φ, and the power-law index, n, for $R_T = 100$, on: (a) stream function at the center of the cavity Ψ_0, (b) Nusselt number Nu, and (c) Sherwood number Sh. exposed to Dirichlet-type boundary conditions	104
Figure 6.23	Effects of the buoyancy ratio, Nu, and the power-law index, n, for $R_T = 100$, and $Le = 5$, on: (a) stream function at the centre of the cavity Ψ_0, (b) Nusselt number Nu, and (c) Sherwood number Sh. exposed to Neumann-type boundary conditions	106
Figure 6.24	Effects of the buoyancy ratio, Nu, and the power-law index, n, for $R_T = 100$, and $Le = 5$, on: (a) stream function at the centre of the cavity Ψ_0, (b) Nusselt number Nu, and (c) Sherwood number Sh. exposed to Neumann-type boundary conditions.	107
Figure 6.25	Bifurcation diagram in terms of Ψ_0, Nu, and Sh as a function of R_T and n for $A = 1$, $Le = 5$, $N = -0.1$: [(a)–(c)] $n = 0.8$ to 1.4.(d) Contours of streamlines, temperature, concentration, and apparent viscosity for $R_T = 35$, $n = 1.1$: $\Psi_0 = 0.9664$, $Nu = 1.2439$, $Sh = 4.0523$, and $\mu_a = 0$ (upper solution). (e) Contours of streamlines, temperature, concentration, and apparent viscosity for $R_T = 35$, $n = 1.1$: $\Psi_0 = 0.0277$, $Nu = 1.0003$, $Sh = 1.0098$, and $\mu_a = 0$ (lower solution) (for Neumann boundary conditions).	108
Figure 6.26	Bifurcation diagram in terms of Ψ_0, Nu, and Sh as a function of R_T and n for $A = 1$, $Le = 5$, $N = -0.1$: [(a)–(c)] $n = 0.8$ to 1.4.(d) Contours of streamlines, temperature, concentration, and apparent viscosity for $R_T = 35$, $n = 1.1$: $\Psi_0 = 0.9664$, $Nu = 1.2439$, $Sh = 4.0523$, and $\mu_a = 0$ (upper solution). (e) Contours of streamlines, temperature, concentration, and apparent viscosity for $R_T = 35$, $n = 1.1$: $\Psi_0 = 0.0277$, $Nu = 1.0003$, $Sh = 1.0098$, and $\mu_a = 0$ (lower solution) (for Dirichlet boundary conditions)	109
Figure 6.27	Numerical solutions for streamlines, isotherms, isoconcentration, and apparent viscosity with $R_T = 50$, $n = 1.2$, $Le = 5$, $N = -0.1$ and $A = 6$ for (a) $\Phi = 0°$, (b) $\Phi = 60°$, (c) $\Phi = 120°$.	112
Figure 6.28	Streamlines, isotherms, isoconcentration, and apparent viscosity for (a) $R_T = 50$, $n = 0.6$, $\Phi = 45$, (b) $R_T = 50$, $n = 1.0$, $\Phi = 45$, (c) $R_T = 50$, $n = 1.4$, $\Phi = 45$	112
Figure 6.29	Effect of inclination angle, Φ, on (a) the horizontal velocity, U, (b) apparent viscosity, μ_a, (c) temperature, T, and (d) concentration, S.	114
Figure 6.30	Effects of inclination angle Φ and power-law index n, for $R_T = 50$, on: (a) stream function at the center of the cavity Ψ_0, (b) Nusselt number Nu, and (c) Sherwood number Sh	115
Figure 6.31	Effects of inclination angle Φ and power-law index n, for $R_T = 50$, on: (a) constant temperature gradient C_T, (b) constant concentration gradient C_S, and (c) maximum inclination angle Φ_{CR}	117

Figure 6.32	Effects of power-law index n, and inclination angle Φ, for $R_T = 50$, on: stream function Ψ_0 at the center of the cavity, (b) Nusselt number Nu, and (c) Sherwood number Sh	118
Figure 6.33	Numerical solutions for the Streamlines, isotherms, concentration, and apparent viscosity fields in a vertical cavity ($\Phi = 90°$) with $R_T = 100$, $Le = 5$, and $N = -1$ for (a) $n = 1.4$, $\Psi_0 = 2.132$, $Nu = 2.161$, $Sh = 4.572$, and $\mu_a = 0.273$ (b) $n = 0.6$, $\Psi_0 = 3.547$, $Nu = 3.910$, $Sh = 6.431$, and $\mu_a = 18.005$ (c) $n = 1.0$, $\Psi_0 = 2.672$, $Nu = 2.733$, $Sh = 5.095$, and $\mu_a = 1.000$	119
Figure 6.34	Effect of power-law index n with $\Phi = 90°$, on (a) the horizontal velocity, U, (b) apparent viscosity, μ_a, (c) temperature, T, and (d) concentration, S.	120
Figure 6.35	Large Rayleigh number R_T and power-law index n effects on (a) the flow intensity Ψ_0 and (b) the Nusselt Nu and Sherwood Sh number.	121
Figure 6.36	Effect of Lewis number Le and power-law index n on (a) the flow intensity Ψ_0, (b) the Nusselt number Nu, and (c) Sherwood number Sh	123
Figure 6.37	Effect of Buoyancy ratio N and power-law index n on (a) the flow intensity Ψ_0, (b) the Nusselt number Nu, and (c) Sherwood number Sh.	124

LIST OF TABLES

Table 1.1	Properties of fluids for water and air at T_0=15°C, P_0=1atm.	11
Table 1.2	Typical values of power distribution model constants for selected substances.	16
Table 1.3	Rheological parameters of the rheological equation of state	19
Table 1.4	Porosity of selected materials.	24
Table 1.5	Permeability of selected materials	24
Table 1.6	Surface per unit volume of selected materials	26
Table 4.1	Convergence tests for specified parameters, $A = 6$, $Le = 5$, $N = -0.1$, $R_T = 100$, $\Phi = 0°$, and $n = 1.2$.	60
Table 4.2	Convergence tests for specified parameters, $A = 6$, $Le = 5$, $N = -0.1$, $R_T = 50$, and $n = 1.2$, and different angles of inclination Φ.	60
Table 4.3	Convergence tests for specified parameters, $A = 6$, $Le = 5$, $N = -1$, $R_T = 100$, and $\Phi = 90°$, and different values of power-law index n	61
Table 4.5	Comparison of Ψ_0, and Nu with previous numerical studied of Amari et al. [29] for $N = 0$, $Le = 5$, and various values of n, with horizontal cavity	61
Table 4.6	Comparison of Ψ_0, Nu and Sh with previous numerical studied of Ben Khelifa et al. [88] for $N = 0.2$, $Le = 10$, and various values of n, with horizontal cavity	62
Table 4.7	Comparison of Ψ_0, and Nu with previous numerical studied of Bian et al. [5] for $R_T = 100$, $n = 1.2$, $N = 0$, and $A = 4$ with various inclination angle Φ.	62
Table 4.8	Comparison of Ψ_0, Nu and Sh with previous numerical studied of Ben Khelifa et al. [120] for $R_T = 200$, $N = 1$, $Le = 10$, $A = 4$, and $\Phi = 90°$ with various values of n	62
Table 5.1	Gauss Points	70
Table 6.1	Dependence of R_{TC}^{sub}, R_{TC}^{tur} and R_{TC}^{sup} on n for $Le = 7.0$ and $N = -0.1$.	79
Table 6.2	Dependence of R_{TC}^{sub}, R_{TC}^{tur} and R_{TC}^{sup} on n for $Le = 5.0$ and $N = -0.1$.	82
Table 6.3	Dependence of R_{TC}^{sub}, R_{TC}^{tur} and R_{TC}^{sup} on N for $Le = 5.0$ and $n = 1.2$.	86
Table 6.4	Dependence of R_{TC}^{sub}, R_{TC}^{tur} and R_{TC}^{sup} on Le for $n = 1.1$ and $N = -0.1$.	87
Table 6.5	the influence of the power-law index, n on the existence of (N_{CR}^{sub}, and N_{CR}^{sup}) for $R_T = 100$, and $Le = 5$.	90
Table 6.6	the different values of $\Psi_0^{Le\to 0,\pm\infty}$, $Nu^{Le\to 0,\pm\infty}$, and $Sh^{Le\to 0,\pm\infty}$ for $R_T = 100$.	92
Table 6.7	Dependence of R_{TC}^{sub}, R_{TC}^{tur} and R_{TC}^{sup} on n for $Le = 5.0$ and $N = -0.1$.	110
Table 6.8	The subcritical values of Le for $R_T = 100$ and $N = -1$	122

NOMENCLATURE

A	aspect ratio of the cavity, L'/H'
C_S	dimensionless concentration gradient in x-direction,
C_T	dimensionless temperature gradient in x-direction,
D	Molecular diffusion coefficient, m^2/s
g	gravitational acceleration, m/s^2
h	consistency index, $Pa\ s^n$
H'	thickness of enclosure, m
j'	constant solute flux per unit area, $kg/(m\ s)$,
k	thermal conductivity, $W/(m\ K)$
K	permeability of porous medium, m^2
L'	length of cavity, m
Le	Lewis number, a/D
n	power-law index
N	buoyancy ratio, $\beta'_S \Delta S'/\beta'_T \Delta T'$
Nu	Nusselt number,
p'	Pressure
q'	constant heat flux per unit area, W/m^2,
R_T	thermal Rayleigh number, $K\rho_0 g\beta'_T \Delta T'(H'/\alpha)^n/\varepsilon$
S	dimensionless concentration
$\Delta S'$	characteristic concentration difference, $j'/\rho D$
Sh	Sherwood number,
T	dimensionless temperature
$\Delta T'$	characteristic temperature difference, $q'L'/k$
$\overrightarrow{V'}$	superficial velocity,
u	dimensionless velocity x-component
v	dimensionless velocity y-component
x, y	cartesian coordinates

Greek symbols

α	fluid thermal diffusivity, m^2/s
β'_S	solute expansion coefficients,
β'_T	thermal expansion coefficients,
ρ	density of fluid, kg/m^3
μ'_a	apparent viscosity in power-law model, $Pa\ s^{n-1}$,
ε	parameter in power-law model, $Pa\ s^n/m^{n-1}$,
ϕ	porosity of the porous medium
σ	heat capacity ratio, $(qC)_p/(qC)_f$
ξ	normalized porosity of the porous medium, $\xi = \phi/\sigma$
Ψ	dimensionless stream function, Ψ'/α
Φ	inclination angle of the cavity

Superscript

$'$	dimensional quantities
sub	Threshold value of subcritical convection
sup	Threshold value of supercritical convection
over	Threshold value of over-stability convection
osc	Value representing the transition from oscillating regime to direct regime
Hopf	Value representing the transition from steady convective regime to oscillatory regime

Operators

$J(f,g)$	$\frac{\partial f}{\partial y}\frac{\partial g}{\partial x}-\frac{\partial f}{\partial x}\frac{\partial g}{\partial y}$

Subscript

max	maximum value
0	condition at the origin of the coordinate system
o	refers to the value taken at the centre of the cavity

GENERAL INTRODUCTION

Convective heat and mass transfer driven by the double diffusive characteristics of non-Newtonian fluids within porous materials find extensive utility across diverse industrial domains such as chemistry, petrochemistry, metallurgy, energy production, and environmental research, among others. Natural convection arises when a temperature gradient is imposed on a fluid, prompting the ascent of warmer fluid and descent of cooler fluid, thereby establishing a circular flow pattern conducive to heat exchange between disparate temperature zones. Given its manifold applications across multiple sectors, this phenomenon has been subject to comprehensive investigation [1-3].

The temperature gradient not only triggers natural convection by causing density fluctuations in the fluid particles but also leads to concentration gradients. this event, encompassing the interplay of thermal buoyancy (due to the temperature gradient) and solutal buoyancy (arising from the concentration gradient), which signs up into the double diffusion domain (thermo-solutal convection), exhibiting intriguing dynamic phenomena.

Addressing a standard thermo-solutal convection quandary involves predicting temperature, concentration, and velocity distributions, as well as the flow vigor, given as function of diverse problem parameters. Additionally, this requires predicting heat transfer rates (denoted by the Nusselt number) and mass transfer rates (denoted by the Sherwood number) at the active boundary.

Non-Newtonian fluids are widely used in various industries, and understanding their rheological characteristics requires interdisciplinary knowledge. The power-law model is a commonly used approach for flow problems in porous media to analyze and comprehend the physics of these fluids [2].

Thesis originality

the primary aim of this investigation was focused on the phenomena of convective flow induced by double diffusion within an inclined porous layer filled with a non-Newtonian fluid, subjected to heating and salting from below. The non-Newtonian fluid behavior has been accurately characterized through the implementation of the power-law model, accepting a diverse range of fluid types, including shear-thinning ($n < 1$), shear-thickening ($n > 1$), and Newtonian fluids ($n = 1$). Employing a time-accurate finite difference method, the complete nonlinear

governing equations were numerically resolved. Additionally, an analytical solution for shallow enclosures was derived.

The outcomes of this study have significantly contributed to a better comprehension of the impact of various governing parameters, including the Rayleigh number R_T, the inclined angle Φ, the cavity aspect ratio A, the buoyancy force N, the normalized porosity ξ, and the Lewis number Le, on the flow intensity and the rates of heat and mass transfer over a wide range of fundamental parameters. The analytical approach applied to horizontal cavity will facilitate the prediction of diverse convective bifurcations, including critical supercritical R_{TC}^{sup}, and subcritical R_{TC}^{sub} marking the initiation of convection. Notably, the shapes of bifurcation branches underwent substantial alterations, particularly in scenarios involving opposing double-diffusive flows. The most noteworthy revelation was the emergence of Bistability bifurcation with increasing shear-thickening behavior of the fluid, leading to the occurrence of two distinct and stable solutions under identical flow conditions, a phenomenon until now unobserved in the context of Newtonian fluids.

Furthermore, aiming to explore the impact of non-zero inclination angles in the system, previous research in this domain has predominantly focused on the scenario of an inclined enclosure being uniformly heated [4,5], and thus did not account for the impact of both thermal and solutal flux rates experienced within the enclosure. The outcomes are expressed in relation to flow intensity, heat transfer rate, and mass transfer rate, and their dependence on the governing parameters is thoroughly examined. The numerical findings presented in this context contribute to an enhanced comprehension of the impact of the power-law index, n, and the angle of inclination, Φ, on natural convection within an inclined enclosure.

Thesis content:

In terms of the manuscript's structure, it comprises seven chapters along with a general introduction. The first chapter of this manuscript initially aims to recall definitions and fundamental concepts related to heat and mass convection. It will be followed by a review of important notions concerning rheology and the properties of Newtonian and non-Newtonian fluids, as well as the rheological models used in this study. The third part will focus essentially on an overview of porous media, accompanied by a detailed exposition of different flow models used in porous media. Furthermore, a bibliographic synthesis on the scientific contribution related to analytical, numerical, and experimental works on natural convection of Newtonian or non-Newtonian fluids is presented at the end of this chapter. The second chapter of the thesis

is dedicated to defining the geometry under study and presenting the mathematical formulation of the problem. This includes the fundamental equations governing the system and the associated boundary conditions. In the third chapter, we developed an analytical solution based on the parallel flow concept method for a shallow porous layer. In this scenario, the governing equations of the problem are reduced to ordinary differential equations that are analytically solvable. In the fourth chapter, we presented the numerical solution methods, opting for the finite difference method to discretize the equations governing our model. At the end of this chapter, we presented the resolution algorithm. The fifth chapter focuses on the various results obtained in this work and their discussions. The sixth chapter is dedicated to the development of a new general numerical technique, based on the finite element method, for studying the stability problem. Finally, in the seventh chapter, we presented the main findings along with a general conclusion and future prospects.

CHAPTER I

GENERALITIES

1.1. HEAT TRANSFER

As a result of temperature differences, one type of energy that is transferred between various systems is heat. Explaining the amount of heat transfer that occurs as a system change from one equilibrium state to another is one of the main aims of thermodynamic analysis. The field of study devoted to determining the speeds at which these energy transfers occur is known as heat transfer. It is noteworthy that the directed movement of energy in the form of heat always occurs from a medium with a higher temperature to one that is colder. When thermal equilibrium is reached and both media have reached the same temperature, the heat transmission process is completed [6].

Heat can be transferred in three different modes: conduction (molecular diffusion), convection (bulk fluid motion), and radiation. All modes of heat transfer require the existence of a temperature difference, and all modes are from the high-temperature medium to a lower-temperature one. In our study, the focus will be specifically on convection. Below we give a brief description of this mode.

1.1.1 HEAT CONVECTION

Convection, which combines the effects of conduction and fluid motion, is a mode of transferring energy between a solid surface and the nearby moving liquid or gas. The convection heat transfer increases with fluid motion speed. Heat transmission between a solid surface and the surrounding fluid occurs solely by conduction when there is no bulk fluid motion. Although bulk motion of the fluid increases heat transmission between the fluid and solid surface, it also makes calculating heat transfer rates more difficult [7].

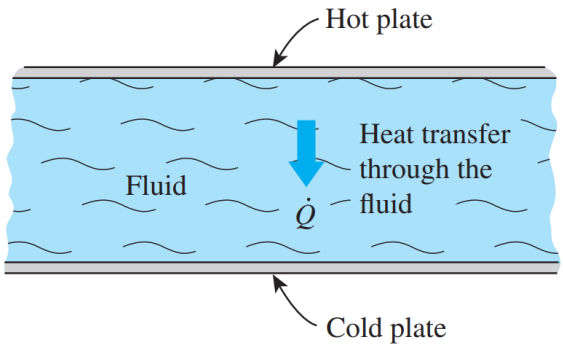


Figure 1.1: heat transfer by convection [6].

Despite the complexity of convection, the rate of convection heat transfer is observed to be proportional to the temperature difference, and is conveniently expressed by Newton's law of cooling as:

$$\dot{Q}_{conv} = hA_s(T_s - T_\infty) \quad (W) \tag{1.1}$$

where

h: convection heat transfer coefficient, $W/m^2.K$

A_s : heat transfer surface area, m^2

T_s : temperature of the surface, $°C$

T_∞ : temperature of the fluid sufficiently far from the surface, $°C$

Convection is classified as natural (or free), forced convection, and mixed convection, according to the nature of the flow.

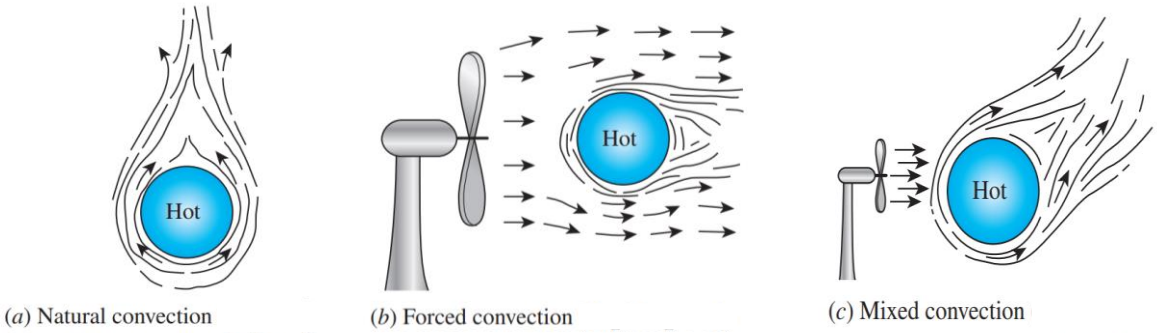


Figure 1.2:The three differents modes of convection [6].

In forced convection, the fluid is forced to flow over a surface or in a pipe by external means such as a pump or a fan. In natural convection, any fluid motion is caused by natural means such as the buoyancy effect, which manifests itself as the rise of warmer fluid and the fall of the cooler fluid, the third mode is mixed convection occur when both inertia and buoyancy forces are equally present and both natural and forced convection effects must be considered [8].

1.2 MASSE TRENSFER

Mass transfer refers to the movement of one or more chemical substances from one location to another. Just as a temperature gradient constitutes the driving potential for heat transfer, a species concentration gradient in a mixture provides the driving potential for transport of that species. The movement of species occurs from regions of higher concentration to regions of lower concentration. The concentration gradient serves as the driving force for mass transfer. This process can occur through various mechanisms, such as diffusion, convection.

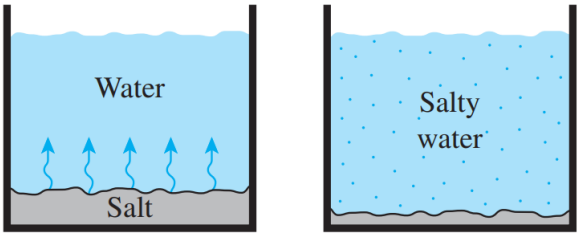


Figure 1.3: mass Transfer [8].

1.2.1 MASSE DIFFUSION

Diffusion is the movement of particles from an area of high concentration to an area of low concentration due to a concentration gradient. the rate of mass diffusion of a chemical species in a stagnant medium in a specified direction is proportional to the local concentration gradient in that direction. This linear relationship between the rate of diffusion and the concentration gradient proposed by Fick in 1855 is known as Fick's law of diffusion and can be expressed as

$$\dot{m}_{diff,A} = -D_{AB} A \frac{d\rho_A}{dx} \qquad (kg/s) \qquad (1.2)$$

Here D_{AB} is the diffusion coefficient (or mass diffusivity) of the species in the mixture, m^2/s.

A : is the area normal to the direction of mass transfer, m^2.

$d\rho_A/dx$: Concentration gradient of the mixture, kg/m^4

1.2.2 MASSE CONVECTION

mass convection (or convective mass transfer) is the mass transfer mechanism between a surface and a moving fluid that involves both mass diffusion and bulk fluid motion. Fluid motion also enhances mass transfer considerably by removing the high concentration fluid near

the surface and replacing it by the lower concentration fluid farther away. By an analogy between heat and mass convection the rate of mass convection can be expressed as

$$\dot{m}_{conv} = h_{mass} A_s \left(C_s - C_\infty \right) \qquad (kg/s) \tag{1.3}$$

where h_{mass} : is the mass transfer coefficient, m/s.

A_s : is the surface area, m^2.

$C_s - C_\infty$: is the mass concentration difference across the concentration boundary layer, kg/m^3.

1.3 THERMO-SOLUTALE CONVECTION

It mainly concerns the study of convective movements (natural flows) induced by a temperature gradient and a concentration gradient in confined or semi-confined spaces. These gradients give rise to a non-uniform distribution of the density of the mixture, which in turn causes convective motion under the effect of gravity. These two gradients can act together or in opposition, depending on the case, thus giving rise to interesting and complicated dynamic behaviors. Several variants are possible: for thermo-solutal convection, both heat and concentration gradients are imposed [9].

Thermo-solutal convection (the existence of a thermal and solutal gradient) is considered by industrialists and scientists to be a very important and lively field because of the multitude of applications such as: separation precedes in the chemical and petroleum industries, the storage of nuclear waste, dispersion of chemical contaminants in groundwater layers, in drying processes for various industrial and household products, in various thermochemical and electrochemical processes, in the storage of liquid gases, in absorption or adsorption heat pumps, in chemical reactors, in oxidation or metal surface treatment processes, and in the migration of moisture into fibers intended for insulation thermal. This has motivated researchers and industrialists to carry out research in this context, the main objective of which is to understand the different mechanisms resulting from the convective movements generated.

1.4 DIMENSIONLESS NUMBERS

In heat and mass convection studies, it is common practice to nondimensionalize the governing equations and combine the variables, which group together into dimensionless numbers in order to reduce the number of total variables. Indeed, we now present the main dimensionless numbers used in this manuscript.

1.4.1 THE RAYLEIGH NUMBER

The Rayleigh number is a dimensionless number named after Lord Rayleigh (1842–1919) used in fluid mechanics and characterizing the importance of convection phenomena within the fluid. If the number of Ra is less than a critical value Ra_c, the transfer of thermal energy occurs essentially by conduction, while beyond this value, it is natural convection which becomes important. Also, its value tells us whether we are in laminar or turbulent for a system in natural convection. The Rayleigh number combines the Prandtl and Grashof numbers, and is given by the expression follows:

$$Ra = Gr\,\mathrm{Pr} = \frac{g\beta(T_s - T_\infty)L_c^3}{\nu\alpha} \tag{1.4}$$

Where Gr is the Grashof number, Pr is the Prandtl number, g is the gravitational acceleration, β is the coefficient of volume expansion, T_s is the temperature of the surface, T_∞ is the temperature of the fluid sufficiently far from the surface, L_c is the characteristic length, and α is the Thermal diffusivity.

1.4.2 THE NUSSELT NUMBER

the Nusselt number is named after Wilhelm Nusselt (1882–1957), is a dimensionless quantity represents the enhancement of heat transfer through a fluid layer as a result of convection relative to conduction across the same fluid layer, defined as

$$Nu = \frac{hL_c}{k} \tag{1.5}$$

where k is the thermal conductivity of the fluid, h is the convection heat transfer coefficient, and L_c is the characteristic length. The larger the Nusselt number, the more effective the convection. A Nusselt number of $Nu = 1$ for a fluid layer represents heat transfer across the layer by pure conduction.

1.4.3 SHERWOOD NUMBER

The Sherwood number is a dimensionless number named after Thomas Kilgore Sherwood (1903–1976) used in mass transfer represent the effectiveness of mass convection. It represents the total heat transfer to the diffusion transfer, defined as

$$Sh = \frac{h_{mass}L_c}{D_{AB}} \tag{1.6}$$

where h_{mass} is the mass transfer coefficient, L_c is the characteristic length, and D_{AB} is the mass diffusivity. If diffusion is solely responsible for the transfer of matter, then the Sherwood number will be worth 1.

1.4.4 LEWIS NUMBER

The Lewis number is a dimensionless number named after Warren Kendall Lewis (1882–1975) used in thermos-solutal convection phenomena, represent the relative magnitudes of heat and mass diffusion in the thermal and concentration boundary layers, and is given by the expression follows:

$$Le = \frac{\alpha}{D_{AB}} \tag{1.7}$$

Where α is the thermal diffusivity, and D_{AB} is the mass diffusivity. When the Lewis number is unity, one can expect the heat and mass transfer by diffusion to be the same.

1.5 BOUSSINESQ APPROXIMATION

The Boussinesq approximation is the basis for most of what is known about natural convection. The application of this approximation to technological and environmental problems can only make sense when the conditions under which Boussinesq's equations are valid are explicitly known. The approximation that we are about to take up, attributed to Boussinesq (1903), was in fact also proposed by Oberbeck [10] for the first time in 1879.

This approximation starts with the usual forms of equations: continuity, motion, and energy, for the Newtonian fluid with variable properties and zero second viscosity, [2]:

$$\frac{\partial \rho}{\partial t} + \rho \frac{\partial V_j}{\partial x_j} = 0 \tag{1.8}$$

$$\rho \frac{DV_i}{Dt} = -\frac{\partial P}{\partial x_i} - \rho g k_i + \frac{\mu \partial \Gamma_{ij}}{\partial x_j} + \Gamma_{ij} \frac{\partial \mu}{\partial x_j} \tag{1.9}$$

$$\rho C_p \frac{DT}{Dt} = \frac{K \partial^2 T}{\partial x_j^2} + \frac{\partial K}{\partial x_j} \frac{\partial T}{\partial x_j} + \alpha T \frac{DP}{Dt} + \mu \Phi \tag{1.10}$$

where $\Gamma_{ij} = \frac{\partial V_i}{\partial x_j} + \frac{\partial V_j}{\partial x_i} - \frac{2}{3} \frac{\partial V_k}{\partial x_k} \delta_{ij}$ *et* $\Phi = \frac{1}{2}\left(\frac{\partial V_i}{\partial x_j} + \frac{\partial V_j}{\partial x_i} \right)$

In order to complete the description of the problem, it is also necessary to know relations for the determination of the properties of fluids. Since the only reversible mode of work for a Newtonian fluid is compression. Its properties are functions of two thermodynamic variables. Therefore, the necessary equations can be written as:

$$\begin{gathered}\rho=\rho(T,P), \qquad C_p=C_p(T,P), \qquad \mu=\mu(T,P) \\ \beta=\beta(T,P), \qquad k=k(T,P)\end{gathered} \tag{1.11}$$

Usually, these functions are imperfectly known and must be inferred from the tabular data. Finally, we will require that most of these properties be adequately estimated by constant values. There is generally no difficulty in assuming linearized Taylor developments, but the special case of water at 4°C should always be kept in mind. It should also be noted that the general approach to this derivation does not rely on the use of variations in linearized properties.

The linearized approximations to equation (1.11) are:

$$\left.\begin{aligned}\rho&=\rho_0\left[1-\beta_T\left(T-T_0\right)+\beta_P\left(P-P_0\right)\right]\\ C_P&=C_{P0}\left[1-a_0\left(T-T_0\right)+b_0\left(P-P_0\right)\right]\\ \mu&=\mu_0\left[1-a_1\left(T-T_0\right)+b_1\left(P-P_0\right)\right]\\ \alpha&=\alpha_0\left[1-a_2\left(T-T_0\right)+b_2\left(P-P_0\right)\right]\\ k&=k_0\left[1-a_3\left(T-T_0\right)+b_3\left(P-P_0\right)\right]\end{aligned}\right\} \tag{1.12}$$

Where

$$\begin{gathered}\beta_T=-\frac{1}{\rho}\frac{\partial\rho}{\partial T}, \quad \beta_P=-\frac{1}{\rho}\frac{\partial\rho}{\partial P}, \quad a_0=\frac{1}{C_P}\frac{\partial C_P}{\partial T}, \quad b_0=\frac{1}{C_P}\frac{\partial C_P}{\partial P}, \quad a_1=\frac{1}{\mu}\frac{\partial\mu}{\partial T} \\ b_1=-\frac{1}{\mu}\frac{\partial\mu}{\partial P}, \quad a_2=\frac{1}{\alpha}\frac{\partial\alpha}{\partial T}, \quad b_2=\frac{1}{\alpha}\frac{\partial\alpha}{\partial P}, \quad a_3=\frac{1}{k}\frac{\partial k}{\partial T}, \quad b_3=\frac{1}{k}\frac{\partial k}{\partial P}\end{gathered} \tag{1.13}$$

And where the index 0 indicates the reference state (T_0, P_0).

As concrete examples of the method just presented, the latter examines the cases of water and air at T_0 = 15°C and P_0 = 1atm. Table 1.1 presents the required constants obtained from [11], unless otherwise specified. For water, the most demanding conditions are expressed by:

$$\left.\begin{aligned}\theta&\le 1.25°C\\ L&\le 2.4\times10^5\,cm\\ L/\theta&<9.9\times10^4\ cm/°C\end{aligned}\right\} \tag{1.14}$$

In the case of air, similar results are obtained. The most demanding conditions are expressed by:

$$\left.\begin{array}{c} \theta \le 28.6°C \\ L \le 8.3\times10^{4}\,cm \\ L/\theta < 1020\ cm/°C \end{array}\right\} \tag{1.15}$$

Table 1.1: Properties of fluids for water and air at T_0=15°C, P_0=1atm.

	Water	**Air**
$\boldsymbol{\rho_0}$ $[\boldsymbol{g/cm^3}]$	1.00	$1.2\text{x}10^{-3}$
$\boldsymbol{C_{P0}}$ $[\boldsymbol{ergs/gm\,C}]$	$1.2\text{x}10^{7}$	10^{7}
$\boldsymbol{v_0}$ $[\boldsymbol{cm^2/s}]$	$1.1\text{x}10^{-2}$	0.145
$\boldsymbol{\beta_T}$ $[\boldsymbol{C^{-1}}]$	$1.5\text{x}10^{-4}$	$3.5\text{x}10^{-3}$
$\boldsymbol{\beta_P}$ $[\boldsymbol{cm^2/dyn}]$	$4.9\text{x}10^{-11}$	10^{-6}
$\boldsymbol{a_0}$ $[\boldsymbol{C^{-1}}]$	$-2.4\text{x}10^{-4}$	$4.5\text{x}10^{-5}$
$\boldsymbol{b_0}$ $[\boldsymbol{cm^2/dyn}]$	$-2.5\text{x}10^{-10}$	$1.9\text{x}10^{-9}$
$\boldsymbol{a_1}$ $[\boldsymbol{C^{-1}}]$	$-2.7\text{x}10^{-2}$	$2.8\text{x}10^{-3}$
$\boldsymbol{b_1}$ $[\boldsymbol{cm^2/dyn}]$	$-2.7\text{x}10^{-2}$	0.0
$\boldsymbol{a_2}$ $[\boldsymbol{C^{-1}}]$	$8.0\text{x}10^{-2}$	$-3.6\text{x}10^{-3}$
$\boldsymbol{b_2}$ $[\boldsymbol{cm^2/dyn}]$	0.0	0.0
$\boldsymbol{a_3}$ $[\boldsymbol{C^{-1}}]$	$1.7\text{x}10^{-3}$	$2.4\text{x}10^{-3}$
$\boldsymbol{b_3}$ $[\boldsymbol{cm^2/dyn}]$	$4.3\text{x}10^{-10}$	0.0

Solving a natural convection problem in a porous medium boil down to predicting the temperature, concentration, and velocity fields as well as the intensity of the flow as a function of the various parameters of the problem. It is also important to predict the corresponding heat transfer and mass transfer rates.

1.6 NON-NEWTONIAN FLUIDS

In contrast to the classical framework of fluid mechanics formulated for Newtonian fluids, the exploration of non-Newtonian fluid dynamics represents a relatively nascent domain within the realm of applied sciences. The escalating significance of non-Newtonian fluids has been acknowledged in disciplines addressing materials, wherein the flow characteristics involving stress and shear rate elude characterization by Newton's law of viscosity [12-15]. Consequently, the discipline of non-Newtonian fluid mechanics is undergoing active development. Broadly categorized, fluids are classified into two principal types: (1) Newtonian, adhering to Newton's law of viscous resistance and maintaining a constant viscosity, and (2) non-Newtonian, deviating from Newton's law of viscosity and manifesting variable viscosity. The behavior of non-Newtonian fluids is typically elucidated through the application of a rheological model or

correlation that explains the relationship between shear stress and shear rate, Examples of substances which exhibit non-Newtonian behavior include solutions and melts of high molecular weight polymers, suspensions of solids in liquids, emulsions, and materials possessing both viscous and elastic properties [11].

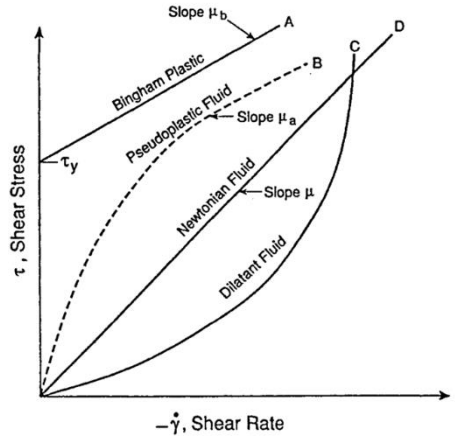


Figure 1.4: Typical shear stress and shear rate relationships for non-Newtonian fluids [16].

In Newtonian fluids, the shear stress τ is linearly related to the shear rate as depicted in figure 1.4, as prescribed by Newton's law of viscosity.

$$\tau = -\mu\dot{\gamma} \tag{1.16}$$

where the coefficient μ is defined as dynamic viscosity of the fluid.

In accordance with the relationships between shear stress and shear rate, non-Newtonian fluids are conventionally classified into three overarching categories [12]: (1) time-independent non-Newtonian fluids, (2) time-dependent non-Newtonian fluids, and (3) viscoelastic non-Newtonian fluids.

1.6.1 TIME-INDEPENDENT FLUIDS

Time-independent fluids are characterized by a condition wherein the shear rate or velocity gradient is a distinct but non-linear function of the instantaneous shear stress τ at a given point. In the context of time-independent fluids, the correlation is expressed as follows:

$$\dot{\gamma} = f(\tau) \tag{1.17}$$

The characterization of time-independent non-Newtonian fluids is achievable through the examination of flow curves depicting shear stress τ against shear rate $\dot{\gamma}$, as illustrated in Figure1.4, and Figure1.5. These fluid types include (a) Bingham plastics, represented by curve A, (b) pseudoplastic fluids exhibiting Shear-thinning behavior, depicted by curve B, and (c) dilatant fluids showcasing shear-thickening tendencies, delineated by curve C.

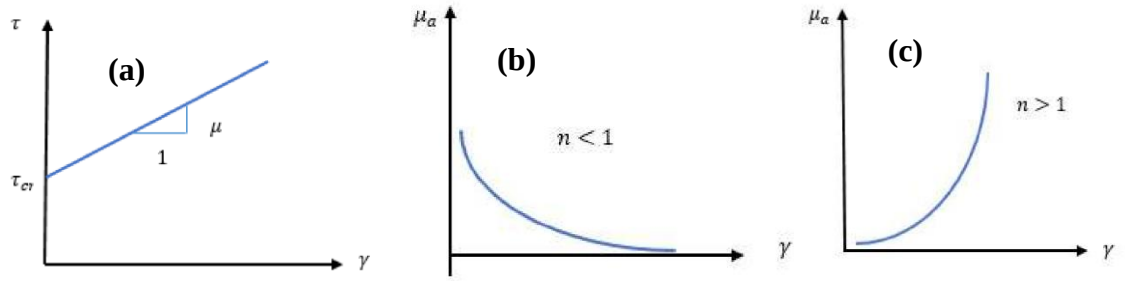


Figure 1.5. Typical Time-independent fluids.

1.6.2 TIME-DEPENDENT FLUIDS

Time-dependent fluids have more complex shear stress and shear rate relationships. In these fluids, the shear rate depends not only on the shear stress, but also on shearing time, or on the previous shear stress rate history of the fluid. These materials are usually classified into two groups, thixotropic fluids and rheopectic fluids, depending upon whether the shear stress decreases or increases in time at a given shear rate and under constant temperature. Typical curves of the time-dependent behavior of non-Newtonian fluids are shown in Fig. 1.6.

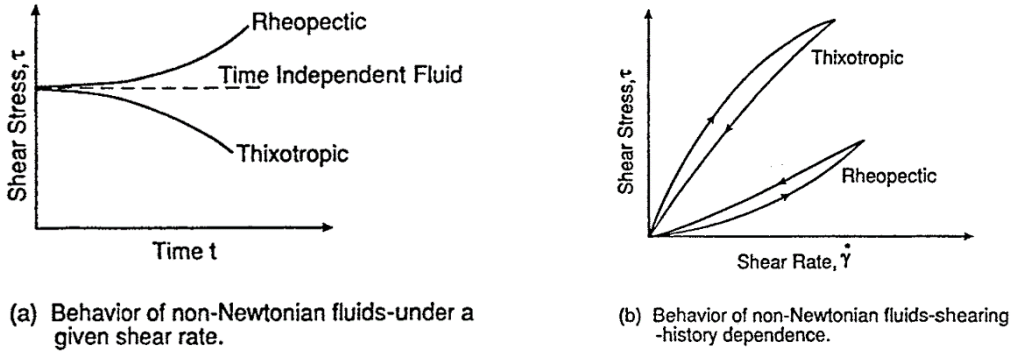


Figure 1.6. Flow curves for time-dependent thixotropic and rheopectic non-Newtonian fluids [12,17].

1.6.3 VISCOELASTIC MATERIAL

A viscoelastic material exhibits both elastic and viscous properties, when they are subjected to a creep test (constant shear stress) in Figure 1.7, and shows partial recovery upon the removal of the deformable shear stress. The rheological properties of such a substance at any instant will be a function of the recent history of the material and cannot be described by relationships between shear stress and shear rate alone, but will require inclusion of the time derivative of both quantities.

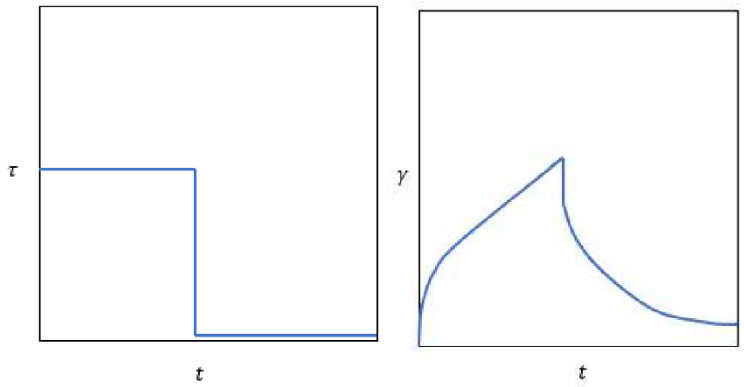


Figure 1.7 Evolution of the strain rate within a viscoelastic fluid during a creep test. [18].

1.7 NON-NEWTONIAN RHEOLOGICAL MODELS

Numerous rheological models have been advanced in scholarly works to portray various non-Newtonian fluids across a spectrum of flow scenarios. It is noteworthy, however, that a substantial proportion of these models are of an empirical nature, originating from exercises involving the fitting of curves. The subsequent discourse provides notable instances of non-Newtonian models categorized within the three aforementioned groups.

1.7.1 POWER-LAW MODEL

Power-Law, or Ostwald-de Waele model [19], is the most widely used rheological model for flow problems in porous media. The power law model has been successfully applied to describe the flow behavior of polymer and foam solutions by a number of authors [20-25]. The relationship between shear stress and shear rate (plotted on double logarithmic coordinates) for a low-shear fluid can often be approximated by a straight line over a limited range of shear (or stress) rates. For this part of the flow curve, an expression of the following form is applicable:

$$\tau = -H(\dot{\gamma})^n \tag{1.18}$$

So, the apparent viscosity for the power-law fluid (or Ostwald-de Waele) is given by:

$$\mu_a = H(\dot{\gamma})^{n-1} \tag{1.19}$$

Where

μ_a: Apparent viscosity.

H: The consistence coefficient.

$\dot{\gamma}$: The rate of shear deformation.

n: The power-law index.

Based on the power-law index, n:

- $0 < n < 1$, The fluid exhibits pseudoplastic or shear thinning behavior. Here, the apparent viscosity μ_a decreases with increasing shear rate $\dot{\gamma}$.
- $n = 1$, The fluid has Newtonian behavior;
- $n > 1$, The fluid exhibits dilatant or shear-thickening behavior. Here, the apparent viscosity μ_a decreases with decreasing shear rate $\dot{\gamma}$.

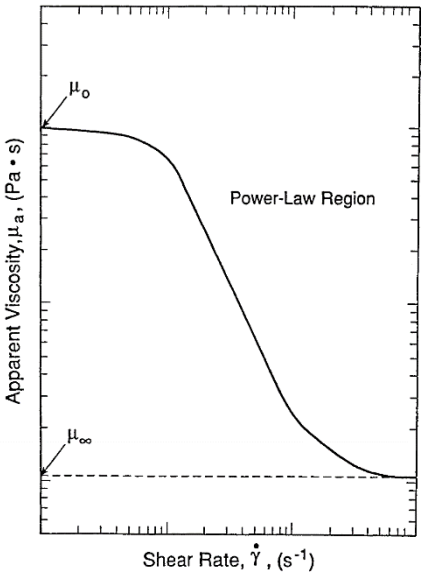


Figure 1.8 Viscosity behavior of pseudoplastic shear-thinning fluids, with maximum and minimum limiting viscosities [16].

Moreover, at both extremely low and exceedingly high velocity gradients, the prevalent observation is that most fluids manifest Newtonian characteristics characterized by constant viscosities, denoted as $\mu_0$and μ_∞, respectively, as illustrated in Figure 1.8. The rationale for this apparent Newtonian behavior in these regions is postulated to arise from complete molecular orientation at high shear rates and, conversely, complete molecular disorientation at very low shear rates.

The power law is the most widely used model in the literature dealing with engineering applications. Table 1.2 provides a compilation of constants (K and n) for various substances.

Table 1.2: Typical values of power distribution model constants for selected substances. [26]

Substance	Temperature (K)	n (−)	K (Pa sn)
Mashed banana	293–315	0.33–0.5	4–10
Chocolate	303	0.5	0.7
Human Blood	300	0.9	0.004
Mayonnaise	298	0.6	5-100
Yoghurt	293	0.5-0.6	25
Polystyrene	463–498	0.25	1.5 - 4.5 × 104
Nylon	493–508	0.65	1.8–2.6×103
Toothpaste	298	0.28	120
Sun-screen lotions	298	0.28	75

1.7.2 CROSS MODEL

It is a model that represents non-Newtonian fluids regardless of time and without critical constraints, it has four parameters (μ_0, β, μ_∞, n), it was proposed by Cross in 1965. [27]. The formulation of the model is as follows:

$$\frac{\mu-\mu_\infty}{\mu_0-\mu_\infty}=\frac{1}{1+k(\gamma)^n} \tag{1.20}$$

where:

k: The characteristic time of entanglement.

n: It will be equal to $2/3$ for all polymers that approach the pseudo-plastic model.

μ_0: The viscosity of the Newtonian bearing at low shear rate.

μ_∞: A second Newtonian plateau with a high shear rate.

$\dot{\gamma}$: The shear strain rate.

This model reduces to the Newtonian model when $k \to 0$. Similarly, when $\mu \ll \mu_0$ and $\mu \gg \mu_\infty$, it reduces to the power law model, equation (1.36).

1.7.3 ELLIS MODEL

This model describes time-dependent fluids that express viscosity as a function of shear rates [28], The apparent viscosity of an Ellis fluid model has 3 parameters (μ_0,$\tau_{1/2}$,$a-1$) and is stated as follows:

$$\mu = \frac{\mu_0}{1+\left(\tau / \tau_{1/2}\right)^{a-1}} \tag{1.21}$$

μ_0: zero-shear viscosity.

$\tau_{1/2}$: shear stress when $\mu = \mu_0/2$.

a: rheological parameter.

The behavior of a Newtonian fluid is found within the limit of $\tau_{1/2} \to \infty$.

1.7.4 BINGHAM MODEL

For Binghamian liquids, i.e., ideal plastic liquids, the shear stress varies linearly with the shear rate but, unlike Newtonian fluids, it is necessary to apply a minimum force to set the fluid in motion. Examples of fluids with yield stress such as sludge, food fluids such as 'mayonnaise and ketchup', toothpaste, suspended zinc or barium sulphate, bread dough, fats, etc.

The equation that governs the behavior of a Bingham fluid is characterized by two constants (τ_0, μ_B):

$$\begin{aligned} \tau &= \tau_0 - \mu_B\dot{\gamma} \quad && for \quad |\tau| > |\tau_0| \\ \dot{\gamma} &= 0 \quad && for \quad |\tau| < |\tau_0| \end{aligned} \tag{1.22}$$

where:

τ: shear stress.

τ_0: the yield stress, which is the stress that must be exceeded for flow to begin.

μ_B: the Bingham plastic viscosity

$\dot{\gamma}$: the shear strain rate.

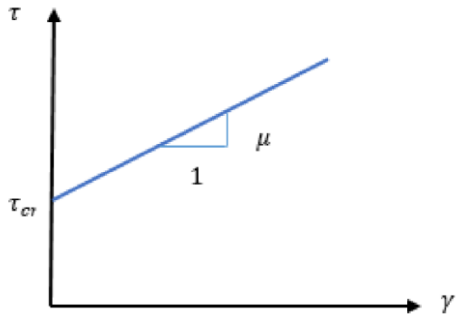


Figure 1.9: Rheogram of an ideal plastic fluid (Bingham fluid). [18].

1.7.5 HERSCHEL-BULKLEY MODEL

The Herschel-Bulkley model is a simple three-parameter rheological model. Despite its simplicity, it can describe Newtonian fluids and all major classes of non-Newtonian fluids regardless of time. This model is expressed mathematically as follows:

$$\tau = \tau_0 + H\dot{\gamma}^n \qquad for \quad \tau > \tau_0$$
$$|\dot{\gamma}| = 0 \qquad for \quad \tau < \tau_0$$

Where τ is the shear stress, τ_0 is the yield stress over which the substance begins to flow, H is the consistency factor, $\dot{\gamma}$ is the shear strain rate, and n is the flow behavior index. The Herschel-Bulkley model reduces to the power law when $\tau_0 = 0$, the Bingham plastic when $n = 1$, and Newton's law for viscous fluids when both conditions are met.

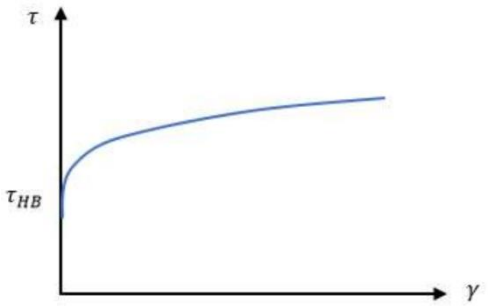


Figure 1.10: Rheogram of a shear-thinning plastic fluid. [29]

This non-Newtonian fluid model was introduced by Winslow Herschel and Ronald Bulkley in 1926. [30]

Table 1.3: Rheological parameters of the rheological equation of state [27].

Types	n	τ_0	Examples
Newtonian	1	0	Water, fruit juice, milk, oil
Shear-thinning	0 < n < 1	0	Applesauce, mashed banana, concentrated orange juice
Shear-thikening	1 < n < ∞	0	Honey (some types), 40% native starch solution
Bingham Plastic	1	> 0	Toothpaste, tomato puree
Herchel-Bulkley	0 < n < ∞	> 0	Fish paste, grape must

1.7.6 SISKO MODEL

This model describes time-independent fluids without critical constraints (Midoux, 1993). [31], and it reads as follows (Brodkey & Hershey, 1988). [32]:

$$\tau = -\gamma(\mu_\infty + K_s|\tau|^{z-1}) \tag{1.23}$$

This model has 3 parameters (μ_∞, K_s, z), and it is well suited for high shear rates (e.g., it adequately describes the behavior of fats)

1.7.7 CARREAU-YASUDA MODEL

The power law model applies over a limited range of the viscosity curve, as this law describes well the Newtonian plateau at low shear rates, i.e., the viscosity is independent of the shear rate. It is necessary to use a model that takes into account the limit values of viscosities μ_0 and μ_∞ at a zero and infinite shear rate. This model has 5 parameters (η_0, η_∞, λ, n, a) and is presented as follows (simple shear). [33]:

$$\frac{\mu-\mu_\infty}{\mu_0-\mu_\infty} = \left[1+(E\gamma)^a\right]^{\left(\frac{n-1}{a}\right)} \tag{1.24}$$

Where

μ_0: viscosity at zero shear rate.

μ_∞: viscosity at infinite shear rate.

E: a time constant.

n: power-law index.

a: The flow index between 0 and 1.

In general, in the CY model, the shear-thinning fluids have a power-law index n (0.1< n<1) and a time constant E' (0.1< E'<100 s). When the value of the time constant E' is very large, the CY model tends towards the power-law model. Similarly, if $n = 1$, $s = 1$, or $E = 0$, we find the case of Newtonian fluids.

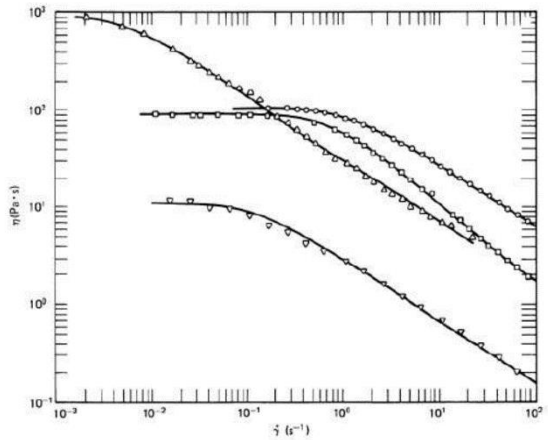


Figure 1.11: Carreau-Yasuda model for three polymer solutions expressing apparent viscosity (vertical axis) as a function of shear rate (horizontal axis). [34].

1.8 POROUS MEDIA

Many configurations of practical interest encountered in heat transfer are characterized by the presence of a fluid flow in a porous medium. It is therefore important to relate the flow structure and heat or mechanical exchanges to the physical properties characterizing the fluid and the porous medium.

A porous medium is any solid matrix with voids or cavities through which a fluid can flow. These voids spaces that can be connected are called pores. Several porous materials are found in nature or industry. They can be stacked logs, fiberglass panels, concrete, rock, oilfield, sand, etc. Figure 1.12 illustrates some examples of porous media. A porous medium is primarily characterized by two related macroscopic properties, namely porosity and permeability.

Because the arrangement and size of these pores are irregular, the variation in the parameters governing this flow will also be irregular. In practice, these parameters are measured at the macroscopic (averaged) scale. The technique used and the spatial method, defined as an appropriate average over a sufficiently large representative elementary volume (R.E.V) [8].

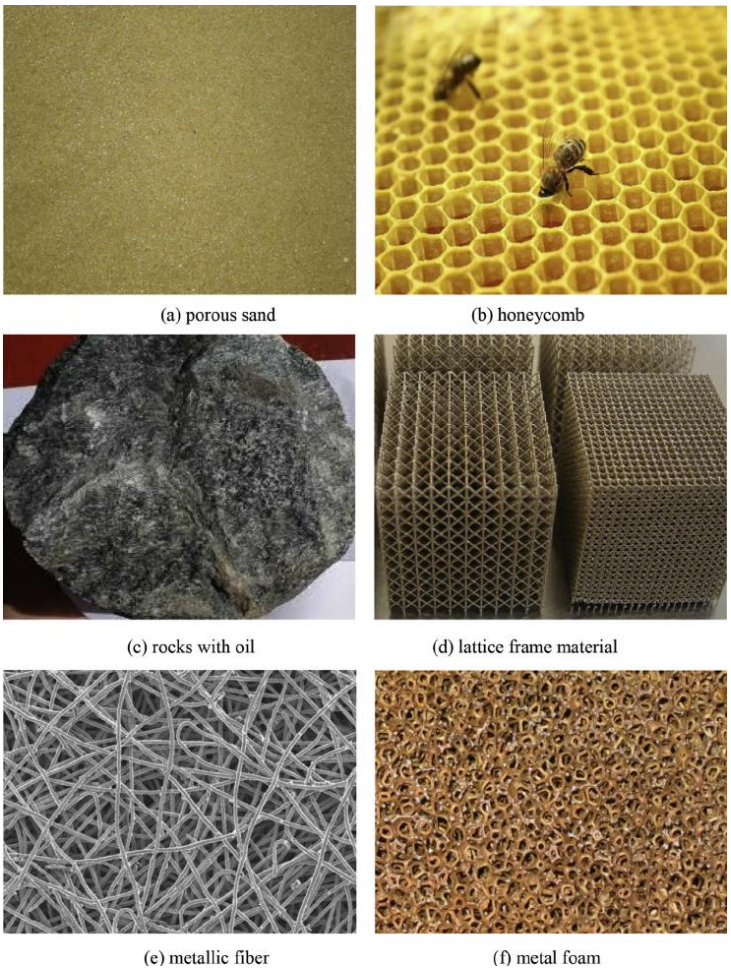


Figure 1.12: Some examples of porous media

1.8.1 CONCEPT OF REPRESENTATIVE ELEMENTARY VOLUME (R.E.V)

When we are interested in the study of physical phenomena in porous media, scales are necessary for their analyses:

- The scale of the pore or cracks (microscopic) within which the local or microscopic quantities (velocity, pressure,) can vary widely (due to the irregularity of the arrangement and size of the pores).
- The scale of the porous or macroscopic medium is characterized by a significant variation in these same quantities defined on average over a certain volume of the porous medium.
- In practice, these quantities are measured on surfaces with multiple pores and are therefore averaged (macroscopic quantities), which means that these quantities vary in time and space.
- The simplest averaging approach used is the Representative Elementary Volume (R.E.V.) approach. In this approach, the macroscopic variable is defined as an

appropriate average over a sufficiently large representative elementary volume. This (R.E.V) is considered:

- Large enough to contain a large number of pores needed to define an overall average property, so as to ensure that fluctuations from one pore to another result in negligible effects.
- Small enough compared to the characteristic length of the solid matrix.

In other words, we can then consider that the porous medium is a R.E.V. This conceptualization introduced by J. Bear makes it possible to reason in terms of an equivalent continuous medium.

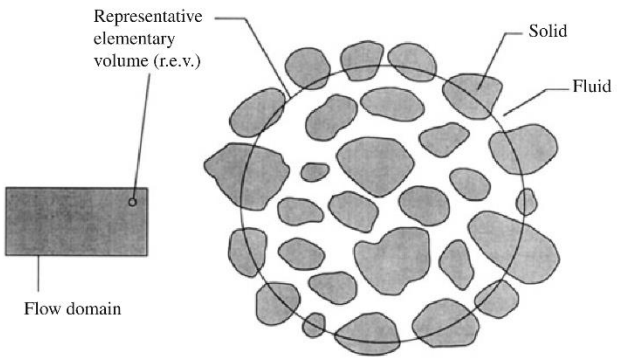


Figure 1.13: The representative elementary volume (r.e.v.): the figure illustrates the intermediate size relative to the sizes of the flow domain and the pores [8].

1.8.2 CLASSIFICATION AND CHARACTERIZATION OF POROUS MEDIA

Porous media are very varied in nature, especially in terms of the geometric structure that defines the pore space. This section introduces some basic concepts related to the structural properties of porous media.

1.8.2.1 CLASSIFICATION

The solid matrix of a porous medium can be [35]:

1.8.2.1.1 Unconsolidated:

The solid phase is then formed of grains or fibers that are not welded together (gravel, sand, silt, glass and steel beads, various materials, etc.); Glass beads are widely used in laboratories to study transfer phenomena in porous media.

1.8.2.1.2 Consolidated:

In this case, the compact solid matrix cannot be divided into grains or fibers (limestone, sandstone, clay, wood, ceramics, sintered powders, plant and animal tissues, etc.).

1.8.2.2 CHARACTERIZATION

Different geometrical and thermo-physical quantities are used to characterize the flow and heat transfer occurring in a porous medium, we can mention:

1.8.2.2.1 Porosity:

The porosity ε of a porous medium is defined as the ratio of the volume of pores to the total volume of the material.

$$\varepsilon = \frac{V_{pore}}{V_{total}} \tag{1.25}$$

V_{pore}: Pore volume.

V_{total}: Total volume of the porous matrix.

This size does not give any information about the distribution of the pores, this is because two materials with the same porosity can have different physical properties. A pore can be connected to other pores (interconnected pores), or it can be isolated. We define then:

- Total porosity:

$$\varepsilon_t = \frac{V_{all\ pores}}{V_{total}} \tag{1.26}$$

- Effective porosity:

$$\varepsilon_e = \frac{V_{accessible\ pore\ volume}}{V_{total}} \tag{1.27}$$

For unconsolidated porous media, $\varepsilon_t = \varepsilon_e$, while for consolidated porous media, the difference between the two porosities can be significant.

Experimental measurements made by Kaviany [36] give in table 1.4 below some values of porosity for different materials.

Table 1.4: Porosity of selected materials.

Materials	Porosity
Foamy material	0.98
Fiberglass	0.88 – 0.93
Wire crimps	0.68 – 0.76
Silica grains	0.65
Black Slate Powder	0.57 – 0.66
Leather	0.56 – 0.59
Catalyst	0.45
Stone granules	0.44 – 0.45
Earth	0.43 – 0.54
Sand	0.37 – 0.50
Silica Powder	0.37 – 0.49
Well-stacked sphere	0.36 – 0.43
Cigarette Filter	0.17 – 0.49
Bricks	0.12 – 0.34
Copper Powder	0.09 – 0.34
Hot Stone, Dolomite	00.04 – 0.10
Coal	0.02 – 0.07

1.8.2.2.2 Permeability:

It is defined as the ability of a porous medium to flow through the pores of the medium. According to Darcy's law (1856), permeability measures the conductance of the flow of a porous matrix:

$$K = -\frac{\mu.\mu_D}{d_p / d_x} \tag{1.28}$$

where μ, u_D, and d_p / d_x are the dynamic viscosity of the fluid, the filtration rate (or Darcienne), and the pressure gradient, respectively.

The table below shows the permeability of some porous materials defined according to Sheidegger [37].

Table 1.5: Permeability of selected materials

Materials	Permeability [m²]
Bricks	$4.8.\ 10^{-15}$– $2.2.10^{-13}$
Hot Stone, Dolomite	$2.0.\ 10^{-15}$– $4.5.10^{-14}$
Leather	$9.5.\ 10^{-14}$– $1.2.\ 10^{-13}$
Black Slate Powder	$4.9.\ 10^{-14}$– $1.2.\ 10^{-13}$
Earth	$2.9.\ 10^{-13}$– $1.4.10^{-11}$
Fiberglass	$2.4.\ 10^{-11}$– $5.1.\ 10^{-11}$

Sand	$2.0.\ 10^{-11}$– $1.8.10^{-10}$
Artificial hair	$8.3.\ 10^{-10}$– $1.2.10^{-9}$
Cork plate	$3.3.\ 10^{-10}$– $1.5.\ 10^{-9}$
Wire crimps	$3.8.\ 10^{-9}$– 1.10^{-8}
Cigarette	$1.1.\ 10^{-9}$

1.8.2.2.3 Tortuosity:

In a porous medium formed by a stack of solid grains, the actual local velocity of the fluid is not quite parallel to the mean direction of flow because of the obstacles constituted by the solid phase. The fluid bypasses the various particles that oppose its passage.

The path followed by a fluid thread is $L_0 > L$ where L is the length of the porous medium.

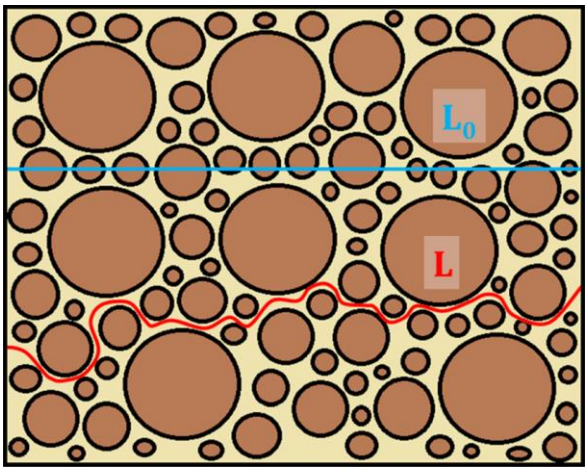


Figure 1.14: Schematic Definition of Tortuosity

Tortuosity is the ratio of the average length of the path traveled by a fluid particle to the length of the sample.

$$\tau = \frac{L_m}{L} \tag{1.29}$$

In the case of porous media consisting of stacks of spherical particles, the tortuosity varies little and remains approximately equal to $\pi / 2$.

1.8.2.2.4 Specific surface area:

The specific surface area is defined as the total area of the voids relative to the unit volume:

$$A_s = \frac{\text{total void area}}{\text{total volume of the medium}} \tag{1.30}$$

The table below shows the permeability of some porous materials defined according to Bejan and Lage [38].

Table 1.6: Surface per unit volume of selected materials

Material	**Surface per unit (volume [cm^{-1}])**
Black slate powder	$7x10^3$–$8.9x10^3$
Catalyst (Fischer-Tropsch,granules only)	$5.6x10^5$
Fiberglass	560–770
Leather	$1.2x10^4$–$1.6x10^4$
Sand	150–220
Silica powder	$6.8x10^3$–$8.9x10^3$
Wire crimps	29–40

1.8.3 FLOW MODELS IN POROUS MEDIA

Because of the geometrical complexity of pore space, the approach of continuous media mechanics to establish models for the conservation of momentum, energy and mass can only be applied after a macroscopic scale has been adopted to establish an equivalence between the dispersed real medium and a fictitious continuous medium. The establishment of macroscopic conservation equations is formally obtained from microscopic equations. The first model was proposed by Darcy (1856).

1.8.3.1 DARCY'S LAW 1875

The theory of flows in porous media is based on the results of experiments carried out by Darcy (1856). Darcy's experiment consists of measuring a flow rate and a load gradient that allow a permeability to be calculated using the formula (1.14). This experiment was initially developed for sands or materials that are not very consistent. The sample is in an R-radius tube, and subjected to a load gradient due to the difference in water height in both upstream and downstream recesses, the levels of which are kept constant. The direction of flow is inverse to

the load gradient. This load gradient can also be determined by measuring the difference in water height (Δh) in two piezometric tubes separated by L (Fig 1.15).

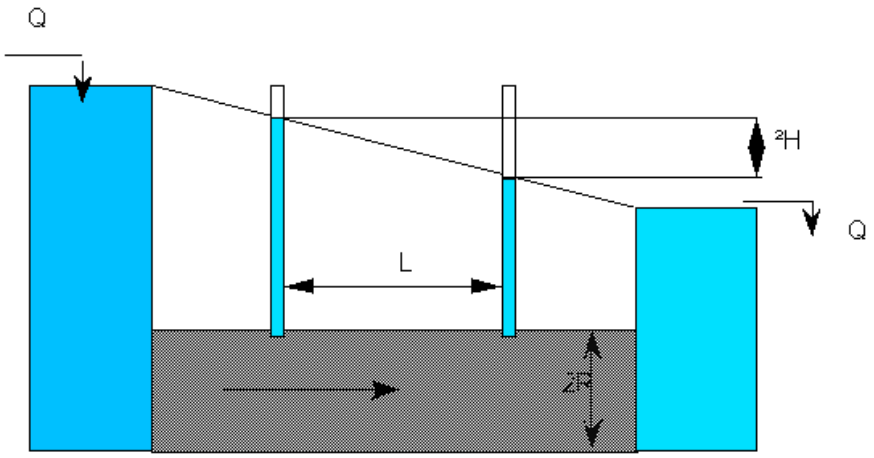


Figure 1.15: Permeability Measuring Device on Consolidated Material.

The filter liquid flows from the top level to the base of the column through the porous layer and rises up into the gauge tubes at decreasing levels in the direction of flow. The piezometric height decreases linearly as a function of the vertical distance travelled; The slope of the piezometric line measures the linear pressure drop:

$$J = \frac{\bar{h}_2 - \bar{h}_1}{L} \tag{1.31}$$

If the porous medium is thin enough, experience shows that the flow rate of the apparatus is proportional to the slope of this line as long as it is not too steep; With the usual sign convention, we have the equation:

$$Q = -KA\frac{\Delta h}{L} \tag{1.32}$$

where K is a constant that depends on both the fluid and the porous medium.

If, instead of reasoning in terms of manometric height, we write the previous law in terms of pressure, we obtain;

$$q = \frac{Q}{A} = -k\left(\frac{P_2 - P_1 + \rho g h}{h}\right) \tag{1.33}$$

The permeability can be considered as significant of the usable surface area for flow, it depends on the geometry of the porous medium. Darcy's law, and therefore permeability, is defined for laminar flow conditions in a homogeneous, isotropic and continuous medium; the fluid does

not interact with the medium. Hydraulic conductivity is defined as k; or permeability coefficient, such as:

$$k = \frac{K}{\mu} \tag{1.34}$$

where k is the hydraulic conductivity is characteristic of the flow conditions in a given material for a given fluid.

The previous scalar expression is then replaced by the following vector relation:

$$\vec{V} = -\frac{K}{\nu}\left(\vec{\nabla}P \pm \vec{g}\right) \tag{1.35}$$

where K is the permeability and υ is the kinematic viscosity of the fluid.

This law is only valid for low-velocity flows and for media with relatively low porosity. If the imposed temperature differences are not too large, the fluid velocities are low enough that the flows can be considered Darcyans. The value of the Reynolds number is used as a criterion to characterize the transition from a Darcy-type laminar flow regime to a Dupuit-type laminar regime. To do this, a pore Reynolds number was defined for flows in porous media. Setting d as the characteristic length that represents the characteristic size of the pores, the Reynolds number is written:

$$\mathrm{Re} = V\frac{d}{u} \tag{1.36}$$

In terms of determining d, Collins (1961) [39] proposed the expression $d = \sqrt{K/\varepsilon}$, while Ward (1964) [41] suggested that $d = \sqrt{K}$ regardless of porosity.

Based on the value of the Reynolds number of pore, Bear (1972) [41] distinguishes three flow regimes. Dybbs and Edwards (1984) [42], using velocity measurements, distinguish several flow regimes that can be classified as follows:

For pore Reynolds numbers less than 1, the flow regime is laminar, viscous forces are predominant, and Darcy's law applies.

When Re is between 1 and 10, boundary layers at the level of the solid pore walls develop. Outside these boundary layers, an inertial flow regime occurs. The inertial forces then become significant and there is no longer any proportionality between the pressure gradient and the

filtration rate: Darcy's law is no longer applicable. This laminar steady flow regime persists up to a Reynolds number of about 150.

For pore Reynolds numbers between 150 and 300, an unsteady laminar flow regime develops. This regime is first oscillatory resulting from the superposition of several distinct period and amplitude modes.

Above Re of the order of 300, the flow regime becomes chaotic, and has the characteristics of a turbulent flow.

1.8.3.2 DUPUIT-DARCY'S LAW

The formulation of Dupuit-Darcy (1863) [43] was tested for flows of the Reynolds number ($Re > 1$). This formulation introduces a drag term of the form of the porous matrix, which is a quadratic term of velocity considered falsely recognized as an inertia term in previous studies, the term is widely answered among the scientific community as Forchheimer (1901) [44] or term inertia.

The general compact form of the Dupuit-Darcy law, including the force of the body for flows in isotropic porous media, is given by:

$$\nabla P' = -\frac{\mu}{K}V' - \frac{\rho C_{DF}}{K^{1/2}}|V'|V' - \rho g \tag{1.37}$$

where P' is the pressure, V' is the infiltration velocity vector, μ is the dynamic viscosity of the fluid, ρ is the density of the fluid K is the permeability of the porous matrix, g is the acceleration of gravity, and C_{DF} is a coefficient independent of the flow and properties of the fluids, but it depends on the regime and behavior of the flow through the geometry of the porous matrix as well as the shape and size grains of the porous medium. In other words, the coefficient of C_{DF} is directly related to the coefficient of the drag (pressure) of a grain or elementary porous solid that delineates the pores within the solid porous matrix. From a hydrodynamic or aerodynamic point of view, a viscous flow around a submerged grain induces a drag force, called airfoil whose coefficient, $C_d = C_{DV} + C_{DF}$, is the sum of the coefficient of the viscous drag coefficient C_{DV} (Darcy-bound) and the drag coefficient C_{DF} (Dupuit-bound). For any Reynolds number the viscous drag is always present, but the shape drag or pressure drag depends on the behavior of the flow around the grain if it is attached or separated. If the flow is attached, at very low Reynolds number, recovery of the pressure gradient around the grain occurs and the shape drag is close to zero and the viscous drag is dominant. However, for a relatively high Reynolds

number and due to the non-Carine shape of the grain, the flow separates and the shape drag becomes significant and overcomes the viscous drag. In a porous matrix, one grain is surrounded by others and the "individual grain" shape drag takes into account the mutual hydrodynamic/aerodynamic interference between the grains. Then, a grain is subjected to a very complex upstream flow and the coefficient of the force of the C_{DF} shaped drag is highly dependent on the shape of the grain and the Reynolds number that influences the flow behavior. Overall, the coefficient of C_{DF} drag depends on the size and shape of the grains of the porous matrix as well as the flow behavior

1.8.3.3 DARCY-BRINKAMAN'S LAW

Brinkman (1947a, 1947b) [49,50] further generalized Darcy's law by introducing a term equivalent to the term viscous dissipation into Stokes's law.

$$\nabla P' = -\frac{\mu}{K}V' - \mu_e \nabla^2 V' + \rho g \tag{1.38}$$

This empirical law is known as the Darcy-Brinkman formulation, which is highly useful for the case of high porosity. The first term to the right of the above equation containing the viscosity μ is the Darcy term and the second term containing the effective viscosity is called the Brinkman term. The difficulty in using this model lies in the evaluation of the equivalent viscosity of the μ_e medium. Indeed, this quantity is a function not only of the porosity of the medium but also of its geometry (tortuosity). Brinkman equated the equivalent viscosity of the medium with that of the fluid ($\mu_e = \mu$). This approximation has been experimentally proven and is consistent with the work of Neal and Nader (1947) [51] and Beckermann and Viskanta (1988) [52]. Brinkman's model thus makes it possible to impose the non-slip condition on the filtration velocity field at the level of impermeable walls.

1.8.3.4 GENERAL MODEL

We generalize the last three equations by introducing a transient term and the convective term ($V'\nabla V'$), which leads to the following equation:

$$\frac{\rho}{\varepsilon}\frac{\partial V'}{\partial t} + \frac{\rho}{\varepsilon^2}\left(V'\nabla V'\right) = -\nabla P' + \rho g - \frac{\mu}{K}V' + \mu_e \nabla^2 V' - \frac{\rho C_{DF}}{K^{1/2}}\left|V'\right|V' \tag{1.39}$$

This equation is equivalent to the Navier-Stokes equation derived from the momentum balance in a fluid medium. It should also be noted that the complexity of a flow in a porous medium can be the result of drag and viscosity effects, and a significant variation in porosity at the walls.

1.9 LITERATURE REVIEW

Natural convection in an inclined fluid-saturated porous medium has been the subject of much research over the past decade, and studies in the literature include analytical and numerical studies, and experimental studies for different types of external and internal flows. Because of their widespread applications, such as in solar energy systems in energy sensor systems, arise in the design of pebble bed nuclear reactors, solar collectors, geothermal energy conversion, and the use of fibrous materials in thermal insulation of buildings and geophysical flows. Natural convection is a fundamental phenomenon in many types of collectors and receivers. The special feature of this study is the focus on flows driven by conditions of uniform heat and mass flow imposed along the perpendicular sidewalls of the porous layer. It is well known that natural convection phenomena are very sensitive to boundary conditions. From where we can find a very large number of studies in the literature related to this phenomenon. Comprehensive reviews of relevant studies on the topic in the bibliography [53-56]

Natural convection in rectangular enclosures with differentially heated vertical walls and adiabatic horizontal walls is one of the most studied configurations for Newtonian flows [57, 58]. In fact, Newtonian behavior at higher shear rates with dynamic viscosity dependencies as a function temperature has been reported, as well as pseudoplasticity at lower shear rates. Non-Newtonian fluids, i.e., those which go against Newton's law of viscosity, have been widely used in many industries such as food, petrochemicals, pharmaceuticals etc. However, when it comes to rheology, non-Newtonian fluids have been widely used. With regard to rheology, non-Newtonian fluids can be classified into Bingham plastic fluids, pseudoplastic fluids and dilatant fluids. In addition, non-Newtonian fluid models can be divided into time-dependent, time-independent and viscoelastic models [59-62]. Moraga et al. [63] studied the 3D natural convection heat transfer of a non-Newtonian power-law fluid in a container placed in an enclosure. The container was filled with a non-Newtonian power-law fluid and surrounded by air. Their results included isotherms and streamlines at different values of Ra for each Newtonian and non-Newtonian power-law fluid. Jahanbakhshi et al. [64] studied the influence of the magnetic field on the natural convection of a non-Newtonian fluid in an L-shaped cavity. They found that the rate of heat transfer increased for shear-thinning fluids and decreased for shear-thickening fluids. They also found that the Nusselt number decreases with increasing Pr when the fluid shear-thins. Lamsaadi et al. [65] have numerically simulated the natural convection of a non-Newtonian fluid in a vertical cavity. Their results show that a shear-thinning fluid contributes to fluid flow and a shear-thickening fluid reduces it. Shear-thinning

fluid also increases heat transfer. Makayssi et al. [66] presented an analytical and numerical experimental study of natural double-diffusion convection in a shallow two-dimensional horizontal enclosure. These authors concluded that the characteristics of fluid flow and heat and mass transfer appear to be highly sensitive to the flow behavior index, n. Thus, compared to the Newtonian case (n = 1), shear-thinning behavior (0 < n < 1) enhances fluid flow and convective heat and mass transfer. Kefayati [67] considered non-Newtonian fluid in a square enclosure and discussed the effect of Reynold's and magnetic field inclination angle on fluid flow. Zyła et al. [68] carried out a rheological study on nanofluids containing a mixture of nanodiamond and graphite with different ash fractions. They also studied a mixture of nanodiamond and graphite with different ash fractions. Non-Newtonian behavior and viscoelastic structure were also observed. The transient buoyant convection of a non-Newtonian fluid in a square enclosure, heated differentially from the vertical, has been studied numerically by Kim et al. [69]. Getachew et al. [70] have described the flow type and heat and mass transfer patterns of double-diffusive inside a porous enclosure saturated with a non-Newtonian fluid of power using scaling arguments, verifying the results obtained by experimental. Moradi et al. [71] have carried out an experimental study of heat transfer rate enhancement of multi-walled carbon nanotube nanofluids in a double-pipe heat exchanger with aluminium porous media. Jena et al. [72] have studied the double-diffusive free convection of a non-Newtonian Ostwald-De Waele fluid inside a 2D cavity with partially active vertical walls. Lounis et al. [73] studied the impact of Dufour and Soret effects on double-diffusive convection in an inclined square enclosure using the Carreau-Yasuda model to model the rheological behavior of a non-Newtonian fluid. Their main conclusion is that for different values of the power-law index, the Lewis number increases heat and mass exchange. Rebhi et al. [74, 75] investigated the convection generated in porous cavities containing a binary fluid and discovered that the drag parameters had a significant impact on the stability and onset of subcritical and Hopf bifurcation. Rebhi et al. [76] studied Rayleigh-Bénard thermosolutal convection instabilities in shallow enclosures with finite aspect ratios were influenced by the rheological behavior of non-Newtonian fluids. They showed that the bistable convection regime exists for every aspect ratio of the enclosure, regardless of the type of thermal and solutal boundary conditions. Bihiche et al. [77] analyzed the effect of buoyancy ratio on natural convection and on heat and mass transfer rates in a horizontal rectangular enclosure filled with a non-Newtonian power-law fluid. The emergence and and development of double-diffusive convection, for both aiding and opposing flows, were also studied.

Consequently, natural convection in rectangular/square cavities filled with porous layers saturated with a non-Newtonian fluid has been studied by many researchers [78-80]. Nield et al. [81] studied the effect of high heterogeneity on the occurrence of vertical density gradient-induced convection in soil. On the occurrence of convection induced by a vertical density gradient in a saturated porous medium governed by Darcy's law. Devakar et al. [82] have simulated the flow of non-Newtonian fluids in a straight, uniform square duct through a porous medium. They observed that the velocity and volumetric flow rate decrease with increasing torque stress parameter and porosity parameter. Uphill et al. [83] studied the flow of nanofluids in porous media. They showed that nanofluids containing particles smaller than the size of water are more efficient in porous media. Lakshmi et al. [84] studied the effect of Soret and Dufour diffusion on natural convection in a saturated porous medium. The results indicate that the Nusselt number increases linearly with increasing Dufour parameter to facilitate buoyancy. Numerical study of Soret and Dufour effects on the natural convection flow of a vertical plate with low-power heat flux embedded in a porous medium studied by Tsai and Huang [85]. Zhu et al. [86] have numerically studied the natural double-diffusive convection of power-law fluids in a porous cube using a generalized non-Darcy model. They found that the impact of different power law indices on convection are mainly manifested in rheological properties, showing that shear-thinning fluids are more efficient at enhancing heat and mass transfer than shear-thickening fluids. Madhua et al. [87] investigated new entropy generation characteristics in the fully developed heat transport of a non-Newtonian Carreau fluid in an inclined microchannel. They found that the velocity is maximal at the center of the microchannel when using increasing values of Grashof number Gr, while entropy production is maximal at the center of the channel. Ben Khelifa et al. [88] have derived an analytical solution to characterize the onset of motion and heat and mass convection for a binary power law fluid in a shallow porous enclosure. The occurrence of nonlinear convection in a horizontal porous layer saturated with a shear-acting fluid is studied by Bensilakhal et al. [89]. The most interesting results of their study are the demonstration of the existence of a bi-stability phenomenon, i.e., the existence of two steady-state solutions, which had not previously been observed in the convection of non-Newtonian fluids.

Many studies have focused on the effect of the shear-thinning of non-Newtonian fluids, which attracts more attention when it comes to heat transfer problems. The Marangoni in a shallow rectangular cavity of a power-law fluid was studied by Naimi [90]. Chen [91] examined the influence of Marangoni convection for a power-law liquid film on an unsteadily stretching

aluminium foil. Lamsaadi [92] studied the natural convection non-Newtonian power-law fluids subjected to transverse temperature gradients, inside a horizontal rectangular space. These authors noted the combined effect of heat flow ratio, power-law index and Rayleigh number on flow intensity and heat transfer rates. Lamsaadi et al. [93] have shown that the depends only on the nominal Rayleigh number Ra and the power-law index, n, for large values of the aspect ratio and the nominal Prandtl number Pr. Habibi et al. [94] described the natural laminar convection of a non-Newtonian fluid between two horizontal eccentric square ducts under equilibrium conditions. Recently, Alloui et al. [95] analyzed the onset of fluid motion for power-law fluids. It was shown that, for shear-thinning fluids, the onset of convection is subcritical. For shear-thickening fluids, convection occurs at a supercritical Rayleigh number of zero. Khali et al. [96] studied double-diffusive convection on a power-law fluid. The results indicate that the fluid structure is more important for thermal base flow. Ohta et al. [97] have numerically investigated transient heat transfer in a square cavity heated from below and cooled from above. For shear-thinning fluids the Sutherby model was used. Their study also reveals that with increasing magnitude of shear-thinning, based on a transient analysis of natural convection of shear-thinning-fluids in rectangular enclosures with differential heating. Hojjat [98] described Reynolds and Prandtle numbers for non-Newtonian fluids, the coefficient index and power-law index are very important in determining the Reynolds number and initial velocity of the fluid at the tube inlet. Reynolds and Prandtl numbers are described as follows for non-Newtonian fluids. Solomatov and Barr [99, 100] have numerically investigated the occurrence of convection in non-Newtonian power-law fluids under the effect of temperature-dependent viscosity. The authors summarize their results in terms of simple scaling relations.

Prasad and Kulacki [101] reported numerical results for the case where a constant heat flux is applied to one vertical wall, and the other vertical wall is isothermally cooled. Mamou [102] analyzed the thermal stability analysis of convection in a vertical porous subjected to different limits of heat and melt. The linear governing equations were solved numerically using the finite element method. It was reported that increasing the porosity of the porous medium delays the onset of oscillatory flows. Karimi-Fard et al. [103] investigated the onset of nonlinear convection and Hopf bifurcation in a vertical porous filled with a binary fluid subject to constant horizontal temperature and concentration gradients for an inclined rectangular cavity. Mihir et al. [104] studied numerically and analytically the multiplicity of stable states in natural convection in rectangular porous layers with conduction isotherms. The results found that at subcritical Rayleigh numbers there is only one stable state. However, multiple stable states

exist, some of which are unstable. Chan et al. [105] studied normal formation in porous media confined by surfaces with rectangular boundaries at different temperatures. Osfer et al. [106] considered numerically and analytically the coupled natural convection in a vertical porous layer subjected to uniform heat and material flows from the side. Oremi et al. [107] studied the natural convection of a binary mixture confined in a long slightly inclined cavity heated from below. Both diffuse binary convection and induced convection were studied both theoretically and numerically. These authors proved the existence of multiple steady states for sufficiently small slopes about the vertical plane. Mamou and Vasseur [108] studied the onset of coupled diffusive heat and mass flows in an inclined fluid layer, when constant heat and mass fluxes are applied at the corresponding boundaries of the layer. They proved, on the basis of the parallel flow approximation, the existence of a subcritical Rayleigh number for the onset of convection of finite amplitude.

Inclined rectangles have received less attention, and one of the main contributions was by Vlasuk [109] performed a numerical integration of the governing equations and determined the heat transfer as a function of the angle of inclination. One of his important results was that the slope angle for maximum heat transfer for the ratio of unit dimensions and Darcy-Riley numbers in the range of 100-350 is approximately 50 degrees. Heat transfer through the porous layer is dominated by convection in the boundary layer system, where the Rayleigh number is very large. In the upper limit of the Rayleigh number, the Darcy flow model is inaccurate because the vertical velocity scale increases as 〖Ra〗^2/3. Gravity-induced thermal diffusion in a rectangular vertical cavity subjected to horizontal thermal gradients as studied by Marcoux et al. [110] for the case of opposing and equal thermal buoyancy forces. The supercritical Rayleigh number for the onset of convection from rest is predicted on the basis of linear stability theory, in terms of the aspect ratio of the cavity. In explaining the main features of the heat and mass transfer phenomenon discussed by Bejan [111], where pure measurement arguments were used to identify and sort out the most fundamental metrics that characterize the flow, temperature and concentration fields in the immediate vicinity of a single submerged vertical surface in a porous medium with different temperature and concentration. A mathematical solution to the equations of mass, energy and appropriate momentum equations led Holst and Aziz [112]. These authors concluded that the maximum convection should occur at an angle of 40° and Rayleigh numbers of 50-60, provided the aspect ratio is one. Alloui et al. [113] numerical study of natural convection in an inclined porous medium. Their results indicated that the effect of the drag coefficient on the existence of multiple steady-state solutions possible

for a surface slightly tilted about the horizontal. Vasseur et al. [114] determined the natural convection in a two-dimensional (2D) oblique porous layer with uniform heat flow from two opposite walls while the other walls were studied analytically and numerically. The authors showed that good agreement was found between analytical predictions and numerical simulations. The multiple steady-state solutions for slightly inclined porous materials, as investigated analytically by Walsh and Dulieu [115]. In a more recent numerical study of natural convection in a fluid-saturated rectangular porous material analyzed by Moya et al. [116]. Their studies revealed that when the bottom wall is at a higher temperature and in a horizontal or near-horizontal position.

For the Newtonian case, flows in such configurations have been the subject of many experimental and numerical studies. Ozoe and Sayama [117] experimentally and numerically on heat transfer in inclined cavities for a range of Rayleigh numbers and tilt angles. Ozu and Sayama [118, 119] in an experimental and numerically calculated values of the Nusselt number for natural convective heat in square and rectangular channels.

Recently, Bian et al. [5] performed numerical studies on the rectangular cavity of natural convection filled with a porous medium saturated with a non-Newtonian fluid, and their results found that the power-law index n seems to have no effect on the extreme angle, for example Nusselt number peaks occur at about 135° for various power-law indices when R = 100. Numerical and analytical study of natural convection in a vertical porous cavity filled with a non-Newtonian binary fluid, characterized by a power-law model, by Ben Khalifa et al. [120]. The natural convection of non-Newtonian fluid in a tilted two-dimensional rectangular cavity investigated by Khezzar et al. [121]. The results showed that increasing the tilt angle from horizontal leads to a sudden decrease in heat transfer rate. Experimental and numerical studies have also confirmed the increase in natural convective strength in rectangular bundles of shear-thinning fluids on microemulsion pastes by Inaba et al. [122] in a Rayleigh-Bénard configuration.

Previous work on natural convection of binary fluids is concerned with the onset of motion in a horizontal porous layer subject to vertical temperature and concentration gradients. In practice. Many researchers have presented analytical and experimental results for a rectangular cavity with vertical walls at constant temperatures, where the walls are insulated horizontal. [123-128].

CHAPTER II

PHYSICAL MODEL AND MATHEMATICAL FORMULATION

2.1 PROBLEM DESCRIPTION

The phenomenon of double-diffusive convection within a confined space is the focus of this study. The two-dimensional geometric setup of our flow is depicted in Fig 2.1. We analyze a scenario involving a rectangular cavity characterized by the following geometric dimensions: length L', height H', and width W', inclined at an angle Φ relative to the horizontal plane, and containing a porous medium saturated with a binary non-Newtonian fluid. The long walls of the cavity are subjected to uniform heat fluxes, q', and mass fluxes, j'. The remaining walls are presumed to be adiabatic and impermeable.

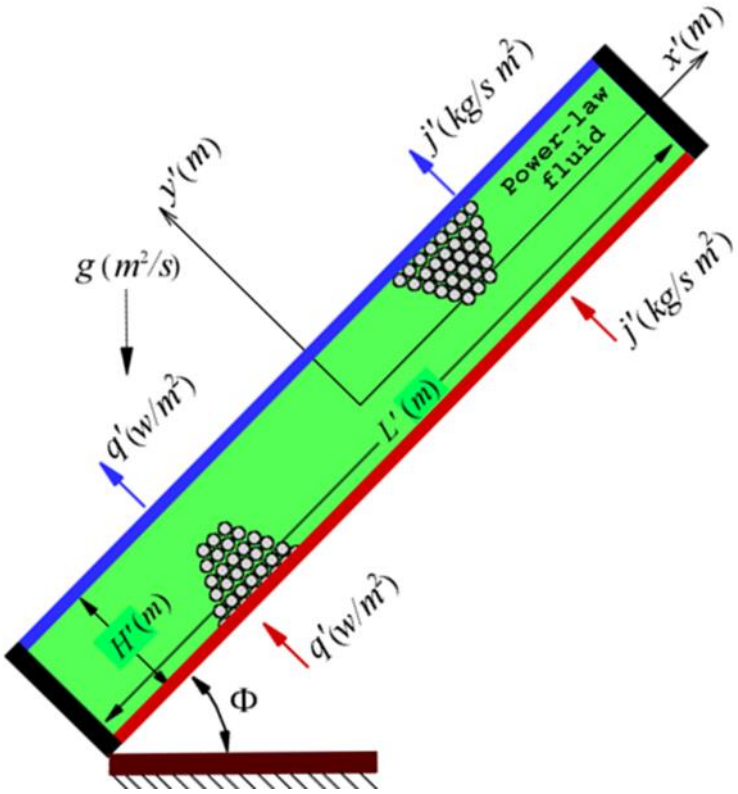


Figure 2.1: Schematic representation of the physical model and the coordinate system.

2.2 SIMPLIFYING ASSUMPTIONS

For a simplified mathematical model, we will incorporate several approximations, such as the Boussinesq approximations, commonly employed in the examination of natural convection.

Therefore, we assume:

- The width of the enclosure, W', is considered significantly larger than the other dimensions (W'/L' and $W'/H' >> 1$), rendering three-dimensional effects insignificant. This simplifies the problem to a two-dimensional scenario, as illustrated in Fig 2.1.
- The solution is a non-Newtonian and incompressible fluid.
- The resulting flow is assumed to be laminar.
- The porous matrix is isotropic, permeable, and homogeneous.
- There is no chemical reaction or heat or mass source.
- Heat transfer by radiation is negligible.
- The interactions between heat and mass transfers, known as the Soret and Dufour effects respectively, are negligible.
- The work induced by viscous and pressure forces is considered negligible.
- The thermophysical properties of the fluid are assumed constant and evaluated at the reference temperature. However, the fluid density in the volume force term varies linearly with temperature. This is expressed by the following relationship:

$$\rho = \rho_0 \left[1 - \beta'_T \left(T' - T'_0\right) - \beta'_S \left(S' - S'_0\right)\right] \tag{2.1}$$

Where, ρ is the density of the non-Newtonian fluid. T' and S' represent the temperature and concentration of the fluid at a specific point within the system, T'_0, S'_0 and ρ_0 represent respectively, the temperature, concentration, and mass density of reference.

β'_T, β'_S respectively are the thermal and solutal expansion coefficients. They are defined by

$$\beta'_T = -\frac{1}{\rho_0}\left(\frac{\partial \rho}{\partial T}\right)_{P',S'}, \quad \beta'_S = -\frac{1}{\rho_0}\left(\frac{\partial \rho}{\partial S}\right)_{P',T'} \tag{2.2}$$

For most fluids, β'_T is positive except for water, which exhibits maximum density near 4°C. However, β'_S can be negative or positive depending on the contribution of the diffusion components to the fluid's density.

2.3 MATHEMATICAL FORMULATION

Taking into account all the assumptions made, the system of partial differential equations governing this problem comprises the continuity equation, the momentum conservation equations, and the energy and mass conservation equations in a porous medium.

For the study of natural convection in porous media, we assume that the porous matrix is solid, permeable, homogeneous, isotropic, and saturated with the fluid. The equations related to heat and mass fluxes in the presence of thermal and solute gradients are given by De Groot and Mazur (1969) [129]:

$$\vec{q}' = -k\nabla T' \tag{2.3}$$

$$\vec{j}' = -\rho D\nabla S' \tag{2.4}$$

Where, k and D signify the thermal conductivity and molecular diffusion coefficient of the species.

For a cavity filled with a binary fluid, the basic equations governing the flow and the transfer of heat and mass are given, respectively, by:

2.3.1 CONTINUITY EQUATION

The continuity equation, which expresses the conservation of mass for a moving fluid, is expressed as follows:

$$\frac{\partial u'}{\partial x'} + \frac{\partial v'}{\partial y'} = 0 \tag{2.5}$$

2.3.2 EQUATION OF MOTION: Darcy's Law

The local formulation of the conservation of momentum equation is written as follows:

$$u' = -\frac{K}{\mu_a'}\left[\frac{\partial P'}{\partial x'} + \rho_0 g\left[1-\beta_T'\left(T'-T_0'\right)-\beta_S'\left(S'-S_0'\right)\right]\cos\Phi\right] \tag{2.6}$$

$$v' = -\frac{K}{\mu_a'}\left[\frac{\partial P'}{\partial y'} - \rho_0 g\left[1-\beta_T'\left(T'-T_0'\right)-\beta_S'\left(S'-S_0'\right)\right]\sin\Phi\right] \tag{2.7}$$

2.3.3 EQUATION OF VISCOSITY

In alignment with earlier findings clarified by Pascal [131, 132], the model describing laminar flow of a non-Newtonian power-law fluid through a porous medium is expressed as follows:

$$\mu_a' = \varepsilon \left(u'^2 + v'^2 \right)^{(n-1)/2} \tag{2.8}$$

Where, $\varepsilon = 2h \Big/ \left[8^{(n+1)/2} \left(K\phi \right)^{(n-1)/2} \left(n/(1+3n) \right)^n \right]$ is a parameter in power-law model.

2.3.3 ENERGY CONSERVATION EQUATION

The first law of thermodynamics establishes relationships between the different forms of energy involved in porous media. The energy equation, in which viscous dissipation terms are neglected, is written as follows:

$$\left(\rho C \right)_p \frac{\partial T'}{\partial t'} + \left(\rho C \right)_f \left(u' \frac{\partial T'}{\partial x'} + v' \frac{\partial T'}{\partial y'} \right) = k \nabla^2 T' \tag{2.9}$$

2.3.4 MASS CONSERVATION EQUATION

The principle of mass conservation leads to the following concentration equation:

$$\phi \frac{\partial S'}{\partial t'} + u' \frac{\partial S'}{\partial x'} + v' \frac{\partial S'}{\partial y'} = D \nabla^2 S' \tag{2.10}$$

In the equations above, V' is the superficial velocity whose components are u' and v' in the x' and y' directions, respectively, P' is the hydrodynamic pressure, ϕ and K the porosity and the permeability of the porous medium respectively, μ'_a, the apparent viscosity, h the consistency index and n the power-law index. the rheological parameters h and n are assumed to be temperature independent. The parameters $(\rho C)_p$ and $(\rho C)_f$ are the thermal heat capacity of the saturated porous medium and the thermal heat capacity of the fluid, respectively.

The dimensionless form of equations (2.5) through (2.10) was established by using the height H' between the two active horizontal walls of the cavity as the reference length. The velocity was dimensionless with respect to the thermal diffusivity, while the temperature and concentration were made dimensionless with respect to the temperature and concentration difference between the two horizontal walls of the cavity.

$$\begin{aligned}(x,y)=(x',y')/H' \quad (u,v)=(u',v')H'/\alpha \quad t=t'\alpha/(\sigma H'^2)\\ \psi=\psi'/\alpha \quad T=(T'-T_0')/\Delta T' \quad \Delta T'=q'H'/k\\ S=(S'-S_0')/\Delta S' \quad \Delta S'=j'H'/\rho D \quad \mu_a=\mu_a'/\varepsilon(\alpha/H')^{n-1}\end{aligned} \tag{2.11}$$

where: α and σ denote the thermal diffusivity of the saturated porous medium and heat capacity ratio respectively. They are defined as:

$$\alpha=\frac{k}{(\rho C)_f}, \qquad \sigma=\frac{(\rho C)_p}{(\rho C)_f} \tag{2.12}$$

By introducing the dimensionless variables (2.11) into equations (2.5)-(2.10), and eliminating the pressure term in Eq. (2.6)- (2.7) we obtain the following dimensionless governing equations describing respectively, the conservation of momentum, energy, and mass.

$$\frac{\partial u}{\partial x}+\frac{\partial v}{\partial y}=0 \tag{2.13}$$

$$\nabla^2\Psi=-\mu_a^{-1}\left[\frac{\partial\Psi}{\partial y}\frac{\partial\mu_a}{\partial y}+\frac{\partial\Psi}{\partial x}\frac{\partial\mu_a}{\partial x}+R_T\left(\left(\frac{\partial T}{\partial x}+N\frac{\partial S}{\partial x}\right)\cos\Phi-\left(\frac{\partial T}{\partial y}+N\frac{\partial S}{\partial y}\right)\sin\Phi\right)\right] \tag{2.14}$$

$$\nabla^2 T=\frac{\partial T}{\partial t}+\frac{\partial\Psi}{\partial y}\frac{\partial T}{\partial x}-\frac{\partial\Psi}{\partial x}\frac{\partial T}{\partial y} \tag{2.15}$$

$$Le^{-1}\nabla^2 S=\xi\frac{\partial S}{\partial t}+\frac{\partial\Psi}{\partial y}\frac{\partial S}{\partial x}-\frac{\partial\Psi}{\partial x}\frac{\partial S}{\partial y} \tag{2.16}$$

$$\mu_a=\left[\left(\frac{\partial\Psi}{\partial x}\right)^2+\left(\frac{\partial\Psi}{\partial y}\right)^2\right]^{\frac{n-1}{2}} \tag{2.17}$$

The dimensionless parameters extracted from Eqs. (2.13)-(2.17) are the thermal Rayleigh number, R_T, the Lewis number, Le, the buoyancy ratio, N, and the normalized porosity, ξ. These parameters are defined as follows:

$$\begin{aligned}R_T=\frac{K\rho_0 g\beta_T'\Delta T'(H'/\alpha)^n}{\varepsilon}, \qquad Le=\frac{\alpha}{D}\\ N=\frac{\beta_S'\Delta S'}{\beta_T'\Delta T'}, \qquad \xi=\frac{\phi}{\sigma}\end{aligned} \tag{2.18}$$

2.4 STREAM FUNCTION EQUATION

Since the flow is considered two-dimensional, there exists a stream function $\Psi(x, y)$ defined by:

$$u = \frac{\partial \Psi}{dy}, \quad v = -\frac{\partial \Psi}{dx} \tag{2.19}$$

2.5 BOUNDARY CONDITIONS

2.5.1 HYDRODYNAMIC BOUNDARY CONDITIONS

These conditions express the impermeability of the cavity walls and are given by:

$$\left.\begin{aligned} u' = 0, \quad \Psi' = 0 \qquad at \qquad x' = \pm\frac{L'}{2} \\ v' = 0, \quad \Psi' = 0 \qquad at \qquad y' = \pm\frac{H'}{2} \end{aligned}\right\} \tag{2.20}$$

2.5.2 THERMAL AND MASS BOUNDARY CONDITIONS

The boundary conditions on the adiabatic and impermeable walls of the cavity are expressed by:

$$\frac{\partial T'}{\partial x'} = \frac{\partial S'}{\partial x'} = 0 \qquad at \qquad x' = \pm\frac{L'}{2} \tag{2.21}$$

Furthermore, the thermal conditions on the active walls are:

$$-k\frac{\partial T'}{\partial y'} = q', \quad -\rho D\frac{\partial S'}{\partial y'} = j' \qquad at \quad y' = \pm\frac{H'}{2} \tag{2.22}$$

2.5.3 DIMENSIONLESS BOUNDARY CONDITIONS

$$\left.\begin{aligned} u = 0, \quad \Psi = 0 \qquad at \qquad x = \pm\frac{A}{2} \\ v = 0, \quad \Psi = 0 \qquad at \qquad y = \pm\frac{1}{2} \end{aligned}\right\} \tag{2.23}$$

$$\frac{\partial T}{\partial x} = \frac{\partial S}{\partial x} = 0 \qquad at \qquad x = \pm\frac{A}{2} \tag{2.24}$$

$$\frac{\partial T}{\partial y} = \frac{\partial S}{\partial y} = -1 \qquad at \quad y = \pm\frac{1}{2} \tag{2.25}$$

where $A = L'/H'$ is the cavity aspect ratio.

2.6 THERMAL AND MASS TRANSFER RATE

In this study, our focus lies in determining the heat and mass transfer rates at a specific position x, which are quantified by the Nusselt and Sherwood numbers, described as:

$$Nu_x = \frac{q'}{k\dfrac{\Delta T'}{H'}} = \frac{1}{T_{(x,-1/2)} - T_{(x,1/2)}} \tag{2.26}$$

$$Sh_x = \frac{j'}{D\dfrac{\Delta S'}{H'}} = \frac{1}{S_{(x,-1/2)} - S_{(x,1/2)}} \tag{2.27}$$

The average values of the Nusselt and Sherwood numbers on the active walls are expressed by:

$$Nu_m = \frac{1}{A}\int_{-A/2}^{+A/2} Nu_x dx \tag{2.28}$$

$$Sh_m = \frac{1}{A}\int_{-A/2}^{+A/2} Sh_x dx \tag{2.29}$$

CHAPTER III

ANALYTICAL SOLUTION

The coupled non-linear partial differential equations that govern the phenomenon of double-diffusive convection in porous media (2.14), (2.15), and (2.16) pose a significant challenge for analytical solutions. However, under specific assumptions, such as a porous layer with a large aspect ratio ($A >> 1$) and active walls subjected to constant heat and mass fluxes, it becomes possible to derive an approximate analytical solution. This approach, based on the concept of parallel flow, allows the analytical prediction of various physical phenomena associated with double diffusive natural convection.

The utilization of the parallel flow concept has been effectively demonstrated by numerous researchers in the investigation of natural convection within shallow enclosure (A>>1). Some notable contributors include Cormack et al. (1974) [133], Sen et al. (1987) [4], Vasseur et al. (1989) [134], Alavyoon (1993) [135], and Mamou et al. (1995b) [136]. This concept operates under the assumption that in cases where the cavity has a large aspect ratio (A>>1), the flow generated tends to align relatively parallel to the long walls of the cavity, thereby allowing the exclusion of the velocity component perpendicular to these walls.

The streamlines, at the center of the cavity, become parallel to the x-axis. In other words, the current function Ψ becomes a function of the y ordinate only. We can then write:

$$\Psi(x,y) \simeq \Psi(y) \tag{3.1}$$

Introducing this approximation (3.1) into the momentum energy and mass conservation equations (2.14), (2.15) and (2.16), it becomes evident that the temperature and concentration profiles can be expressed as the sum of two components: one representing a linear longitudinal variation, while the other describes the transverse distribution.

$$\left.\begin{aligned} T(x,y) &\simeq C_T x + \theta_T(y) \\ S(x,y) &\simeq C_S x + \theta_S(y) \end{aligned}\right\} \tag{3.2}$$

Where, C_T and C_S are unknown constants temperature and concentration gradients in the x-direction.

In situations where heat and mass fluxes are imposed, the energy and mass balances within the control volume (as illustrated in Fig 2.1) are expressed as per Trevisan and Bejan [106] in the following manner:

$$\int_{-1/2}^{+1/2} \frac{\partial T}{\partial x} dy = \int_{-1/2}^{+1/2} \frac{\partial \Psi}{\partial y} T dy \tag{3.3}$$

$$\int_{-1/2}^{+1/2} \frac{\partial S}{\partial x} dy = Le \int_{-1/2}^{+1/2} \frac{\partial \Psi}{\partial y} S dy \tag{3.4}$$

upon substituting the approximations (3.1), (3.2) and (3.3) into equations (2.14), (2.15), and (2.16), and presuming that the heat and mass fluxes are in a steady state, we deduce the following ordinary differential equations:

$$\frac{d}{dy}\left[\frac{d\Psi}{dy} \left| \frac{d\Psi}{dy} \right|^{n-1} \right] = -R_T \left[\left(\frac{\partial T}{\partial x} + N \frac{\partial S}{\partial x} \right) \cos\Phi - \left(\frac{\partial T}{\partial y} + N \frac{\partial S}{\partial y} \right) \sin\Phi \right] \tag{3.5}$$

$$\frac{d^2 \theta_T}{dy^2} = C_T \frac{d\Psi}{dy} \tag{3.6}$$

$$\frac{d^2 \theta_S}{dy^2} = C_S Le \frac{d\Psi}{dy} \tag{3.7}$$

Now we will evaluation the analytical and the semi-analytical solutions in the case of horizontal layer and inclined layer, respectively.

3.1 HORIZONTAL LAYER: $\Phi = 0°$ AND $\Phi = 180°$

For $\Phi = 0°$, the momentum equation (3.5) is written as follows:

$$\frac{d}{dy}\left[\frac{d\Psi}{dy} \left| \frac{d\Psi}{dy} \right|^{n-1} \right] = -\Lambda \tag{3.8}$$

where: $\Lambda = R_T \left(C_T + N C_S \right)$

There are now tow cases to discuss. The first when the fluid is non-Newtonian (i.e. Power-law index $n \neq 1$) for a shear-thinning fluids ($n < 1$) and shear-thickening fluids ($n > 1$), the secand is a special case with power-law index $n = 1$ (i.e. Newtonian fluids).

3.1.1 NON-NEWTONIAN FLUID $n \neq 1$

The stream function, temperature, and concentration profiles of Eqs. (3.8), (3.6), and (3.7) satisfying the boundary conditions given by Eq. (2.23), and (2.25) are:

$$\Psi(y) = -(m)^{-1}\left[\Lambda\right]^{1/n}\left[|y|^{m} - (1/2)^{m}\right] \tag{3.9}$$

$$T(y) = C_T x \; - \; \left[\Lambda\right]^{1/n}(m)^{-1} C_T y\left[(m+1)^{-1}|y|^{m} - (1/2)^{m}\right] - y \tag{3.10}$$

$$S(y) = C_S x \; - \; \left[\Lambda\right]^{1/n}(m)^{-1} LeC_S y\left[(m+1)^{-1}|y|^{m} - (1/2)^{m}\right] - y \tag{3.11}$$

where: $m = 1 + 1/n$.

The expression of the velocity distribution u along y derived from the stream function is:

$$u(y) = -\left[\Lambda\right]^{1/n}|y|^{1/n} \tag{3.12}$$

By substituting the stream function, temperature, concentration Eqs. (3.9), (3.10), and (3.11) at $x = 0$ into Eqs. (3.3), and (3.4), we get the following expression of C_T, and C_S:

$$C_T = \frac{b\left[\Lambda\right]^{m-1}}{a + \left[\Lambda\right]^{2m-2}} \tag{3.13}$$

$$C_S = \frac{bLe\left[\Lambda\right]^{m-1}}{a + Le^2\left[\Lambda\right]^{2m-2}} \tag{3.14}$$

With,

$$a = (m+1)(2m+1)2^{2m-1}, \qquad b = (2m+1)2^{m-1} \tag{3.15}$$

After algebraic manipulation we obtain the following expression:

$$\begin{aligned} Le^2\left[\Lambda\right]^{4m-3} + \left(Le^2+1\right)a\left[\Lambda\right]^{2m-1} - (1+NLe)abR_T\left[\Lambda\right]^{m-1} - \\ (Le+N)bLeR_T\left[\Lambda\right]^{3m-3} + a^2\left[\Lambda\right] = 0 \end{aligned} \tag{3.16}$$

Equations (3.16) has been solved numerically for Λ using the method of Newton-Raphson.

From Eqs. (3.10), (3.11), (3.13), (3.14), (2.26) and (2.27), the Nusselt and Sherwood numbers are given by:

$$Nu = \frac{a + \left[\Lambda\right]^{2m-2}}{a + \left(1 - 2^{-m}\left(m+1\right)^{-1} b\right)\left[\Lambda\right]^{2m-2}} \tag{3.17}$$

$$Sh = \frac{a + Le^{2}\left[\Lambda\right]^{2m-2}}{a + \left(1 - 2^{-m}\left(m+1\right)^{-1} b\right) Le^{2}\left[\Lambda\right]^{2m-2}} \tag{3.18}$$

In the context of parallel flow, $Nu = Nu_c$ and $Sh = Sh_c$, where Nu_c and Sh_c are respectively, the Nusselt and Sherwood numbers at the center of the porous layer ($x = 0$).

When the Rayleigh number R_T becomes very large, ($R_T \to \infty, \Lambda \to \infty$); the Nusselt and Sherwood numbers asymptotically tend to:

$$Nu^{-1} = Sh^{-1} = 1 - 2^{-m}\left(m+1\right)^{-1} b \tag{3.19}$$

For this situation, the asymptotic expressions for the temperature and concentration gradient and the flow intensity are obtained as follows:

$$\left.\begin{aligned} C_T &= \left[b\left[R_T\left(1 + NLe^{-1}\right)\right]^{1-m}\right]^{1/m} \\ C_S &= Le^{-1} C_T \\ \Psi_0 &= 2^{-m} m^{-1}\left(R_T\left(1 + NLe^{-1}\right) b^{1/m}\right)^{m-1} \end{aligned}\right\} \tag{3.20}$$

In the case of simple diffusion, $N = 0$, the asymptotic expressions for the temperature gradient and C_T and the flow intensity Ψ_0 are obtained as follows:

$$\left.\begin{aligned} C_T &= \left(bR_T^{1-m}\right)^{1/m} \\ \Psi_0 &= 2^{-m} m^{-1}\left(R_T b^{1/m}\right)^{m-1} \end{aligned}\right\} \tag{3.21}$$

For the case of $\Phi = 180°$ (i.e. the cavity is upturned), the only values of C_T and C_S are zero for which $\Psi_0 = 0$, $Nu_c = 1$, and $Sh_c = 1$.

3.1.2 NEWTONIAN FLUID $n = 1$

In this case we consider the power-law index $n = 1$. The equations (3.9), (3.10), and (3.11) become as follows:

$$\Psi(y) = -(1/2)[\Lambda]\left[|y|^2 - (1/2)^2\right] \tag{3.22}$$

$$T(y) = C_T x \; - \; [\Lambda](1/2)C_T y\left[(1/3)|y|^2 - (1/2)^2\right] - y \tag{3.23}$$

$$S(y) = C_S x \; - \; [\Lambda](1/2)LeC_S y\left[(1/3)|y|^2 - (1/2)^2\right] - y$$

The expression of the velocity distribution u along y become as follows:

$$u(y) = - \; [\Lambda]|y| \tag{3.24}$$

The expression of C_T, and C_S become as follows:

$$C_T = \frac{10\Lambda}{\Lambda^2 + 120} \tag{3.25}$$

$$C_S = \frac{10Le\Lambda}{Le^2\Lambda^2 + 120} \tag{3.26}$$

The Nusselt and Sherwood numbers are given by:

$$Nu = \frac{1440 + 12[\Lambda]^2}{1440 + 2[\Lambda]^2} \tag{3.27}$$

$$Sh = \frac{1440 + 12Le^2[\Lambda]^2}{1440 + 2Le^2[\Lambda]^2} \tag{3.28}$$

When, $(R_T \rightarrow \infty, \Lambda \rightarrow \infty)$; the Nusselt and Sherwood numbers asymptotically tend to:

$$Nu = Sh = 6$$

In this scenario, the asymptotic formulations for the temperature and concentration gradients, along with the flow intensity, can be derived as follows:

$$\left.\begin{aligned} C_T &= \sqrt{b\left[R_T\left(1+NLe^{-1}\right)\right]^{-1}} \\ C_S &= Le^{-1}C_T \\ \Psi_0 &= \left(R_T\left(1+NLe^{-1}\right)\sqrt{b}\right)/8 \end{aligned}\right\} \tag{3.29}$$

In the scenario of simple diffusion, where $N = 0$, the asymptotic expressions for the temperature gradient C_T and the flow intensity Ψ_0 can be obtained as follows:

$$\left.\begin{aligned} C_T &= \sqrt{b/R_T} \\ \Psi_0 &= \left(R_T\sqrt{b}\right)/8 \end{aligned}\right\}$$

3.2 INCLINED LAYER: $0° \leq \Phi \leq 180°$

In this case, by using the boundary conditions, Eq. (2.25), and performing a first integration into Eqs. (3.6), and (3.7), it is found that the temperature and the concentration equations are:

$$\frac{d\theta_T}{dy} = C_T\Psi - 1 \tag{3.30}$$

$$\frac{d\theta_S}{dy} = LeC_S\Psi - 1 \tag{3.31}$$

Through Eqs. (3.5), (3.30) and (3.31) it is found that the momentum equation can be formulated as follows:

$$\frac{d}{dy}\left[\frac{d\Psi}{dy}\left|\frac{d\Psi}{dy}\right|^{n-1}\right] - R_T\left(C_T + NLeC_S\right)\Psi\sin\Phi = -R_T\left[\left(C_T + NC_S\right)\cos\Phi + \left(N+1\right)\sin\Phi\right] \tag{3.32}$$

It is apparent that applying the boundary conditions in the x-direction, as described in Eq. (2.24), directly under the parallel flow approximation is not possible. Nonetheless, by combining Eqs. (3.3) and (3.4) with Eqs. (3.30), (3.31), and (3.2), the following expressions of C_T and C_S can be derived:

$$C_T = \frac{\int_{+1/2}^{-1/2}\Psi\left(y\right)dy}{1+\int_{+1/2}^{-1/2}\Psi^2\left(y\right)dy} \tag{3.33}$$

$$C_S = \frac{Le\int_{-1/2}^{+1/2}\Psi(y)\,dy}{1+Le^2\int_{-1/2}^{+1/2}\Psi^2(y)\,dy} \tag{3.34}$$

The equation (28), with initial values estimated for C_T and C_S and subject to boundary conditions outlined in Eqs. (2.23)-(2.25), is numerically solved employing the TRIDAG method to determine the stream function field Ψ. Initially, this equation is discretized via a finite difference approach. Subsequently, utilizing the Simpson integration scheme, new values for C_T and C_S are derived by executing the numerical integration described in Eqs. (3.33) and (3.34). This iterative process persists until convergence is attained for C_T, C_S, and Ψ. Intentionally chosen initial solutions are utilized, coupled with a relaxation technique, to expedite convergence and stabilize the sought-after solutions. Following this, the temperature and concentration fields, T and S, are evaluated by solving Eqs. (3.30) and (3.31), along with their corresponding boundary conditions detailed in Eqs. (2.24) and (2.25). Consequently, the Nusselt and Sherwood numbers are computed using Eqs. (2.28) and (2.29). Remarkably, this semi-analytical method significantly reduces computational time compared to the numerical procedure required for solving the complete governing equations (2.14)-(2.16).

CHAPTER IV

NUMERICAL SOLUTION

This chapter employs a numerical approach to solve the non-linear differential equations. The method proposed relies on the finite difference technique, a classical numerical method dating back to the 18th century, pioneered by Euler. This method is particularly well-suited and straightforward for problems involving simple geometries. It involves discretizing the continuous equations at specified nodes on a pre-defined mesh, as illustrated in Fig. 4.1.

In a Cartesian coordinate system, each node is designated by the pair of indices (i, j) indicating the lines of intersection of the mesh. The neighboring nodes are implicitly defined by increasing or decreasing one of the indices by a unit increment.

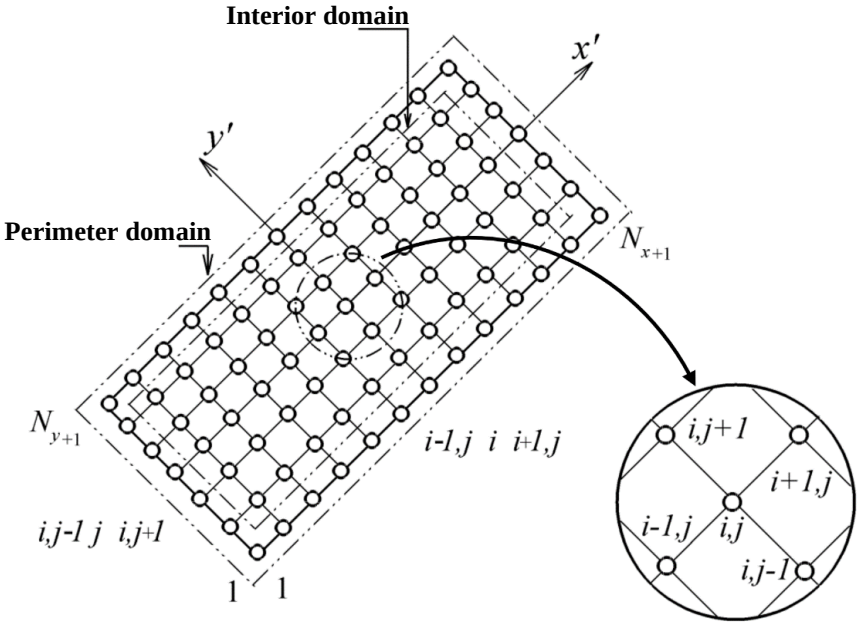


Figure 4.1: Mesh of the calculation domain in (i, j).

For simple geometry problems Fig. 4.1, the finite difference method used to solve numerically the governing equations (2.14)-(2.16). The energy and concentration equations are discretized with a second-order centered scheme. For each time step the implicit method with alternating directions (ADI) of Peaceman and Rachford [137] gives rise to two tri-diagonal matrix systems to be solved, one resulting from the implicit discretization in x and the other of the implicit discretization in y. The (ADI) method divides the time step into two equal parts, in the first half-time step, the system is implicitly in x but explicitly in y and in the second half-time step, the system is implicitly in y and explicitly in x. For each time step, the solution is obtained by

scanning the computational domain in the x direction then in y-direction. Knowing the fields of temperature and concentration at time $(n+1)\Delta t$, to solve the discretized motion equation (2.14) at each time step successive over relaxation method (SOR) proposed by Frankel (1950) [138] is used which is an explicit method directly giving the value of Ψ to the instant $(n+1)\Delta t$, at the considered node, provided a sufficient number of iterations for the desired convergence criterion is satisfied.

4.1 DISCRETIZATION OF THERMAL BOUNDARY CONDITIONS

The boundary conditions (2.24) and (2.25) are discretized using a second-order right and left-centered finite difference scheme, which depends on the specific wall under consideration.

According to the adiabatic and impermeable walls: $\frac{\partial T}{\partial x} = \frac{\partial S}{\partial x} = 0$

$$T_{1,j} = \frac{4T_{2,j} - T_{3,j}}{3}, \qquad S_{1,j} = \frac{4S_{2,j} - S_{3,j}}{3} \quad \text{at} \quad x = -\frac{A}{2} \tag{4.1}$$

$$T_{Nx+1,j} = \frac{4T_{Nx,j} - T_{Nx-1,j}}{3}, \qquad S_{Nx+1,j} = \frac{4S_{Nx,j} - S_{Nx-1,j}}{3} \quad \text{at} \quad x = \frac{A}{2} \tag{4.2}$$

According to the active walls: $\frac{\partial T}{\partial x} = \frac{\partial S}{\partial x} = -1$

$$T_{i,1} = \frac{4T_{i,2} - T_{i,3} + 2\Delta y}{3}, \qquad S_{i,1} = \frac{4S_{i,2} - S_{i,3} + 2\Delta y}{3} \quad \text{at} \quad y = -\frac{1}{2} \tag{4.3}$$

$$T_{i,Ny+1} = \frac{4T_{i,Ny} - T_{i,Ny-1} - 2\Delta y}{3}, \qquad S_{i,1} = \frac{4S_{i,Ny} - S_{i,Ny-1} - 2\Delta y}{3} \quad \text{at} \quad y = \frac{1}{2} \tag{4.4}$$

4.2 DISCRETIZATION OF THE ENERGY EQUATION

The energy equation is resolved using the Alternating Directions Implicit (ADI) method. The energy equation (2.14) is rewritten as follows:

$$\frac{\partial T}{\partial t} + \frac{\partial (uT)}{\partial x} + \frac{\partial (vT)}{\partial y} = \frac{\partial^2 T}{\partial x^2} + \frac{\partial^2 T}{\partial y^2} \tag{4.5}$$

The Alternating Direction Implicit (ADI) method is a numerical technique used to solve partial differential equations (PDEs), especially when they are of the parabolic type, such as the energy and the concentration equations. The ADI method is based on the alternating direction implicit scheme, where the partial derivatives with respect to each spatial variable are approximated

implicitly, while those with respect to the other variables are approximated explicitly in a time-marching procedure. This alternation of directions allows for greater stability and accuracy in the solution.

Implicit in x and explicit in y scheme

This is a centered time scheme $(n+1/2)$ for the x-derivatives and a forward time (n) for the y-derivatives, each term of equation (4.5) is discretized as follows:

$$\left.\frac{\partial^2 T}{\partial x^2}\right|_{i,j} = \frac{T_{i+1,j}^{n+1/2} - 2T_{i,j}^{n+1/2} + T_{i-1,j}^{n+1/2}}{\Delta x^2}, \qquad \left.\frac{\partial^2 T}{\partial y^2}\right|_{i,j} = \frac{T_{i,j+1}^{n} - 2T_{i,j}^{n} + T_{i,j-1}^{n}}{\Delta y^2} \tag{4.6}$$

$$\left.\frac{\partial (uT)}{\partial x}\right|_{i,j} = \frac{u_{i+1,j}^{n} T_{i+1,j}^{n+1/2} - u_{i-1,j}^{n} T_{i-1,j}^{n+1/2}}{2\Delta x}, \qquad \left.\frac{\partial (vT)}{\partial y}\right|_{i,j} = \frac{v_{i,j+1}^{n} T_{i,j+1}^{n} - v_{i,j-1}^{n} T_{i,j-1}^{n}}{2\Delta y} \tag{4.7}$$

$$\left.\frac{\partial T}{\partial t}\right|_{i,j} = 2\frac{T_{i,j}^{n+1/2} - T_{i,j}^{n}}{\Delta t} \tag{4.8}$$

Substituting equations (4.6)-(4.8) into equation (4.5), we obtain a tridiagonal matrix system of the form:

$$A_i T_{i+1,j}^{n+1/2} + B_i T_{i,j}^{n+1/2} + C_i T_{i-1,j}^{n+1/2} = D_i \tag{4.9}$$

with:

$$A_i = \frac{u_{i+1,j}^{n}}{2\Delta x} - \frac{1}{\Delta x^2}, \quad B_i = \frac{2}{\Delta t} + \frac{2}{\Delta x^2}, \quad C_i = -\frac{u_{i-1,j}^{n}}{2\Delta x} - \frac{1}{\Delta x^2}$$

$$D_i = \left[-\frac{v_{i,j+1}^{n}}{2\Delta y} + \frac{1}{\Delta y^2}\right] T_{i,j+1}^{n} + \left[\frac{2}{\Delta t} - \frac{2}{\Delta y^2}\right] T_{i,j}^{n} + \left[\frac{v_{i,j-1}^{n}}{2\Delta y} + \frac{1}{\Delta y^2}\right] T_{i,j-1}^{n}$$

Replacing the boundary conditions (4.1)-(4.4) in the equation (4.9) we obtain the implicit discrete form in x in the following form:

For $i = 2$ $$\left(A_2 - \frac{1}{3}C_2\right) T_{3,j}^{n+1/2} + \left(B_2 + \frac{4}{3}C_2\right) T_{2,j}^{n+1/2} = D_2 \tag{4.10}$$

For $i = Nx$ $$\left(\frac{4}{3}A_{Nx} + B_{Nx}\right) T_{Nx}^{n+1/2} + \left(C_{Nx} - \frac{1}{3}A_{Nx}\right) T_{Nx-1,j}^{n+1/2} = D_{Nx} \tag{4.11}$$

Implicit in y and explicit in x scheme

This is a centered time scheme $(n+1/2)$ for the x-derivatives and a forward time $(n+1)$ for the y-derivatives. The discretization of the partial derivatives is given by:

$$\left.\frac{\partial^2 T}{\partial x^2}\right|_{i,j} = \frac{T_{i+1,j}^{n+1/2} - 2T_{i,j}^{n+1/2} + T_{i-1,j}^{n+1/2}}{\Delta x^2}, \qquad \left.\frac{\partial^2 T}{\partial y^2}\right|_{i,j} = \frac{T_{i,j+1}^{n+1} - 2T_{i,j}^{n+1} + T_{i,j-1}^{n+1}}{\Delta y^2} \tag{4.12}$$

$$\left.\frac{\partial (uT)}{\partial x}\right|_{i,j} = \frac{u_{i+1,j}^{n} T_{i+1,j}^{n+1/2} - u_{i-1,j}^{n} T_{i-1,j}^{n+1/2}}{2\Delta x}, \qquad \left.\frac{\partial (vT)}{\partial y}\right|_{i,j} = \frac{v_{i,j+1}^{n} T_{i,j+1}^{n+1} - v_{i,j-1}^{n} T_{i,j-1}^{n+1}}{2\Delta y} \tag{4.13}$$

$$\left.\frac{\partial T}{\partial t}\right|_{i,j} = 2\frac{T_{i,j}^{n+1} - T_{i,j}^{n+1/2}}{\Delta t} \tag{4.14}$$

By substituting equations (4.12)-(4.14) into equation (4.5), we obtain a tridiagonal matrix system of the form:

$$E_i T_{i,j+1}^{n+1} + F_i T_{i,j}^{n+1} + G_i T_{i,j-1}^{n+1} = H_i \tag{4.15}$$

With:

$$E_j = \left[\frac{1}{\Delta y^2} - \frac{v_{i,j+1}^{n}}{2\Delta y}\right], \quad F_j = -\left[\frac{2}{\Delta t} + \frac{2}{\Delta y^2}\right], \quad G_j = \left[\frac{v_{i,j-1}^{n}}{2\Delta y} + \frac{1}{\Delta y^2}\right]$$

$$H_j = \left[\frac{u_{i+1,j}^{n}}{2\Delta x} - \frac{1}{\Delta x^2}\right] T_{i+1,j}^{n+1/2} + \left[\frac{2}{\Delta x^2} - \frac{2}{\Delta t}\right] T_{i,j}^{n+1/2} - \left[\frac{u_{i-1,j}^{n}}{2\Delta x} + \frac{1}{\Delta x^2}\right] T_{i-1,j}^{n+1/2}$$

Replacing the boundary conditions (4.1)-(4.4) in equation (4.15) we obtain the implicit discrete form in y in the following form:

For $j = 2$

$$\left(E_2 - \frac{1}{3}G_2\right) T_{i,3}^{n+1} + \left(F_2 + \frac{4}{3}G_2\right) T_{i,2}^{n+1} = H_2 - \frac{2\Delta y}{3} G_2 \tag{4.16}$$

For $j = Ny$

$$\left(\frac{4}{3}E_{Ny} + F_{Ny}\right) T_{i,Ny}^{n+1} + \left(G_{Ny} - \frac{1}{3}E_{Ny}\right) T_{i,Ny-1}^{n+1} = H_{Ny} + \frac{2\Delta y}{3} E_{Ny} \tag{4.17}$$

4.3 DISCRETIZATION OF THE CONCENTRATION EQUATION

Likewise, the concentration equation (2.15) is discretized following the same steps as the previous paragraph.

The concentration equation (2.15) is rewritten as follows:

$$\xi\frac{\partial S}{\partial t}+\frac{\partial(uS)}{\partial x}+\frac{\partial(vS)}{\partial y}=Le^{-1}\left[\frac{\partial^2 S}{\partial x^2}+\frac{\partial^2 S}{\partial y^2}\right] \tag{4.18}$$

Implicit in x and explicit in y scheme

In a manner analogous to the preceding steps, the algebraic equation corresponding to the discretization of the concentration equation is provided as:

$$A_i S_{i+1,j}^{n+1/2}+B_i S_{i,j}^{n+1/2}+C_i S_{i-1,j}^{n+1/2}=D_i \tag{4.19}$$

With:

$$A_i=\left[\frac{u_{i+1,j}^n}{2\Delta x}-\frac{1}{\Delta x^2 Le}\right],\quad B_i=\left[\frac{2\xi}{\Delta t}+\frac{2}{\Delta x^2 Le}\right],\quad C_i=-\left[\frac{u_{i-1,j}^n}{2\Delta x}+\frac{1}{\Delta x^2 Le}\right]$$

$$D_i=\left[-\frac{v_{i,j+1}^n}{2\Delta y}+\frac{1}{\Delta y^2 Le}\right]S_{i,j+1}^n+\left[\frac{2\xi}{\Delta t}-\frac{2}{\Delta y^2 Le}\right]S_{i,j}^n+\left[\frac{v_{i,j-1}^n}{2\Delta y}+\frac{1}{\Delta y^2 Le}\right]S_{i,j-1}^n$$

Replacing the boundary conditions (4.1)-(4.4) in equation (4.19) we obtain the implicit discrete form in x in the following form:

For $i=2$
$$\left(A_2-\frac{1}{3}C_2\right)S_{3,j}^{n+1/2}+\left(B_2+\frac{4}{3}C_2\right)S_{2,j}^{n+1/2}=D_2 \tag{4.20}$$

For $i=Nx$
$$\left(\frac{4}{3}A_{Nx}+B_{Nx}\right)S_{Nx}^{n+1/2}+\left(C_{Nx}-\frac{1}{3}A_{Nx}\right)S_{Nx-1,j}^{n+1/2}=D_{Nx} \tag{4.21}$$

Implicit in y and explicit in x scheme

$$E_i S_{i,j+1}^{n+1}+F_i S_{i,j}^{n+1}+G_i S_{i,j-1}^{n+1}=H_i \tag{4.22}$$

With:

$$E_j=\left[\frac{1}{\Delta y^2 Le}-\frac{v_{i,j+1}^n}{2\Delta y}\right],\quad F_j=-\left[\frac{2}{\Delta t}+\frac{2}{\Delta y^2 Le}\right],\quad G_j=\left[\frac{v_{i,j-1}^n}{2\Delta y}+\frac{1}{\Delta y^2 Le}\right]$$

$$H_j=\left[\frac{u_{i+1,j}^n}{2\Delta x}-\frac{1}{\Delta x^2 Le}\right]S_{i+1,j}^{n+1/2}+\left[\frac{2}{\Delta x^2 Le}-\frac{2}{\Delta t}\right]S_{i,j}^{n+1/2}-\left[\frac{u_{i-1,j}^n}{2\Delta x}+\frac{1}{\Delta x^2 Le}\right]S_{i-1,j}^{n+1/2}$$

Replacing the boundary conditions (4.1)-(4.4) in equation (4.22) we obtain the implicit discrete form in y in the following form:

For $j = 2$

$$\left(E_2 - \frac{1}{3}G_2\right)S_{i,3}^{n+1} + \left(F_2 + \frac{4}{3}G_2\right)S_{i,2}^{n+1} = H_2 - \frac{2\Delta y}{3}G_2 \tag{4.23}$$

For $j = Ny$

$$\left(\frac{4}{3}E_{Ny} + F_{Ny}\right)S_{i,Ny}^{n+1} + \left(G_{Ny} - \frac{1}{3}E_{Ny}\right)S_{i,Ny-1}^{n+1} = H_{Ny} + \frac{2\Delta y}{3}E_{Ny} \tag{4.24}$$

4.4 DISCRETIZATION OF THE VELOCITY

The components of the velocity field are deduced from the stream function through equations (2.19). Employing a first-order centered finite difference scheme, the discretization of these equations yields:

$$u_{i,j}^{n+1} = \frac{\Psi_{i,j+1}^{n+1} - \Psi_{i,j-1}^{n+1}}{2\Delta y} \tag{4.25}$$

$$v_{i,j}^{n+1} = \frac{\Psi_{i+1,j}^{n+1} - \Psi_{i-1,j}^{n+1}}{2\Delta x} \tag{4.26}$$

4.5 DISCRETIZATION OF VELOCITY BOUNDARY CONDITIONS

The velocity boundary conditions are discretized using a third-order centered finite difference scheme on the right and left sides.

$$\left.\begin{aligned} u_{1,j} &= 0, \qquad v_{1,j} = -\frac{4\Psi_{2,j} - 3\Psi_{1,j} - \Psi_{3,j}}{2\Delta x}, \qquad \text{at} \quad x = -\frac{A}{2} \\ u_{Nx+1,j} &= 0, \quad v_{Nx+1,j} = -\frac{3\Psi_{Nx+1,j} - 4\Psi_{Nx,j} - \Psi_{Nx-1,j}}{2\Delta x}, \quad \text{at} \quad x = +\frac{A}{2} \end{aligned}\right\} \tag{4.27}$$

$$\left.\begin{aligned} v_{i,1} &= 0, \qquad u_{i,1} = \frac{4\Psi_{i,2} - 3\Psi_{i,1} - \Psi_{i,3}}{2\Delta y}, \qquad \text{at} \quad y = -\frac{1}{2} \\ v_{i,Ny+1} &= 0, \quad u_{i,Ny+1} = \frac{3\Psi_{i,Ny+1} - 4\Psi_{i,Ny} - \Psi_{i,Ny-1}}{2\Delta y}, \quad \text{at} \quad y = +\frac{1}{2} \end{aligned}\right\} \tag{4.28}$$

4.6 DISCRETIZATION OF THE VISCOSITY

Substituting Eqs (4.25)-(4.28) into equation (2.17) yields the discrete viscosity as follows:

$$\mu_{a(i,j)}^{n+1} = \left[\left(u_{i,j}^{n+1}\right)^2 + \left(v_{i,j}^{n+1}\right)^2\right]^{(n-1)/2} \tag{4.29}$$

4.7 DISCRETIZATION OF THE MOTION EQUATION

The motion equation of the porous medium, governed by the power law, can be expressed in the following manner:

$$\mu_a\left[\frac{\partial^2\Psi}{\partial^2 x}+\frac{\partial^2\Psi}{\partial y^2}\right]+\frac{\partial\Psi}{\partial y}\frac{\partial\mu_a}{\partial y}+\frac{\partial\Psi}{\partial x}\frac{\partial\mu_a}{\partial x}=-R_T\left[\left(\frac{\partial T}{\partial x}+N\frac{\partial S}{\partial x}\right)\cos\Phi-\left(\frac{\partial T}{\partial y}+N\frac{\partial S}{\partial y}\right)\sin\Phi\right] \quad (4.30)$$

Each term of the motion equation (4.30) is discretized using a standard centered scheme.

$$\left.\frac{\partial^2\Psi}{\partial x^2}\right|_{i,j}=\frac{\Psi_{i+1,j}^{n+1}-2\Psi_{i,j}^{n+1}+\Psi_{i-1,j}^{n+1}}{\Delta x^2},\qquad \left.\frac{\partial^2\Psi}{\partial y^2}\right|_{i,j}=\frac{\Psi_{i,j+1}^{n+1}-2\Psi_{i,j}^{n+1}+\Psi_{i,j-1}^{n+1}}{\Delta y^2} \quad (4.31)$$

$$\left.\frac{\partial T}{\partial x}\right|_{i,j}=\frac{T_{i+1,j}^{n+1}-T_{i-1,j}^{n+1}}{2\Delta x},\qquad \left.\frac{\partial T}{\partial y}\right|_{i,j}=\frac{T_{i,j+1}^{n+1}-T_{i,j-1}^{n+1}}{2\Delta y} \quad (4.32)$$

$$\left.\frac{\partial S}{\partial x}\right|_{i,j}=\frac{S_{i+1,j}^{n+1}-S_{i-1,j}^{n+1}}{2\Delta x},\qquad \left.\frac{\partial S}{\partial y}\right|_{i,j}=\frac{S_{i,j+1}^{n+1}-S_{i,j-1}^{n+1}}{2\Delta y} \quad (4.33)$$

$$\left.\frac{\partial \mu_a}{\partial x}\right|_{i,j}=\frac{\mu_{a(i+1,j)}^{n+1}-\mu_{a(i-1,j)}^{n+1}}{2\Delta x},\qquad \left.\frac{\partial \mu_a}{\partial y}\right|_{i,j}=\frac{\mu_{a(i,j+1)}^{n+1}-\mu_{a(i,j-1)}^{n+1}}{2\Delta y} \quad (4.34)$$

By substituting expressions (4.25)-(4.29) and (4.31)-(4.34) into equation (4.30), we derive the general form of the following function.

$$\begin{aligned}\Psi_{i,j}^{(n+1),(k+1)}=(1-\omega)\Psi_{i,j}^{(n+1),k}+\omega\Big\{&a_{px}\left(\Psi_{i+1,j}^{(n+1),k}-\Psi_{i-1,j}^{(n+1),(k+1)}\right)+a_{py}\left(\Psi_{i,j+1}^{(n+1),k}-\Psi_{i,j-1}^{(n+1),(k+1)}\right)+\\ &a_{cx}\left(\Psi_{i+1,j}^{(n+1),k}+\Psi_{i-1,j}^{(n+1),(k+1)}\right)+a_{cy}\left(\Psi_{i,j+1}^{(n+1),k}+\Psi_{i,j-1}^{(n+1),(k+1)}\right)+a_{TSx}\Big[\left(T_{i+1,j}^{n+1}-T_{i-1,j}^{n+1}\right)+\\ &N\left(S_{i+1,j}^{n+1}-S_{i-1,j}^{n+1}\right)\Big]+a_{TSy}\Big[\left(T_{i,j+1}^{n+1}-T_{i,j-1}^{n+1}\right)+N\left(S_{i,j+1}^{n+1}-S_{i,j-1}^{n+1}\right)\Big]\Big\}\end{aligned} \quad (4.35)$$

With

$$\begin{aligned}&a_p=2\mu_{a(i,j)}^{n+1}\left[\frac{1}{\Delta y^2}+\frac{1}{\Delta x^2}\right],\quad a_{px}=\frac{\mu_{a(i+1,j)}^{n+1}-\mu_{a(i-1,j)}^{n+1}}{4\Delta x^2 a_p},\quad a_{py}=\frac{\mu_{a(i,j+1)}^{n+1}-\mu_{a(i,j-1)}^{n+1}}{4\Delta y^2 a_p}\\ &a_{cx}=\frac{\mu_{a(i,j)}^{n+1}}{\Delta x^2 a_p},\quad a_{cx}=\frac{\mu_{a(i,j)}^{n+1}}{\Delta y^2 a_p},\quad a_{TSx}=\frac{R_T\cos\Phi}{2\Delta x a_p},\quad a_{TSy}=-\frac{R_T\sin\Phi}{2\Delta y a_p}\end{aligned} \quad (4.36)$$

The parameter ω is the over-relaxation factor, which ranges from 1 to 2, to accelerate convergence. Its optimal value, ω_{opt} depends on the shape of the domain, the mesh, and the type of boundary conditions.

For a rectangular domain with a uniform mesh, ω_{opt} is given by:

$$\omega_{opt} = \frac{2}{\varsigma^2}\left[1-\sqrt{1-\varsigma^2}\right], \quad \text{with} \quad \varsigma = \left[\frac{\cos\left(\pi/N_{x+1}\right)+\left(\Delta x^2/\Delta y^2\right)\cos\left(\pi/N_{y+1}\right)}{1+\Delta x^2/\Delta y^2}\right] \tag{4.37}$$

where $Nx+1$ and $Ny+1$ are the number of nodes along the x and y directions, respectively.

4.8 CALCULATION ALGORITHM

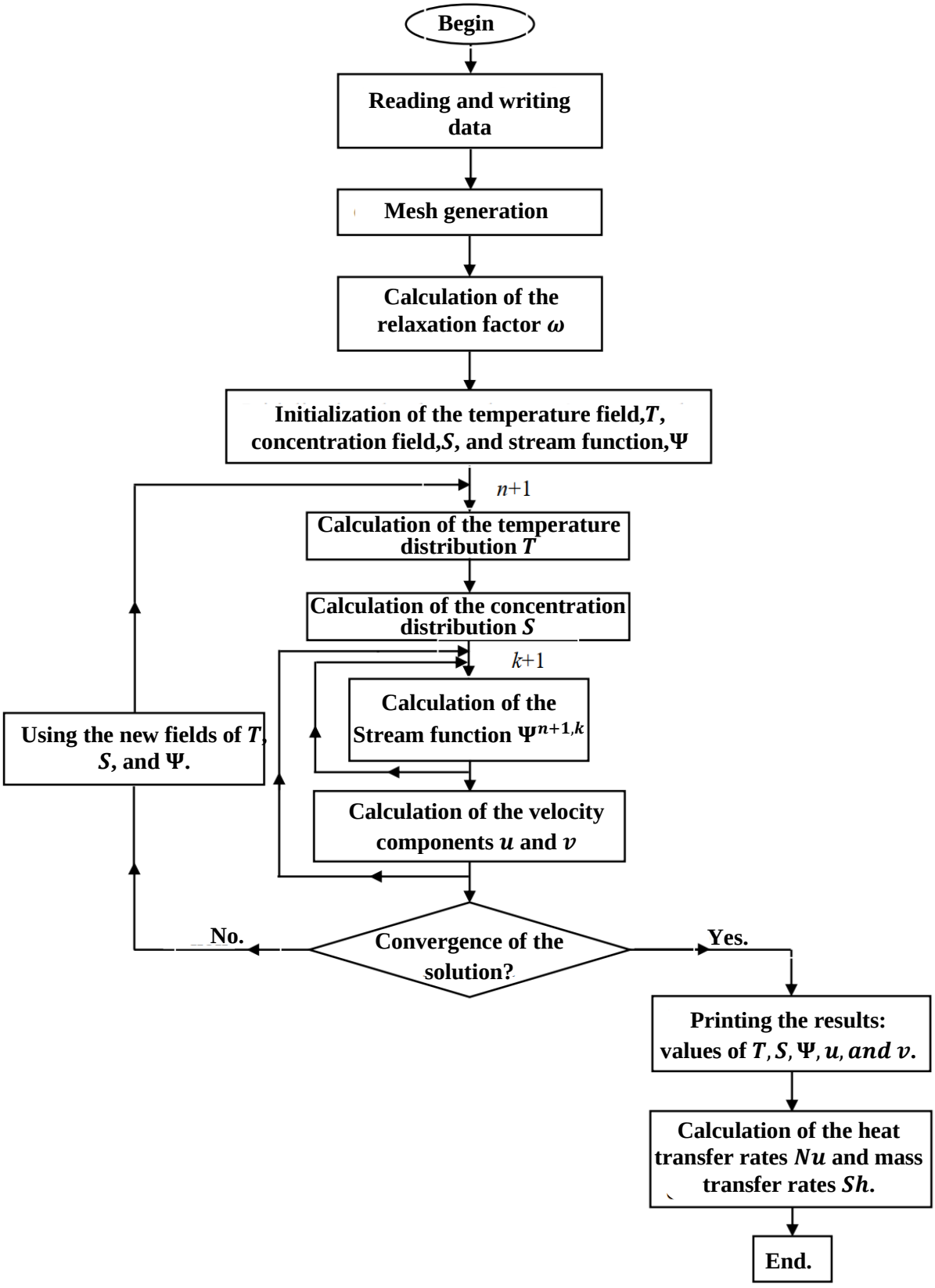
The main steps of our calculation algorithm are:

1. Mesh generation.
2. Initialization and data reading.
3. Calculation of the over-relaxation factor.
4. Implementation of initial conditions for temperature, T, concentration, S, and stream function, Ψ.
5. Determination of the initial velocity field, $u_{i,j}$ and $v_{i,j}$.
6. Determination of the initial viscosity field, $\mu_{a(i,j)}$.
7. Start of the time loop.
   7.1. Solving the energy equation (4.9) and (4.15) by the ADI method and calculating the temperature field $T_{i,j}$.
   7.2. Solving the concentration equation (4.19) and (4.22) by the ADI method and calculating the concentration field $S_{i,j}$.
   7.3. Solving the motion equation (4.35) by the SOR method and calculating the stream function field $\Psi_{i,j}$.
   7.4. Determining the velocity field $u_{i,j}$ and $v_{i,j}$.
   7.5. Determination of viscosity field, $\mu_{a(i,j)}$.
   7.6. Repeat step (7.1) until the solution converges to a steady or oscillating solution.
8. Printing results.
9. End of the program.

The convergence criterion during the resolution of equation (4.35) is given by:

$$\frac{\sum_i \sum_j \left|\Psi_{i,j}^{k+1} - \Psi_{i,j}^{k}\right|}{\sum_i \sum_j \left|\Psi_{i,j}^{k}\right|} \leq 10^{-6} \tag{4.38}$$

4.9 CALCULATION ORGANIGRAM



4.10 MESH CHOICE

The selection of mesh size involves a delicate balance between computational efficiency and result precision. The process involves iteratively refining the grid until the numerical solution converges to the analytical solution developed in the subsequent section, meeting a predetermined accuracy threshold. This convergence is achieved under the stipulated values for A, Le, N, n, Φ, and R_T. A uniform grid of dimensions 256x154, as outlined in Table 1, and Table 2, has proven to be suitable for accurately modeling the flow, temperature, and concentration fields within a cavity of size 6to 10. Time-step sizes for simulations have been chosen in the range of 10^{-6} to 10^{-3}.

Table 4.1. Convergence tests for specified parameters, $A = 6$, $Le = 5$, $N = -0.1$, $R_T = 100$, $\Phi = 0°$, and $n = 1.2$.

	Numerical solution				**Analytical**
Grids	40x20	100x60	160x100	220x140	**solution**
$\boldsymbol{\Psi_0}$	3.0342	2.9574	2.9462	2.9392	2.9269
$\boldsymbol{Nu}$	2.9153	3.0033	3.0219	3.0303	3.0280
$\boldsymbol{Nu_m}$	2.7292	2.8213	2.8404	2.8493	-
$\boldsymbol{Sh}$	5.0314	5.3053	5.3772	5.4287	5.4358
$\boldsymbol{Sh_m}$	5.1010	5.3920	5.4691	5.5238	-

Table 4.2. Convergence tests for specified parameters, $A = 6$, $Le = 5$, $N = -0.1$, $R_T = 50$, and $n = 1.2$, and different angles of inclination Φ.

		Numerical solution				**Semi-analytical solution**
Grids		60x40	100x60	160x100	250x150	
$\boldsymbol{\Phi = 0°}$	Ψ_0	1.971	1.952	1.942	1.937	1.929
	Nu	2.160	2.173	2.173	2.172	2.168
	Sh	4.997	5.098	5.142	5.158	5.167
$\boldsymbol{\Phi = 60°}$	Ψ_0	2.074	2.054	2.042	2.037	2.030
	Nu	2.346	2.372	2.381	2.384	2.385
	Sh	5.447	5.627	5.716	5.754	5.778
$\boldsymbol{\Phi = 90°}$	Ψ_0	1.741	1.717	1.704	1.698	1.693
	Nu	2.045	2.060	2.065	2.066	2.067
	Sh	5.334	5.529	5.626	5.669	5.697
$\boldsymbol{\Phi = 120°}$	Ψ_0	1.261	1.246	1.227	1.221	1.216
	Nu	1.598	1.601	1.601	1.602	1.601
	Sh	4.765	4.937	5.021	5.058	5.083

Table 4.3. Convergence tests for specified parameters, $A = 6$, $Le = 5$, $N = -1$, $R_T = 100$, and $\Phi = 90°$, and different values of power-law index n.

Grids		Numerical solution				Semi-analytical solution
		60x40	100x60	160x100	250x150	
$\mathbf{n = 0.6}$	Ψ_0	3.795	4.037	4.794	3.598	3.574
	Nu	4.029	3.811	3.912	3.788	3.786
	Sh	6.423	5.938	6.334	5.986	5.962
$\mathbf{n = 1.0}$	Ψ_0	2.721	2.685	2.676	2.675	2.675
	Nu	2.580	2.652	2.694	2.715	2.728
	Sh	4.622	4.804	4.928	4.998	5.040
$\mathbf{n = 1.4}$	Ψ_0	2.314	2.173	2.152	2.157	2.113
	Nu	2.140	2.132	2.151	2.159	2.157
	Sh	4.383	4.346	4.466	4.529	4.573

4.11 VALIDATION OF NUMERICAL CODE

To assess the accuracy of our current numerical solutions, Tables 4.5 and 4.6 provide the numerical results, including the center stream function Ψ_0 value, as well as the local Nusselt Nu and Sherwood Sh numbers. We conduct a thorough comparison with the findings of Amari et al. [29] and Ben Khelifa et al. [88] in the case of a horizontal layer $\Phi = 0°$. For the inclined layer $\Phi \neq 0°$, we compare our results with those documented by Bian et al. [5], as displayed in Table 4.7. Additionally, Table 4.8 presents a comparison with the study of Ben Khelifa et al. [120] for the case of a vertical layer $\Phi = 90°$. These comparisons demonstrate a high level of agreement.

Table 4.5. Comparison of Ψ_0, and Nu with previous numerical studied of Amari et al. [29] for $N = 0$, $Le = 5$, and various values of n, with horizontal cavity

n		$A = 6$ and $R_T = 100$				
		Analytical	Amari et al. [29] study	Present study	Present study vs analytical	Present study vs Amari et al. [29]
0.6	Ψ_0	6.701	6.762	6.742	0.61%	0.30%
	Nu	6.000	5.997	5.929	1.19	1.14
1.0	Ψ_0	3.708	3.708	3.706	0.05	0.05
	Nu	3.750	3.750	3.737	0.35	0.35
1.4	Ψ_0	2.448	2.468	2.474	1.06	0.24
	Nu	2.553	2.553	2.558	0.20	0.20

Table 4.6. Comparison of Ψ_0, Nu and Sh with previous numerical studied of Ben Khelifa et al. [88] for $N = 0.2$, $Le = 10$, and various values of n, with horizontal cavity.

		$A = 6$ and $R_T = 25$				
n		Analytical solution	Present study	Present study vs analytical	Ben Khelifa et al. [88]	Present study vs Ben Khelifa et al. [88]
0.6	Ψ_0	2.54	2.55	0.39%	2.60	1.94%
	Nu	3.22	3.22	0.00	3.27	1.54
	Sh	7.22	7.30	1.10	7.25	0.69
1.0	Ψ_0	1.47	1.47	0	1.48	0.68
	Nu	1.81	1.81	0	1.81	0
	Sh	5.75	5.75	0	5.75	0
1.6	Ψ_0	1.00	1.02	1.98	1.01	0.99
	Nu	1.36	1.37	0.73	1.64	18.09
	Sh	4.98	4.97	0.20	4.98	0.20

Table 4.7. Comparison of Ψ_0, and Nu with previous numerical studied of Bian et al. [5] for $R_T = 100$, $n = 1.2$, $N = 0$, and $A = 4$ with various inclination angle Φ.

Φ		**Analytical**	**Present study**	**Bian et al. [5] study**	**Vs analytical**	**Vs Bian et al. [5]**
0°	Ψ_0	2.966	2.980	2.994	0.47 %	0.47 %
	Nu	3.058	3.062	-	0.13	-
60°	Ψ_0	2.693	2.701	2.727	0.30	0.96
	Nu	3.195	3.195	-	0.00	-
120°	Ψ_0	1.400	1.405	1.412	0.36	0.50
	Nu	1.860	1.860	-	0.00	-

Table 48.. Comparison of Ψ_0, Nu and Sh with previous numerical studied of Ben Khelifa et al. [120] for $R_T = 200$, $N = 1$, $Le = 10$, $A = 4$, and $\Phi = 90°$ with various values of n.

n		**Analytical**	**Present study**	**Ben Khelifa et al. [120]**	**Vs analytical**	**Vs Ben Khelifa et al. [120]**
0.4	Ψ_0	3.968	3.996	4.050	0.70 %	1.34 %
	Nu	11.396	11.986	12.530	5.05	4.44
	Sh	43.360	47.949	51.620	10.08	7.38
1.0	Ψ_0	2.413	2.422	2.570	0.37	5.93
	Nu	4.176	4.182	4.180	0.14	0.05
	Sh	13.837	13.753	13.790	0.61	0.27
1.6	Ψ_0	1.876	1.885	2.040	0.48	7.91
	Nu	2.538	2.539	2.530	0.04	0.36
	Sh	7.958	7.975	7.980	0.21	0.06

Figure 4.2 portrays the impact of the aspect ratio, A, on several parameters including the flow intensity Ψ_0, Nusselt numbers ($Nu_c$and Nu_m), and Sherwood numbers ($Sh_c$and Sh_m) under specific conditions $n = 1.1$, $R_T = 100$, $Le = 5$, and $N = -0.1$. As the aspect ratio A increases from $A = 1.0$, the flow intensity Ψ_0 decreases, whereas both Nusselt numbers (Nu_c and Nu_m), and Sherwood numbers (Sh_c and Sh_m) exhibit an increase. Previous studies by Vasseur et al. [114], Hasnaoui [139], and Mamou [140] have indicated that when a cavity is heated with constant heat flux, the analytical solution, considering the assumption of parallel flow, remains valid especially when the aspect ratio, A, exceeds a threshold of ($A \geq 4$), while for our case when a cavity heated and salted with constant heat and mass flux, the solution remains valid when the aspect ratio is greater than or equal to 6 ($A \geq 6$).Consequently, the numerical solution tends to converge asymptotically toward the analytical solution, diminishing the influence of end effects in the cavity.

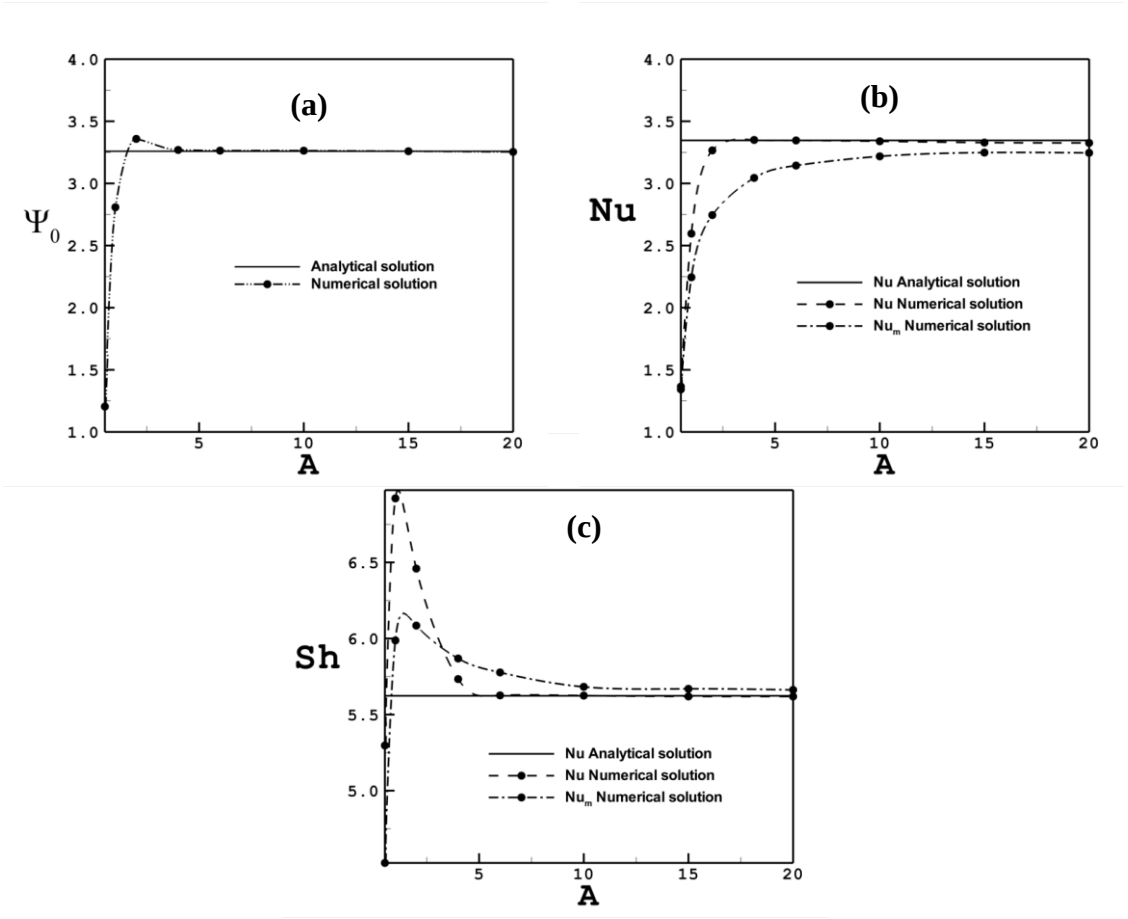


Figure 4.2: Influence of the cavity aspect ratio, A, on (a) the flow intensity at the cavity center, Ψ_0, (b) the heat transfers, (Nu_c and Nu_m), (c) the mass transfers, (Sh_c and Sh_m), for $n = 1.1$, $R_T = 100$, $Le = 5$, and $N = -0.1$.

CHAPTER V:

LINEAR STABILITY ANALYSIS IN A POROUS LAYER

It is well established, both theoretically and practically, that spontaneous convection in laterally heated and bottom-heated cavities differs fundamentally from each other, Bejan [141]. The reason for this discrepancy is that in cavities heated from below, convective motions may only be observed if the imposed thermal gradient is greater than a specific value, which is referred to as the critical threshold. The system under consideration's geometric configuration is depicted in Figure 2.1, where a binary fluid is saturated in a porous medium. Several studies have been conducted in the past by numerous authors, including Nield [142], Taunton and Lightfoo [143], Poulikakos [144], Mamou et al. [145], and Mamou [146], to investigate the instability problem in a horizontal porous layer subject to various boundary conditions. These studies have revealed the existence of supercritical Rayleigh numbers that characterize the convection threshold. They also looked at the circumstances under which oscillating and superstable convection regimes exist. When the thermal and solutal volume forces are equal but acting in different directions $N = -1$, it is also feasible for the fluid to remain at rest in the case of a vertical layer. There has not been much research done in the past on the stability of this kind of setup. This is a result of the fundamental equations' complexity, which makes it challenging to discover analytical solutions. Bertholz [147], Ghorayeb and Mojtabi [148], Joly et al. [149], and Mamou [102] were interested in studying the initiation of double-diffusive and Soret-effect convection in vertical cavities for various boundary conditions in the case of an infinite vertical porous layer subjected to gradients of constant temperature and concentration. They ascertained the critical Rayleigh number values that denote the critical convection threshold. It has been noted that many solutions exist and that subcritical convection motion occurs, i.e., at a Rayleigh number lower than the supercritical Rayleigh.

The thesis's fifth chapter examines the layer's linear stability when it saturates a porous medium. It is separated into two sections: the first part studies the case of the instability of the resting state, which happens when the volume forces caused by the thermal and solutal effects are opposite ($N < 0$), where the concentration acts as a stabilizing agent in the system and delays the start of convection. The second section studies the case of a vertical cavity that is subjected to volume forces of the same magnitude and in the opposite direction ($N = -1$). In the latter case, the density of the fluid is uniform in the cavity and the resulting thrust force is zero. Convection is feasible, but only above a certain point, when the Lewis number deviates from

unity. In order to forecast when the oscillatory bifurcation known as Hopf's will begin, the second section of this chapter is devoted to the study of convective flow. Following that, we apply the traditional linear stability approach to find the critical Rayleigh number and the flow structure at the convection threshold. In the latter, the system's steady state is perturbed hydrodynamically, and the perturbation's temporal evolution is observed. It is possible to ascertain if this bifurcation is oscillating or stationary using linear stability analysis. This analysis allows us to establish not just the crucial stability threshold but also the flow's structure, as we will see later in this chapter.

It should be noted that the fluid's steady state is characterized by:

$$\left.\begin{aligned} \Psi_b &= 0 \\ T_b &= S_b = -y \end{aligned}\right\}.. \tag{5.1}$$

The solution at the start of convection is as follows:

$$\left.\begin{aligned} \Psi &= \Psi_b + \psi(x,y,t) \\ T &= T_b + \theta(x,y,t) \\ S &= S_b + \phi(x,y,t) \end{aligned}\right\} \tag{5.2}$$

It is the sum of the base solution and a hydrodynamic disturbance (ψ, θ, ϕ). The base solution ($\Psi_b, \mathrm{T}_b, \mathrm{S}_b$) represents either the state of pure conduction or an established convective state.

5.1 THEORY OF LINEAR STABILITY FOR CONVECTIVE FLOW

This section investigates the stability of the parallel flow that is given by (3.5)-(3.7) and (3.32). When the flow reaches a critical Rayleigh number R_{TC}^{Hopf}, it starts to oscillate. This bifurcation point needs to be found by a flow stability study. Examine the parallel flow that is represented by equations (3.5)-(3.7), and (3.32). The global flow is assumed to be the superposition of the base flow at the onset of the instability. Together with an infinitesimal perturbation, $\Psi_b(x,y) \approx \Psi_b(y)$, $T_b(x,y) \approx C_T x + \theta_T(y)$, and $S_b(x,y) \approx C_S x + \theta_S(y)$.

$$\left.\begin{aligned} \Psi_p(x,y,t) &= \psi_0 e^{pt+iay} F(y) \\ T_p(x,y,t) &= \theta_0 e^{pt+i\alpha y} G(y) \\ S_p(x,y,t) &= \phi_0 e^{pt+i\alpha y} H(y) \end{aligned}\right\} \tag{5.3}$$

where i is the pure complex number and p is the perturbation's growth rate. The wavenumber is represented by the real number a, and the unknown functions $F(y)$, $G(y)$, and $H(y)$ satisfy

the boundary conditions given by (2.23)-(2.25). The equation $\Psi_p(x,y,t)$, $T_p(x,y,t)$, and $S_p(x,y,t)$ characterize the perturbed functions of the current function, temperature, and concentration, while ψ_0, θ_0, and ϕ_0 are small constant amplitudes.

The apparent viscosity, denoted as μ_a, can be further decomposed as:

$$\mu_a = \mu_{a,b} + \mu_{a,p} \tag{5.4}$$

Here, $\mu_{a,p}$ and $\mu_{a,b} = \left(\frac{\partial \Psi_b}{\partial y}\right)^{n-1}$ represent the perturbation and basic apparent viscosity, respectively.

The linearized form of the perturbed apparent viscosity is expressed as follows:

$$\mu_{a,p} = (n-1)\left(\frac{\partial \Psi_b}{\partial y}\right)^{n-1} \frac{\partial \Psi_p}{\partial y} \tag{5.5}$$

Introducing (5.3) into equations (2.14), (2.15) and (2.16), and neglecting the second-order nonlinear terms, we obtain the following linear system:

$$(nD^2 - \alpha^2)(D\Psi_b)^{n-1} f + n(n-1)(D\Psi_b)^{n-2} D^2\Psi_b Df = -R_T (g + Nh) \tag{5.6}$$

$$(C_T D - i\alpha DT_b) f + (\alpha^2 + i\alpha D\Psi_b - D^2) g = -pg \tag{5.7}$$

$$(C_S D - i\alpha DS_b) f + (Le^{-1}\alpha^2 + i\alpha D\Psi_b - Le^{-1}D^2) h = -p\xi h \tag{5.8}$$

where:

$$\psi_0 F = f, \quad \theta_0 G = g, \quad \phi_0 G = h, \quad D = \frac{d}{dy} \tag{5.9}$$

The corresponding boundary conditions are:

$$f = 0, \qquad Dg = Dh = 0, \qquad x = \pm\frac{A}{2}, \qquad y = \pm\frac{1}{2} \tag{5.10}$$

5.2 NUMERICAL SOLUTION

The finite element approach can be utilized to find the numerical solution of the perturbation equations.

5.2.1 VARIATIONAL FORMULATION

Partial differential equations with space-time boundary conditions are used to describe the behavior of the system. The weighted Galerkin residue method, also referred to as the weak formulation, is then necessary for the discretization of equations (5.6)-(5.8). The variational formulation of equations (5.6)-(5.8) obtained by multiplying equation (5.6) by $\omega(y)$ and equations (5.7) and (5.8) by $\vartheta(y)$ and integrating on the domain of y is as follows:

$$\int_{-1/2}^{1/2}(nD^2-\alpha^2)\left(D\Psi_b\right)^{n-1} f\,\omega dy + n(n-1)\int_{-1/2}^{1/2}\left(D\Psi_b\right)^{n-2} D^2\Psi_b Df D\omega dy = -R_T\left(\int_{-1/2}^{1/2} g\omega dy + N\int_{-1/2}^{1/2} h\omega dy\right) \tag{5.11}$$

$$\int_{-1/2}^{1/2}\left(C_T D - i\alpha DT_b\right) f\,\vartheta dy + \int_{-1/2}^{1/2}\left(\alpha^2 + i\alpha D\Psi_b\right) g\vartheta dy + \int_{-1/2}^{1/2} DgD\vartheta dy = -p\int_{-1/2}^{1/2} g\vartheta dy \tag{5.12}$$

$$\int_{-1/2}^{1/2}\left(C_S D - i\alpha DS_b\right) f\,\vartheta dy + \int_{-1/2}^{1/2}\left(Le^{-1}\alpha^2 + i\alpha D\Psi_b\right) h\vartheta dy + Le^{-1}\int_{-1/2}^{1/2} DhD\vartheta dy = -p\xi\int_{-1/2}^{1/2} h\vartheta dy \tag{5.13}$$

where $\omega(y)$ and $\vartheta(y)$ are admissible functions satisfying the boundary conditions given by (5.10).

These days, finite element programs are a common tool for industrial product design and analysis. The finite element method's application has grown significantly. A geometric transformation will be used to go from the reference element to the real element. Given the one-dimensional nature of equations (5.11)-(5.13), we select the cubic Hermit element with three nodes and a uniform mesh (Fig 5.1). In every node, the function and its initial derivative are the unknowns.

In each reference element, the interpolation functions of the Hermite element are given by the following expressions:

$$\left.\begin{aligned} N_1 &= \frac{1}{4}\left(2-3\eta+\eta^3\right) \quad , \qquad N_2 = \frac{l}{8}\left(1-\eta-\eta^2+\eta^3\right) \\ N_3 &= \frac{1}{4}\left(1-\eta-\eta^2+\eta^3\right) \quad , \qquad N_4 = \frac{l}{8}\left(1-\eta-\eta^2+\eta^3\right) \end{aligned}\right\} \tag{5.14}$$

Where: $y = y_0 + \frac{Dy}{2}\eta, \quad dy = \frac{Dy}{2}d\eta$ et $y_0 = (y_1 + y_2)/2$



a) Real element b) Reference element

Figure 5.1: Schematic representation of the cubic Hermite element.

The unknown profiles of the concentration $h(y)$, temperature $g(y)$, and stream function $f(y)$ are estimated in each element by:

$$K^e(y) = \sum_{j=1}^{4} N_j(y) K_j^e \tag{5.15}$$

where K denotes $f(y)$, $g(y)$, $h(y)$, and $N_j(y)$ are the Hermite functions, and $f_j^e(y)$, $g_j^e(y)$, and $h_j^e(y)$ are the elemental nodal unknown values.

For each equation, we construct an elementary matrix system by taking the approximations (5.15) into the variational formulation (5.11)-(5.13), substituting $\omega(y)$ and $\vartheta(y)$ by N_j, and then integrating on the reference element. We are left with the following global matrix system after assembling the elementary matrices that each component of the computational domain produces.

$$\left[K_\psi\right]\{f\} = R_T\left(\left[B_\psi\right]\{g\} + N\left[B_\psi\right]\{h\}\right) \tag{5.16}$$

$$\left[B_\theta\right]\{f\} + \left[K_\theta\right]\{g\} = -p\left[M_\theta\right]\{g\} \tag{5.17}$$

$$\left[B_\phi\right]\{f\} + Le^{-1}\left[K_\phi\right]\{h\} = -p\xi\left[M_\phi\right]\{h\} \tag{5.18}$$

The constants $\left[K_\psi\right]$, $\left[B_\psi\right]$, $\left[C_\psi\right]$, $\left[B_\theta\right]$, $\left[K_\theta\right]$, $\left[M_\theta\right]$, $\left[B_\phi\right]$, $\left[K_\phi\right]$, and $\left[M_\phi\right]$ are square matrices with dimensions $m \times m$, where $m = 2N_{ey} + 1$ (with N_{ey} being the number of elements in the y −direction) within the domain of $\Omega = \{y \in [-1/2, 1/2]\}$. The vectors f, g,

and h represent unknown eigenvectors of dimension m. The elementary matrices corresponding to these vectors are derived as follows:

$$\left.\begin{aligned}
\left[B_\psi\right]^e &= \int_{-1}^{1} i\alpha N_j N_i \frac{\Delta y}{2} d\eta \\
\left[B_\theta\right]^e &= \int_{-}^{1}\left(C_T \frac{\partial N_j}{\partial \eta} - i\alpha \frac{\partial T_b}{\partial \eta} N_j\right) N_i d\eta \\
\left[B_\phi\right]^e &= \int_{-1}^{1}\left(C_s \frac{\partial N_j}{\partial \eta} - i\alpha \frac{\partial S_b}{\partial \eta} N_j\right) N_i d\eta \\
\left[K_\psi\right]^e &= \int_{-1}^{1}\left(n\left(\frac{\partial \Psi_b}{\partial \eta}\right)^{n-1}\left(\frac{2}{\Delta y}\right)^{n-1}\frac{\partial N_j}{\partial \eta}\frac{\partial N_i}{\partial \eta} - \right. \\
&\qquad n(n-1)\left(\frac{\partial \Psi_b}{\partial \eta}\right)^{n-2}\frac{\partial^2 \Psi_b}{\partial \eta^2}\left(\frac{2}{\Delta y}\right)^{n-1} N_j \frac{\partial N_i}{\partial \eta} + \\
&\qquad \left.\alpha^2\left(\frac{\partial \Psi_b}{\partial \eta}\right)^{n-1}\left(\frac{\Delta y}{2}\right)^{n-2} N_j N_i\right) d\eta \\
\left[K_\theta\right]^e &= \int_{-1}^{1}\left(\frac{\Delta y}{2}\alpha^2 N_j N_i + i\alpha \frac{\partial \Psi_b}{\partial \eta} N_j N_i + \frac{2}{\Delta y}\frac{\partial N_j}{\partial \eta}\frac{\partial N_i}{\partial \eta}\right) d\eta \\
\left[K_\phi\right]^e &= \int_{-1}^{1}\left(\frac{\Delta y}{2}\alpha^2 N_j N_i + i\alpha Le \frac{\partial \Psi_b}{\partial \eta} N_j N_i + \frac{2}{\Delta y}\frac{\partial N_j}{\partial \eta}\frac{\partial N_i}{\partial \eta}\right) d\eta \\
\left[M_\theta\right]^e &= \left[M_\phi\right]^e = \int_{-1}^{1} N_j N_i \frac{\Delta y}{2} d\eta
\end{aligned}\right\} \tag{5.19}$$

Galerkin's integration is used to obtain a weak formulation of equations (5.16)-(5.18). The integration of linear equations by the finite element method, after assembly into the global matrix system, is obtained as follows:

$$\begin{bmatrix}
\left[K_\psi\right] & -R_T\left[B_\psi\right] & -R_T N\left[B_\psi\right] \\
\left[B_\theta\right] & \left[K_\theta\right] & 0 \\
\left[B_\phi\right] & 0 & Le^{-1}\left[K_\phi\right]
\end{bmatrix}
\begin{Bmatrix} f \\ g \\ h \end{Bmatrix} = p
\begin{bmatrix}
0 & 0 & 0 \\
0 & -\left[M_\theta\right] & 0 \\
0 & 0 & -\xi\left[M_\phi\right]
\end{bmatrix}
\begin{Bmatrix} f \\ g \\ h \end{Bmatrix} \tag{5.20}$$

Upon transforming the integrals within the reference element as illustrated in Figure 5.1, the Gaussian integration method facilitates the exact computation of integrals using five Gaussian points along the coordinate direction of η. Each integral can be evaluated as follows:

$$\int_{-1}^{1} f(\eta) d\eta = \sum_{j=1}^{4} f\left(\eta_j\right)\omega_j \tag{5.21}$$

Where η_j is the Gaussian integration point coordinate and ω_j is the Gaussian weight. They are given in Table 5.1.

Table 5.1: Gauss Points

j	η_j	ω_j
1	-0.90617984	0.23692688
2	-0.53846931	0.47862867
3	0.00000000	0.56888888
4	0.53846931	0.47862867
5	0.90617984	0.23692688

5.3 STABILITY OF THE REST STATE

5.3.1 LINEAR STABILITY THEORY

The Rest State is given by:

$$\Psi_b = 0, \quad T_b = S_b = -y \tag{5.22}$$

The matrix systems (5.16)-(5.18) reduce to:

$$\left[K_\psi\right]\{f\} = R_T\left(\{g\} + N\{h\}\right)\left[B_\psi\right] \tag{5.23}$$

$$p\left[M_\theta\right]\{g\} - \left[B_\theta\right]\{f\} = -\left[K_\theta\right]\{g\} \tag{5.24}$$

$$p\xi\left[M_\phi\right]\{h\} - \left[B_\phi\right]\{f\} = -Le^{-1}\left[K_\phi\right]\{h\} \tag{5.25}$$

5.3.2 MARGINAL STABILITY: P=0

We can determine the supercritical convection threshold through marginal stability. From equations (5.23)-(5.25), we can deduce for marginal stability $p = 0$ that:

$$\left[K_\psi\right]\{f\} = R_T\left(\{g\} + N\{h\}\right)\left[B_\psi\right] \tag{5.26}$$

$$\left[B_\theta\right]\{f\} = \left[K_\theta\right]\{g\} \tag{5.27}$$

$$\left[B_\phi\right]\{f\} = Le^{-1}\left[K_\phi\right]\{h\} \tag{5.28}$$

The combination of equations (5.26)-(5.28) leads us to the following eigenvalue problem:

$$\left(\left[E\right]-\lambda\left[I\right]\right)\left\{f\right\}=0 \tag{5.29}$$

where $[I]$ is the identity matrix, $\{f\}$ is the unknown vector, and $[E]$ is the $m \times m$ matrix defined by:

$$\left[E\right]=\left[K_{\psi}\right]^{-1}\left[B_{\psi}\right]\left(\left[K_{\theta}\right]^{-1}\left[B_{\theta}\right]+NLe\left[K_{\phi}\right]^{-1}\left[B_{\phi}\right]\right) \tag{5.30}$$

and λ are the associated eigenvalues given by:

$$\lambda=\frac{1}{R_T} \tag{5.31}$$

From the perspective of mathematics, equation (5.29) is an eigenvalue problem. A non-trivial solution to the system of equations can be found if and only if its determinant $[E-\lambda I]$ equals zero. Finding all the eigenvalues $\{\lambda_i\}$ and eigenvectors fi that satisfy equation (5.29) follows from this. These are ascertained by means of the EigPack library's subroutines. The formulas (5.27) and (5.28) can be used to derive the profiles $g(y)$ and $h(y)$ after the eigenvectors $\{f_i\}$ are known.

We rearrange the eigenvalues λ_i with $i=1,\ldots m$ of the matrix $[E]$ as follows:

$$\lambda_1 \le \lambda_2 \le \lambda_3 \le \ldots\ldots \le \lambda_{m-1} \le \lambda_m \tag{5.32}$$

Where λ_1 is the minimum eigenvalue and λ_m is the maximum eigenvalue. The corresponding eigenvectors are given by $\{f_i\}$. In general, the maximum eigenvalue, λ_m, is positive and represents the smallest critical Rayleigh number above which stationary convection is possible. The minimum eigenvalue, λ_1 is usually zero or negative and represents the largest critical Rayleigh number below which convection flow is possible. Then the supercritical Rayleigh number characterizing the convection threshold for Newtonian fluids is given by:

$$R_{TC}^{\sup}=\frac{R^{\sup}}{1+NLe} \quad \text{with} \quad \left.\begin{array}{ll} R^{\sup}=\dfrac{1}{\lambda_1}, & \text{if} \quad 1+NLe<0 \\ R^{\sup}=\dfrac{1}{\lambda_m}, & \text{if} \quad 1+NLe>0 \end{array}\right\} \tag{5.33}$$

5.3.3 TRANSIENT STABILITY: $p \neq 0$

The previous section presented the application of the finite element approach to the computation of the temperature, concentration, and stream function profiles (f, g, and h), as well as the related critical Rayleigh number R^{sup}, which indicates the commencement of supercritical convection. The different critical Rayleigh numbers that characterize the areas of either increasing or oscillatory convection are found in this section.

Given that the admissible functions $\omega(x,y)$ and $\vartheta(x,y)$ found in the variational formulation (Eqs. (5.16)-(5.18)) are arbitrary functions, we can designate as admissible the functions $f(x,y)$, $g(x,y)$, and $h(x,y)$. Consequently, the following linear equations are the result of the weak version of the perturbation equations (5.16)-(5.18):

$$\psi_0 \mathcal{K}_\psi = R_T \left(\theta_0 + N\phi_0\right)\mathcal{B} \tag{5.34}$$

$$p\theta_0 \mathcal{M} - \psi_0 \mathcal{L} = -\theta_0 \mathcal{K} \tag{5.35}$$

$$p\xi\phi_0 \mathcal{M} - \psi_0 \mathcal{L} = Le^{-1}\phi_0 \mathcal{K} \tag{5.36}$$

where $\mathcal{B}, \mathcal{K}_\psi, \mathcal{K}, \mathcal{L}$ and $\mathcal{M}$ are constants defined by:

$$\left.\begin{aligned} \mathcal{B} &= \int_\Omega \frac{\partial G}{\partial y} F d\Omega, \quad \mathcal{K}_\psi = \int_\Omega \left(\nabla F\right)^2 d\Omega \\ \mathcal{K} &= \int_\Omega \left(\nabla G\right)^2 d\Omega, \quad \mathcal{L} = -\int_\Omega \frac{\partial F}{\partial x} G d\Omega \\ \mathcal{M} &= \int_\Omega G^2 d\Omega \end{aligned}\right\} \tag{5.37}$$

From equations (5.35) and (5.36), we can deduce the following expressions for θ_0 and ϕ_0:

$$\theta_0 = \frac{\psi_0 \mathcal{L}}{p\mathcal{M} + \mathcal{K}} \tag{5.38}$$

$$\phi_0 = \frac{\psi_0 \mathcal{L}}{p\xi\mathcal{M} + Le^{-1}\mathcal{K}} \tag{5.39}$$

By substituting equations (5.38) and (5.39) into equation (5.34), we obtain the second-order polynomial dispersion equation in terms of the parameter p.

$$\xi^2 Le^2 p^2 - \gamma\xi Le p_1 p - \gamma^2 p_2 = 0 \tag{5.40}$$

Where:

$$\left.\begin{aligned} p_1 &= R_T^0 Le\left(\xi + N\right) - \left(1 + \xi Le\right) \\ p_2 &= \xi Le\left[R_T^0\left(1 + NLe\right) - 1\right] \\ R_T^0 &= \frac{R_T}{R^{\sup}} \end{aligned}\right\} \tag{5.41}$$

and the constants R^{sup} and γ are given by:

$$R^{\sup} = \frac{\mathcal{K}_\psi \mathcal{K}}{\mathcal{BL}}, \quad \gamma = \frac{\mathcal{K}}{\mathcal{M}} \tag{5.42}$$

CHAPTER VI

RESULTS AND DISCUSSION

This chapter is dedicated to presenting the analytical and numerical findings for a porous cavity subjected to constant heat flux q' and mass flux j' along the long walls, while the other walls are adiabatic and impermeable. This investigation encompasses configurations in horizontal, inclined, and vertical orientations. Initially, the focus is on a horizontal cavity (i.e., $\Phi = 0°$), followed by an examination of an inclined cavity (i.e., $\Phi \neq 0°$). The study concludes by analyzing a vertical cavity (i.e., $\Phi = 90°$) under the scenario where the Buoyancy forces have equal intensity but in opposing directions $N = -1$. This problem is characterized by several dimensionless parameters: the power-law index, n, the Rayleigh number, R_T, the buoyancy ratio, N, the Lewis number, Le, the normalized porosity, ξ, the aspect ratio, A, of the cavity, and the inclination angle Φ.

6.1 HORIZONTAL LAYER: $\Phi = 0°$

The results of this section focus on the effect of the power-law index, n, the Rayleigh number, R_T, the buoyancy ratio, N, and the Lewis number, Le, on the bistability convective flows, heat and mass transfer behaviors, and on the thresholds of the onset of various convective bifurcations in a porous layer, as predicted by the analytical solution. The findings have been confirmed through numerical analysis of the complete governing equations. The primary revelation in this research involves identifying a convective bistability phenomenon occurs from the interactional effect between the slower diffusing component and the shear-thickening fluids ($n > 1$) properties. The study encompasses both numerical and analytical outcomes, which fall within the following typical ranges: 0.6 to 1.4 for n, 0.01 to 20.0 for Le, and -4 to 4 for N.

Our research is primarily concerned with the onset of bifurcation. Consequently, we restrict our analysis to Rayleigh numbers R_T of relatively modest magnitudes, specifically $R_T \leq 100$, in close proximity to the critical points. Furthermore, in order to establish the presence of bistability in convection across various aspect ratio and thermal and solutal boundary conditions, we systematically vary the parameter A within the range of 1 to 10, while adopting Dirichlet and Neumann boundary conditions. This approach serves to generalize the conditions under which bistability in convection phenomena can manifest.

6.1.1 CASE OF SHALLOW LAYER: $A \gg 1$

Our initial investigation focuses on a shallow enclosure, benefiting from the availability of an analytical solution to provide guidance in this context.

Figure. 6.1 present the contours of streamlines, Ψ, temperature, T, concentration, S, horizontal velocity, U, and apparent viscosity, μ_a, obtained numerically, for two different liquids with power-law index of $n = 0.6$ and 1.4 and for a Newtonian fluid ($n = 1$), at $R_T = 100$, $Le = 5$, and $N = -0.1$. The streamlines are uniformly distributed with designated increments, $\Delta\Psi$, spanning from zero at the boundaries to the maximum value, Ψ_{max}, at the center. The isotherms and isoconcentration lines are uniformly distributed between the successive positions of the peak temperature T_{max} and maximum concentration S_{max} situated lower edge of the right vertical wall. On the other hand, the minimum temperature T_{min} and minimum concentration S_{min} are situated along the upper edge of the left vertical wall. Notably, the dimensionless temperature and concentration at the cavity's center are both normalized to zero.

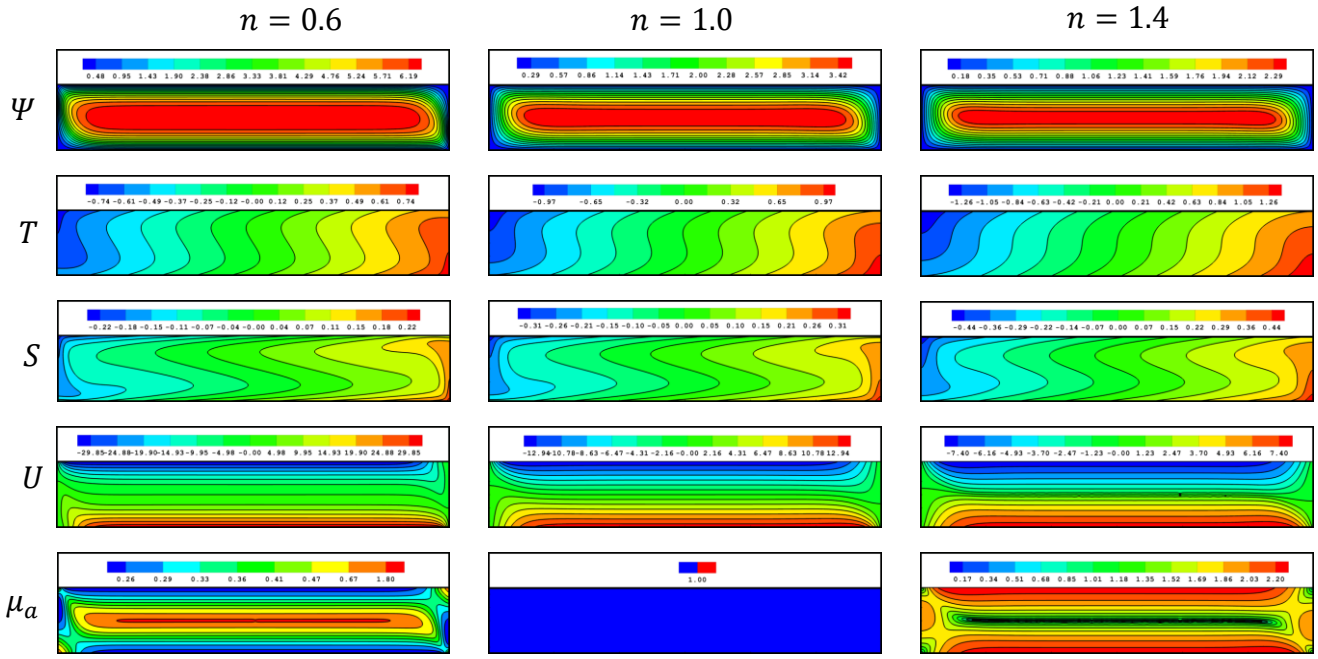


Figure 6.1: Contours of streamlines, Ψ, Temperature, T, Concentration, S, horizontal velocity, U, and apparent viscosity, μ_a, for $R_T = 100$, $Le = 5$, $N = -0.1$ and various values of n

Furthermore, owing to the centrosymmetry inherent in the problem, the minimum and maximum temperatures, as well as concentrations, exhibit equivalent magnitudes but with opposite signs. The horizontal velocity lines are uniformly distributed from the maximum velocity, U_{max}, located on the lower horizontal wall and the minimum velocity, U_{min}, on the upper horizontal wall. The apparent viscosity lines are uniformly distributed with specified

increments $\Delta\mu_a$ between the minimum value, μ_{amin}, on the center of cavity and the extremum value, μ_{amax}, on the center when $n = 0.6$, this is the opposite of $n = 1.4$, and it's clearly constant ($\mu_a = 1$) when $n = 1$. The numerical findings depicted in Figure 6.1 validate the theoretical assumption made in the analytical solution, indicating that the flow patterns within the central region of the cavity remain parallel regardless of the power-law index, n. It is important to note. However, that the scope of this current investigation is confined to the examination of unicellular convection exclusively.

Figures 6.2(a)-(d) show the horizontal velocity, U, apparent viscosity, μ_a, temperature, T, and (d) concentration, S, profiles at the center of the layer ($x = 0$) for $R_T = 100$, $Le = 5$, $N = -0.1$, and various values of n. the results are presented for $-0.5 \leq y \leq 0.5$. The analytical solution, represented by solid lines, aligns closely with the numerical results, denoted by solid circles, demonstrating a favorable agreement between the present analytical solution and the numerical solution.

Figure 6.2(a) reveals a noticeable decrease in velocity with increasing values of the power-law index, n, and highlights that the maximum velocity values occur at the boundaries. This behavior stems from the modeling of the porous medium in accordance with Darcy's law, permitting fluid slip at the solid boundary. Notably, for a Newtonian fluid, the velocity distribution follows a linear pattern, in agreement with the findings of Amari et al. [29] and Vasseur et al. [56]. The depiction of apparent viscosity in Figure 6.2(b) elucidates a diminishing trend as the power-law index, n, decreases. This signifies a reduction in the significance of convective motion when the fluid exhibits shear-thickening behavior ($n > 1$). Conversely, contrasting effects are observed for shear-thinning fluids ($n < 1$), as evidenced in Figure 6.2(b). These observed phenomena align with the findings reported by Amari et al. [29], Dharmadhikari and Kale [57], as well as Chen and Chen [58, 59], and it's clearly constant ($\mu_a = 1$) in the case of Newtonian fluid ($n = 1$). In Figures 6.2(c) and (d), it is observed that the temperature and concentration profiles exhibit an augmentation with increasing values of the power-law index, n. Additionally, all curves maintain a constant slope at $y = -0.5$ and $y = 0.5$, attributed to the imposition of a constant heat and mass flux on the horizontal walls.

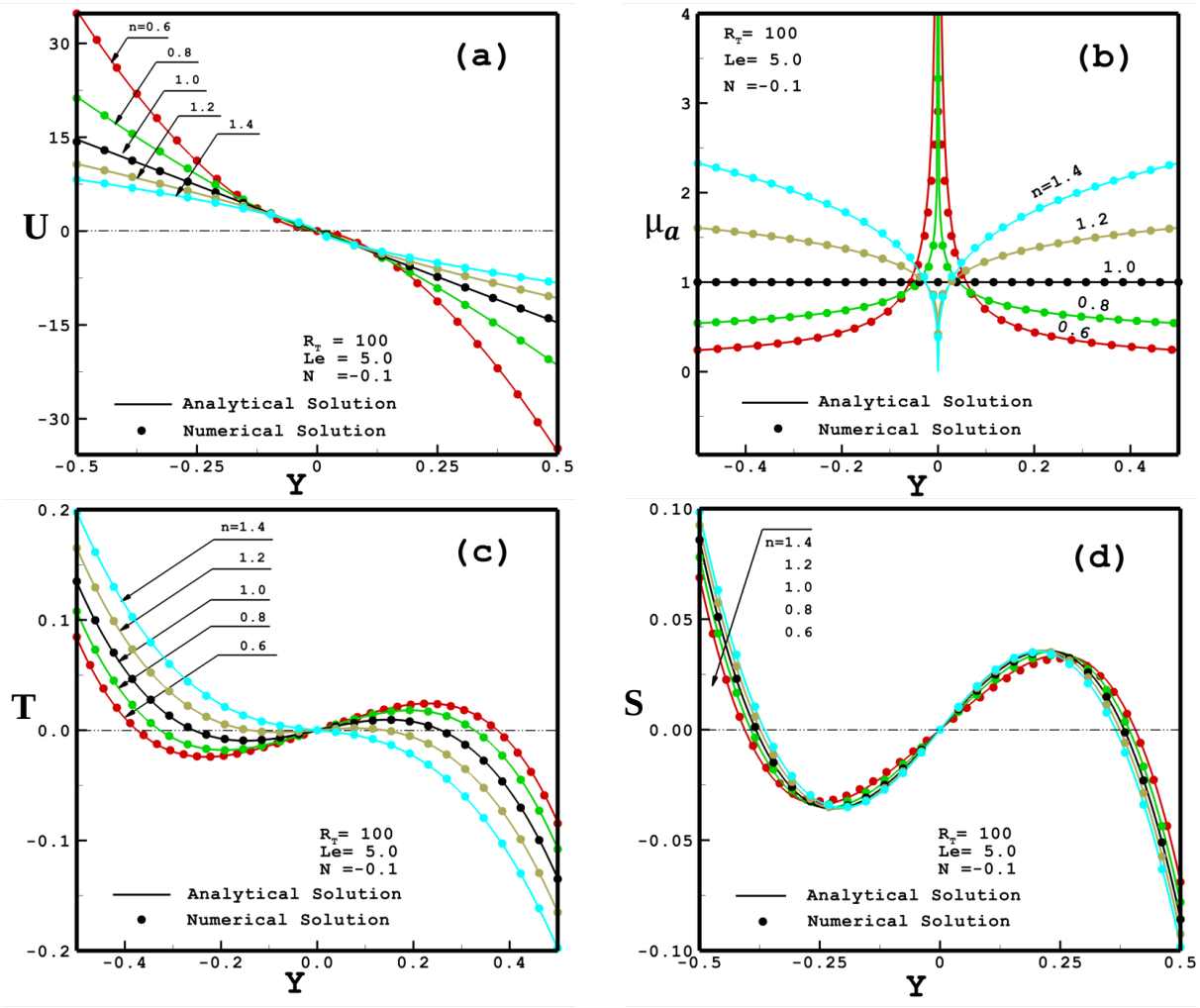


Figure 6.2: Effect of the power-law index, n, on (a) the horizontal velocity, U, (b) apparent viscosity, μ_a, (c) temperature, T, and (d) concentration, S

As an introductory exploration into the identification of Bistability in convection, we present a graphical representation with an algorithmic scale in zoomed image Figure 6.3, illustrating the Bistability bifurcation concerning flow intensity as a function of the Rayleigh number. The figure encompasses three distinct Rayleigh number thresholds, each bearing significance. Specifically, it is well-established that, in the context of a negative buoyancy ratio ($N < 0$), a threshold similar to that of subcritical flows emerges, denoted as R_{TC}^{sub}. This threshold may manifest either below or above the supercritical threshold, R_{TC}^{sup}. Furthermore, an additional threshold, referred to as R_{TC}^{tur}, consistently surpassing R_{TC}^{sup}, delineates a hypothetical backward bifurcation, symbolized by a dashed-dotted arrow. This backward bifurcation exhibits a transition from low to high finite amplitude convective states, forming an "S"-shaped bifurcation pattern.

The phenomenon of Bistability bifurcation, achieved through systematic variations in Rayleigh numbers in both ascending and descending sequences, engenders a hysteresis loop. Within this

loop, high and low convective states persist concurrently under identical flow boundary conditions and governing parameters. In Figure 6.3, we depict three distinctive Bistability regimes. The first of these regimes, referred to as the subcritical regime, manifests when the subcritical threshold R_{TC}^{sub} is significantly lower than the supercritical threshold R_{TC}^{sup}, specifically when, n, is less than 1.107. The second regime, known as the transcritical regime, materializes when R_{TC}^{sub} equal R_{TC}^{sup}, denoting a condition where, n, equals 1.107. The third regime, termed the supercritical regime, emerges when R_{TC}^{sub} considerably exceeds R_{TC}^{sup}, signifying, n, values greater than 1.107. Across all three of these regimes, the characteristic "S" shaped bistability bifurcation remains intact, resulting in the coexistence of two distinct and stable convective states. Notably, the bistability in convection ceases to exist when the lower and upper bifurcation points, R_{TC}^{sub} and R_{TC}^{tur}, converge (i.e., when n equal 1.55), giving rise to a well-defined inflection convection state characterized by a sharp increase in heat and solute transfer rates.

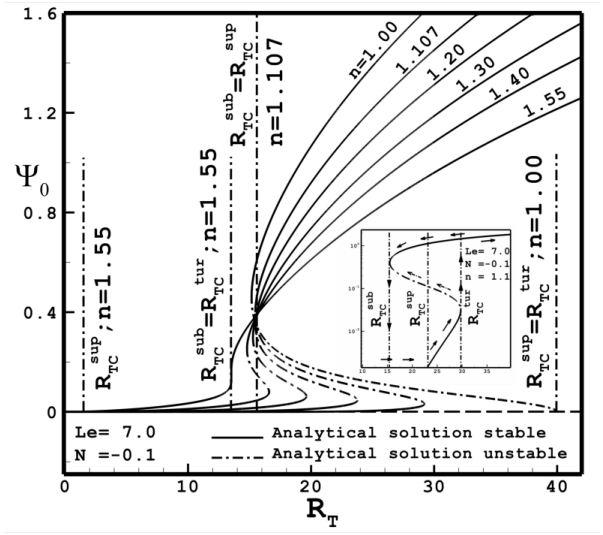


Figure. 6.3. Bifurcation diagram in terms of Ψ_0 as the function of R_T and n

Table 6.1 provides a comprehensive presentation of the critical Rayleigh numbers denoting the onset of motion (R_{TC}^{sub}, R_{TC}^{tur} and R_{TC}^{sup}) as a function of the power-law index, n. A discernible trend emerges from the table, underscoring the notable influence of the power-law index, particularly in the context of thickening fluids. It is remarkable that such an influence does not manifest in the case of shear-thinning fluids, highlighting a significant distinction in the behavior of bistability convection.

Table 6.1: Dependence of R_{TC}^{sub}, R_{TC}^{tur} and R_{TC}^{sup} on n for $Le = 7.0$ and $N = -0.1$.

n	R_{TC}^{sub}	R_{TC}^{tur}	R_{TC}^{sup}
0.6	11.95	…	1314.69
0.8	13.90	…	232.48
1.0	15.17	40.00	40.00
1.1	15.46	29.72	16.47
1.2	15.50	23.77	6.75
1.3	15.28	19.62	2.76
1.4	14.80	16.59	1.12

In Figure 6.4, characteristic bifurcation diagrams are presented, illustrating the dependencies of Ψ_0, Nu, and Sh on R_T and n under the specified conditions of $Le = 5$ and $N = -0.1$. The outcomes encompass a range of power-law index, spanning from $n = 0.6$ to 1.4. The curves featured in the plots represent the predictions derived from the present analytical/numerical nonlinear models. The solid lines denote the stable branches, while the long-dashed lines signify unstable branches. The numerical solutions derived from the full governing equations are represented by solid circles. Notably, Good agreement is observed between the results of these two nonlinear theories. The profile obtained for a Newtonian fluid $n = 1.0$ corresponds to convection induced by the imposition of a constant heat and mass flux on the horizontal boundaries of the system. This configuration leads to the emergence of a saddle-node bifurcation at a subcritical Rayleigh number, denoted as $R_{TC}^{sub} = 15.63$. The determination of the subcritical Rayleigh number involved a numerical search within the analytical model, where the value of R_T was identified such that the inverse of the derivative of Ψ_0 with respect to R_T equaled zero. With an increasing in the power-law index, denoted as n, the bifurcation behavior undergoes a notable transformation contingent upon the magnitude of power-law index. Across the range of cases spanning from $1 < n < 1.3$, the bifurcation curve exhibits the distinctive presence of two turning saddle-node points (R_{TC}^{sub} and R_{TC}^{tur}). These points connect the two stable branches, delineated by an intervening unstable branch represented by long-dashed lines. The upper stable branch, originating from R_{TC}^{sub}, aligns with the conventional subcritical bifurcation observed earlier for $n = 1$. Conversely, the lower stable branch, commencing at R_{TC}^{sup}, corresponds to a supercritical bifurcation. However, it is noted that the latter exist within the interval of $R_{TC}^{sup} \leq R_T \leq R_{TC}^{tur}$. Under these circumstances, a bistability regime manifests itself between the two thresholds ($R_{TC}^{sub} \leq R_T \leq R_{TC}^{tur}$).

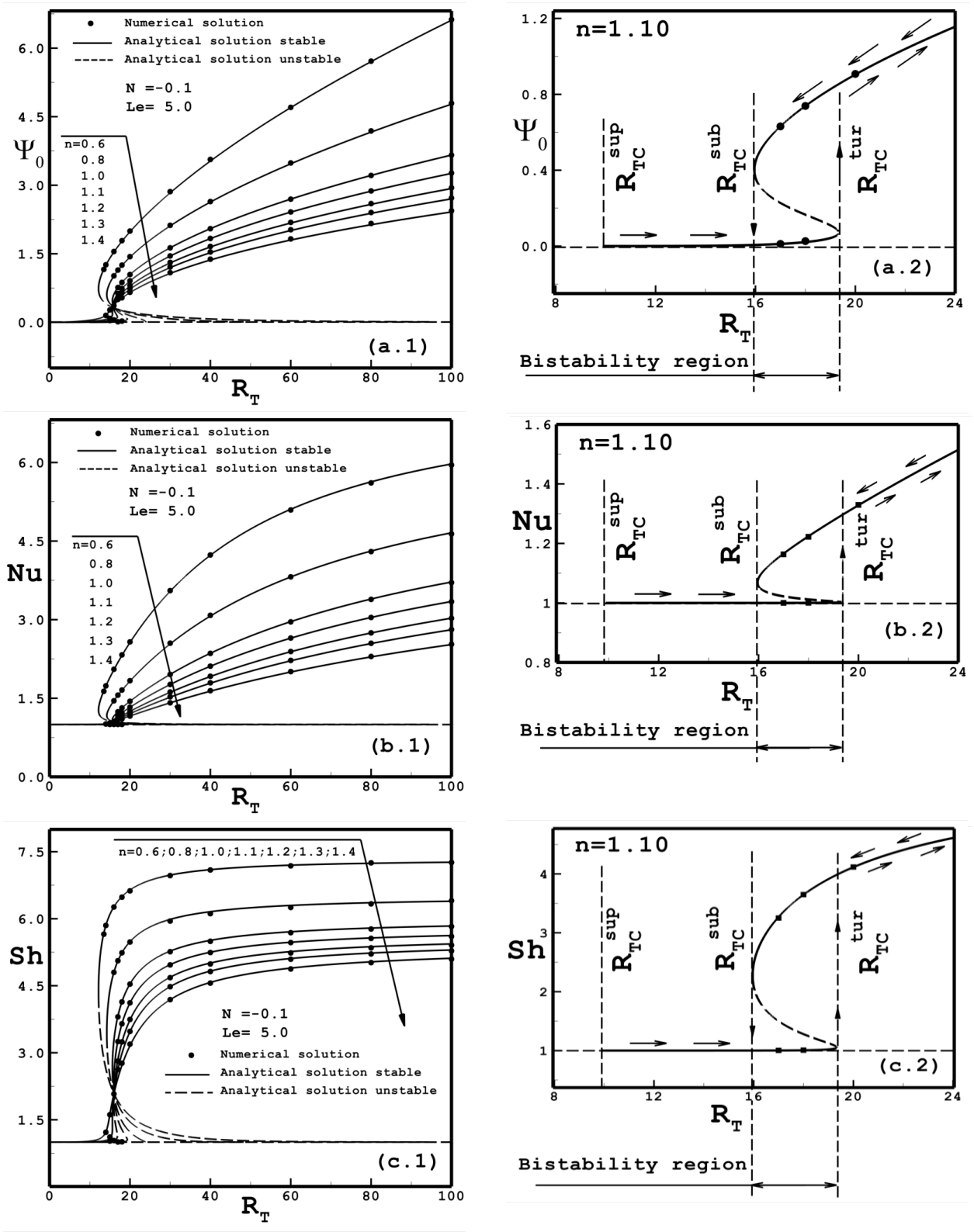


Figure. 6.4. Bifurcation diagram as a function of R_T and n: (a) flow intensity Ψ_0, (b) Nusselt number Nu, and (c) Sherwood number, Sh.

Beyond the supercritical Rayleigh number, R_{TC}^{sup}, the outcomes derived from the numerical solution of the full governing equations suggest that, when initiating computations from the initial rest state conditions, the solution traces a hysteresis loop as illustrated by arrows in the zoom included in Figure 6.4(a.2; b.2 and c.2). Corresponding heat and solute transfer rates are presented in Figures 5(b) and 5(c). Under the specified conditions of $N = -0.1$ and $Le = 5$, the presence of bistability bifurcation is confirmed within the power-law index range of $1 < n < 1.3$. Notably, for $n \leq 1$, the observed bifurcation assumes a subcritical.

Within the zone of Bistability, Figure 6.5 showcases the solutions at $R_T = 18$, obtained through the numerical resolution of the comprehensive governing equations. These visual representations encompass streamlines, isotherms, isoconcentrates, and apparent viscosities, presented in a sequential order from top to bottom. The solution portrayed in Figure 6.5(b), attributed to the lower branch, originates from the initiation of numerical calculations using the initial rest state conditions. However, the solution related to the upper branch, Figure 6.5(a), is exclusively attained by following the delineated hysteresis path on the curve for $n = 1.1$, with an increase in the power-law index, the region of bistability contracts, as evidenced by the outcomes derived for $n = 1.1$, and diminishes entirely as the fluid became more and more shear-thickening, exemplified in instances with $n = 1.3$.

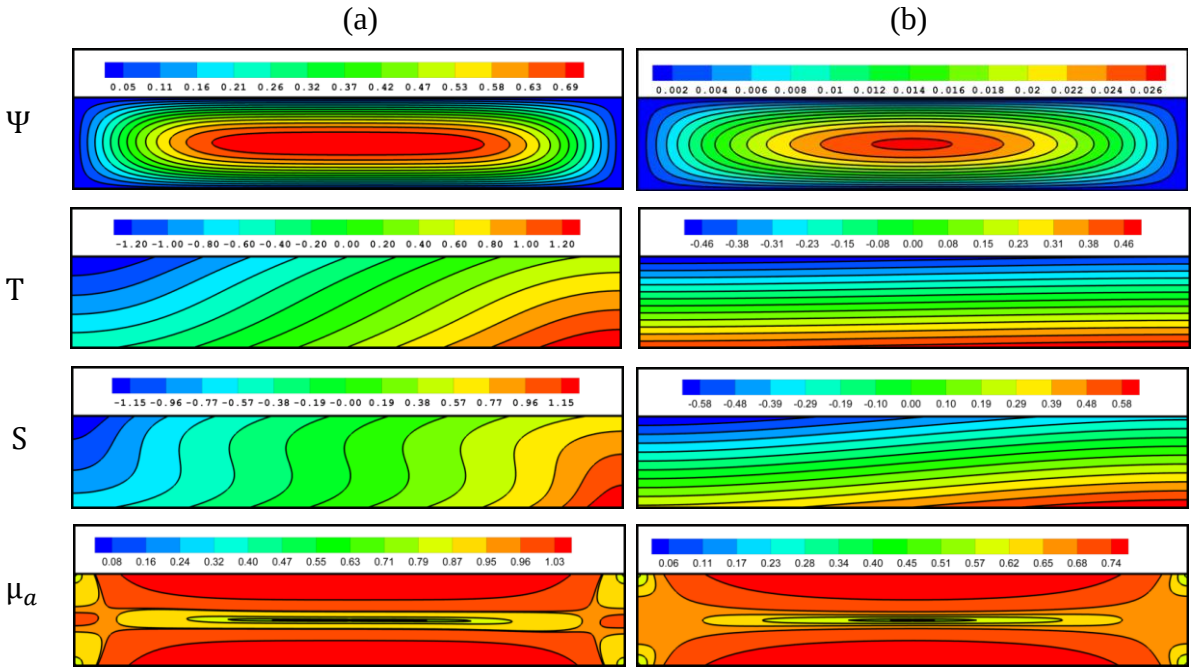


Figure. 6.5. Contours of streamlines, Ψ_0, temperature, T, concentration, S, and apparent viscosity μ_a.

In such circumstances, a resultant pitchfork-type bifurcation emerges, characterized by the transition from the rest state to a convective regime, occurring at a supercritical Rayleigh number, R_{TC}^{sup}.

Table 6.2 gives the critical values of the Rayleigh numbers characterizing the onset of motion (R_{TC}^{sup}, R_{TC}^{sub}, and R_{TC}^{tur}) as a function of the power-law index, n. This table clearly indicates that bistability convection was significantly affected by the power-law index, n.

Table 6.2. Dependence of R_{TC}^{sub}, R_{TC}^{tur} and R_{TC}^{sup} on n for $Le = 5.0$ and $N = -0.1$.

n	R_{TC}^{sub}	R_{TC}^{tur}	R_{TC}^{sup}
0.6	12.18	…	788.90
0.8	14.24	…	139.50
1.0	15.63	24.00	24.00
1.1	15.96	19.33	9.88
1.2	15.96	16.87	4.05
1.3	15.63	15.63	1.98
1.4	…	…	0.67

In Figure 6.6, a stability diagram is presented to illustrate the influence of the power-law index denoted as, n, and the buoyancy ratio, N, on critical Rayleigh numbers that govern the onset of subcritical R_{TC}^{sub} and supercritical R_{TC}^{sup} convection, as well as an additional critical point denoted as R_{TC}^{tur}, which corresponds to a turning saddle-node point where a backward bifurcation occurs, resulting in a transition from lower to higher convective states. These findings are presented within the context of $Le = 5.0$. Upon initial examination, it becomes evident that R_{TC}^{sub}, R_{TC}^{sup}, and R_{TC}^{tur} exhibit significant decreases as the buoyancy ratio, N, increases. This decrease can be attributed to the collaborative influence of shear-thickening behavior and the slower diffusing solute, which collectively augment the subcritical convection phenomenon. When the buoyancy ratio N approaches or exceeds approximately -0.02, a bistability convection regime becomes evident. This region is distinctly outlined as a triangular area, as depicted in the zoomed image in Figure 6.6 for the case of $N = -0.14$. Notably, it becomes evident that bistability convection exclusively occurs in the context of shear-thickening fluid ($n > 1$) and opposing flow conditions where ($N < 0$), This is the opposite of

what reported by Rebhi et al. [76], where the bistability occurs in the context of shear-thinning fluid ($n < 1$) and aiding flow conditions where ($N > 0$).

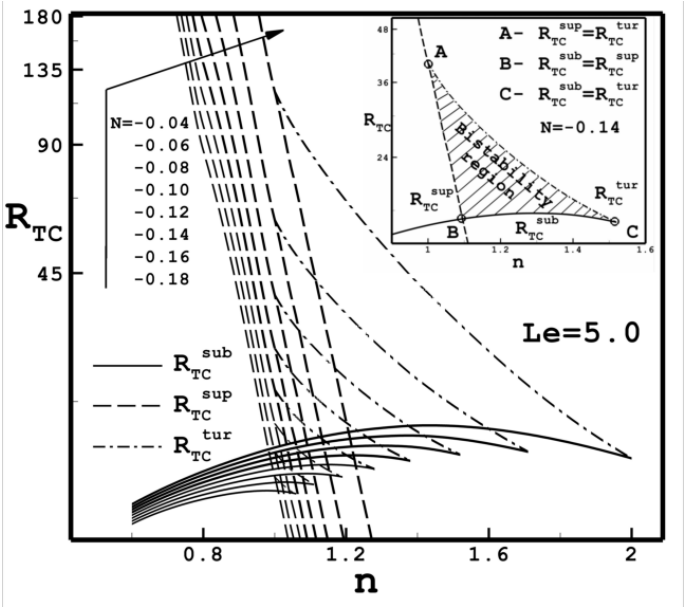


Figure 6.6: Buoyancy ratio, N, and power-law index, n, effects on the critical Rayleigh numbers (R_{TC}^{sub}, R_{TC}^{tur}, and R_{TC}^{sup})

For a specific buoyancy ratio value of $N = -0.14$, the graph clearly demonstrates that the subcritical regime, R_{TC}^{sub} is observed to be the lowest among the three critical values i.e., ($R_{TC}^{sub} < R_{TC}^{sup} < R_{TC}^{tur}$). a co-dimension two point emerges within the transcritical regime where $R_{TC}^{sup} = R_{TC}^{sub} = 17.26$, for a power-law index, with $n = 1.107$, indicated as point (B) in the zoomed image. This transcritical regime extends until $n = 1.52$, where $R_{TC}^{sup} = R_{TC}^{tur} = 16.89$, indicated as point (C), and a point (A) demonstrates a weak dependence on the power-law index $n = 1$ and $R_{TC}^{sup} = R_{TC}^{tur} = 40$. The boundaries of the bistability region are delineated by the triangle (ABC) as illustrated in the zoomed image. In summary, as the buoyancy ratio value with ($N < 0$) decreases, the value of the power-law index n increases, the presence of bistability becomes increasingly evident, regardless of n exceeding 1.0. However, it is noteworthy that the extent of the bistability region exhibits significant sensitivity to the buoyancy ratio, N, and the power-law index, n, expanding as N, and n decreases (refer to Figure 6.6 and Figure 6.4 for the range $-0.04 \leq N \leq -0.18$,and $1 < n < 3$). It is pertinent to observe that as shear-thickening behavior becomes more pronounced, it promotes Newtonian thermosolutal subcritical convection $n = 1$, leading to a notable reduction in the threshold for subcritical convection.

A more comprehensive depiction of the impact of buoyancy ratio, N, and Rayleigh number, R_T, on Ψ_0, Nu, and Sh is presented in Figure 6.7 for $Le = 5$ and $n = 1.2$. The outcomes are derived for varying buoyancy ratio values from 0.2 to -0.2. As evident from Figures 6.7(a)–(c), for a given Rayleigh number, both the intensity of convection, Ψ_0, and the ensuing heat, Nu, and solute, Sh, transfer rates exhibit a decline as the buoyancy ratio, N, diminishes. The plot notably illustrates the influence of N on the existence of various bifurcation curves, as elucidated in Figure 6.7. Consequently, a decrease in the buoyancy ratio, N, leads to the evolution of bifurcation curves from subcritical to supercritical behavior.

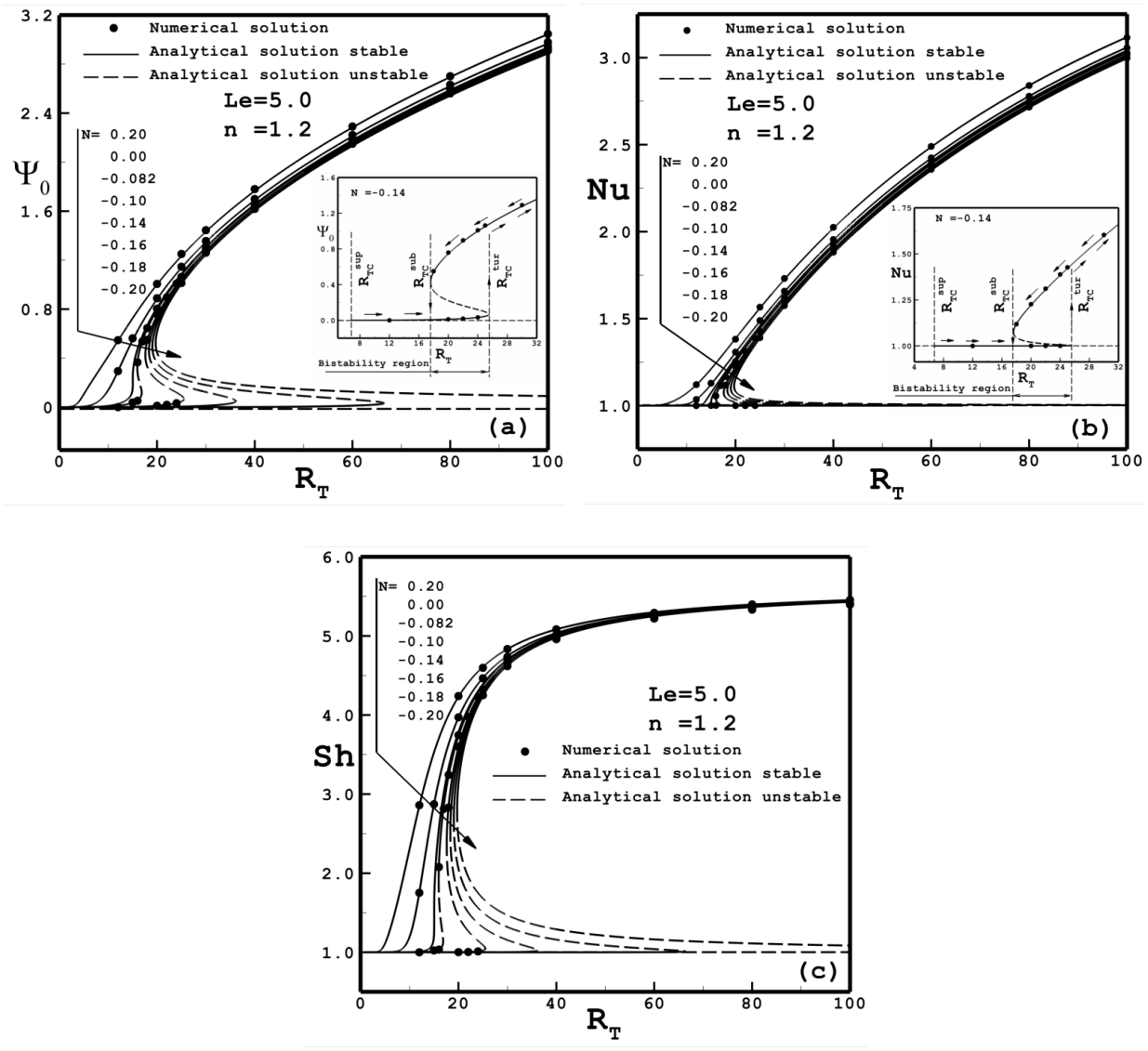


Figure. 6.7. Bifurcation diagram as a function of R_T and N: (a) flow intensity Ψ_0, (b) Nusselt number Nu, and (c) Sherwood number Sh

Generally, the influence of N on the onset of motion (R_{TC}^{sup}, R_{TC}^{sub}, and R_{TC}^{tur}) is elucidated in Figure 6.6. Under the specified conditions of a power-law index, $n = 1.2$, and a Lewis number, $Le = 5$, the presence of bistability bifurcation is confirmed within the buoyancy ratio range of $N = -0.18$ to -0.082, (i.e., under opposing flow conditions $N < 0$), Notably, for $N = -0.2$, the observed bifurcation assumes a subcritical.

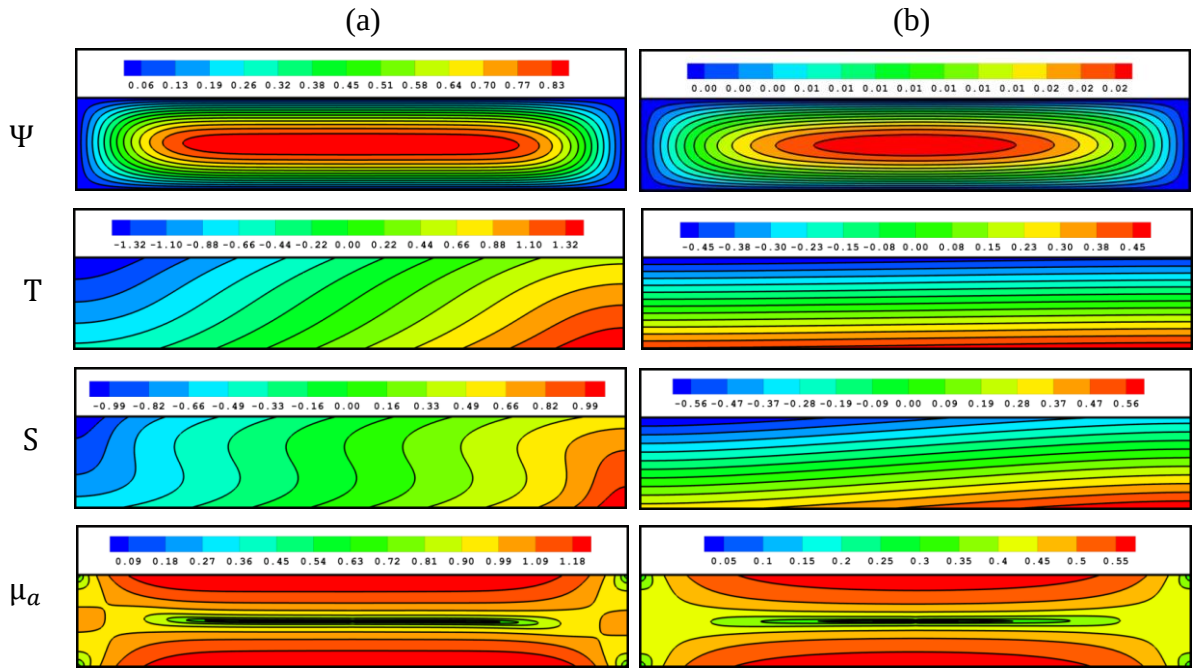


Figure. 6.8. Contours of streamlines, Ψ_0, temperature, T, concentration, S, and apparent viscosity μ_a

In the region characterized by bistability, the solutions corresponding to $R_T = 22$, derived from the numerical solution of the comprehensive governing equations, are depicted in Figure 6.8. These graphical representations sequentially present streamlines, isotherms, isoconcentrates, and apparent viscosities from top to bottom. The solution illustrated in Figure 6.8(b), representing the lower branch, is obtained by initializing the numerical computations with the rest state as the initial conditions. Conversely, the solution for the upper branch, as shown in Figure 6.8(a), is exclusively acquired by tracing the hysteresis path delineated on the curve for $N = -0.14$. As the buoyancy ratio becomes large, the bistability region shrinks, as shown by the results obtained for $N = -0.14$, and it completely disappears when the buoyancy ratio becomes very large, as displayed for thermal convection $N = 0$ and for the aiding flow ($N > 0$). For this situation, the resulting pitchfork type bifurcation, characterized by a transition from the rest state to a convective regime, takes place at a supercritical Rayleigh number, R_{TC}^{sup}.

Table 6.3 provides the critical Rayleigh numbers, delineating the onset of motion (R_{TC}^{tur}, R_{TC}^{sub}, and R_{TC}^{tur}), as functions of the buoyancy ratio, N. This table clearly indicates the impact of the buoyancy ratio, N, on bistability convection.

Table 6.3: Dependence of R_{TC}^{sub}, R_{TC}^{tur} and R_{TC}^{sup} on N for $Le = 5.0$ and $n = 1.2$.

N	R_{TC}^{sub}	R_{TC}^{tur}	R_{TC}^{sup}
0.20	...	…	1.01
0.00	...	…	2.02
-0.082	15.04	15.04	3.43
-0.10	15.96	19.33	9.88
-0.14	17.61	25.51	6.75
-0.16	18.35	36.14	10.13
-0.18	19.05	66.49	20.27
-0.20	19.73	…	$+\infty$

In Figure 6.9, a stability diagram is presented to illustrate the influence of the power-law index denoted as, n, and the Lewis number, Le, on critical Rayleigh numbers discus in figure 6.6. These findings are presented within the context of $N = -0.1$. Upon initial examination, it becomes evident that the bistability region presented in zoomed image Figure 6.9(a) decrease as the Lewis number, Le, decrease until a value of $Le = 2.4$, where $R_{TC}^{sub} = R_{TC}^{sup} = R_{TC}^{tur}$ and $n = 1$, when the values of Le exceeds approximately 10 the bistability regime disappear the invers of Rebhi et al [76]. For this interval of Lewis number, Le, and with an increasing of Le, the domain of n expands and remains above 1.

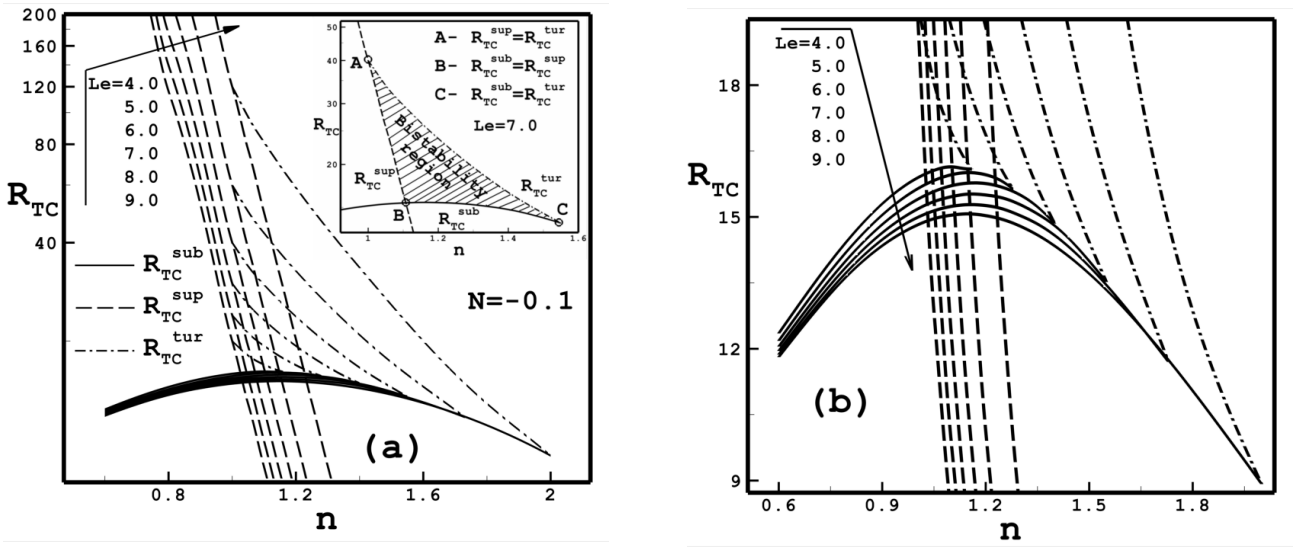


Figure 6.9: Effect of Lewis number, Le, and Power-law index, n, on the critical Rayleigh numbers (R_{TC}^{sub}, R_{TC}^{tur}, and R_{TC}^{sup}).

An alternative perspective on the influence of the Lewis number, Le, on Ψ_0, Nu, and Sh, with fixed parameters $n = 1.1$ and $N = -0.1$, is delineated in Figure 6.10. Within the defined range of governing parameters, the analytical model predicts that the occurrence of bistability bifurcation is not exist when the Lewis number is below 3.4. As the Lewis number progressively increases, the bistability region manifests and undergoes significant expansion, persisting within the range below 10, indicative of thermal diffusion dominant over mass diffusion. The graphical representation in Figure 6.10 provides insight into the notable impact of the magnitude of the Lewis number on the characteristic "S"-bifurcation shape within the bistability region. Specifically, the "S"-bifurcation curve becomes increasingly conspicuous with higher Lewis numbers (i.e., $Le = 7$ and 9). At the subcritical bifurcation point, the flow exhibits finite amplitude, marking a discernible transition from a rest state to a convective state. This transition is characterized by a sudden and substantial augmentation in flow intensity, Nusselt, and Sherwood numbers. Such enhancements are attributed to a pronounced reduction in the apparent viscosity, as depicted in Figures 6.10(a)–(c).

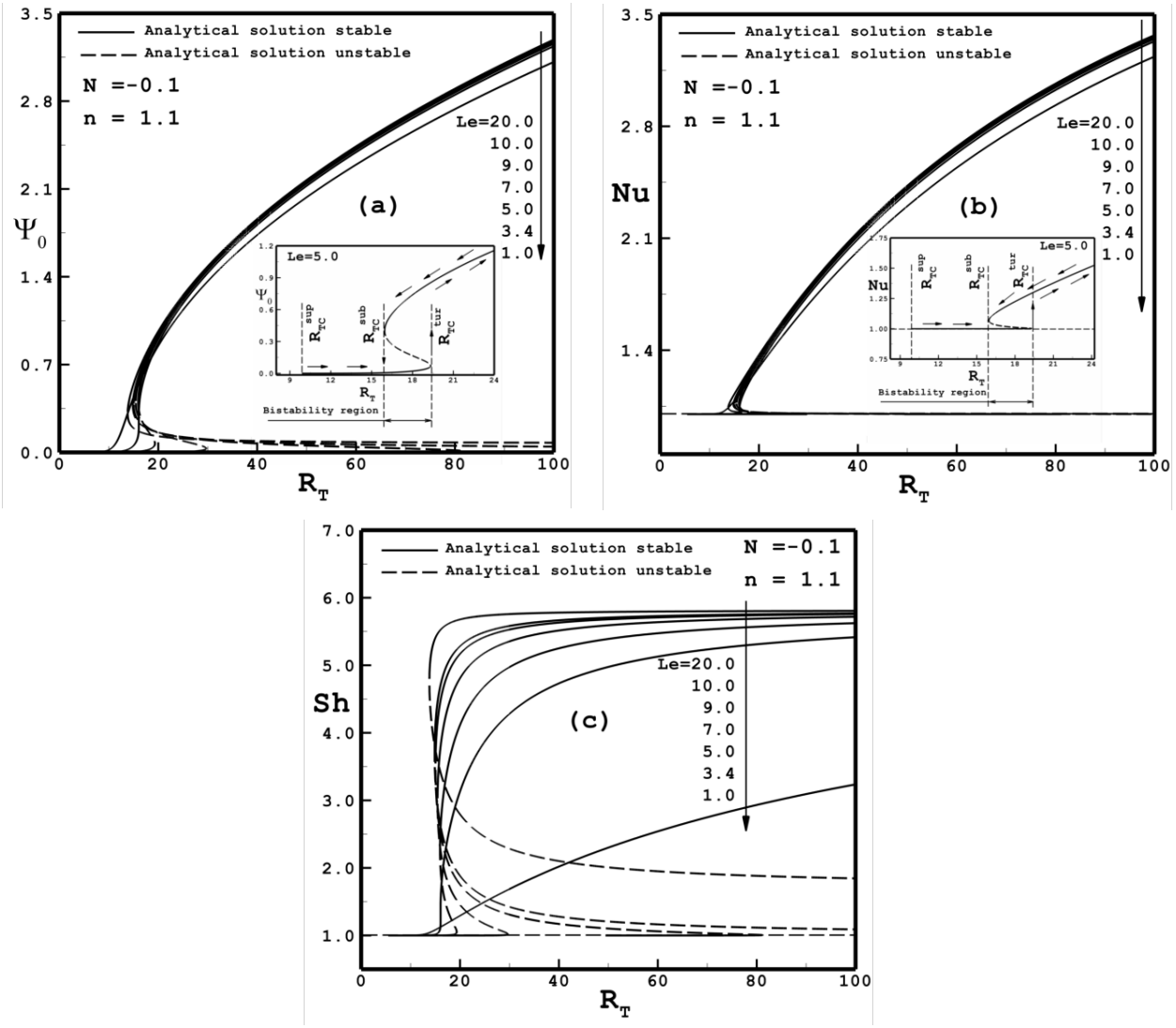


Figure. 6.10. Bifurcation diagram as a function of R_T and Le: (a) flow intensity Ψ_0, (b) Nusselt number Nu, and (c) Sherwood number Sh.

Table 6.4 shows the impact of the Lewis number, Le, on the critical Rayleigh numbers (R_{TC}^{sub}, R_{TC}^{tur}, and R_{TC}^{sup}) for $n = 1.1$, and $N = -0.1$. It was found that the bistability regime occurs when Lewis number, Le, values are within the domain]3.4; 10[.

Table 6.4: Dependence of R_{TC}^{sub}, R_{TC}^{tur} and R_{TC}^{tur} on Le for $n = 1.1$ and $N = -0.1$.

Le	R_{TC}^{sub}	R_{TC}^{tur}	R_{TC}^{sup}
1.0	…	…	5.49
3.4	16.07	16.07	7.51
5.0	15.96	19.33	9.88
7.0	15.46	29.72	16.47
9.0	15.04	81.14	49.41
10.0	14.87	…	$+\infty$
20.0	13.81	…	$+\infty$

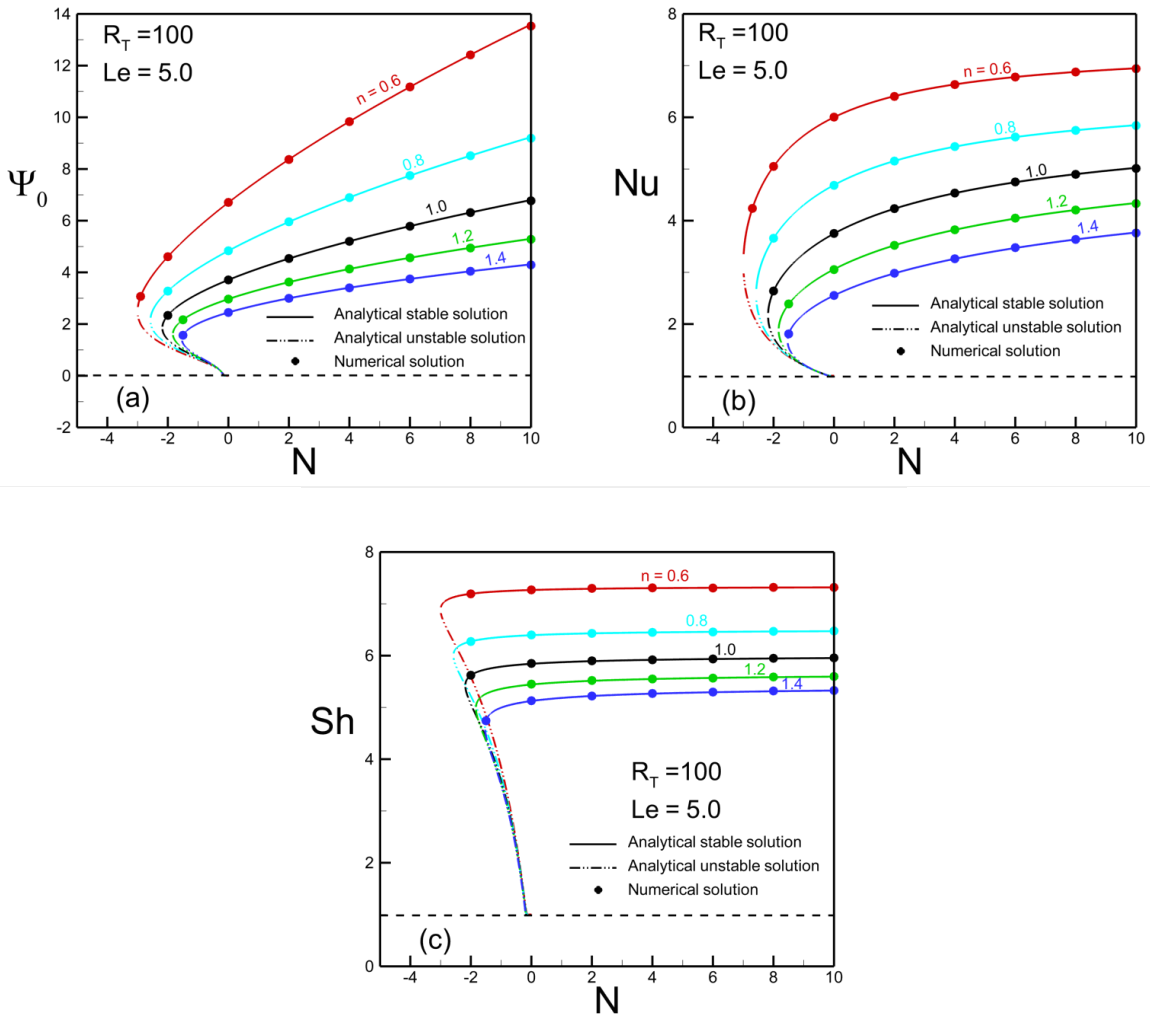


Figure. 6.11. Effect of the buoyancy ratio, N, and Power-law index, n, on (a) flow intensity Ψ_0, (b) Nusselt number Nu, and (c) Sherwood number Sh.

Figure. 6.11 exhibits the variations of Ψ_0, Nu, and Sh as a function of the buoyancy ratio, N, and the power-law index n, for $R_T = 100$ and $Le = 5$. The solid lines denote stable branches, while the dashed-dotted-dotted lines signify unstable branches. The numerical solutions are depicted using solid circles. Significantly, a notable agreement is observed in the results derived from these two nonlinear theories. Generally, it is observed from Figures 6.11(a)-(c) that, for fixed values of N, the magnitude of convection Ψ_0, as well as the resulting heat transfer Nu and solute transfer Sh, decrease with increasing power-law index, n. The plot notably demonstrates how n affects the presence of subcritical bifurcation, N_{CR}^{sub}, as clarified in Table. 6.5. Consequently, a reduction in the buoyancy ratio, N, from 10 to a subcritical value of N_{CR}^{sub}, as shown in Figure. 6.11, results in a decrease in the magnitude of convection Ψ_0, the Nusselt

number Nu, and the Sherwood number Sh. From Figure. 6.11, it can be observed that the supercritical buoyancy ratio, N_{CR}^{sup}, remains unaffected by the power-law index, n.

Table. 6.5 presents the critical values of the buoyancy ratio (N_{CR}^{sub}, and N_{CR}^{sup}) denoting the initiation of motion relative to the power-law index, n. It is evident from this table that subcritical buoyancy ratio, N_{CR}^{sub}, is notably influenced by the power-law index, n.

Table 6.5: the influence of the power-law index, n on the existence of (N_{CR}^{sub}, and N_{CR}^{sup}) for $R_T = 100$, and $Le = 5$.

n	N_{CR}^{sub}	N_{CR}^{sup}
0.6	-2.99	-0.10
0.8	-2.56	-0.10
1.0	-2.18	-0.10
1.2	-1.83	-0.10
1.4	-1.53	-0.10

Figure 6.12(a)-(c) depict the variations of Ψ_0, Nu, and Sh as a function of Lewis number, Le, and power-law index, n, with $R_T = 100$, $N = 0.0, N = -0.1,$ and $N = -0.8$. In the figure, the numerical solutions (solid circles), stable analytical solutions (solid lines), and unstable analytical solutions (dotted lines) are indicated. A significant agreement between the numerical and analytical results is evident. The intensity of flow Ψ_0, the Nusselt number Nu and the Sherwood number Sh decreases with increasing n, while for given values of Le and n, the intensity of flow Ψ_0, Nu, and Sh decreases with decreasing of buoyancy ratio N. Figure 6.12(a) and (b) illustrates that the intensity of flow, Ψ_0, and the Nusselt number, Nu, tends to $\Psi_0^{Le\to 0,\pm\infty}$ and $Nu^{Le\to 0,\pm\infty}$successively, as indicated in Table 6.5 at small or very large values of Lewis number, Le. For a simple diffusion $N = 0.0$, Ψ_0, and Nu remains constant (i.e. $\Psi_0 = \Psi_0^{Le\to 0,\pm\infty}$, and $Nu = Nu^{Le\to 0,\pm\infty}$) across a range of Le from 0.0001 to 100, then it starts to change gradually for values of Le between 0.1, and 1.0 depending on the power-law index n at $N = -0.1$. Conversely, for $N = -0.8$, where the buoyancy forces induced by the thermal and solutal effects are opposing each other and of the same order of magnitude, a notable decrease in the intensity of flow and heat transfer is observed with increasing Le. Respectively at $Le = 1.11$, and $Le = 1.25$ for $n = 1.0$, and $n = 1.4$ the convective flow becomes purely diffusive, as solutal effects dominate and hinder convective motion entirely. This dominance persists until $Le = 1.40$ and $Le = 2.30$ respectively for $n = 1.0$ and $n = 1.4$, beyond which thermal effects

regain control through a subcritical bifurcation. Initially, the intensity of flow, Ψ_0, and the Nusselt number increases with Le, then stabilizes at a constant value dependent solely on the power-law index, n, and the Rayleigh number, R_T. However, Figure 6.12(c) indicates that mass transfer tends towards conductivity at lower Le values, regardless of N. For $N = -0.1$, Sh initially increases with Le before approaching the value of $Sh^{Le\to 0,\pm\infty}$ as indicated in table 6.5. In contrast, for $N = -0.8$, the evolution of Sh with Le differs significantly due to the dominance of solutal forces over thermal forces. As Le increases, solutal effects become more prominent, gradually impeding convective flow until reaching a steady state at $Le = 1.11$ and $Le = 1.25$ respectively for $n = 1.0$ and $n = 1.4$. This state persists until $Le = 1.40$ and $Le = 2.30$ respectively for $n = 1.0$ and $n = 1.4$, beyond which Sh asymptotically approaches the value of $Sh^{Le\to 0,\pm\infty}$.

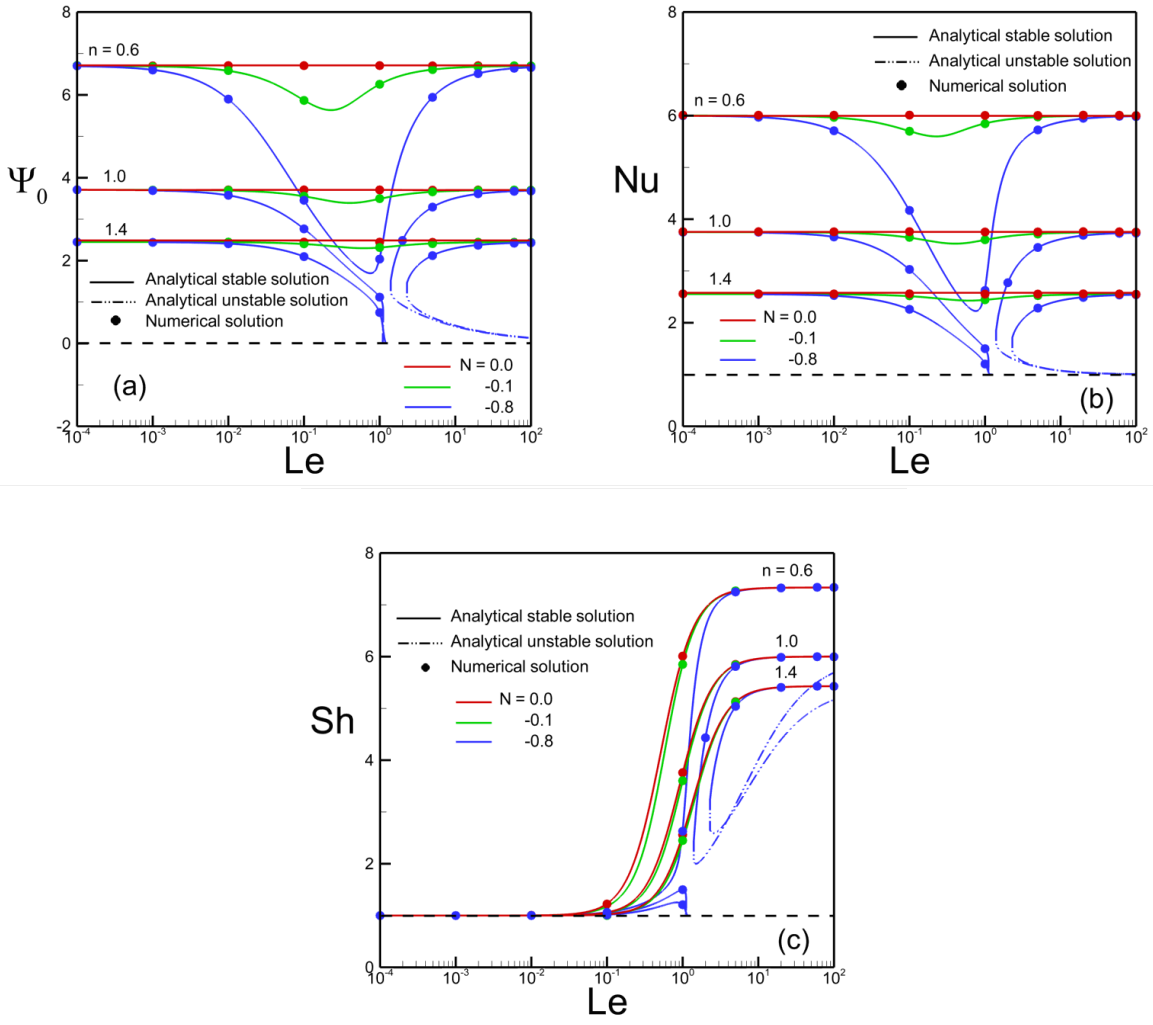


Figure 6.12: Effect of the Lewis number, Le, and Power-law index, n, on (a) flow intensity Ψ_0, (b) Nusselt number Nu, and (c) Sherwood number Sh. For $N = 0.0, -0.1, and\ -0.8$.

Table 6.6: the different values of $\Psi_0^{Le\to 0,\pm\infty}$, $Nu^{Le\to 0,\pm\infty}$, and $Sh^{Le\to 0,\pm\infty}$ for $R_T = 100$.

n	$\Psi_0^{Le\to 0,\pm\infty}$	$Nu^{Le\to 0,\pm\infty}$	$Sh^{Le\to 0,\pm\infty}$
0.6	6.701	6.000	7.333
1.0	3.708	3.750	6.000
1.4	2.448	2.553	5.428

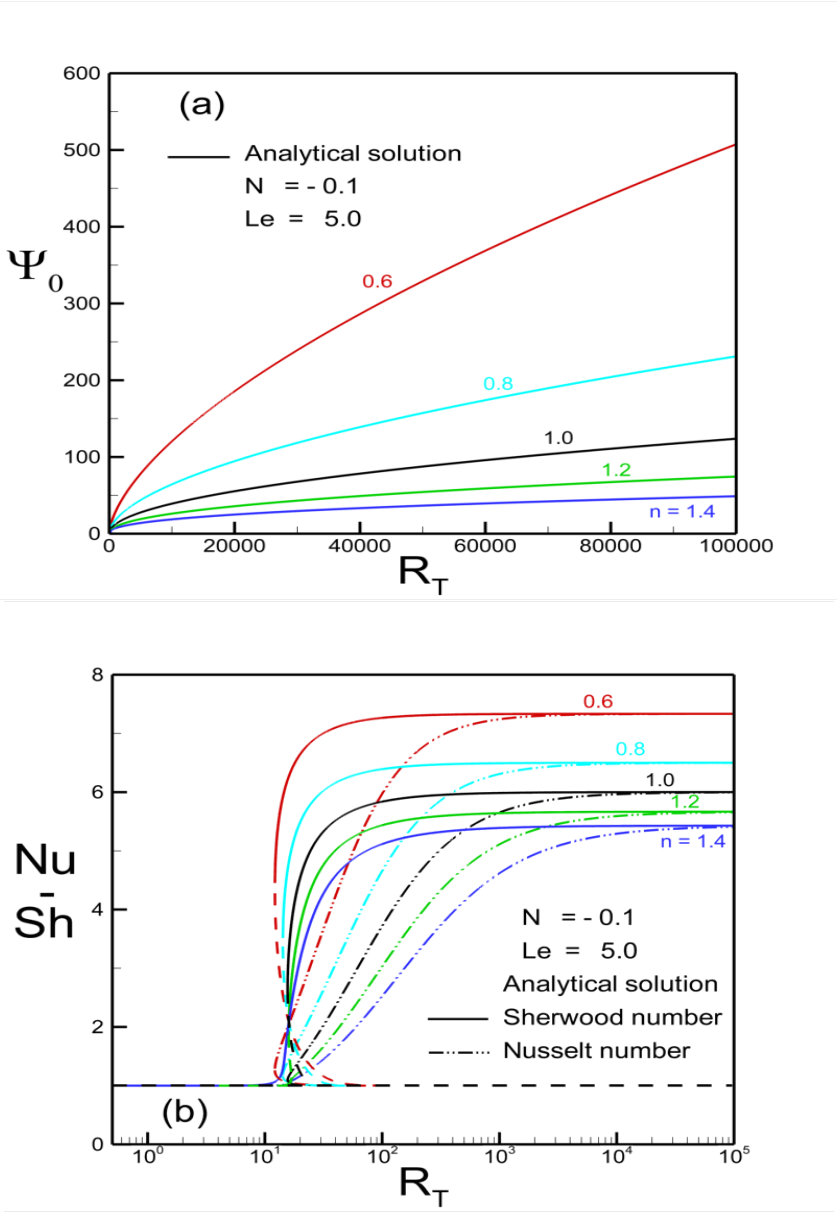


Figure 6.13: Large Rayleigh number R_T and power-law index n effects on (a) the flow intensity Ψ_0 and (b) the Nusselt Nu and Sherwood Sh number.

Figures 6.13(a) and (b) illustrate how the stream function, Ψ_0, Nusselt number, Nu, and Sherwood number, Sh, vary with R_T and n for a fixed Le value of 5 and N of -0.1. The solid lines on the graphs represent the predictions derived from the analytical solution presented in this study. The outcomes for the R_T range spanning from 0 to 100 and various values of power-

law index n have been previously addressed (see for instant Figure 6.4). Figure 6.13(a) illustrates, as expected, the intensity of convective, Ψ_0, increasingly rises with both R_T and n. However, as depicted in Figures 6.13(b), it becomes evident that for high R_T values, both the Nusselt number, Nu, and the Sherwood number, Sh, approach a stable constant value determined by only the power-law index, n, irrespectively of Le and N. The results indicate that when $R_T \to +\infty$, $Nu(Sh) \to 7.33; 6.50; 6.00; 5.66; 5.42$ for $n = 0.6; 0.8; 1.0; 1.2; 1.4$ respectively.

we can find these values by substitution of various values of the power-law index, n, in Equation (3.19).

An alternative way to show the impact of buoyancy ratio, N, on the intensity of flow, Ψ_0, as well as heat, Nu, and mass, Sh, transfers rate, was investigated concerning the power-law index n. The buoyancy ratio, N, ranged from 3 to -0.5. The findings are depicted in Figure 6.14. For a given value of n, and as N rises, there is an augmentation in the intensity of flow, Ψ_0. Likewise, with increasing n, the intensity of flow, Ψ_0, is minimal for shear-thickening fluids, whereas it increases for small values of n in shear-thinning fluids. Figures 6.14(b) and (c) depict the trend of Nu and Sh as they escalate with N. When n declines from 1.4 to 0.6, Nu and Sh gradually approach an asymptotic value contingent upon N, ranging from 3 to -0.5. This phenomenon arises from the heightened volumetric forces within the momentum equation. Furthermore, the augmented buoyancy ratio amplifies both heat and mass transfer. Notably, mass transfer attains its maximum asymptotic value more rapidly compared to heat transfer. This discrepancy is directly linked to the Lewis number ($Le = 5$) affecting mass transfer, particularly as n diminishes, transitioning from shear-thickening fluids ($n = 1.4$) to shear-thinning fluids ($n = 0.6$).

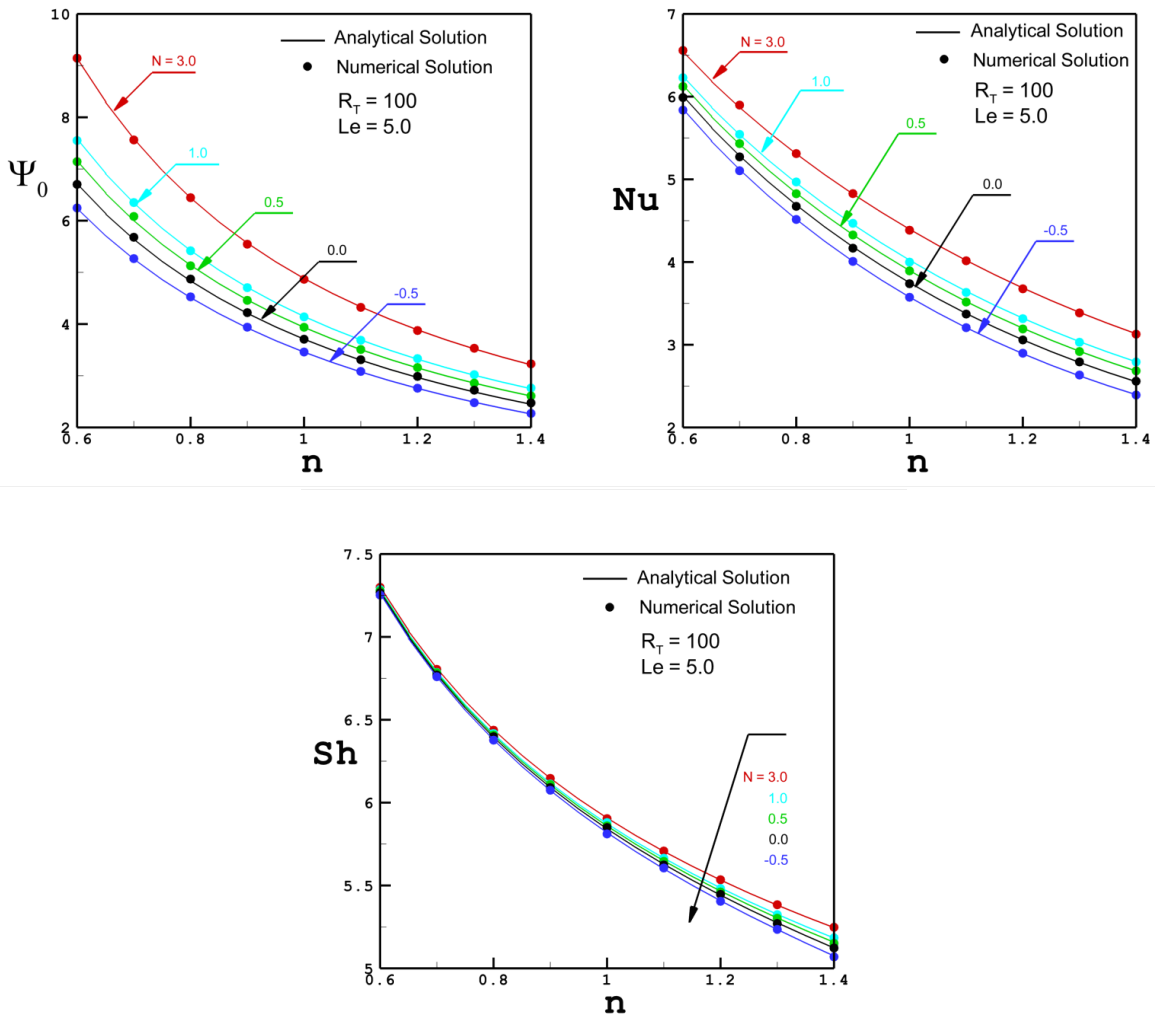


Figure 6.14: Effect of the power-law index, n, and the buoyancy ratio, N, on: (a) the flow intensity at the center of the cavity Ψ_0, (b) the Nusselt number, Nu, and (c) the Sherwood number, Sh, for $R_T = 100$, $Le = 5$.

4.1.2 CASE OF SQUARE CAVITY: $A = 1$

In this section, we examine the scenario of a square cavity with $A = 1$, under the influence of constant temperature and concentration gradients. The vertical walls of the cavity are adiabatic and impermeable, whereas the horizontal walls experience Neumann-type boundary conditions for both thermal and solutal aspects (constant heat and concentration fluxes), alongside Dirichlet-type conditions (imposed constant temperature and concentration). Given the absence of an analytical model for this setup, all findings presented herein are projections derived from the numerical code detailed in Chapter 4.

The streamlines, Ψ, temperature, T, concentration, S, and apparent viscosity, μ_a, computed numerically for $R_T = 100$, $Le = 5$, and $N = -0.1$, across different values of the power-law index, n (0.6, 1.0, and 1.4), are depicted in Figures (6.15), and (6.16) under Neumann-type and Dirichlet-type boundary conditions, respectively. The impact of the power-law index, n, under Neumann-type boundary conditions as depicted in Figure 6.15 reveals a uniform distribution of streamlines with designated increments, $\Delta\Psi$, reaching its highest value, Ψ_{max}, near the center and ending at zero at the borders. Moreover, the increase in the power-law index, n, from $n = 0.6$ to $n = 1.4$ substantially diminishes the intensity of convective motion within the porous layer, as evidenced by the stream function value at the cavity's center: $\Psi_0 = 5.317$ for $n = 0.6$, $\Psi_0 = 3.145$ for $n = 1.0$, and $\Psi_0 = 2.064$ for $n = 1.4$.

The isotherms and iso-concentration lines, which exhibit less distortion, suggest that heat and mass transfer tend towards diffusive behavior. Consequently, as depicted in Figure. 6.15, both temperature and concentration gradients are significantly suppressed with an increase in n, leading to the emergence of parallel constant temperature and concentration lines. For instance, at these conditions, $Nu = 4.783$ and $Sh = 9.699$ for $n = 0.6$, $Nu = 2.929$ and $Sh = 7.380$ for $n = 1.0$, and $Nu = 1.897$ and $Sh = 5.776$ for $n = 1.4$.

The apparent viscosity, μ_a, lines exhibit a consistent distribution from the center, where $\mu_a = 11.909$ for $n = 0.6$, $\mu_a = 1.000$ for $n = 1.0$, and $\mu_a = 0.132$ for $n = 1.4$, to the cavity edges.

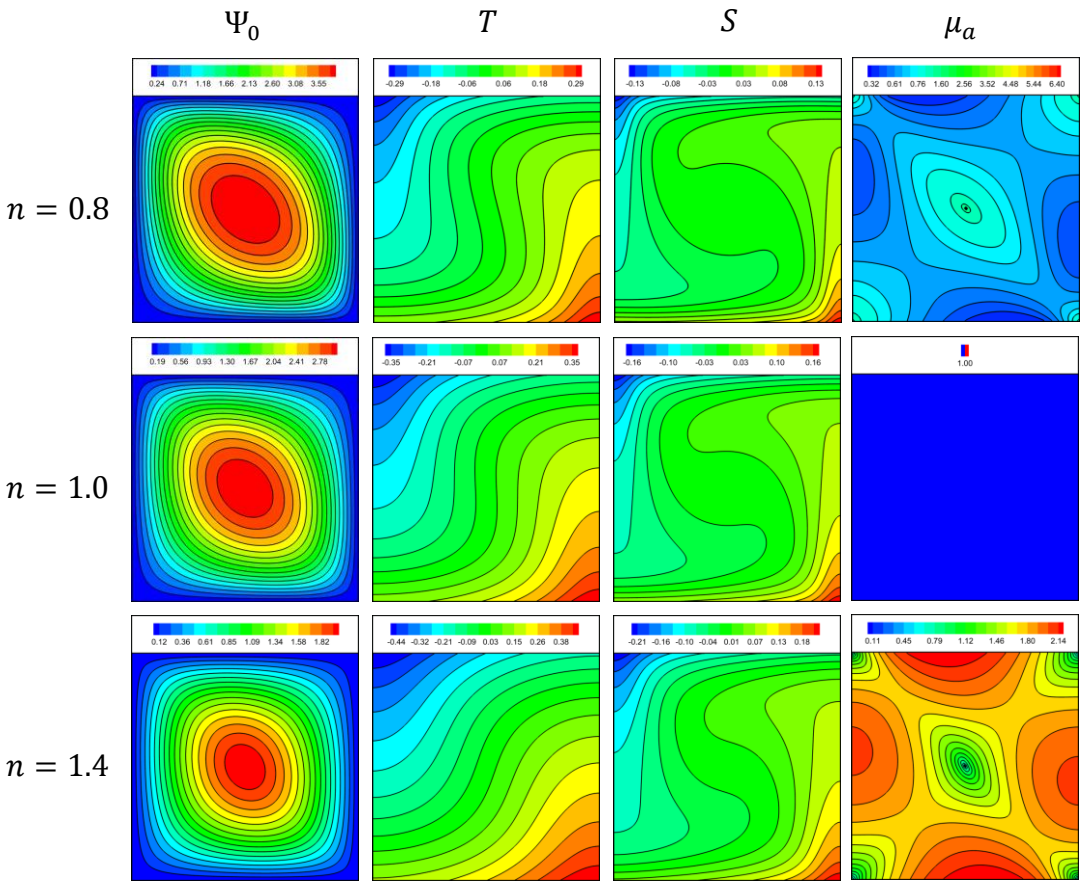


Figure 6.15: Contours of streamlines, Ψ, Temperature, T, Concentration, S, horizontal velocity, U, and apparent viscosity, μ_a, for $R_T = 100$, $Le = 5$, $N = -0.1$ and various values of n, with Neumann-type boundary conditions

Figure 6.16 presents similar results to Figure 6.15, showcasing streamlines, Ψ, temperature, T, concentration, S, and apparent viscosity, μ_a. However, it's notable that when applying Neumann boundary conditions, the values of stream function, temperature, concentration, and apparent viscosity are lower compared to applying Dirichlet boundaries. For instance, for $n = 0.6$, $\Psi_0 = 12.766$, $Nu = 5.946$and $Sh = 12.955$, and $\mu_a = 10.761$; for $n = 1.0$, $\Psi_0 = 5.123$, $Nu = 2.736$and $Sh = 6.445$, and $\mu_a = 1.000$; and for $n = 1.4$, $\Psi_0 = 2.016$, $Nu = 1.371$ and $Sh = 3.442$, and $\mu_a = .037$.

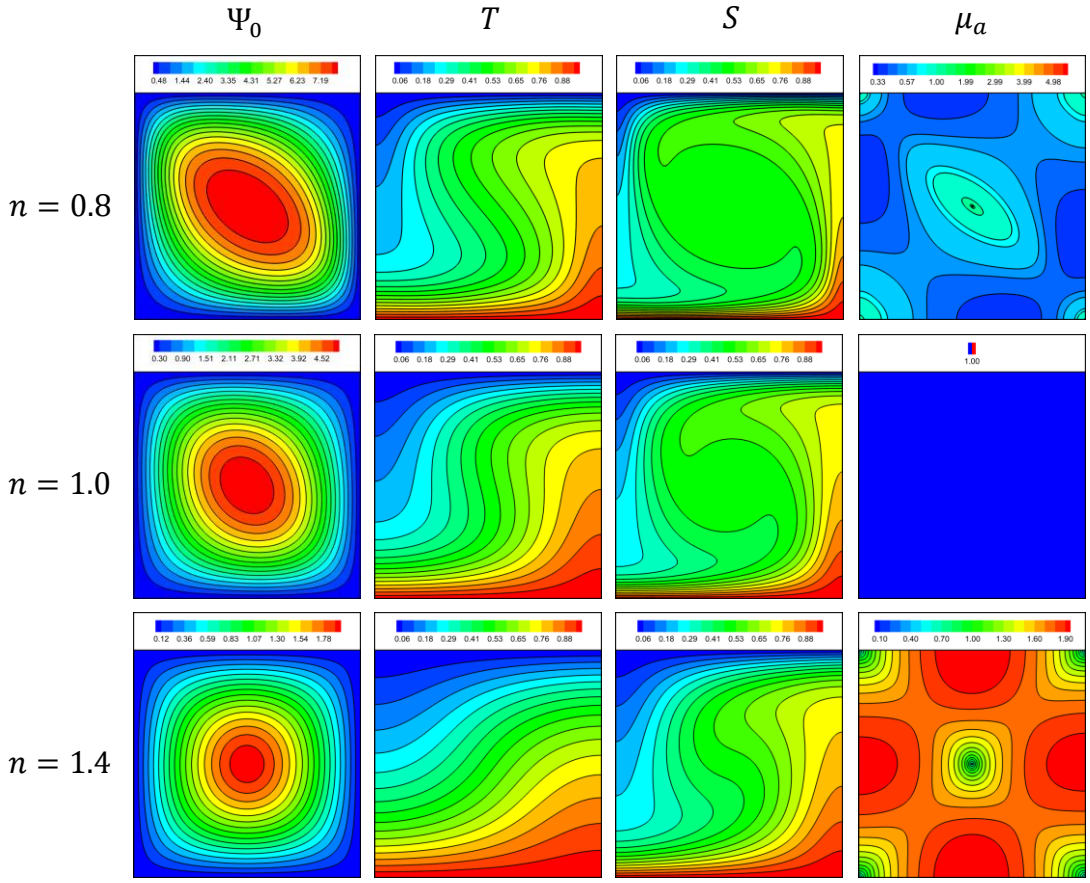


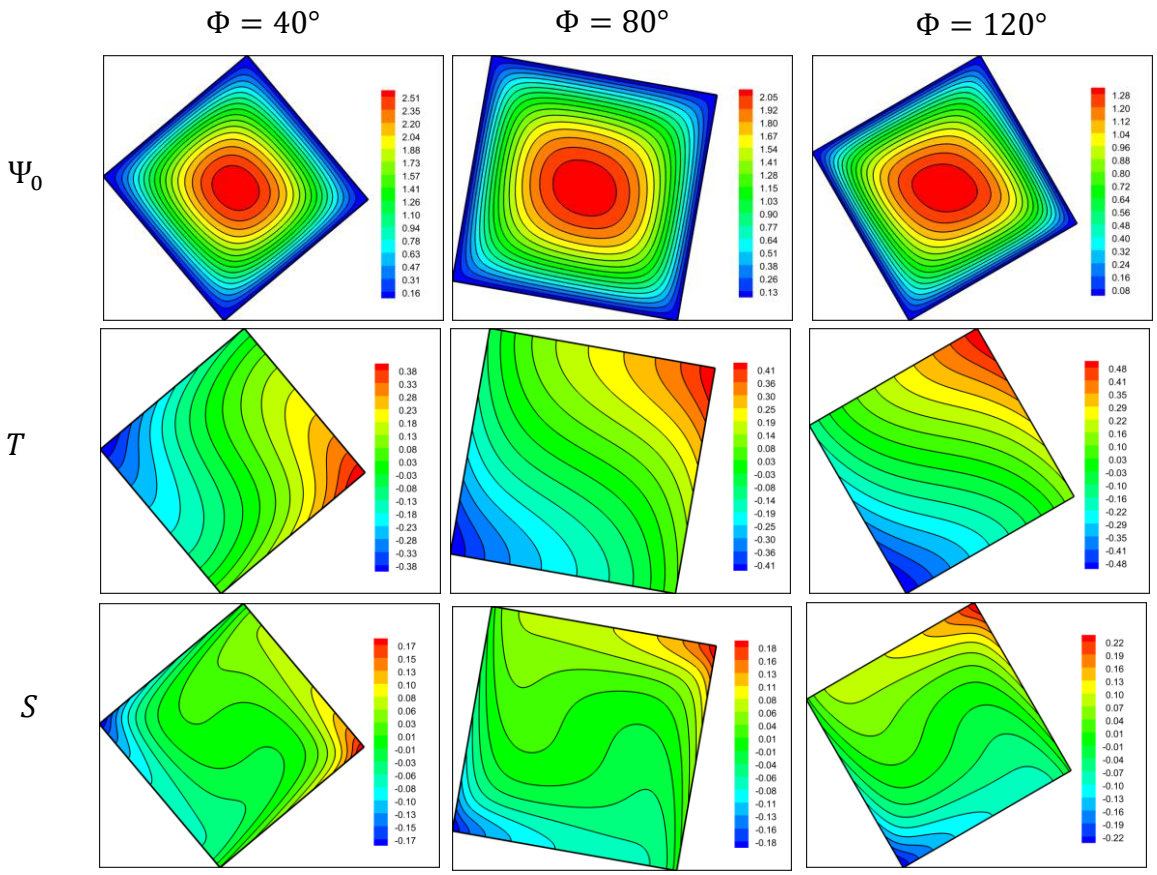
Figure 6.16: Contours of streamlines, Ψ, Temperature, T, Concentration, S, horizontal velocity, U, and apparent viscosity, μ_a, for $R_T = 100$, $Le = 5$, $N = -0.1$ and various values of n, with Dirichlet-type boundary conditions

Figures (6.17) and (6.18) portray the numerically computed streamlines, Ψ, temperature, T, concentration, S, and apparent viscosity, μ_a, for $R_T = 100$, $Le = 5$, $N = -0.1$, and $n = 1.2$, spanning various inclination angles, Φ, from 0° to 180°. These figures illustrate the influence of Φ under both Neumann-type and Dirichlet-type boundary conditions, showcasing consistent trends in the contours of stream function, temperature, concentration, and apparent viscosity.

The streamlines exhibit a uniform distribution with specified increments, ΔΨ, peaking at its maximum value, Ψ_{max}, near the center and diminishing to zero at the perimeters. Additionally, an increase in the inclination angle, Φ, notably reduces the intensity of convective motion within the porous layer, indicated by the stream function value at the center of the cavity: $\Psi_0 = 2.668$ for $\Phi = 40°$, $\Psi_0 = 2.181$ for $\Phi = 80°$, and $\Psi_0 = 1.361$ for $\Phi = 120°$ under Neumann-type boundary conditions, and $\Psi_0 = 4.363$ for $\Phi = 40°$, $\Psi_0 = 3.703$ for $\Phi = 80°$, and $\Psi_0 = 2.211$ for $\Phi = 120°$ under Dirichlet-type boundary conditions.

The isotherms and iso-concentration lines display a uniform distribution between the maximum temperature, T_{max}, and the minimum temperature, T_{min}, as well as between the maximum concentration, S_{max}, and the minimum concentration, S_{min}. Consequently, both temperature and concentration gradients are notably attenuated with an increase in Φ. For example, under these circumstances, the Nusselt number, Nu, and Sherwood number, Sh, take specific values: under Neumann-type boundary conditions $Nu = 2.679$ and $Sh = 7.882$ for $\Phi = 40°$, $Nu = 2.328$ and $Sh = 7.829$ for $\Phi = 80°$, and $Nu = 1.594$ and $Sh = 6.242$ for $\Phi = 120°$. Similarly, under Dirichlet boundary conditions, these values are: $Nu = 2.124$ and $Sh = 5.354$ for $\Phi = 40°$, $Nu = 1.800$ and $Sh = 4.824$ for $\Phi = 80°$, and $Nu = 1.334$ and $Sh = 3.681$ for $\Phi = 120°$.

The apparent viscosity, represented by $\mu_a$lines, displays a uniform distribution from the center to the cavity edges. Specifically, μ_a values are observed to be 0.312 for $\Phi = 40°$, 0.230 for $\Phi = 80°$, and 0.132 for $\Phi = 120°$ under Neumann-type boundary conditions, and for a Dirichlet boundary conditions $\mu_a = 0.205$ for $\Phi = 40°$, $\mu_a = 0.439$ for $\Phi = 80°$, and $\mu_a = 0.332$ for $\Phi = 120°$. However, it is noteworthy that when applying Neumann boundary conditions, the stream function and the apparent viscosity values are lower compared to when using Dirichlet boundaries, The converse holds for the temperature and concentration.



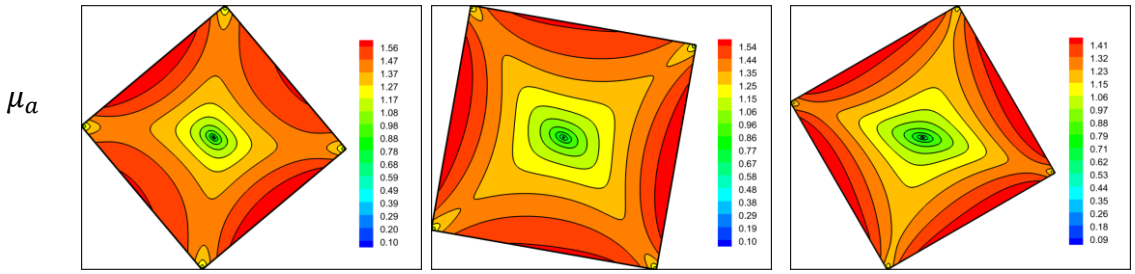


Figure 6.17: Contours of streamlines, Ψ, Temperature, T, Concentration, S, horizontal velocity, U, and apparent viscosity, μ_a, for $R_T = 100$, $Le = 5$, $N = -0.1$, $n = 1.2$ and various values of Φ, with Neumann-type boundary conditions

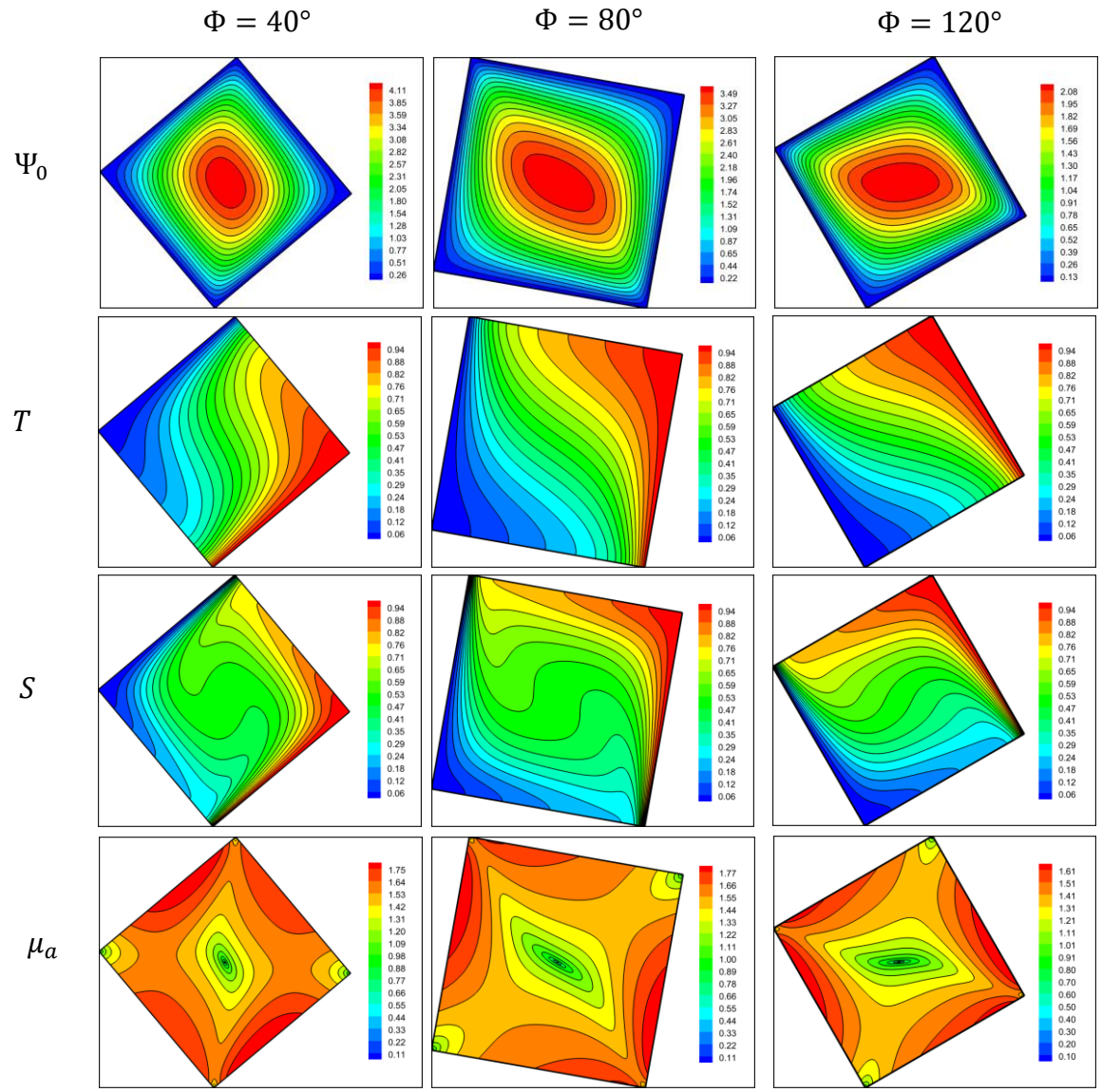


Figure 6.18: Contours of streamlines, Ψ, Temperature, T, Concentration, S, and apparent viscosity, μ_a, for $R_T = 100$, $Le = 5$, $N = -0.1$, $n = 1.2$ and various values of Φ, with Dirichlet-type boundary conditions

Figure 6.19 presents the numerical results of the profiles of the stream function, Ψ, the horizontal velocity, U, the apparent viscosity, μ_a, temperature, T, and concentration, S, under a Neumann-type boundary conditions, obtained at the centre of the cavity ($x = 0$), for different values of power-law index, n, respectively. For: $R_T = 100$, $N = -0.1$, $Le = 5$, and $\Phi = 0°$. As shown in Figure 6.19 (a), the intensity of the flow increases with the decrease in the power-law index, while the fluid becomes increasingly shear-thinning. Hence, there is a preference for the circulation of flux within the cavity. A comparable pattern is noted in relation to the horizontal velocity U, as illustrated in figure 6.15 (b) which diminishes with the rise in the power-law index, n. Furthermore, it's worth mentioning that the horizontal velocity U is more prominent at the cavity border and absent in the central area. Notably, in the case of a Newtonian fluid, the velocity distribution adheres to a linear configuration.

The representation of apparent viscosity in Figure 6.19(c) illustrates a declining pattern as the power-law index, n, decreases. This indicates a decrease in the prominence of convective motion when the fluid demonstrates shear-thickening behavior ($n > 1$). Conversely, contrasting effects are noted for shear-thinning fluids ($n < 1$), while it remains consistently constant ($\mu_a = 1$) for Newtonian fluids ($n = 1$).

Figure 6.19 (d) illustrates that with a decrease in the power index, n, the temperature between the horizontal walls diminishes, leading to a notable rise in the convective heat transfer rate, represented by the Nusselt number. This trend is similarly observed in the concentration profiles depicted in Figure 6.19(e). It's noted that the disparity in concentration between the two horizontal walls diminishes significantly, enhancing mass transfer, represented by the Sherwood number.

Figure 6.20 exhibits a pattern similar to that of Figure 6.19, under Dirichlet-type boundary conditions, with certain distinctions worth mentioning. Notably, the values of stream function Ψ, horizontal velocity U, apparent viscosity μ_a, temperature T, and concentration S under Neumann-type boundary conditions are lower compared to those under Dirichlet-type boundary conditions. The temperature and concentration values are set to 1 at the bottom wall of the cavity, in accordance with adherence conditions.

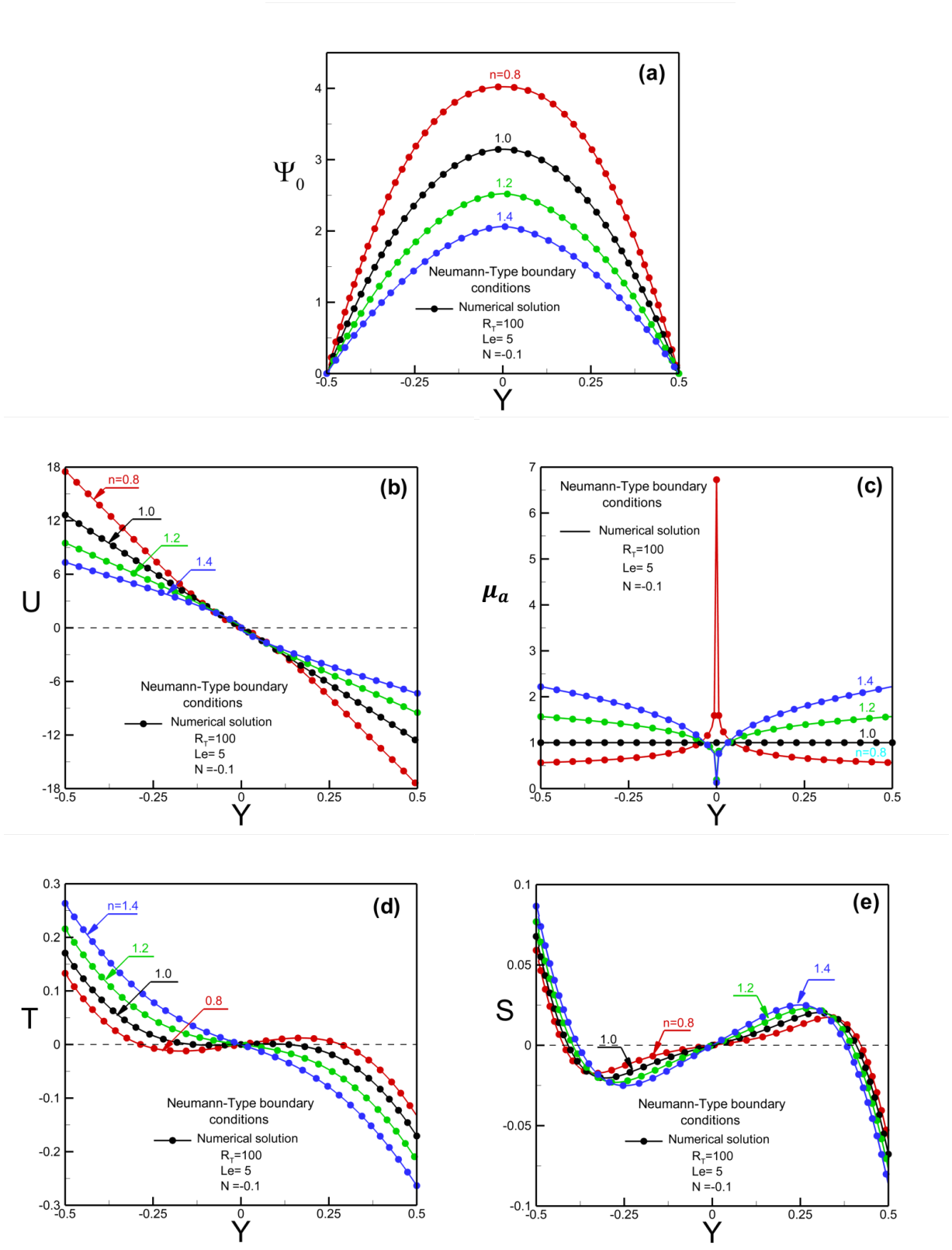


Figure 6.19: Effect of the power-law index, n, on the profiles of (a) the horizontal velocity, U, (b) apparent viscosity, μ_a, (c) temperature, T, and (d) concentration, S, under Neumann-type boundary conditions

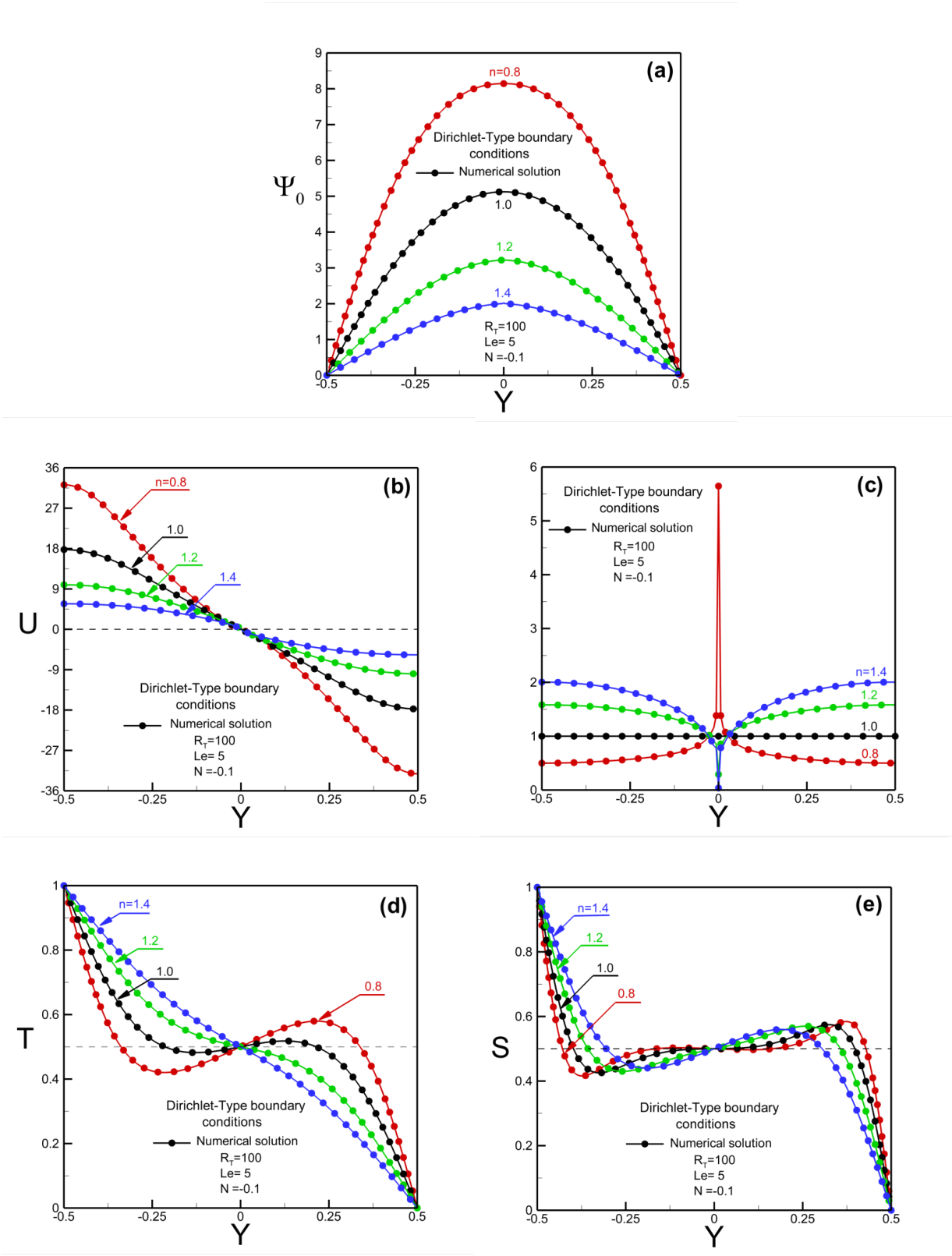


Figure 6.20: Effect of the power-law index, n, on the profiles of (a) the horizontal velocity, U, (b) apparent viscosity, μ_a, (c) temperature, T, and (d) concentration, S, under Dirichlet-type boundary conditions

Figure 6.21 illustrates the impact of the inclination angle, Φ, on the intensity of flow, Ψ_0, the Nusselt number, Nu, and the Sherwood number, Sh, under Neumann-type boundary conditions. The investigation is conducted for $R_T = 100$, $Le = 5$, $N = -0.1$, and varying values of the power-law index, n. The curves depicted in the graphs represent the predictions of the current numerical nonlinear models. The results brightly demonstrate that Φ profoundly influences the strength of convection and subsequent heat and mass transfer. It is evident that as the inclination angle decreases from 180° to 0°, the intensity of flow Ψ_0, Nusselt Number Nu, and Sherwood number Sh initially increase, reaching their peaks at approximately $\Phi \approx 20°$, $\Phi \approx 45°$, and $\Phi \approx 60°$, respectively, before declining. The impact of the power-law index, n, on the stream function, Ψ_0, Nusselt Number Nu, and Sherwood number Sh is depicted in Figures 6.21(a)-6c), considering values of n ranging from 0.6 to 1.4. Generally, it is observed from Figure 6.21(a) that an increase in n, for a given Φ, notably diminishes the intensity of convective motion. Consequently, both heat and mass transfer rates are significantly impeded with higher values of n, as depicted in Figures 6.21(b) and 6.21(c).

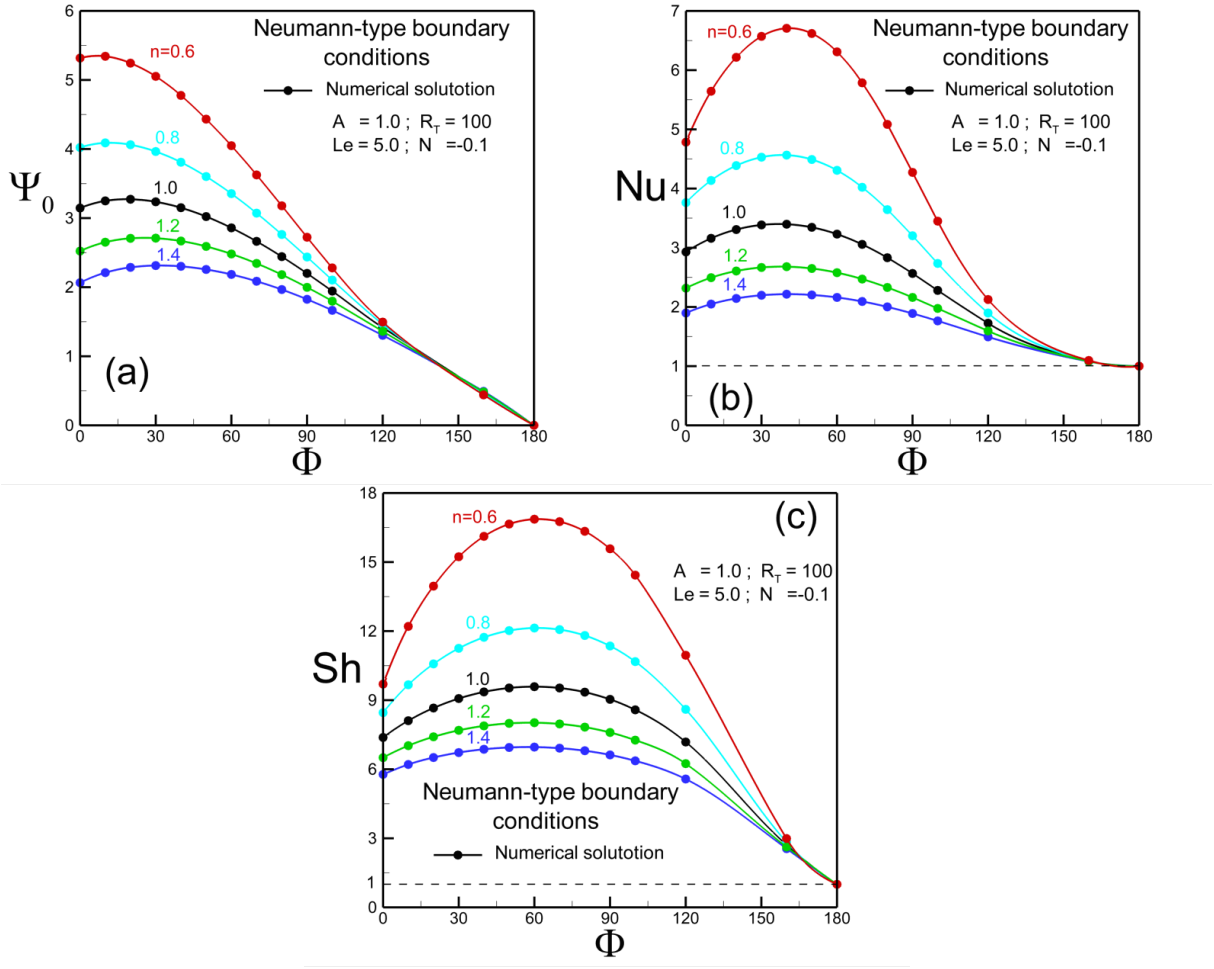


Figure 6.21 Effects of the inclination angle, Φ, and the power-law index, n, for $R_T = 100$, on: (a) stream function at the center of the cavity Ψ_0, (b) Nusselt number Nu, and (c) Sherwood number Sh. exposed to Neumann-type boundary conditions.

Employing identical governing parameters as illustrated in Figure 6.21, Figure 6.22 portrays characteristic outcomes for an enclosure exposed to Dirichlet-type boundary conditions. Furthermore, it showcases the influences of the power-law index, n, and the inclination angle, Φ. Analogous to the observations in Figure 6.21, where Neumann boundary conditions are applied, comparable conclusions and insights emerge. Specifically, for shear-thinning fluids ($n < 1$), the magnitudes of the stream function, Ψ_0, Nusselt number, Nu, and Sherwood number, Sh, under Dirichlet-type boundary conditions are notably greater than those under Neumann-type boundary conditions.

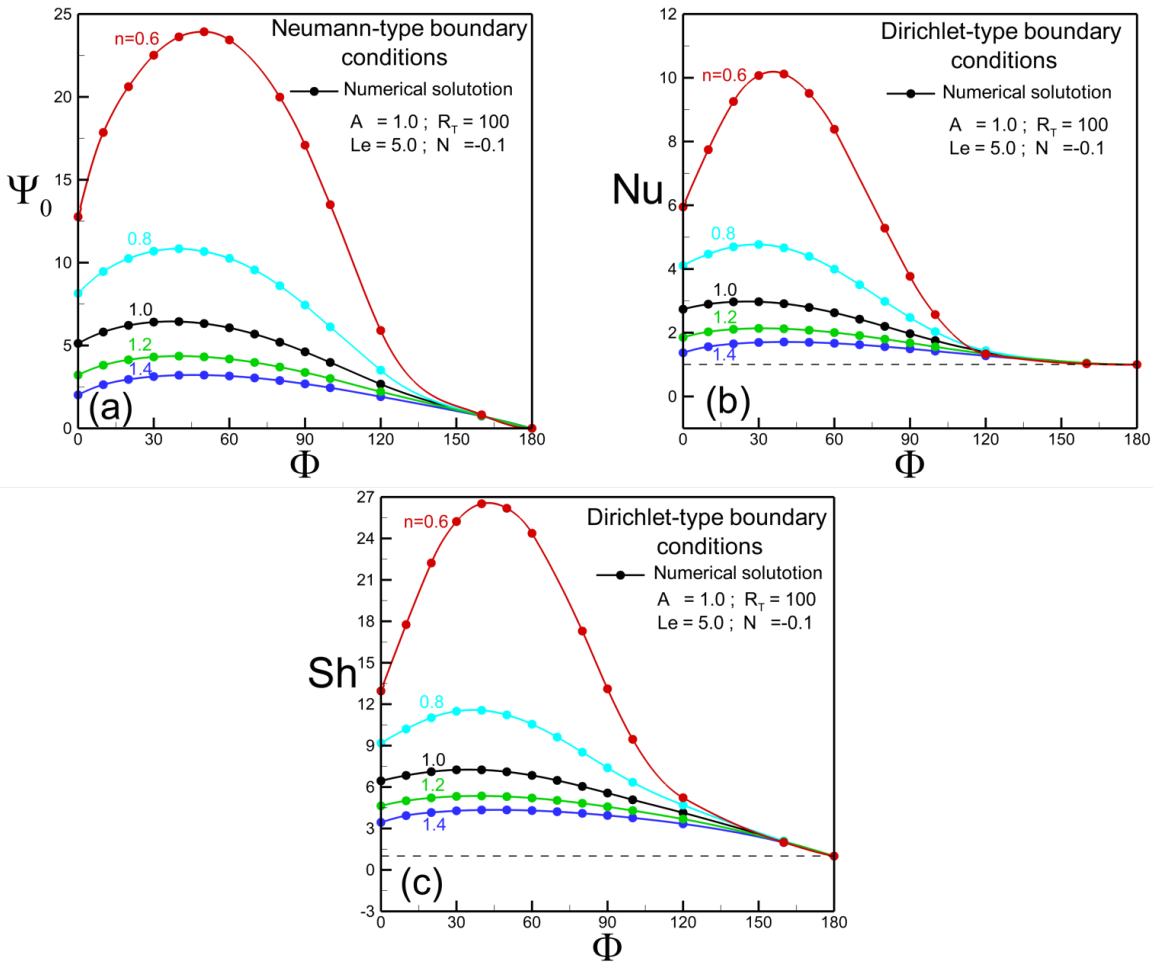
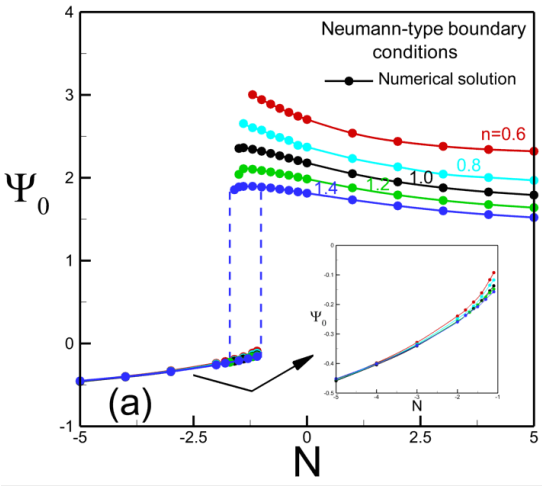
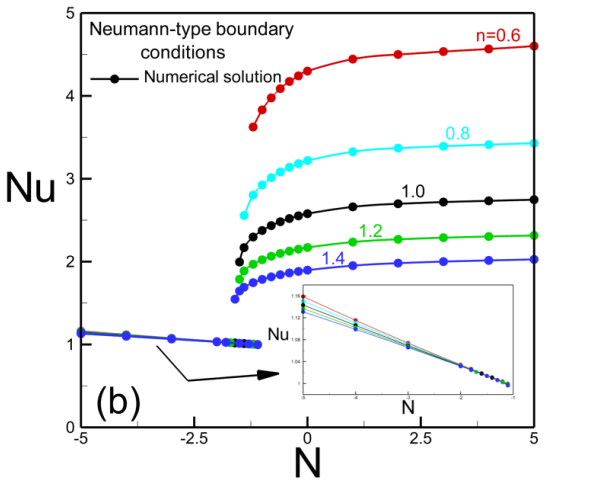


Figure 6.22 Effects of the inclination angle, Φ, and the power-law index, n, for $R_T = 100$, on: (a) stream function at the center of the cavity Ψ_0, (b) Nusselt number Nu, and (c) Sherwood number Sh. exposed to Dirichlet-type boundary conditions.

For $R_T = 100$, $Le = 5$, $\Phi = 90°$, and different values of the power-law index, n, Figures 6.23(a)-(c) depict the influence of the buoyancy ratio, N, on the intensity of flow, Ψ_0, the Nusselt number, Nu, and the Sherwood number, Sh, under Neumann-type boundary conditions. The buoyancy ratio varies between –5 and 5, covering aiding solutal-dominated flow ($N = 5$), fully thermally dominated flow ($N = 0$), and opposed but solutal-dominated flow ($N = -5$). As the power-law index, n, rises, Figure 6.23(a)-(c) illustrate a declining trend in the intensity of flow, the Nusselt number, and Sherwood number for a given value of buoyancy ratio, N. This trend persists irrespectively of aiding or opposing flow. The streamlines depicted in Figure 6.23(a) reveal that under conditions of simple diffusion (i.e., $N = 0$), convective motion arises solely from temperature gradients, leading to a counter-clockwise thermal circulation ($\Psi_0 > 0$). The flow behavior, as shown in Figure 6.23(a), is highly dependent on whether the buoyancy ratio is higher or lower than the critical buoyancy ratio, $N_{cr} = -1.2, -1.4, -1.5, -1.5, -1.6$, respectively, for $n = 0.6, 0.8, 1.0, 1.2, 1.4$. For these values of N_{cr}, the thermal effects continue to predominate, resulting in Ψ_0 being positive, as shown in Figure 6.23(d.1). The flow circulation becomes clockwise ($\Psi_0 < 0$) when N is smaller than -1, as indicated by the streamlines in Figure 6.23(d.2). At this point, the heat and solute buoyant forces are in opposition to one another. It is observed that for values of N between -1 and N_{cr} there is tow stable solution for each value of, n, and there is a transition of flow from counter-clockwise to a clockwise as depicted in figure 6.23(d).





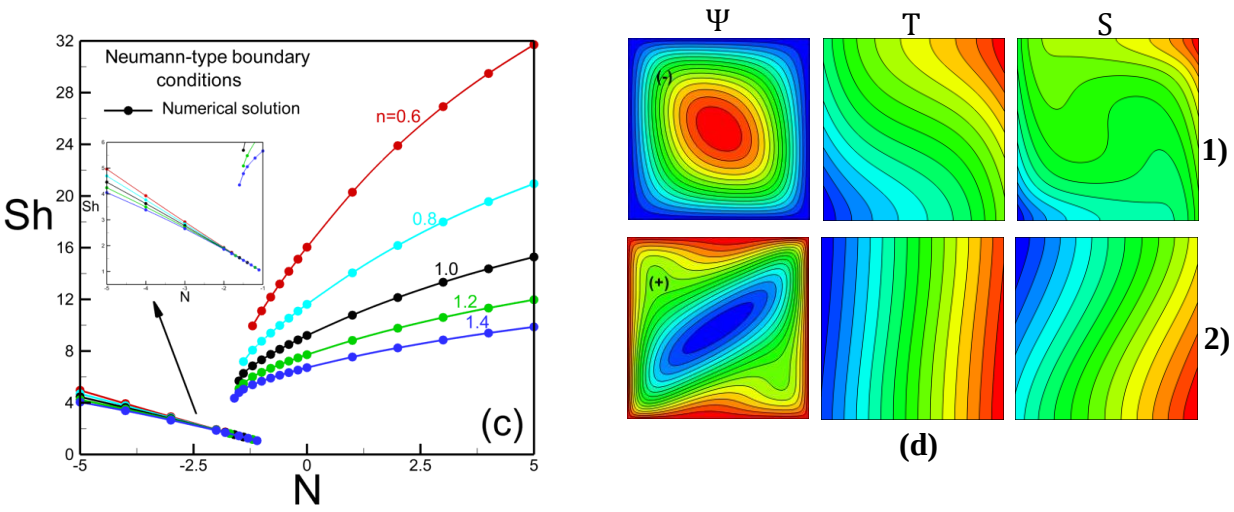
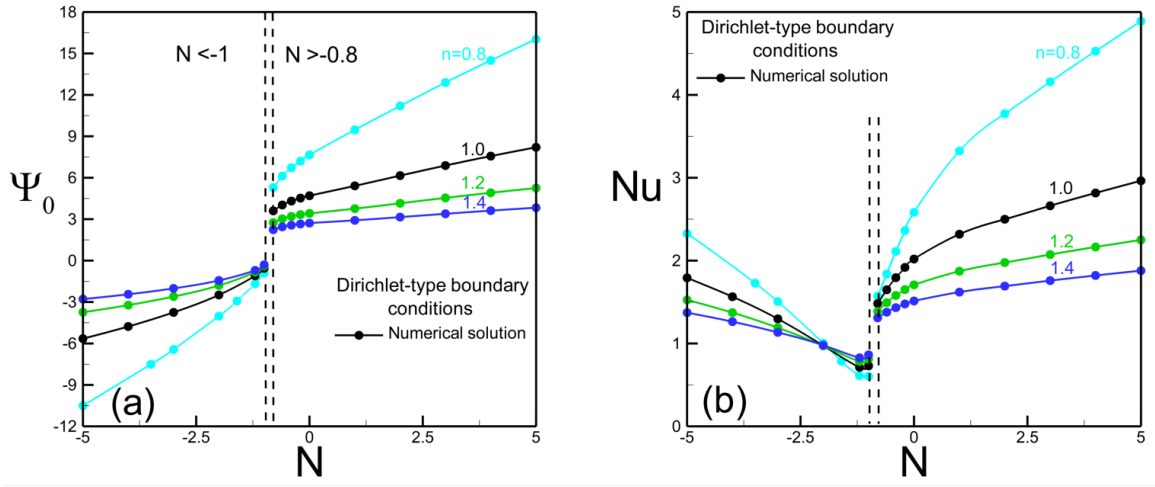


Figure 6.23: Effects of the buoyancy ratio, Nu, and the power-law index, n, for $R_T = 100$, and $Le = 5$, on: (a) stream function at the centre of the cavity Ψ_0, (b) Nusselt number Nu, and (c) Sherwood number Sh. exposed to Neumann-type boundary conditions

Using the same governing parameters as in Figure 6.23, Figure 6.24 illustrates the effects of the buoyancy ratio, N, and the power-law index, n, for a cavity subjected to Dirichlet-type boundary conditions. Moreover, it is worth noting that each figures contains two curves one start from $N = -0.8$ to 5 which represent a counter-clockwise motion as illustrated by Figure 6.24(a) and 6.24(d.1), and the other start from $N = -1$ to -5 which represent a clockwise motion as illustrated by Figure 6.24(a) and 6.24(d.2). It is intriguing to note that for all the values we looked at, the values of flow intensity Ψ_0, Nu, and Sh tend to rise as the absolute values of N grow. It is found that when the power-law index, n, is increased, the strength of fluid movement, the Nusselt number Nu and the Sherwood number Sh, decreases.



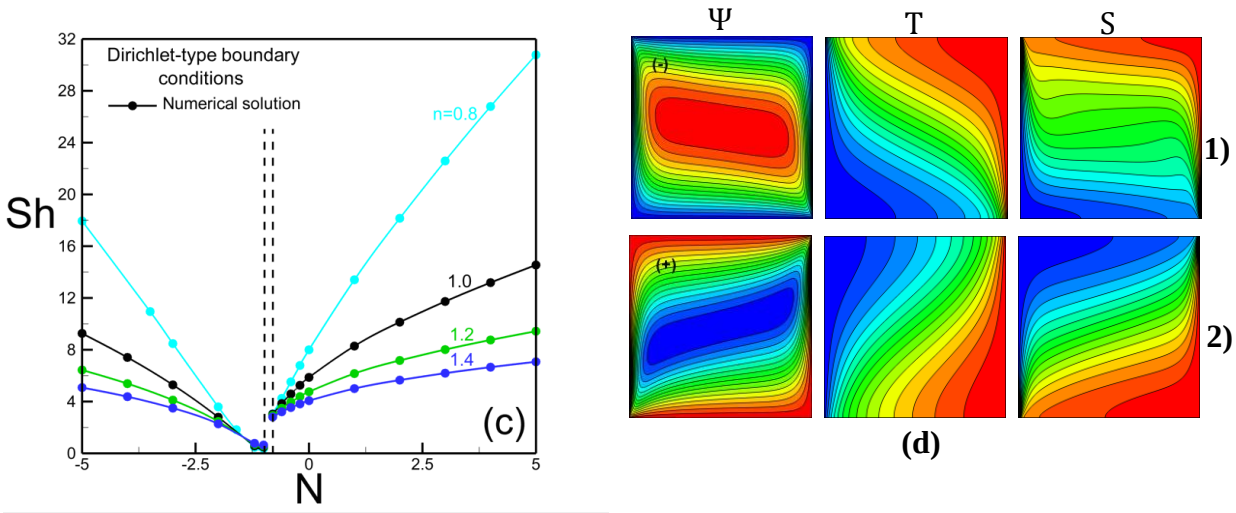


Figure 6.24: Effects of the buoyancy ratio, Nu, and the power-law index, n, for $R_T = 100$, and $Le = 5$, on: (a) stream function at the centre of the cavity Ψ_0, (b) Nusselt number Nu, and (c) Sherwood number Sh. exposed to Neumann-type boundary conditions

In the case of shallow enclosures, the asymptotic/numerical nonlinear theories' prediction of the convective flow's rheological behavior is highly useful in understanding the shapes of the bifurcation curves and in guiding the investigation of alternative flow configurations, in the absence of asymptotic or analytical solutions. Within this segment, we examine a square enclosure ($A = 1$) that has inflexible bounds. As a result, the outcomes shown below are the predictions of the numerical solution of the full governing equations. Figures 6.25(a)-(c) depict the numerical outcomes of various convective flow bifurcations, presenting flow intensities Ψ_0, Nusselt number Nu, and Sherwood number Sh as functions of R_T under Neumann boundary conditions for distinct values of the power-law index, n. The solid lines in the plots result from a curve fitting process applied to the numerical data, while the dotted-dashed lines are introduced manually to delineate the hypothetical unstable bifurcation branches. As illustrated in Figures 6.25(a)-(c), the observed trends align qualitatively with prior results as illustrated in Figure 6.4. within the context of a shallow enclosure. The flow intensity, Nusselt number, and Sherwood number exhibit a diminishing trend with increasing power-law index. In the case of shear-thinning fluids, the regime consistently remains supercritical. Conversely, for shear-thickening fluids, the bifurcation curves transition from a supercritical behavior to a bistability convective state as the power-law index, n, decreases. This behavior is exemplified by the curve shown in the inset of Figure 6.25(a) for $n = 1.1$, featuring two stable branches connected by an unstable branch (dashed-dotted line). Illustrative representations of streamlines, isotherms,

isoconcentrates, and contours of apparent viscosity, acquired for $R_T = 35$, are depicted in Figures 6.25(d) and (e). Notably, two distinct solutions coexist under identical governing parameter values. The solution portrayed in Figure 6.25(d), representing the upper stable branch, can be derived by initiating the numerical simulation with finite amplitude flow as initial conditions, following the hysteresis loop denoted by arrows along the bifurcation curves for $n = 1.1$. Conversely, the solution corresponding to the lower stable branch, as shown in Figure 6.25(e), is attained by commencing the numerical procedure from a pure conduction state as the initial condition.

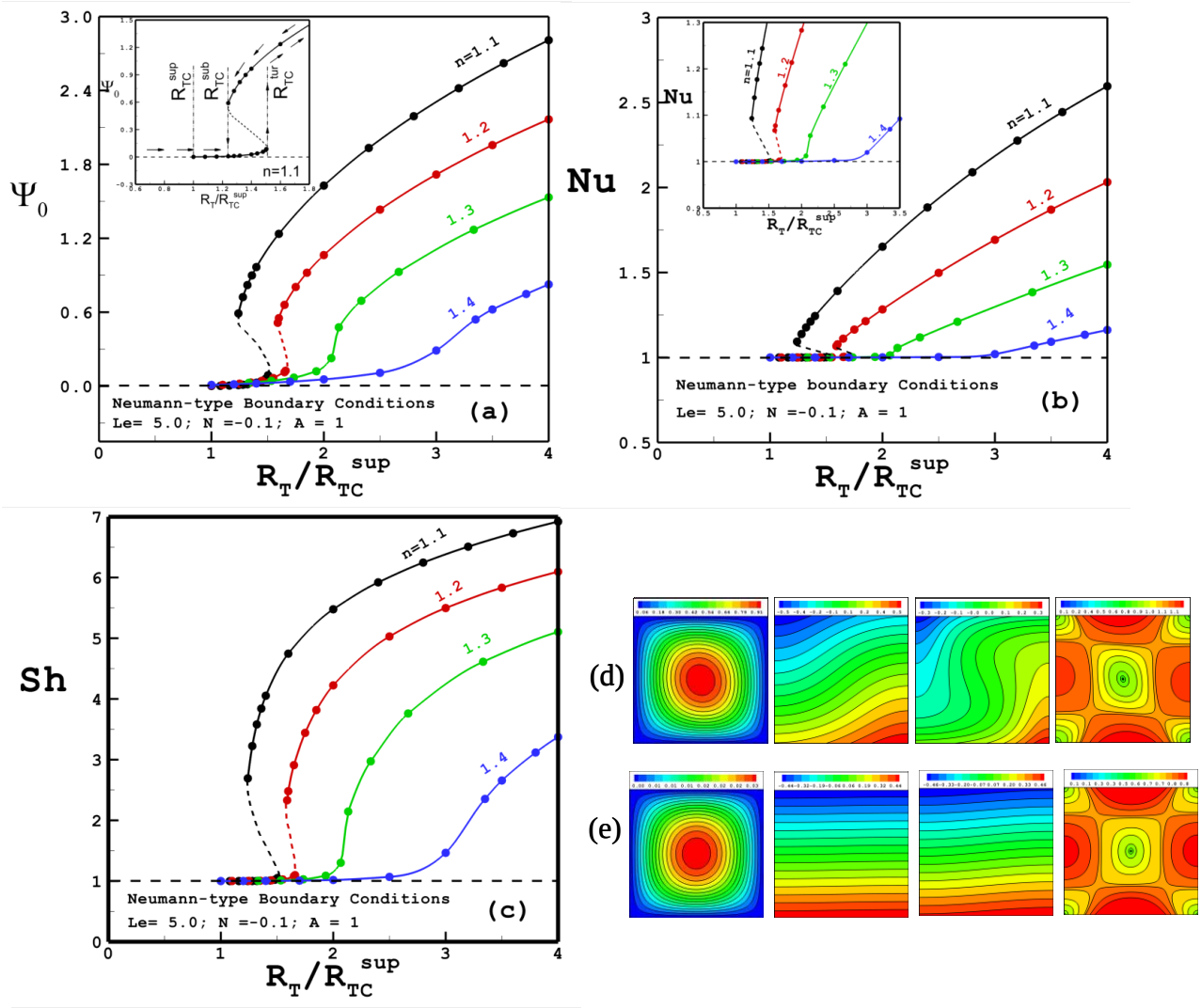


Figure 6.25: Bifurcation diagram in terms of Ψ_0, Nu, and Sh as a function of R_T and n for $A = 1$, $Le = 5$, $N = -0.1$: [(a)–(c)] $n = 0.8$ to 1.4.(d) Contours of streamlines, temperature, concentration, and apparent viscosity for $R_T = 35$, $n = 1.1$: $\Psi_0 = 0.9664$, $Nu = 1.2439$, $Sh = 4.0523$, and $\mu_a = 0$ (upper solution). (e) Contours of streamlines, temperature, concentration, and apparent viscosity for $R_T = 35$, $n = 1.1$: $\Psi_0 = 0.0277$, $Nu = 1.0003$, $Sh = 1.0098$, and $\mu_a = 0$ (lower solution) (for Neumann boundary conditions).

Figure 6.26 presents representative outcomes for an enclosure subjected to Dirichlet-type thermal and solutal boundary conditions, employing the same governing parameters as used in Figure 6.25. The influence of the shear-thickening effect is also showcased. Similar to the case with Neumann boundary conditions in Figure 6.25, comparable remarks and observations can be extended to the results, leading to consistent conclusions affirming the presence of Bistability convection for Dirichlet thermal and solutal boundary conditions. This affirmation is supported by the bifurcation curves depicted in Figures 6.26(a)-(c) and the presentation of two distinct numerical solution flow patterns in Figures 6.26(d)-(e) for $n = 1.1$ and $R_T = 66$. The impact of shear-thickening on bistability convection and heat transfer rate behaviors, as evidenced in both Figures 6.25 and 6.26, closely aligns with observations reported for a shallow enclosure with Neumann boundary conditions.

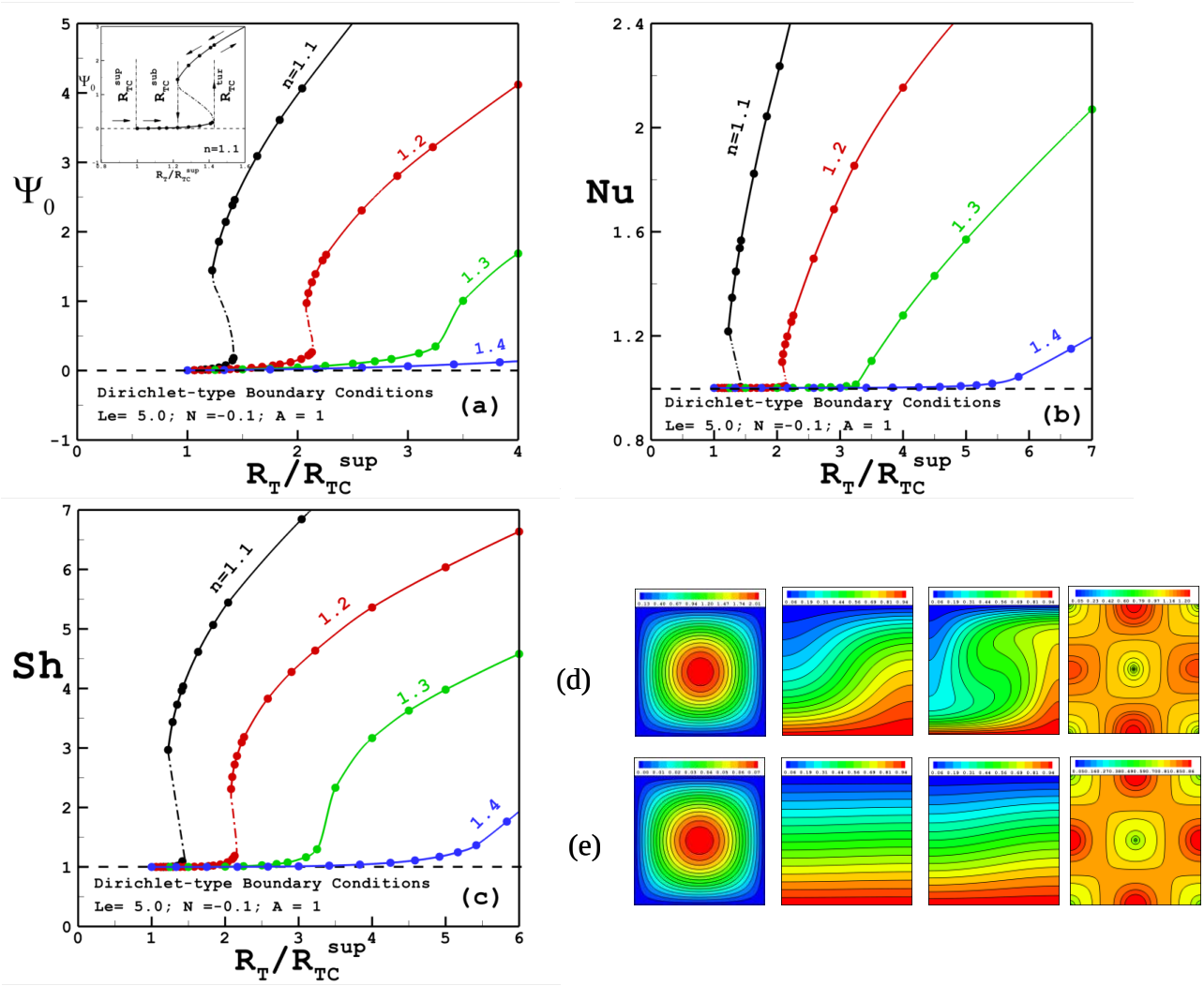


Figure 6.26: Bifurcation diagram in terms of Ψ_0, Nu, and Sh as a function of R_T and n for $A = 1$, $Le = 5$, $N = -0.1$: [(a)–(c)] $n = 1.1$ to 1.4.(d) Contours of streamlines, temperature, concentration, and apparent viscosity for $R_T = 66$, $n = 1.1$: $\Psi_0 = 2.1419$, $Nu = 1.4471$,

$Sh = 3.7272$, and $\mu_a = 0.4986$ (upper solution). (e) Contours of streamlines, temperature, concentration, and apparent viscosity for $R_T = 66$, $n = 1.1$: $\Psi_0 = 0.0767$, $Nu = 1.0007$, $Sh = 1.0177$, and $\mu_a = 0.4227$ (lower solution) (for Dirichlet boundary conditions).

Table. 3 provides a detailed plot of the critical Rayleigh numbers (R_{TC}^{sub}, R_{TC}^{tur}, and R_{TC}^{sup}) as a function of the power-law index, n, which indicate the onset of motion. This table clearly shows that, under both Neumann-type (left) and Dirichlet-type (right) boundary conditions, the power-law index, n, has a considerable impact on bi-stability convection.

Table 6.7: Dependence of R_{TC}^{sub}, R_{TC}^{tur} and R_{TC}^{sup} on n for $Le = 5.0$ and $N = -0.1$.

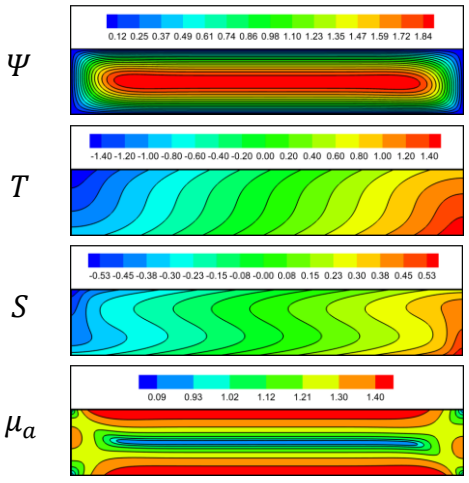
	Neumann-type boundary conditions			**Dirichlet-type boundary conditions**		
$\boldsymbol{n}$	R_{TC}^{sub}	R_{TC}^{tur}	R_{TC}^{sup}	R_{TC}^{sub}	R_{TC}^{tur}	R_{TC}^{sup}
1.1	31	37.6	27	60	69.5	45
1.2	31.8	33.2	18	64.5	66	25
1.3	-	-	12	-	-	16
1.4	-	-	7	-	-	12

6.2 INCLINED LAYER: $-180° \leq \Phi \leq +180°$

The analysis of double-diffusive convection in the considered porous layer is characterized by the specification of several parameters, including the Rayleigh number R_T, the power-law index n, the inclination angle of cavity Φ, the buoyancy ratio N, and the Lewis number Le. The semi-analytical solution provides predictions that are verified by numerical analyses of the full governing equations for a tall cavity ($A >> 1$). The study encompasses a range of parameters: 0.4 to 1.8 for n, which include shear-thinning ($n < 1$) and shear thickening ($n > 1$) fluids, -180 to 180 for Φ, 10^{-2} to 10 for Le, and -5 to 5 for N.

Figure. 6.27-6.28 presents the contours of streamlines, Ψ, Temperature, T, Concentration, S, and apparent viscosity, μ_a, obtained numerically, for a fluid with power-law index, $n = 1.2$, and different angle of iclination $\Phi = 0,60$, and 120 presented in figure. 6.27(a)-(c), and for $\Phi = 45$, and different liquids with power-law index of $n = 0.6$ and 1.4 and for a Newtonian fluid ($n = 1$) presented in Fig6.28(a)-(c), at $R_T = 50$, $Le = 5$, and $N = -0.1$. The intensity of flow, Ψ_0, in the core region of the enclosure is essentially parallel while the temperature T, and the concentration S in the core of the cavity are linearly stratified in the x direction, the apparent viscosity, μ_a, lines are uniformly distributed between the center, and the edges of the cavity and the extremum value, and it's clearly constant when n=1.

The numerical findings depicted in Figure. 6.27-6.28 validate the theoretical assumption of parallel flow, indicating that the flow patterns within the central region of the cavity remain parallel regardless of the power-law index, n, when the aspect ratio $A >> 6$. For this reason, most of the numerical results reported here were obtained for $10 \geq A \geq 6$ with typically 250×150 mesh points



(a)

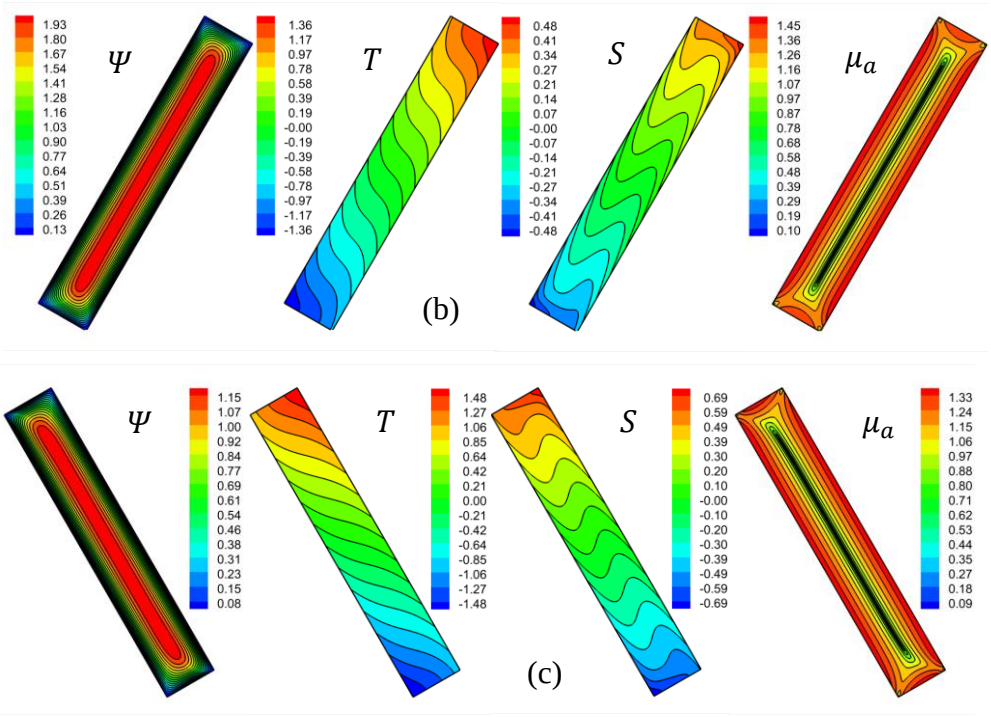


Figure 6.27: Numerical solutions for streamlines, isotherms, isoconcentration, and apparent viscosity with $R_T = 50$, $n = 1.2$, $Le = 5$, $N = -0.1$ and $A = 6$ for (a) $\Phi = 0°$, (b) $\Phi = 60°$, (c) $\Phi = 120°$.

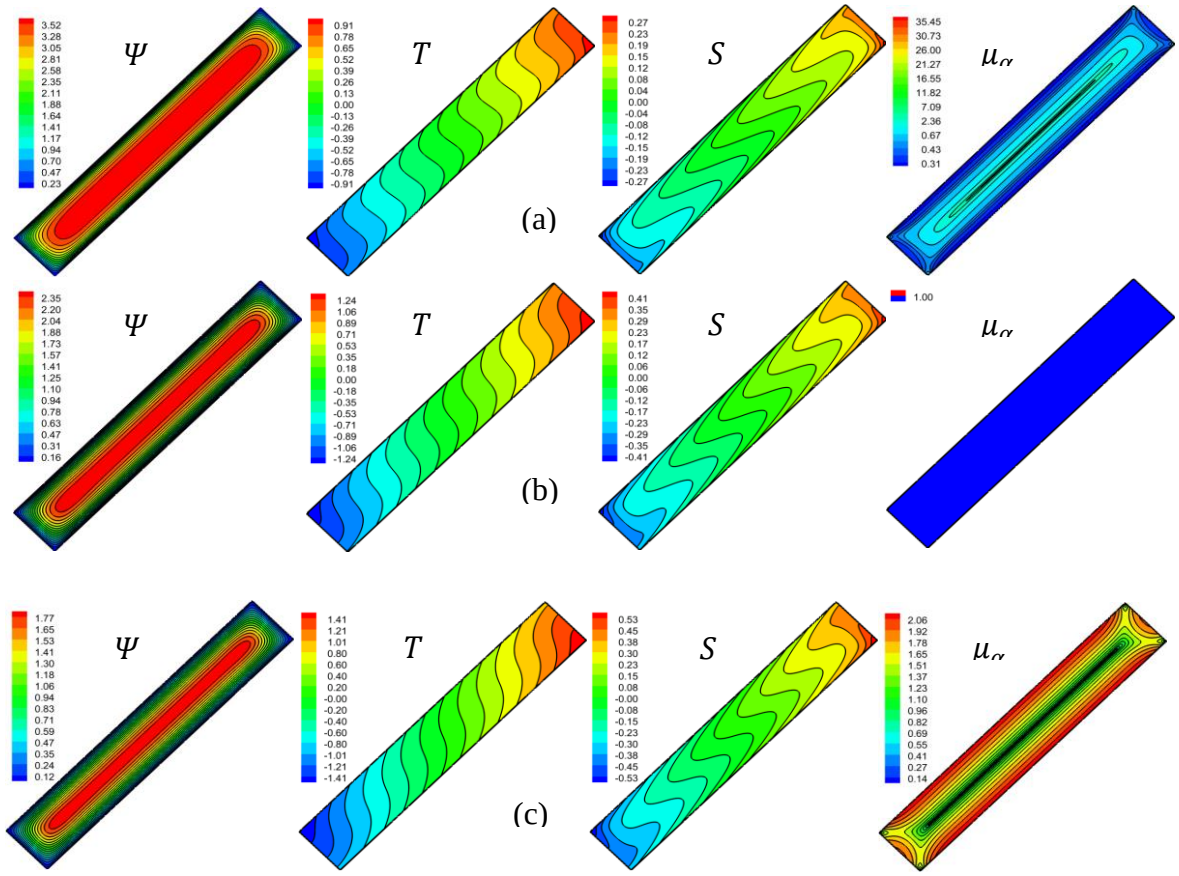
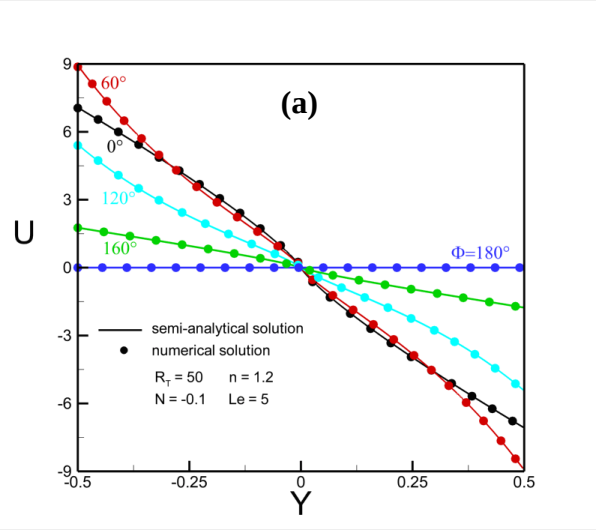
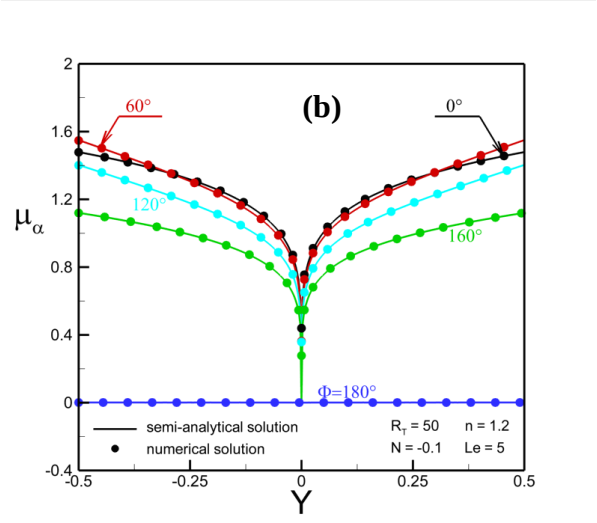


Figure. 6.28: Streamlines, isotherms, isoconcentration, and apparent viscosity for (a) $R_T = 50$, $n = 0.6$, $\Phi = 45$, (b) $R_T = 50$, $n = 1.0$, $\Phi = 45$, (c) $R_T = 50$, $n = 1.4$, $\Phi = 45$.

Figures 6.29(a)-(d) depict profiles of horizontal velocity U, apparent viscosity μ_a, temperature T, and concentration S at the center of the layer $x = 0$ for specified values of $R_T = 50$, $Le = 5$, $N = -0.1$, $n = 1.2$, and varying inclination angles Φ. The results are showcased within the range $-0.5 \leq y \leq 0.5$. The semi-analytical solution, depicted by solid lines, closely aligns with the numerical results, represented by solid circles, thereby indicating a favorable agreement between the current semi-analytical approach and the numerical solution. Figure 6.28 illustrates a rise in velocity concurrent with an increase in the inclination angle Φ until it reaches the maximal angle Φ_{max} (refer to Figure. 6.30). Subsequently, commencing from this angle, the velocity begins to decline as the inclination angle Φ increases until it diminishes entirely at $\Phi = 180°$. This phenomenon arises from the amplification of the inclination angle, resulting in the gradual dissipation of both temperature and mass gradients. A similar trend is observed concerning the apparent viscosity μ_a, which decreases until the cessation of convective motion at $\Phi = 180°$. Additionally, it's noteworthy that the apparent viscosity μ_a is more pronounced at the cavity edges and absent in the central region due to the fluid exhibiting dilatant behavior with a power-law index of $n = 1.2$. In Figures 6.29(c)-(d), it is evident that the temperature and concentration profiles demonstrate a growth with the increasing inclination angle, Φ. Additionally, at $\Phi = 180°$ show a linear behavior of temperature and concentration due to the absence of temperature and mass gradient.





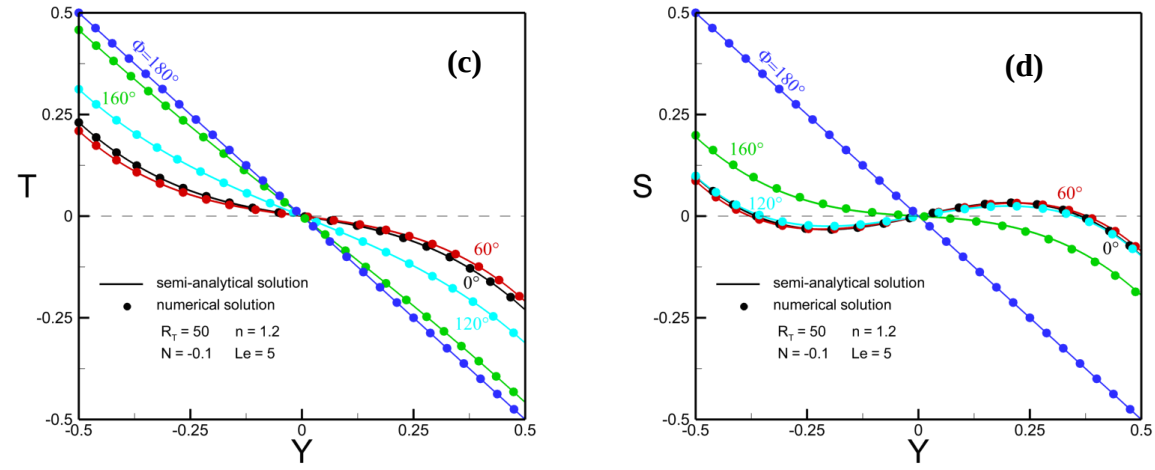


Figure 6.29: Effect of inclination angle, Φ, on (a) the horizontal velocity, U, (b) apparent viscosity, μ_a, (c) temperature, T, and (d) concentration, S.

The effects of the inclined angle, Φ, and the power-law index, n, on the strength of convection Ψ_0, the heat transfer rate, Nu, and the solute transfer rate, Sh, is presented in Figure 6.30(a)-(c) for $R_T = 50$, $Le = 5$ and $N = -0.1$. Results are obtained for values of the power-law index, n, between 0.6 to 1.4. The curves depicted in the graphs are the predictions of the present asymptotic/numerical nonlinear models. The solid lines correspond to stable branches, while the dashed-dotted-dotted lines denote unstable branches. The numerical solutions derived from the complete governing equations are depicted using solid circles. Remarkably, a noteworthy concordance is evident between the outcomes generated by these two nonlinear theories. Initially, it is apparent that concerning the strength of convection Ψ_0 curve, either the upper or lower half independently resembles half of a heart shape. Furthermore, regarding the Nusselt Nu and Sherwood Sh numbers, combining the first and second quadrants yields a butterfly-like shape, a phenomenon similarly noted by Sen et al. [3] and Alloui et al. [113]. In general, it is seen from Figures 6.30(a)-(c) that for a given inclined angle, Φ, both the strength of convection Ψ_0, the resulting heat transfer Nu, and solute transfer Sh decrease as the power-law index, n, increases, this aligns with the observations in Figures 6.31(c) and 6.31(b), where the substantial circulation diminishes C_T and C_S while augmenting Nu and Sh, as anticipated. The curve depicting the strength of convection, Ψ_0, indicates that the first and third (or second and fourth) quadrants delineate the natural (or antinatural) flows. Within the first (or third) quadrant, positive (or negative) Ψ_0 denotes counterclockwise (or clockwise) motion. The plot effectively demonstrates that as the inclination angle decreases from 180 to Φ_{CR}, as illustrated in the zoomed image in Figure 6.30(a), the strength of convection Ψ_0, the Nusselt number Nu, and

the Sherwood number Sh initially rise, reaching a peak at $\Phi = \Phi_{max}^{\Psi_0}$, Φ_{max}^{Nu}, and Φ_{max}^{Sh}, respectively, where $\Phi_{max}^{\Psi_0}$, Φ_{max}^{Nu}, and Φ_{max}^{Sh} are indicated in Fig. 6.30(d), and subsequently decline. At sufficiently large inclinations Φ, within a given configuration of governing parameters, the graph shows that the solutions for Ψ_0, Nu, and Sh are singular. For slight tilt angles Φ, two stable solutions and an unstable one are possible. Among the stable solutions, one is natural solution, while the other is antinatural solution

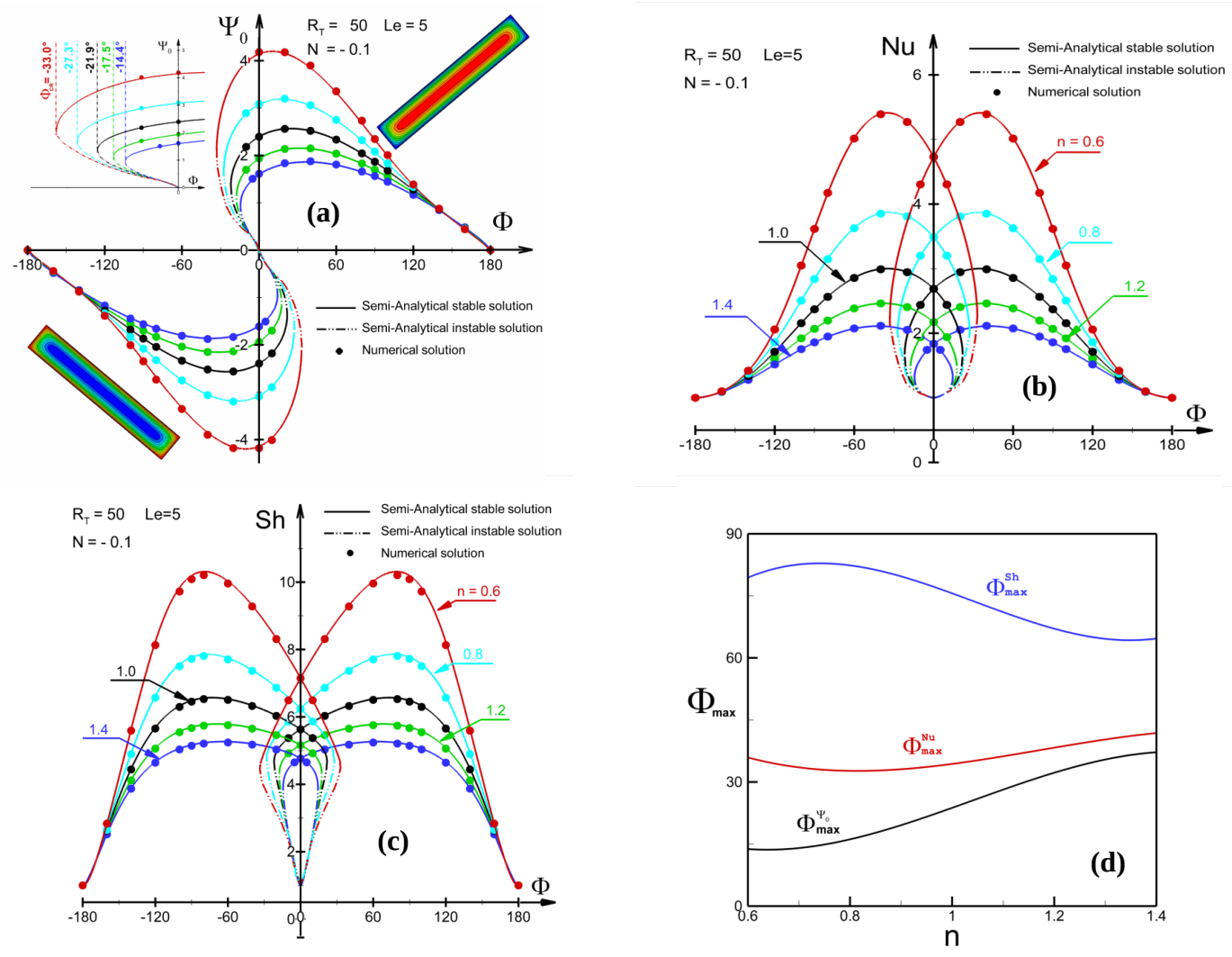
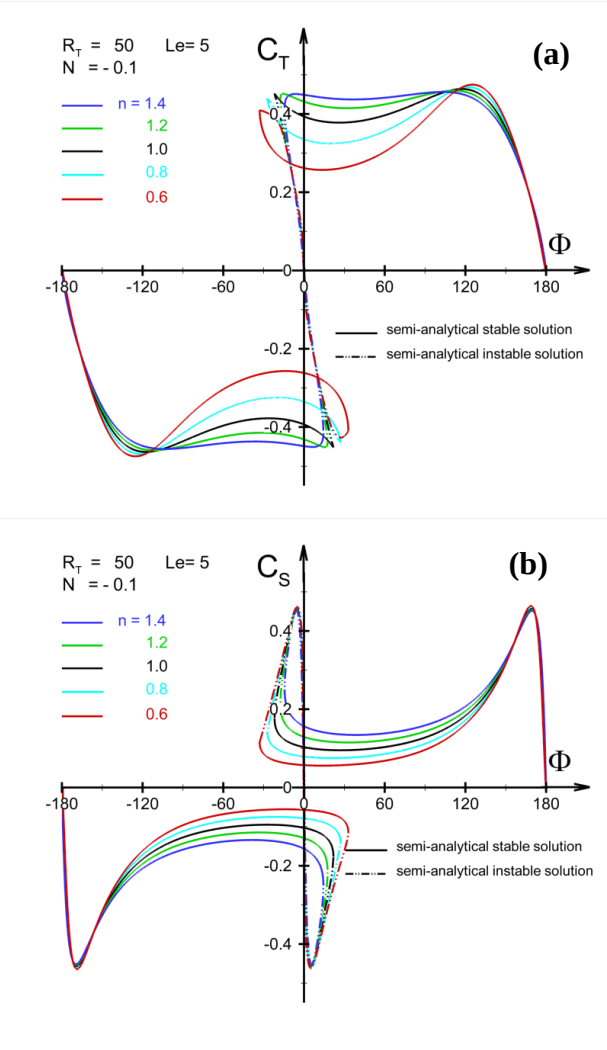


Figure 6.30: Effects of inclination angle Φ and power-law index n, for $R_T = 50$, on: (a) stream function at the center of the cavity Ψ_0, (b) Nusselt number Nu, and (c) Sherwood number Sh.

Figures 6.31(a)-(b) depict the values of C_T and C_S, representing the constant temperature and concentration gradient in the x-direction, respectively, for $R_T = 50$, plotted as functions of the inclination angle Φ and power-law index n. In the graph, solid lines corresponding to positive (negative) values of Φ indicate the natural (antinatural) solutions, while the dashed-dotted-

dotted lines represent the unstable solutions. The graphs clearly demonstrate that, for a fixed inclination angle Φ, the constant temperature and concentration gradients $C_T$and C_T, respectively, diminish consistently with a decrease in n. This conclusion aligns with the observations in Figures 6.29(b) and (c), where the substantial circulation diminishes C_T and C_S while augmenting Nu and Sh, as anticipated. Eventually, it is noted that the power-law index n additionally influences the range within which multiple solutions manifest. Hence, Figs. 6.30(a)-(c) and 6.31(a)-(b) illustrate that, for a specified value of n, multiple steady states are viable within the range of $-\Phi_{CR} < \Phi < \Phi_{CR}$. Fig. 6.31(c) illustrates the variation of the critical tilt angle Φ_{CR} relative to the power-law index n. It is observed that with an increase in the power-law index n, the interval of tilt angles conducive to multiple steady states diminishes notably. Specifically, when n exceeds 1.8 and falls below 0.4, Φ_{CR} assumes values of $\Phi_{CR} = -11.8$ and $\Phi_{CR} = -35$, respectively.



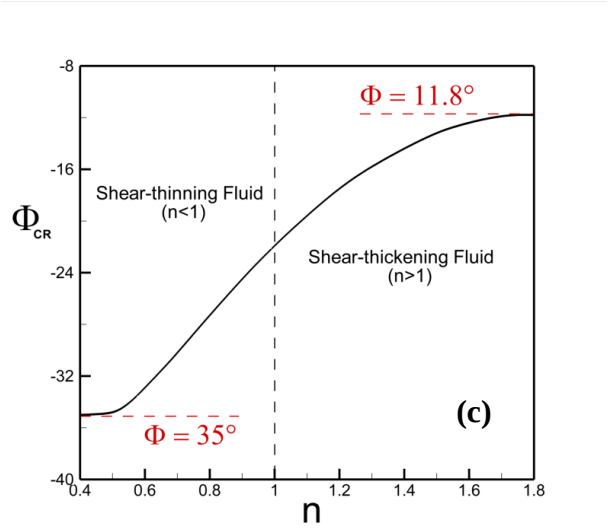


Figure 6.31: Effects of inclination angle Φ and power-law index n, for $R_T = 50$, on: (a) constant temperature gradient C_T, (b) constant concentration gradient C_S, and (c) maximum inclination angle Φ_{CR}

Figure 6.32(a)-(c) displays the variation of the strength convection Ψ_0, Nusselt number Nu, and Sherwood number Sh as a function of the power-law index n for $R_T = 50$, $Le = 5$ and $N = -0.1$, with various inclination angles Φ. The findings reveal that at inclination angles conducive to high natural convection strength ($\Phi = 0°$ and 60°), there is a notable decline in Ψ_0, Nu, and Sh as the power-law index n increases. Conversely, at significantly large Φ values (160° and 180°), where the strength of convection, heat transfer, and solute transfer are predominantly conductive, Ψ_0, Nu, and Sh remain constant regardless of the value of n. As depicted in Figure 8, the elevation of the power-law index n diminishes the strength of convection Ψ_0, heat and solute transfer, eventually leading to Ψ_0 approaching zero and Nu and Sh converging to 1 for sufficiently large n, irrespective of the layer's inclination angle.

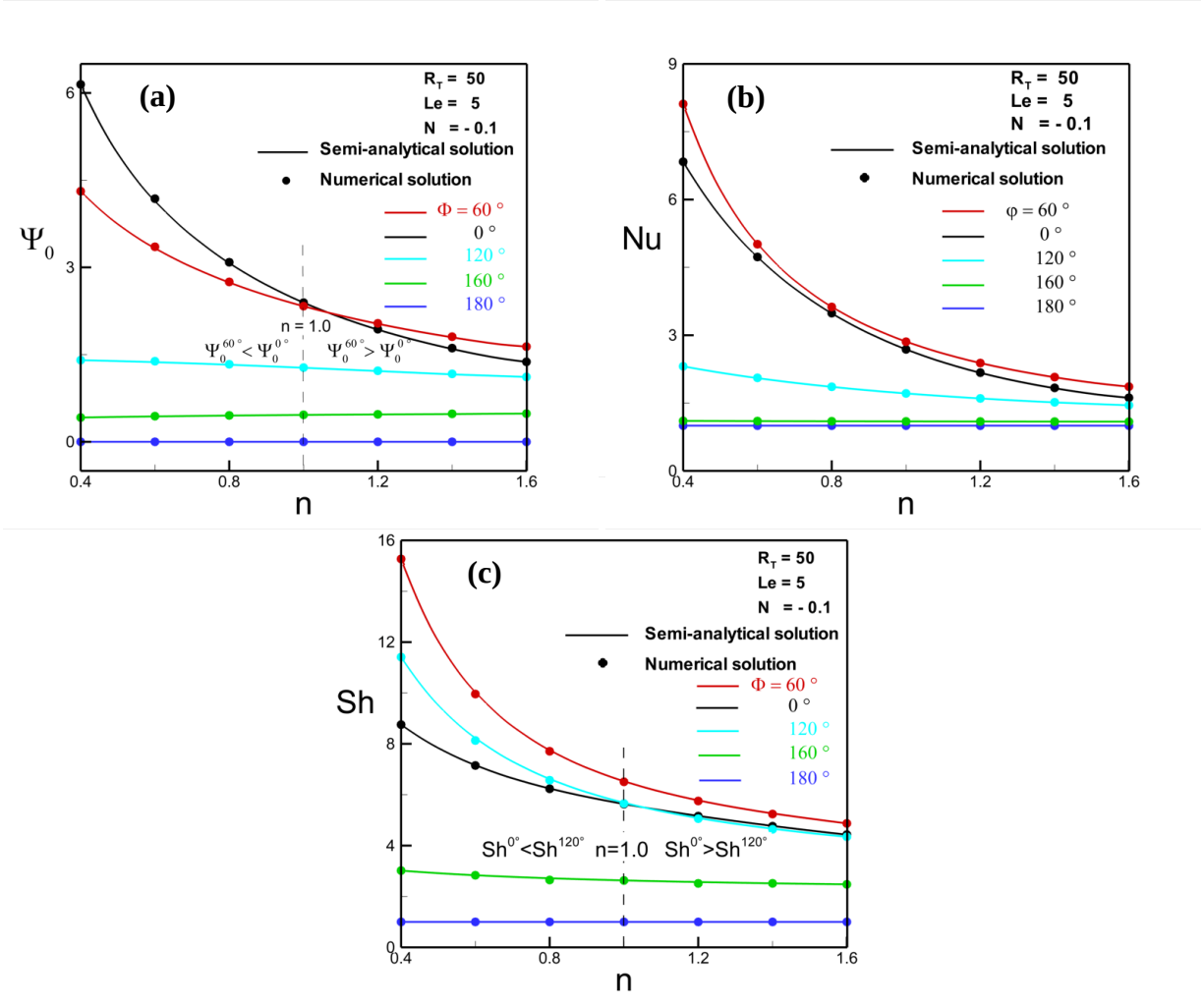


Figure 6.32: Effects of power-law index n, and inclination angle Φ, for $R_T = 50$, on: stream function Ψ_0 at the center of the cavity, (b) Nusselt number Nu, and (c) Sherwood number Sh.

6.3 VERTICAL LAYER: $\Phi = 90°$

In this section, we investigate a vertical porous layer (i.e., an inclined layer with Φ=90°) where the Buoyancy forces have equal intensity but in opposing directions $N = -1$

Figure. 6.33 presents the contours of streamlines, Ψ, Temperature, T, Concentration, S, and apparent viscosity, μ_a, obtained numerically, for a vertical cavity heated from the where $R_T = 100$, $Le = 5$, $N = -1$, and $\Phi = 90$, and different values of power-law index n. The intensity of flow, Ψ_0, in the core region of the enclosure is essentially parallel while the temperature T, and the concentration S in the core of the cavity are linearly stratified in the x-direction, The apparent viscosity, μ_a, lines are uniformly distributed between the center, and the edges of the cavity and the extremum value, and it's clearly constant when n=1.

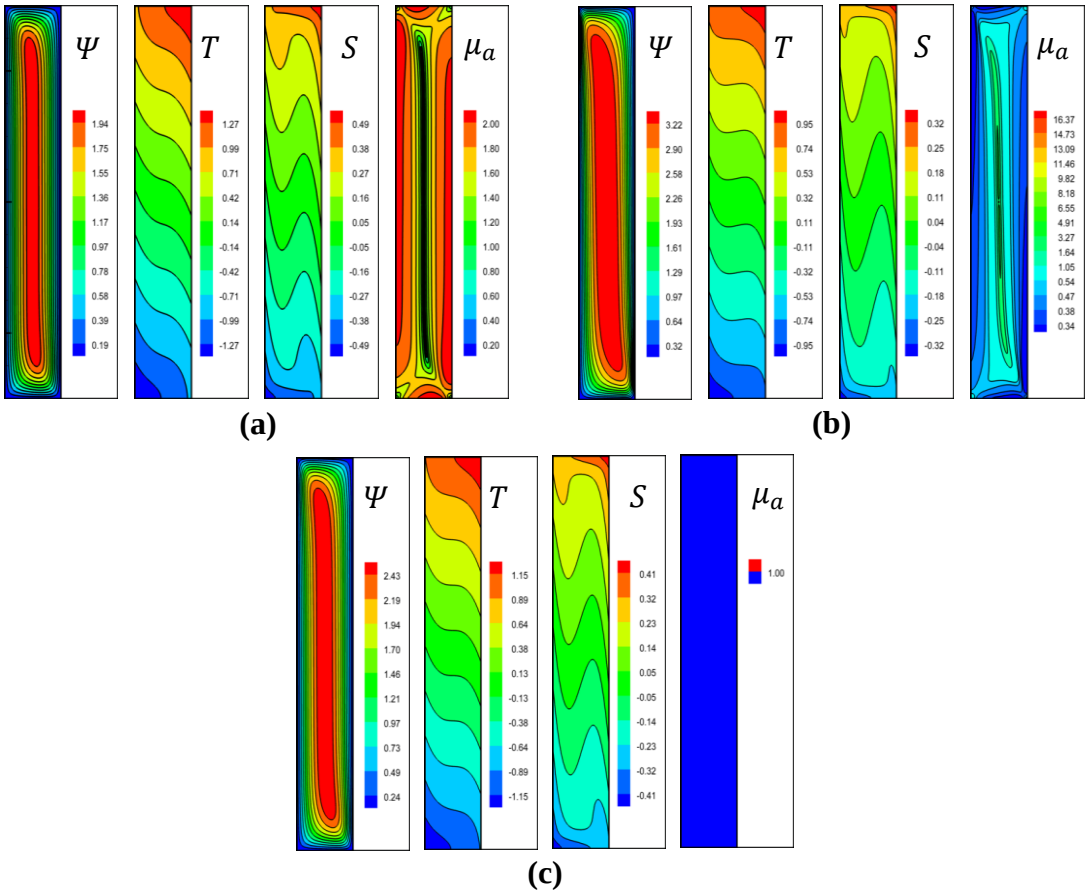


Figure 6.33: Numerical solutions for the Streamlines, isotherms, concentration, and apparent viscosity fields in a vertical cavity ($\Phi = 90°$) with $R_T = 100$, $Le = 5$, and $N = -1$ for (a) $n = 1.4$, $\Psi_0 = 2.132$, $Nu = 2.161$, $Sh = 4.572$, and $\mu_a = 0.273$ (b) $n = 0.6$, $\Psi_0 = 3.547$, $Nu = 3.910$, $Sh = 6.431$, and $\mu_a = 18.005$ (c) $n = 1.0$, $\Psi_0 = 2.672$, $Nu = 2.733$, $Sh = 5.095$, and $\mu_a = 1.000$

Figures 6.34 depict the influence of the power-law index n on vertical velocity U, apparent viscosity μ_a temperature T, and concentration S profiles at the mid-height of the porous layer (i.e., $x = 0$) for $0.6 < n < 1.4$, with $R_T = 100$, $N = -1$, and $Le = 5$. These figures demonstrate that the asymptotic semi-analytical solution, represented by solid lines, aligns closely with the numerical results denoted by solid circles. In Figure 6.34(a), the vertical velocity visibly diminishes with increasing n, rendering it negligible at the center and pronounced at the cavity's sides. This trend is mirrored in Figure 6.34(b) concerning the apparent viscosity, where it is large at the sides for shear-thickening fluids ($n > 1$) and minimal for shear-thinning fluids, while in the center, the inverse holds true. Notably, in the case of Newtonian fluid ($n = 1$), the apparent viscosity remains constant ($\mu_a = 1$). Figures 6.34(c)-(d) reveal that both temperature and concentration profiles exhibit enhancement with rising values of the power-law index, n. Furthermore, all curves exhibit a consistent slop at the boundary as a result of the constant heat and mass flux applied to the vertical walls.

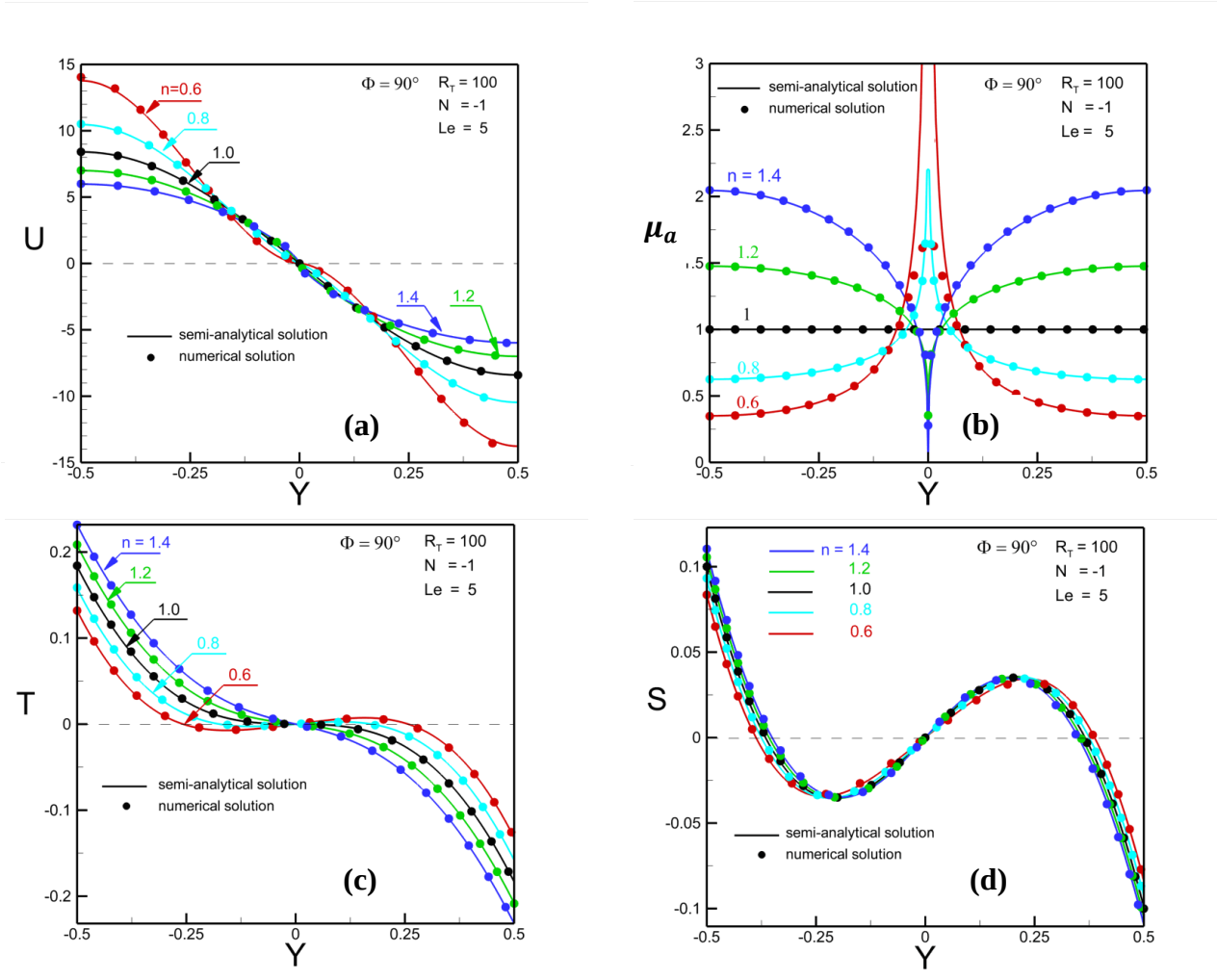


Figure 6.34: Effect of power-law index n with $\Phi = 90°$, on (a) the horizontal velocity, U, (b) apparent viscosity, μ_a, (c) temperature, T, and (d) concentration, S.

Figure. 6.35. illustrates the evolution of the strength of convection Ψ_0, and the Nusselt Nu number, and Sherwood Sh numbers as a function of the Rayleigh number R_T, with various values of the power-law index n for $Le = 5$, $N = -1$. For high R_T values, only the asymptotic trend of the semi-analytical solution is accounted for due to the numerical results deviating from the semi-analytical solution at high Rayleigh numbers. Generally, it is observed from Figures 6.35(a)-(b) that for a given Rayleigh number R_T, both the strength of convection Ψ_0, and the Nusselt number Nu, and Sherwood Sh number increase as the power-law index, n, decreases. It is also noted that Ψ_0 increases monotonically with R_T, as depicted in Figure 6.35(a), whereas in Figure 6.35(b), the Nusselt number Nu, and Sherwood number Sh rise asymptotically towards constant values $Nu = Sh = 6.129, 5.600, 5.278, 5.065, 4.913$ for $n = 0.6, 0.8, 1.0, 1.2, 1.4$ respectively. These constants depend solely on the value of the power-law index n, irrespective of the values of N and Le.

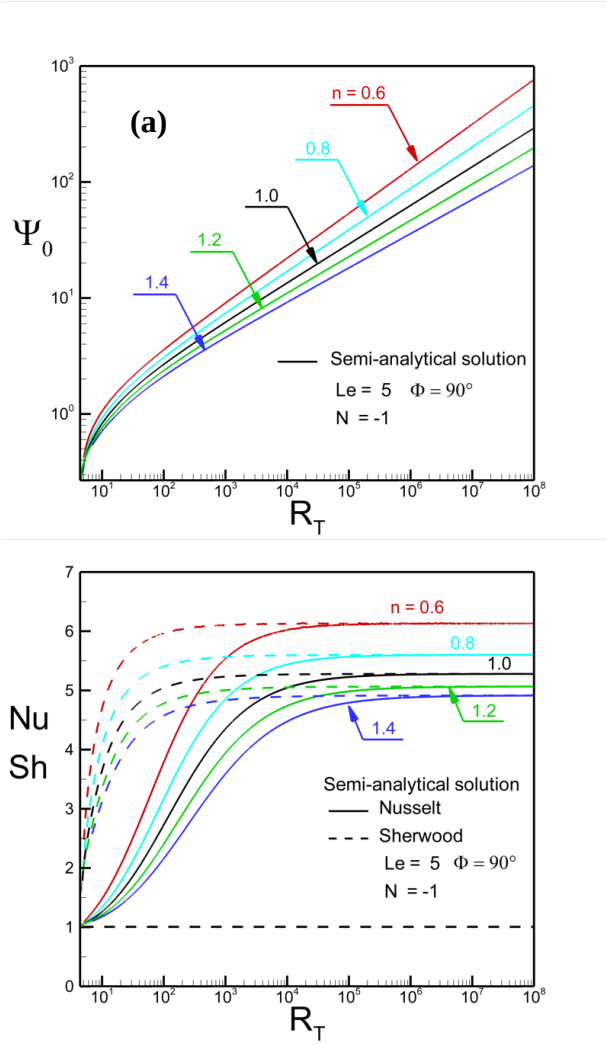


Figure 6.35: Large Rayleigh number R_T and power-law index n effects on (a) the flow intensity Ψ_0 and (b) the Nusselt Nu and Sherwood Sh number.

The variations of Ψ_0, Nu, and Sh as a function of Lewis number Le, and the power-law index n, for $R_T = 100$ and $N = -1$, are exhibited in Figure 6.36(a)-(c). The subcritical values of Le for the selected R_T and N are outlined in Table 4. Between these limits, heat and mass transfer occur solely via conduction. Excluding these boundaries, two regions emerge in each figure where two convective solutions originate from the fluid's rest state: one is stable (solid line), and the other is unstable (dashed line). From Figure 6.36(a)-(c), a notable concurrence is observed between the semi-analytical and numerical outcomes, represented by solid circles. It is evident that for a given Le value, both the convective strength Ψ_0, Nu, and Sh increase as the power-law index, n, decreases. For $Le < 1$, the mass transfer predominates the convective flow and accentuates the heat transfer. Conversely, for $Le > 1$, the convective strength, along with the heat and mass transfer rates, augments with Le, eventually leveling off with a high Le value. The flow's rotational direction is directly contingent on the Lewis number's value. As depicted in Figure 6.36(a) and 6.36(d), the flow rotates clockwise ($\Psi_0 < 0$) when $Le < 1$ and counterclockwise ($\Psi_0 > 0$) when $Le > 1$.

To elucidate the flow rotation's direction, let's examine the case with $Le > 1$. In such a scenario, where the thermal diffusivity, α, surpasses the mass diffusivity, D, both analytical and numerical solutions concur that the flow's circulation is counterclockwise. With $\alpha > D$, the volume of mass transported by convection along the vertical cavity walls outweighs the heat's volume. Consequently, the quantity of heat transferred through the system supersedes that of mass. This creates a dominant horizontal temperature gradient. As thermal effects contribute to a density decrease on the right side of the cavity and a density increase on the left side, a counterclockwise flow circulation is induced.

Table 6.8: The subcritical values of Le for $R_T = 100$ and $N = -1$

	Power-law index n				
Le	0.6	0.8	1.0	1.2	1.4
$\boldsymbol{Le_{<1}^{sub}}$	0.87	0.85	0.83	0.80	0.77
$\boldsymbol{Le_{>1}^{sub}}$	1.12	1.15	1.17	1.190	1.20

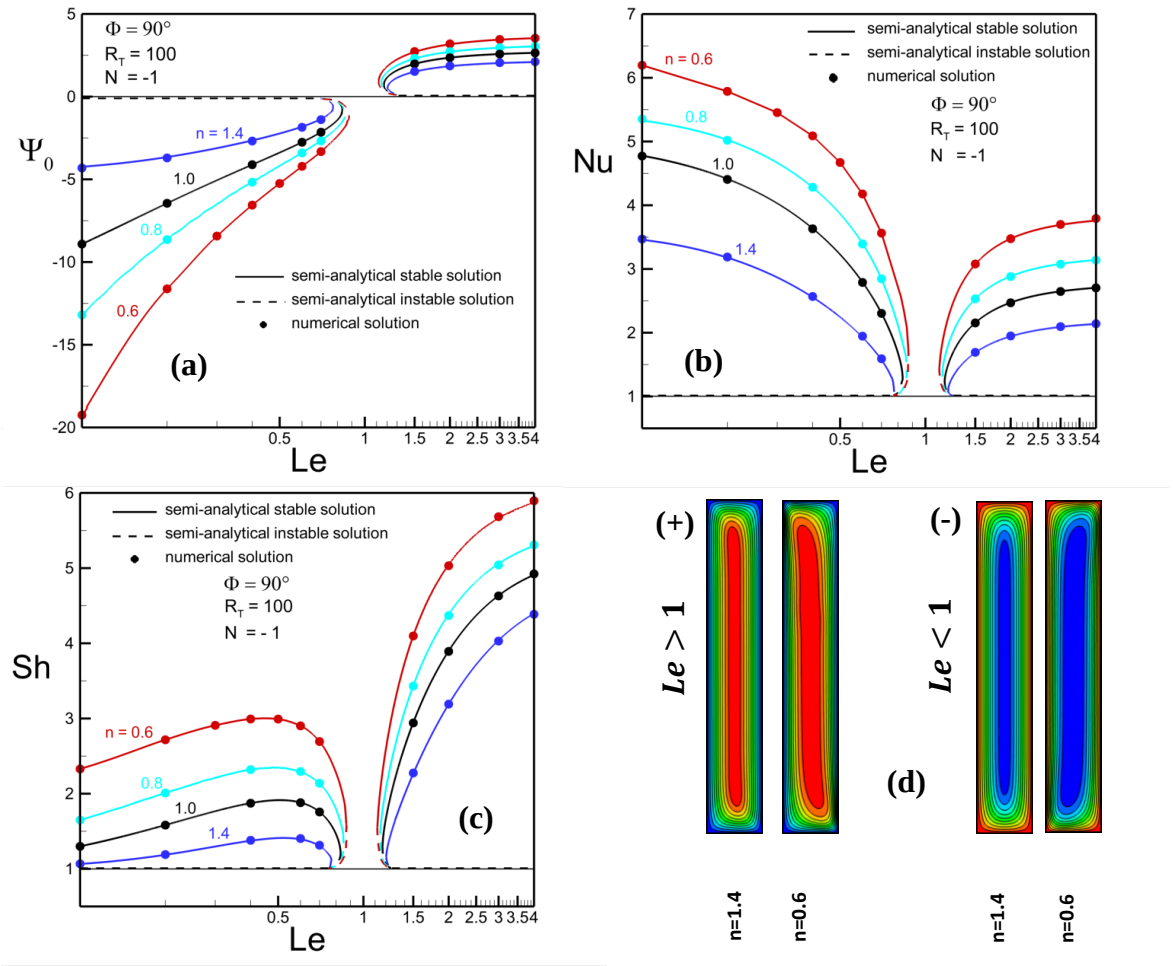


Figure 6.36: Effect of Lewis number Le and power-law index n on (a) the flow intensity Ψ_0, (b) the Nusselt number Nu, and (c) Sherwood number Sh.

An alternative perspective on the influence of the Buoyancy ratio, N, and power-law index n on Ψ_0, Nu, and Sh, with $R_T = 100$, $Le = 5$, $N = -1$ and $\Phi = 90°$, is delineated in Figure. 6.37(a)-(c). The buoyancy ratio N, which is determined by the strength of solutal fluxes applied to the vertical walls of the enclosure, ranges from -5 to 5. This encompasses conditions ranging from flow dominated by solutal effects $N = 5$ to purely thermal-driven flow $N = 0$ to counter-solutal flow $N = -5$. The graph reveals two distinct curves for each value of n. One curve begins from $N = 5$, reaching a subcritical value of $N_n^{sub} = 1.31$; -1.43; -1.55; -1.67; -1.79, respectively for $n = 0.6$; 0.8; 1.0; 1.2; 1.4, while the other starts from -5 and extends to -1, irrespective of n. Within the buoyancy ratio range of $N_n^{sub} < N < -1$, there are two solutions depicted, with the upper solution exhibiting counterclockwise flow ($\Psi_0 > 0$) and the lower solution clockwise flow ($\Psi_0 < 0$). The transition between these solutions is highlighted in Figure 6.37(d) for $n =$ 0.6 and 1.4, with $N = -1.2$ and -1.4

respectively. In the special case of $N = -1$, the buoyancy forces from thermal and solutal effects are equal and opposite, rendering the rest state a feasible solution to the governing equations.

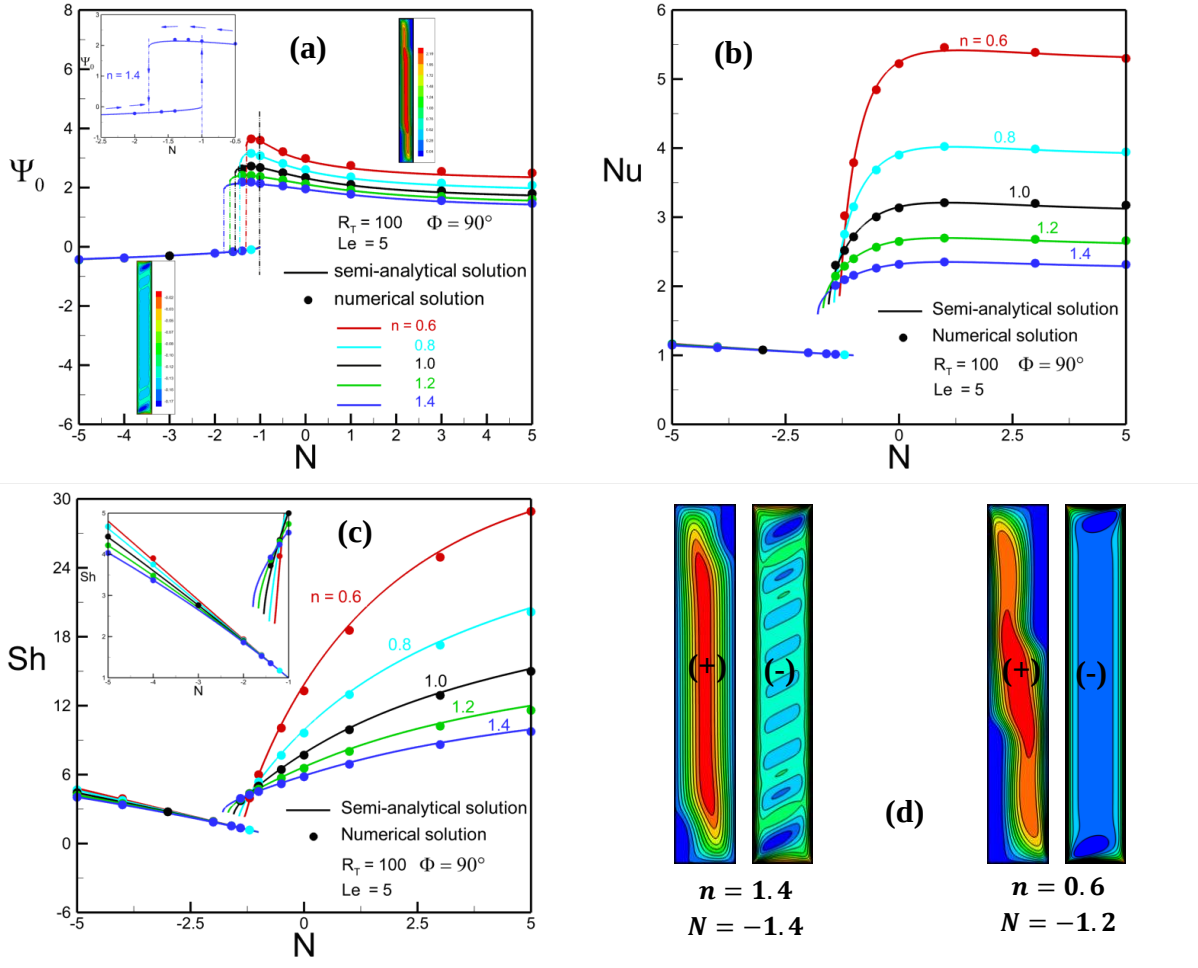


Figure 6.37: Effect of Buoyancy ratio N and power-law index n on (a) the flow intensity Ψ_0, (b) the Nusselt number Nu, and (c) Sherwood number Sh.

CHAPTER VII:

GENERAL CONCLUSIONS

This doctoral thesis delved into the heat and mass transfers driven by natural convection arising from double diffusion within an inclined rectangular porous layer saturated with a binary fluid. The system was subjected to Neumann-type thermal and solute boundary conditions, involving constant heat and concentration fluxes, or Dirichlet-type conditions, with imposed constant temperature and concentration. The formulation of the governing equations of the system was based on the power-law model.

Utilizing the Boussinesq approximation, we formulated a mathematical model to describe the convective flow and heat and mass transfer phenomena. Addressing this problem, we adopted two distinct approaches to tackle the resultant equations comprehensively. Initially, we employed a numerical method relying on a finite difference scheme. The system of equations is discretized employing the Alternate Direction Implicit (ADI) method. Additionally, for resolving the stream function equation, we utilized the Successive Over-Relaxation (SOR) method. Subsequently, for shallow cavities ($A \gg 1$) exposed to constant heat and mass fluxes, we derived analytical solutions utilizing the parallel flow approximation. A linear stability analysis is also conducted to predict various critical Rayleigh numbers marking different convection thresholds. Both the fundamental equations and the linear stability equations have been numerically solved, utilizing the finite element method.

This thesis extensively deliberates on the impact of each problem parameter. These parameters encompass the Rayleigh number, R_T, the power-law index, n, the cavity's aspect ratio, A, the buoyancy force ratio, N, the normalized porosity, ξ, the Lewis number, Le, and the inclination angle, Φ. The validation of the computational codes has been conducted by comparing the obtained results with those documented in existing literature.

The main findings derived from the current analysis are outlined as follows:

7.1 HORIZONTAL LAYER ($A \gg 1$)

(a) For the first part, results are presented for the velocity, apparent viscosity, temperature and concentration fields, revealing a significant sensitivity to the power law-index n. It is shown that an increasing in the power-law index (dilatant fluids) enhancing the apparent viscosity

while a decreasing (pseudoplastic fluids) reduces it, and it's constant for the case of Newtonian fluid $(n = 1)$, it is observed that the temperature and concentration profiles exhibit an augmentation with increasing values of the power-law index, n.

(b) It was observed that the intensity of convection $\Psi_0$and the resulting heat Nu and mass Sh transfer rates experienced enhancement with a decrease in the value of n, and N, while reduces it when Le decrease.

(c) The resulting nonlinear solution indicated that the threshold of finite amplitude motion occurred at a supercritical Rayleigh number (R_{TC}^{sup}), which considerably decreased upon increasing the power-law index n, and N, and Le decrease.

(d) Specifically, the manifestation of Bistability convection phenomena, denoted by the coexistence of two distinct stable solutions under identical flow and boundary conditions, is contingent upon specific values of n, N, and Le. Notably, this phenomenon is associated with the characteristics of a dilatant fluid $(n > 1)$ and opposing buoyancy forces $(N < 0)$. The bistability bifurcation was observed to traverse three saddle-node points, corresponding to the thresholds R_{TC}^{sub}, R_{TC}^{sup}, and R_{TC}^{tur}. This bifurcation exhibited three branches, resulting in an "S" shape curve. The first branch bifurcated forward from $R_{TC}^{sup}$to R_{TC}^{tur}, the second bifurcated backward from $R_{TC}^{tur}$to R_{TC}^{sub}but was deemed unstable, and a third stable branch bifurcated forward from R_{TC}^{sub}. Furthermore, it was demonstrated that this bistability phenomenon could manifest irrespective of the aspect ratio of the enclosure and the types of thermal and solutal boundary conditions.

(e) In the case of opposing convective flows, there was a collaborative influence of both shear-thinning and slow-diffusing solute effects, resulting in the augmentation of subcritical convective flows. Conversely, for aiding convective flows, a cooperative impact of shear-thickening and slow-diffusing solute effects was observed, leading to the enhancement of supercritical convective flows.

(f) The occurrence of Bistability convection was attributed to the cooperative counteracting influences within the fluid system. Specifically, the dilatant fluid. Simultaneously, the slower diffusing component in the binary mixture tended to maintain uniformity within the core region of the system while establishing a pronounced solute gradient near the walls.

7.2 SQUARE LAYER ($A = 1$)

(a) Depending on the power law index n and specific values of the governing parameters, the orientation of the cavity has an important effect on the intensity of flow, the heat and mass transfer rates. Regardless of the selected power-law index, n, the highest heat and mass transfer rates under both Neumann-type and Dirichlet-type boundary conditions are observed within the angular ranges of $(10° < \Phi < 70°)$ and $(20° < \Phi < 90°)$, respectively.

(b) The stream function Ψ_0, Nusselt number Nu, and Sherwood number Sh exhibit significantly higher values under Dirichlet-type boundary conditions compared to Neumann-type boundary conditions.

(c) For an inclined cavity with $\Phi = 90°$ (i.e., a vertical cavity), increasing the buoyancy ratio, N, enhances heat and mass transfer due to the dominant buoyancy force. Additionally, the transition from a conductive regime to a convective regime is highly dependent on the power-law index, n, under both Neumann-type and Dirichlet-type boundary conditions.

(d) The phenomenon of bi-stability, characterized by the coexistence of two distinct stable solutions, has been demonstrated in a square cavity under both Neumann-type and Dirichlet-type boundary conditions. This occurrence is notably associated with the properties of dilatant fluids ($n > 1$) and opposing buoyancy forces ($N < 0$).

(e) The power-law index, n, increasingly affected the bi-stability zone. It was discovered that when values of n are increased, the bistability region diminishes and eventually disappears.

7.3 INCLINED LAYER ($A \gg 1$)

(a) The spatial orientation of the enclosure significantly influences convective heat and mass transfer for specific values of the Rayleigh number R_T and the power-law index n. Irrespective of the chosen power-law index, n, optimal heat and mass transfer rates are observed when the layer is successively heated from the bottom within the angular range of $(0° < \Phi < 90°)$ and $(60° < \Phi < 120°)$. The Nusselt number peaks, associated with a given Rayleigh number, are contingent upon certain angles, denoted as Φ_{max}, with their values varying notably with the power-law index, n. As an illustration, for $R_T = 50$, the corresponding Φ_{max} is 40° when $n = 1.2$ and 36° when $n = 0.8$.

7.4 VERTICAL LAYER ($A \gg 1$)

(a) It was noticed that for an inclined cavity with $\Phi = 90°$ (i.e., Vertical cavity), the Nusselt number Nu and the Sherwood number Sh tend to asymptotic constant values for specific n. These constants are exclusively determined by the power-law index n, regardless of the values of N and Le.

(b) For Lewis values less than 1, mass transfer dominates the convective flow, causing a clockwise rotation. Conversely, for $Le > 1$, the flow rotates counterclockwise, and with high Le values, the convection strength, along with heat and mass transfer rates, tends to be constant.

(c) For buoyancy ratios N below -1, the transition zone between thermally driven single-cell rotation and solute-driven single-cell rotation is highly reliant on the power-law index n of the non-Newtonian fluid.

Comprehending double-diffusive convection in porous media, particularly with non-Newtonian fluids, holds considerable importance for both societal and academic realms. This understanding finds practical applications across diverse industries like solar energy systems, nuclear reactors, and industrial processes, offering avenues for enhancing energy efficiency and reduced environmental impact.

The research outcomes have the potential to enrich academia by pushing the boundaries of comprehension regarding intricate fluid dynamics phenomena. Moreover, they can play a pivotal role in refining mathematical models and computational methodologies, thereby facilitating more precise simulations of natural convection across various scenarios.

Moreover, the methodologies utilized in this study, comprising numerical and semi-analytical solutions, provide valuable instruments for forthcoming inquiries in related domains. Researchers can leverage these approaches to delve into supplementary parameters, enhance prevailing models, and tackle novel research inquiries. In essence, the outcomes derived from this research hold promise for catalyzing advancements in both practical applications and theoretical comprehension across the scientific community.

7.5 RECOMMENDATIONS AND PERSPECTIVES

In this investigation, the mathematical model relies on several simplifications. In practical scenarios, porous media exhibit anisotropic behavior, and fluid characteristics deviate from Newtonian assumptions. To advance our comprehension, it would be valuable to:

- reexamine this investigation using a non-Newtonian model, accounting for porous media anisotropy with varying permeability and thermal conductivity.
- Exploring alternative geometric configurations beyond those explored herein would also be insightful.
- Moreover, extending the model to encompass three-dimensional analyses, accommodating intricate geometries and diverse boundary conditions, is suitable.

A pivotal goal, necessitating substantial effort, is to validate the attained outcomes through experimental validation.

REFERENCES

[1] Ostrach, S. (1972). Natural convection in enclosures. In Advances in heat transfer (Vol. 8, pp. 161-227). Elsevier.

[2] Wu, Y. S., & Pruess, K. (1996). Flow of non-Newtonian fluids in porous media. In Advances in porous media (Vol. 3, pp. 87-184). Elsevier.

[3] Chandrasekhar, S. (2013). Hydrodynamic and hydromagnetic stability. Courier Corporation.

[4] Sen, M., Vasseur, P., & Robillard, L. (1987). Multiple steady states for unicellular natural convection in an inclined porous layer. International journal of heat and mass transfer, 30(10), 2097-2113.

[5] Bian, W., Vasseur, P., & Bilgen, E. (1994). Natural convection of non-Newtonian fluids in an inclined porous layer. Chemical Engineering Communications, 129(1), 79-97.

[6] Cengel, Y. A., Ghajar, A. J., & Kanoglu, M. (2011). Heat and mass transfer: fundamentals and applications.

[7] Bergman, T., Lavine, A., Incropera, F. P., & Dewitt, D. P. (2016). Fundamentals of Heat and Mass Transfer. Instructor, 201609.

[8] Nield, D. A., & Bejan, A. (2006). Convection in porous media (Vol. 3, pp. 629-982). New York: springer.

[9] Étude de la Convection Thermosolutale dans un Milieu Confiné Saturé par un Polluant de Type Non-Newtonien Par Lounis Selma Soutenue le 13/10/2023.

[10] Oberbeck, A. (1879). About the heat conduction of liquids, taking into account the flows resulting from temperature differences. Annals of Physics, 243(6), 271-292.

[11] Batchelor, G. K. (1967). An introduction to fluid dynamics. Cambridge university press. [12] Skelland, A.H.P., 1967. Non-Newtonian Flow and Heat Transfer, Wiley, New York, N.Y. Sorbie, K.S., Parker, A., and Chfford, P.J., 1987. Experimental and theoretical study of polymer flow.

[13] Böhme, G. (2012). Non-Newtonian fluid mechanics. Elsevier.

[14] Astarita, G., & Marrucci, G. (1974). Principles of non-Newtonian fluid mechanics.

[15] Crochet, M. J., Davies, A. R., & Walters, K. (2012). Numerical simulation of non-Newtonian flow. Elsevier.

[16] Hughes, W.F. and Brighton, J.A., 1967. Theory and Problems of Fluid Dynamics. Schaum's Outline Series, McGraw-Hill, N.Y., pp. 230-241.

[17] Bear, J., 1972. Dynamics of Fluids in Porous Media. American Elsevier, New York, N.Y..

[18] Boualit. A.H, thèse doctorat en science (2011), Universite M'hamed Bougara Boumerdes.

[19] Bird, R.B., Stewart, W.E., and Lightfoot, E.N., 1960. Transport Phenomena. Wiley, New York, N.Y

[20] Christopher, R.H. and Middleman, S., 1965. Power-law flow through a packed tube. I & EC Fundamentals, 4(4): 422-426.

[21] McKinley, R.M., Jahns, H.O., Harris, W.W., and Greenkorn, R.A., 1966. Non-Newtonian flow in porous media. AIChE J., 12(1): 17-20.

[22] Gogarty, W.B., 1967a. Rheological properties of pseudoplastic fluids in porous media. Soc. Pet. Eng.J., 149-159.

[23] Harvey, A.H. and Menzie, D.E., 1970. Polymer solution flow in porous media. Soc. Pet. Eng. J.,111-118.

[24] Mungan, N., 1972. Shear viscosities of ionic polyacrylamide solutions. Soc. Pet. Eng. J., 469-473

[25] Hirasaki, G.J. and Pope, G.A., 1974. Analysis of factors influencing mobility and adsorption in the flow of polymer solution through porous media. Soc. Pet. Eng. J., 337-346.

[26] Guazzelli, E. (2001). Rhéologie des fluides complexes.

[27] Baird, D. G., & Collias, D. I. (2014). Polymer processing: principles and design. John Wiley & Sons.

[28] Sochi, T. (2010). Non-Newtonian flow in porous media. Polymer, 51(22), 5007-5023.

[29] Amari, B., Vasseur, P., & Bilgen, E. (1994). Natürliche Konvektion nicht-Newtonscher Fluide in einer horizontalen porösen Schicht. Wärme-und Stoffübertragung, 29, 185-193.

[30] Landry, M. P., Frigaard, I. A., & Martinez, D. M. (2006). Stability and instability of Taylor–Couette flows of a Bingham fluid. Journal of Fluid Mechanics, 560, 321-353.

[31] Midoux, N. (1985). Mécanique et rhéologie des fluides en génie chimique. Paris: Technique et documentation.

[32] Brodkey, R. S., & Hershey, H. C. (1988). Transport past immersed bodies. In Transport Phenomena. McGraw-Hill New York.

[33] Carreau, P. J. (1972). Rheological equations from molecular network theories. Transactions of the Society of Rheology, 16(1), 99-127.

[34] Bird, R. B., Armstrong, R. C., & Hassager, O. (1987). Dynamics of polymeric liquids. Vol. 1: Fluid mechanics.

[35] Bories, S., Mojtabi, A., Prat, M., & Quintard, M. (2008). Transferts de chaleur dans les milieux poreux: Conduction, convection, rayonnement. Techniques de l'ingénieur. Génie énergétique, (BE8250).

[36] Kaviany, M. (2012). Principles of heat transfer in porous media. Springer Science & Business Media.

[37] Scheidegger, A. E. (1957). The physics of flow through porous media. University of Toronto press.

[38] Bejan, A., & Lage, J. L. (1991). Heat transfer from a surface covered with hair. In Convective heat and mass transfer in porous media (pp. 823-845). Dordrecht: Springer Netherlands.

[39] Collins, R. E. (1976). Flow of fluids through porous materials.

[40] Ward, J. C. (1964). Turbulent flow in porous media. Journal of the hydraulics division, 90(5), 1-12.

[41] Bear, J. (2013). Dynamics of fluids in porous media. Courier Corporation.

[42] Dybbs, A., & Edwards, R. V. (1984). A new look at porous media fluid mechanics—Darcy to turbulent. Fundamentals of transport phenomena in porous media, 199-256..

[43] Dupuit, J. E. (1863). Etudes théoriques et pratiques sur le mouvement des eaux dans les canaux découverts et à travers les terrains perméables avec des considérations relatives au régime des grandes eaux, au débouché à leur donner, et à la marche des des alluvions dans les rivières à fond mobile. Dunod, éditeur.

[44] Forchheimer, P. H. (1901). Wasserbewegung. Ver. Dtsch. Ing., 45, 1782-1788.

[45] Joseph, D. D., Nield, D. A., & Papanicolaou, G. (1982). Nonlinear equation governing flow in a saturated porous medium. Water Resources Research, 18(4), 1049-1052.

[46] Beavers, G. S., Sparrow, E. M., & Rodenz, D. E. (1973). Influence of bed size on the flow characteristics and porosity of randomly packed beds of spheres.

[47] Coulaud, O., Morel, P., & Caltagirone, J. P. (1988). Numerical modelling of nonlinear effects in laminar flow through a porous medium. Journal of Fluid Mechanics, 190, 393-407.

[48] Ergun, S. (1952). Fluid flow through packed columns. Chemical engineering progress, 48(2), 89.

[49] Brinkman, H. C. 1947a A calculation of the viscous force exerted by a flowing fluid on a dense swarm of particles. Appl. Sci. Res. A 1, 27–34. [1.5.3]

[50] Brinkman, H. C. 1947b On the permeability of media consisting of closely packed porous particles. Appl. Sci. Res. A 1, 81–86. [1.5.3]

[51] Neale, G., & Nader, W. (1974). Practical significance of Brinkman's extension of Darcy's law: coupled parallel flows within a channel and a bounding porous medium. The Canadian Journal of Chemical Engineering, 52(4), 475-478.

[52] Beckermann, C., & Viskanta, R. (1988). Double-diffusive convection during dendritic solidification of a binary mixture. PhysicoChemical Hydrodynamics, 10(2), 195-213.

[53] Vadász, P. (2008). Nanofluid suspensions and bi-composite media as derivatives of interface heat transfer modeling in porous media. In Emerging Topics in Heat and Mass Transfer in Porous Media: From Bioengineering and Microelectronics to Nanotechnology (pp. 283-326). Dordrecht: Springer Netherlands.

[54] Mebarek-Oudina, F., & Bessaïh, R. (2016). Oscillatory magnetohydrodynamic natural convection of liquid metal between vertical coaxial cylinders. Journal of Applied Fluid Mechanics, 9(4), 1655-1665.

[55] Ingham, D. B., & Pop, I. (Eds.). (2005). Transport phenomena in porous media III (Vol. 3). Elsevier.

[56] Vafai, K. (Ed.). (2015). Handbook of porous media. Crc Press.

[57] de Vahl Davis, G. "Natural convection of air in a square cavity: a bench mark numerical solution." International Journal for numerical methods in fluids 3.3 (1983): 249-264.

[58] Aydin, Orhan, Ahmet Ünal, and Teoman Ayhan. "Natural convection in rectangular enclosures heated from one side and cooled from the ceiling." International journal of heat and mass transfer 42.13 (1999): 2345-2355.

[59] Yang, Liu, and Yuhan Hu. "Toward TiO2 nanofluids-Part 2: applications and challenges." Nanoscale research letters 12 (2017): 1-21.

[60] Mahian, Omid, et al. "Recent advances in modeling and simulation of nanofluid flows-Part I: Fundamentals and theory." Physics reports 790 (2019): 1-48.

[61] Selimefendigil, Fatih, and Hakan F. Öztop. "Corrugated conductive partition effects on MHD free convection of CNT-water nanofluid in a cavity." International Journal of Heat and Mass Transfer 129 (2019): 265-277.

[62] Pordanjani, Ahmad Hajatzadeh, et al. "An updated review on application of nanofluids in heat exchangers for saving energy." Energy Conversion and Management 198 (2019): 111886.

[63] Moraga, Nelson O., Germán P. Parada, and Diego A. Vasco. "Power law non-Newtonian fluid unsteady conjugate three-dimensional natural convection inside a vessel driven by surrounding air thermal convection in a cavity." International Journal of Thermal Sciences 107 (2016): 247-258.

[64] Jahanbakhshi, Akram, Afshin Ahmadi Nadooshan, and Morteza Bayareh. "Magnetic field effects on natural convection flow of a non-Newtonian fluid in an L-shaped enclosure." Journal of Thermal Analysis and Calorimetry 133 (2018): 1407-1416.

[65] Lamsaadi, M., Naimi, M., Hasnaoui, M., & Mamou, M. (2006). Natural convection in a vertical rectangular cavity filled with a non-Newtonian power law fluid and subjected to a horizontal temperature gradient. Numerical Heat Transfer, Part A: Applications, 49(10), 969-990.

[66] Makayssi, T., et al. "Natural double-diffusive convection in a shallow horizontal rectangular cavity uniformly heated and salted from the side and filled with non-Newtonian power-law fluids: the cooperating case." Energy conversion and Management 49.8 (2008): 2016-2025.

[67] Kefayati, GH R. "Simulation of vertical and horizontal magnetic fields effects on non-Newtonian power-law fluids in an internal flow using FDLBM." Computers & Fluids 114 (2015): 12-25.

[68] Żyła, Gaweł, Jacek Fal, and Patrice Estellé. "The influence of ash content on thermophysical properties of ethylene glycol based graphite/diamonds mixture nanofluids." Diamond and Related Materials 74 (2017): 81-89.

[69] Kim, G. B., Hyun, J. M., & Kwak, H. S. (2003). Transient buoyant convection of a power-law non-Newtonian fluid in an enclosure. International journal of heat and mass transfer, 46(19), 3605-3617.

[70] Getachew, D., D. Poulikakos, and W. J. Minkowycz. "Double diffusion in a porous cavity saturated with non-Newtonian fluid." Journal of Thermophysics and Heat Transfer 12.3 (1998): 437-446.

[71] Moradi, Ahmad, et al. "An experimental study on MWCNT–water nanofluids flow and heat transfer in double-pipe heat exchanger using porous media." Journal of Thermal Analysis and Calorimetry 137.5 (2019): 1797-1807.

[72] Jena, Sofen K., et al. "Thermo-solutal buoyancy-opposed free convection of a binary Ostwald–De Waele fluid inside a cavity having partially-active vertical walls." Journal of the Taiwan Institute of Chemical Engineers 51 (2015): 9-19.

[73] Lounis, Selma, et al. "Thermo-Solutal Convection of Carreau-Yasuda Non-Newtonian Fluids in Inclined Square Cavities Under Dufour and Soret Impacts." CFD Letters 14.3 (2022): 96-118.

[74] Rebhi, R., Mamou, M., Vasseur, P., & Alliche, M. (2016). Form drag effect on the onset of non-linear convection and Hopf bifurcation in binary fluid saturating a tall porous cavity. International Journal of Heat and Mass Transfer, 100, 178-190.

[75] Rebhi, Redha, Mahmoud Mamou, and Patrick Vasseur. "Bistability and hysteresis induced by form drag in nonlinear subcritical and supercritical double-diffusive Lapwood convection in shallow porous enclosures." Journal of Fluid Mechanics 812 (2017): 463-500.

[76] Rebhi, Redha, Mahmoud Mamou, and Noureddine Hadidi. "Bistability bifurcation phenomenon induced by non-Newtonian fluids rheology and thermosolutal convection in Rayleigh–Bénard convection." Physics of Fluids 33.7 (2021).

[77] Bihiche, K., M. Lamsaadi, and M. Hasnaoui. "Multiple steady state solutions for double-diffusive convection in a shallow horizontal rectangular cavity uniformly heated and salted

from the side and filled with non-Newtonian power-law fluids." Journal of Non-Newtonian Fluid Mechanics 283 (2020): 104349.

[78] Benhadji, K., and P. Vasseur. "Double diffusive convection in a shallow porous cavity filled with a non-Newtonian fluid." International communications in heat and mass transfer 28.6 (2001): 763-772.

[79] Amari, B., P. Vasseur, and E. Bilgen. "Natural convection of non-Newtonian fluids in a horizontal porous layer." Waerme-und Stoffuebertragung;(Germany) 29.3 (1994).

[80] Kefayati, GH R. "Simulation of double diffusive natural convection and entropy generation of power-law fluids in an inclined porous cavity with Soret and Dufour effects (Part II: Entropy generation)." International Journal of Heat and Mass Transfer 94 (2016): 582-624.

[81] Nield, D. A., A. V. Kuznetsov, and Craig T. Simmons. "The effect of strong heterogeneity on the onset of convection in a porous medium: 2D/3D localization and spatially correlated random permeability fields." Transport in porous media 83 (2010): 465-477.

[82] Devakar, M., et al. "Fully developed flow of non-Newtonian fluids in a straight uniform square duct through porous medium." Journal of the Association of Arab Universities for Basic and Applied Sciences 23 (2017): 66-74.

[83] Uphill, Stephen J., Terence Cosgrove, and Wuge H. Briscoe. "Flow of nanofluids through porous media: Preserving timber with colloid science." Colloids and Surfaces A: Physicochemical and Engineering Aspects 460 (2014): 38-50.

[84] Narayana, PA Lakshmi, P. V. S. N. Murthy, and Adrian Postelnicu. "Soret and Dufour effects on free convection of non-Newtonian power law fluids with yield stress from a vertical flat plate in saturated porous media." Journal of Porous Media 12.10 (2009).

[85] Tsai, R., and J. S. Huang. "Numerical study of Soret and Dufour effects on heat and mass transfer from natural convection flow over a vertical porous medium with variable wall heat fluxes." Computational Materials Science 47.1 (2009): 23-30.

[86] Zhu, Q. Y., Y. J. Zhuang, and H. Z. Yu. "Three-dimensional numerical investigation on thermosolutal convection of power-law fluids in anisotropic porous media." International journal of heat and mass transfer 104 (2017): 897-917.

[87] Madhu, Macha, et al. "Performance of second law in Carreau fluid flow by an inclined microchannel with radiative heated convective condition." International Communications in Heat and Mass Transfer 117 (2020): 104761.

[88] Khelifa, N. Ben, et al. "Natural convection in a horizontal porous cavity filled with a non-Newtonian binary fluid of power-law type." Journal of Non-Newtonian Fluid Mechanics 169 (2012): 15-25.

[89] Bensilakhal, Sara, et al. "Bi-stability Study of Double Diffusive Convection Using the Carreau-Yasuda Model in a Shallow Horizontal Porous Layer Filled with a Non-Newtonian Fluid." Journal of Advanced Research in Fluid Mechanics and Thermal Sciences 101.1 (2023): 137-159.

[90] Naimi, M., M. Hasnaoui, and J. K. Platten. "Marangoni convection of non-Newtonian power law fluids in a shallow rectangular cavity." Engineering Computations 17.6 (2000): 638-668.

[91] Chen, Chien-Hsin. "Marangoni effects on forced convection of power-law liquids in a thin film over a stretching surface." Physics Letters A 370.1 (2007): 51-57.

[92] Lamsaadi, M., et al. "Parallel flow convection in a shallow horizontal cavity filled with non-Newtonian power-law fluids and subject to horizontal and vertical uniform heat fluxes." Numerical Heat Transfer, Part A: Applications 53.2 (2007): 178-203.

[93] Lamsaadi, M., M. Naimi, and M. Hasnaoui. "Natural convection heat transfer in shallow horizontal rectangular enclosures uniformly heated from the side and filled with non-Newtonian power law fluids." Energy conversion and Management 47.15-16 (2006): 2535-2551.

[94] Matin, M. Habibi, I. Pop, and S. Khanchezar. "Natural convection of power-law fluid between two-square eccentric duct annuli." Journal of Non-Newtonian Fluid Mechanics 197 (2013): 11-23.

[95] Alloui, Z., et al. "The onset of convection of power-law fluids in a shallow cavity heated from below by a constant heat flux." Journal of Non-Newtonian Fluid Mechanics 196 (2013): 70-82.

[96] Khali, Samir, et al. "Double diffusive convection of power law fluids through taylor–Couette flow." Journal of Thermophysics and Heat Transfer 36.2 (2022): 328-341.

[97] Ohta, Mitsuhiro, et al. "A numerical study on natural convective heat transfer of pseudoplastic fluids in a square cavity." Numerical Heat Transfer: Part A: Applications 41.4 (2002): 357-372.

[98] Hojjat, M., et al. "Rheological characteristics of non-Newtonian nanofluids: experimental investigation." International Communications in Heat and Mass Transfer 38.2 (2011): 144-148.

[99] Solomatov, V. S., and A. C. Barr. "Onset of convection in fluids with strongly temperature-dependent, power-law viscosity." Physics of the Earth and Planetary Interiors 155.1-2 (2006): 140-145.

[100] Solomatov, V. S., and A. C. Barr. "Onset of convection in fluids with strongly temperature-dependent, power-law viscosity: 2. Dependence on the initial perturbation." Physics of the Earth and Planetary Interiors 165.1-2 (2007): 1-13.

[101] Prasad, V., & Kulacki, F. A. (1984). Natural convection in a rectangular porous cavity with constant heat flux on one vertical wall.

[102] Mamou, M. (2002). Stability analysis of thermosolutal convection in a vertical packed porous enclosure. Physics of Fluids, 14(12), 4302-4314.

[103] Karimi-Fard, M., Charrier-Mojtabi, M. C., & Mojtabi, A. (1999). Onset of stationary and oscillatory convection in a tilted porous cavity saturated with a binary fluid: Linear stability analysis. Physics of Fluids, 11(6), 1346-1358.

[104] Sen, M., Vasseur, P., & Robillard, L. (1987). Multiple steady states for unicellular natural convection in an inclined porous layer. International journal of heat and mass transfer, 30(10), 2097-2113.

[105] Chan, B. K. C., Ivey, C. M., & Barry, J. M. (1970). Natural convection in enclosed porous media with rectangular boundaries.

[106] Trevisan, O. V., & Bejan, A. (1986). Mass and heat transfer by natural convection in a vertical slot filled with porous medium. International Journal of Heat and Mass Transfer, 29(3), 403-415.

[107] Ouriemi, M., Vasseur, P., & Bahloul, A. (2005). Natural convection of a binary fluid in a slightly inclined shallow cavity. Numerical Heat Transfer, Part A: Applications, 48(6), 547-565.

[108] Mamou, M., & Vasseur, P. (1999). Hysterisis effect on thermosolutal convection with opposed buoyancy forces in inclined enclosures. International communications in heat and mass transfer, 26(3), 421-430.

[109] M. P. Vlasuk, Convective heat transfer in a porous layer (in Russian) (1972), 4th All Union Heat and Mass Transfer Conf., Minsk.

[110] MARCOUX, M., Charrier-Mojtabi, M. C., & BERGEON, A. (1998). Naissance de la thermogravitation dans un mélange binaire imprégnant un milieu poreux. Entropie (Paris), 34(214), 31-36.

[111] A. Bejan, Convection Heat Tranfer (1984). Wiley, New York, pp. 335-338.

[112] Holst, P. H., & Aziz, K. (1972). A theoretical and experimental study of natural convection in a confined porous medium. The Canadian Journal of Chemical Engineering, 50(2), 232-241.

[113] Alloui, Z., Rebhi, R., Mamou, M., & Vasseur, P. (2017). Effects of quadratic drag on natural convection in a tilted porous layer with uniform heat flux from the side. International Journal of Heat and Mass Transfer, 115, 314-325.

[114] Vasseur, P., Satish, M. G., & Robillard, L. (1987). Natural convection in a thin, inclined, porous layer exposed to a constant heat flux. International Journal of Heat and Mass Transfer, 30(3), 537-549.

[115] Walch, J. P., & Dulieu, B. (1979). Free convection in a slightly inclined rectangular box filled with a porous medium. International Journal of Heat and Mass Transfer, 22, 1607-1612.

[116] Moya, S. L., Ramos, E., & Sen, M. (1987). Numerical study of natural convection in a tilted rectangular porous material. International journal of heat and mass transfer, 30(4), 741-756.

[117] Ozoe, H., Sayama, H., & Churchill, S. W. (1975). Natural convection in an inclined rectangular channel at various aspect ratios and angles—experimental measurements. International Journal of Heat and Mass Transfer, 18(12), 1425-1431.

[118] Hiroyuki, O., Hayatoshi, S., & Churchill, S. W. (1974). Natural convection in an inclined square channel. International Journal of Heat and Mass Transfer, 17(3), 401-406.

[119] Hiroyuki, O., Kazumitsu, Y., Hayatoshi, S., & Churchill, S. W. (1974). Natural circulation in an inclined rectangular channel heated on one side and cooled on the opposing side. International Journal of Heat and Mass Transfer, 17(10), 1209-1217.

[120] Khelifa, N. B., Alloui, Z., Beji, H., & Vasseur, P. (2012). Natural convection in a vertical porous cavity filled with a non-newtonian binary fluid. AIChE Journal, 58(6), 1704-1716.

[121] Khezzar, L., Siginer, D., & Vinogradov, I. (2012). Natural convection of power law fluids in inclined cavities. International Journal of Thermal Sciences, 53, 8-17.

[122] Inaba, H., Dai, C., & Horibe, A. (2003). Natural convection heat transfer of microemulsion phase-change-material slurry in rectangular cavities heated from below and cooled from above. International Journal of Heat and Mass Transfer, 46(23), 4427-4438.

[123] Malashetty, M. S., & Swamy, M. (2010). The onset of convection in a binary fluid saturated anisotropic porous layer. International journal of Thermal sciences, 49(6), 867-878.

[124] Bahloul, A., Boutana, N., & Vasseur, P. (2003). Double-diffusive and Soret-induced convection in a shallow horizontal porous layer. Journal of Fluid Mechanics, 491, 325-352.

[125] Seki, N., Fukusako, S., & Inaba, H. (1978). Heat transfer in a confined rectangular cavity packed with porous media. International Journal of Heat and Mass Transfer, 21(7), 985-989.

[126] Bankvall, C. G. (1974). Natural convection in vertical permeable space. Wärme-und Stoffübertragung, 7(1), 22-30.

[127] Weber, J. E. (1975). The boundary-layer regime for convection in a vertical porous layer. International Journal of Heat and Mass Transfer, 18(4), 569-573.

[128] Burns, P. J., Chow, L. C., & Tien, C. L. (1977). Convection in a vertical slot filled with porous insulation. International Journal of Heat and Mass Transfer, 20(9), 919-926.

[129] De Groot, S. R., & Mazur, P. (2013). Non-equilibrium thermodynamics. Courier Corporation.

[130] Pascal, H. (1983). Rheological behaviour effect of non-Newtonian fluids on steady and unsteady flow through a porous medium. International Journal for Numerical and Analytical Methods in Geomechanics, 7(3), 289-303.

[132] Pascal, H. (1986). Rheological effects of non-Newtonian behavior of displacing fluids on stability of a moving interface in radial oil displacement mechanism in porous media. International journal of engineering science, 24(9), 1465-1476.

[133] Cormack, D. E., Leal, L. G., & Imberger, J. J. (1974). Natural convection in a shallow cavity with differentially heated end walls. Part 1. Asymptotic theory. Journal of fluid Mechanics, 65(2), 209-229.

[134] Vasseur, P., Wang, C. H., & Sen, M. (1989). The Brinkman model for natural convection in a shallow porous cavity with uniform heat flux. Numerical Heat Transfer, 15(2), 221-242.

[135] Alavyoon, F. (1993). On natural convection in vertical porous enclosures due to prescribed fluxes of heat and mass at the vertical boundaries. International Journal of Heat and Mass Transfer, 36(10), 2479-2498.

[136] Mamou, M., Bilgen, E., Gobin, D., & Vasseur, P. (1995). Double-diffusive convection in an inclined slot filled with porous medium. European journal of mechanics. B, Fluids, 14(5), 629-652.

[137] Peaceman, D. W., & Rachford, Jr, H. H. (1955). The numerical solution of parabolic and elliptic differential equations. Journal of the Society for industrial and Applied Mathematics, 3(1), 28-41.

[138] Frankel, S. P. (1950). Convergence rates of iterative treatments of partial differential equations. Mathematics of Computation, 4(30), 65-75.

[139] Hasnaoui M, (1991). Étude numérique de la convection dans un champ de cavité. Thèse de doctorat,École Polytechnique de Montréal, Canada.

[140] Mamou, M. (1998). Convection thermosolutale dans des milieux poreux et fluides confinés. Ecole polytechnique de Montreal.

[141] Bejan, A. (2013). Convection heat transfer. John wiley & sons.

[142] Nield, D. A. (1968). Onset of thermohaline convection in a porous medium. Water Resources Research, 4(3), 553-560.

[143] Taunton, J. W., Lightfoot, E. N., & Green, T. (1972). Thermohaline instability and salt fingers in a porous medium. The Physics of Fluids, 15(5), 748-753.

[144] Poulikakos, D. (1986). Double diffusive convection in a horizontal sparcely packed porous layer. International communications in heat and mass transfer, 13(5), 587-598.

[145] Mamou, M., Bilgen, E., Gobin, D., & Vasseur, P. (1995). Double-diffusive convection in an inclined slot filled with porous medium. European journal of mechanics. B, Fluids, 14(5), 629-652.

[146] Mamou, M. (2003). Stability analysis of the perturbed rest state and of the finite amplitude steady double-diffusive convection in a shallow porous enclosure. International journal of heat and mass transfer, 46(12), 2263-2277.

[147] Bertholz, R. F. (1978). Instability of steady natural convection in a vertical layer. J. J. Fluid Mechanics, 84, 743-768.

[148] Ghorayeb, K., & Mojtabi, A. (1997). Double diffusive convection in a vertical rectangular cavity. Physics of Fluids, 9(8), 2339-2348.

[149] Joly, F., Vasseur, P., & Labrosse, G. (2001). Soret instability in a vertical Brinkman porous enclosure. Numerical Heat Transfer: Part A: Applications, 39(4), 339-35